Università degli Studi di Ferrara

DOCTORAL COURSE IN CHEMICAL SCIENCES

CYCLE XXXIV

DIRECTOR Prof. Alberto Cavazzini

New Components for Dye Sensitized Solar Cells

Scientific/Disciplinary Sector (SDS) CHIM/03

Candidate

Dott. Marchini Edoardo

Supervisor

Prof. Stefano Caramori

Co-Supervisor

Prof. Alessandro Massi

Years 2018/2022

INDEX

INTRODUCTION

The total world energy consumption is drastically increasing, the US Energy Information Administration has predicted that the energy demand will rise up from 19 TW in 2015 to 25 TW in 2040[1] even if the conventional processes, characterized by coal, crude oil, and natural gas, will provide up to 75% of the requirement.[1] It is estimated that oil and natural gas reserves will last only for other 50-60 years.[2] Furthermore, the employment of fossil fuels has been considered the main reason of the global warming and environmental pollution.[3] Greenhouse gas emissions have been rapidly increasing, and it is estimate to reach >1300 ppm CO_2eq by 2100 (430 ppm in 2011) which could cause the global mean surface temperature to increase up to ca. 5 °C.[3] The worldwide scientists have been spending their efforts to develop and commercialize renewable energy technologies such as solar, wind, biomass, geothermal and hydropower. The sun has the great advantage to be free, abundant, accessible to all and to have a spectrum that covers a wide range of wavelengths from 280 (4.43 eV) to 2500 nm (0.5 eV) (**Figure 0a**), with the peak power in the yellow region of the visible spectrum, at about 2.5 eV. At high noon on a cloudless day, the surface of the Earth at average latitudes receives 1000 watts of solar power per square meter (1 kW/m^2). Such standard irradiance is expressed as Air Mass 1.5 (AM 1.5G) condition.

(a) (b)

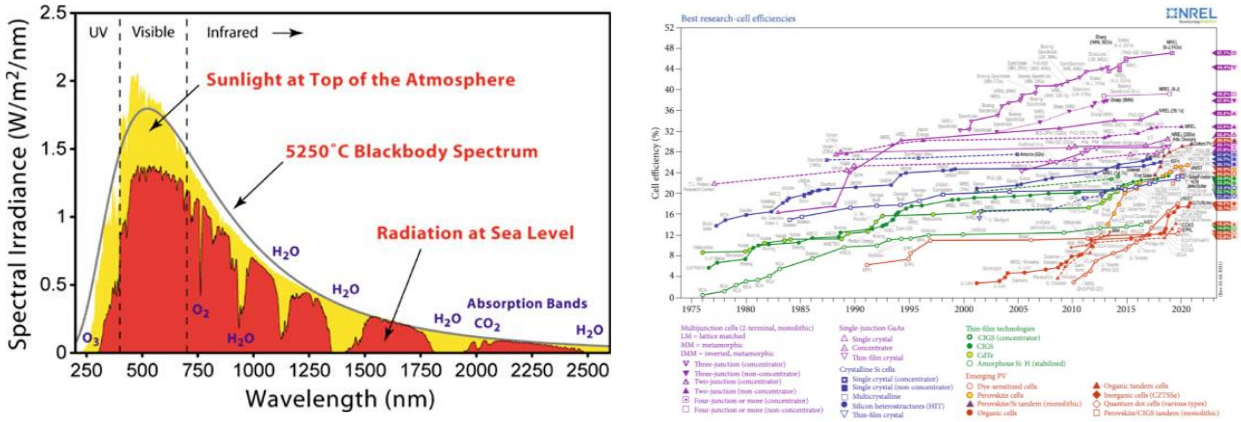

Figure 0: (a) Spectral distribution of solar irradiance, (b) Best solar cells efficiencies chart (2016) as recorded by NREL (National Renewable Energy Lab)

In the recent years, the research related to the photovoltaic devices has been rapidly increasing as well as their power conversion efficiency (PCE%), as depicted in **Figure 0b**. The silicon junctions are the most widespread technology, their market increased over the past two decades, although their cost is decreasing, the large-scale industrial production requires extensive and demanding processes, both in terms of production costs and both in terms of environmental impact.[4] Third-generation PV such as Dye Sensitized Solar Cells (DSSCs), Organic Solar Cells (OSCs), Perovskite Solar Cells (PSCs) and Organic Quantum Dots (OQDs) are actually under investigation as alternative technology. Recently the worldwide scientists have been spending their effort to study these systems and to increase the PCE%. To commercialize the PV devices it is not required only a high efficiency but some requirements should by met such as minimum cost, maximum initial performances as well as minimum loss of performances over time.[5] To date these alternative technologies have not yet achieved large-scale production but, the scientist's target is to increase the Power Conversion Efficiency, to increase the stability of the selected materials over the time as well as to employ low-cost materials and production processes.

AIM of the thesis

The focus of this thesis is about the investigation of new components for Dye Sensitized Solar Cells. The first experimental chapter will present a new family of Ru(II)-tetrazolato complexes and their performances will be compared with those one obtained with the well-known standard Ruthenium **N719**. A Conspicuous part will be related to the investigation of new Fe(II)NHC-based complexes in collaboration with the University of Lorraine. The first project will present the optimization of the electrolyte mixture as well as of the semiconductor substrate of a first homoleptic complex namely **C1**, increasing the literature reported efficiency from 0.13% to 1%.[6] Other two chapters will be related to the design and characterization of heteroleptic Fe(II)NHC complexes with the aim to improve the excited state directionality. A final chapter will be focused on the realization of a PEDOT-based alternative counter electrode produced by electro-polymerization of the EDOT monomer in an ecofriendly aqueous medium.

CHAPTER 1: Theoretical aspects

1.1 General Features of Dye Sensitized Solar Cells

Since the discovery of the Photoelectric Effect by the French scientist Edmond Becquerel,[7] worldwide scientists have been spending their efforts to generate electricity from the sun. This resource is freely accessible to all, it is possible to convert its light into electricity or into fuels as Hydrogen. Photovoltaic technology takes advantage of the fact that photons falling on a semiconductor can create electron–hole pairs, and at a junction between two different materials, this effect can set up an electric potential difference across the interface. Silicon junctions (p-n) are the main popular commercial photovoltaic devices, constituted by a stable element, abundant and non-toxic. These p-n junctions can harvest a large portion of the visible and NIR spectra thanks to their band gap close to 1.1 eV; considering only the radiative recombination pathways, theoretically, these systems are able to reach a PCE% close to 30%.[8] Besides these photovoltaic devices, third-generation PV must be cited, such as Dye Sensitized Solar Cells, Organic Solar Cells, Perovskite Solar Cells and Organic Quantum Dots. Since their first appearance in the early '90s in the Gräztel and O'Regan works,[9] DSSCs have attracted the interest of many scientists as alternative systems able to replace the traditional silicon junctions. DSSCs are characterized by unique features like transparency, capability to harvest diffuse light,[10] a wide pallet of colors that facilitate its building integration in indoor and outdoor conditions[11, 12] and low-cost. It is estimated a short payback period of less than 1 year[10] due to the use of accessible and less stringent materials as well as the possibility to pass from a laboratory prototype to industrial scale production. The main constituent components can be summarized as follow: 1) a transparent conductive substrate (glass or plastic) covered by a thin conductive oxide layer (TCO), generally composed of fluorine-doped tin oxide (FTO) with low sheet resistance or indium-doped tin oxide (ITO) with higher resistance; 2) a wide band-gap mesoporous semiconductor as TiO_2 in the anatase crystalline form; 3) a sensitizer anchored to the semiconductor nanoparticles that can be an inorganic complex as for example Ruthenium or Iron or otherwise organic molecules; 4) an electrolyte composed by a redox couple such as I^-/I_3^-, Co(II)/(III) or Cu(I)/(II) and 5) a counter electrode made of a transparent substrate as FTO or ITO with a thin layer of Pt or alternative systems like conductive polymers.

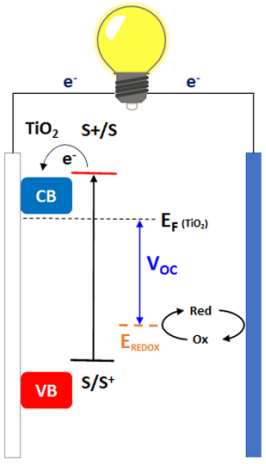

Figure 1.1: Schematic representation of the main components and processes involved in the functioning of DSSCs

The **Figure 1.1** summarizes the main processes involved in the solar to current conversion technology.[13-16] Upon absorption of sunlight, the sensitizer can inject electrons from its excited state into the conduction band of the semiconductor, its reduced form will be regenerated by the reduced form of the redox couple. Electrons in the TiO_2 are moved through the nanoparticles to the FTO collector by hopping. They will be available in the external circuit to generate an electric work and then they will be available at the counter electrode to regenerate the redox mediator.

1.1.0 Semiconductors: an overview

Semiconductors represent probably the most efficient way to convert solar energy into electrical or chemical energy.[17] The infinite number of atoms that compose solids leads to consider these substrates in terms of bands constitute of atomic orbitals or individual atoms:[18] as a result of the large numbers of interacting orbitals, the spacing of electronic energies within a band, arising from a given quantum state, becomes so small that the band can be effectively considered a continuum of energy levels, however the energy gap between the groups of levels, corresponding to different atomic quantum states, is preserved. The main interest bands are the highest occupied, namely Valence Band (VB) and the lowest unoccupied, namely Conduction Band (CB) (**Figure 1.2**).

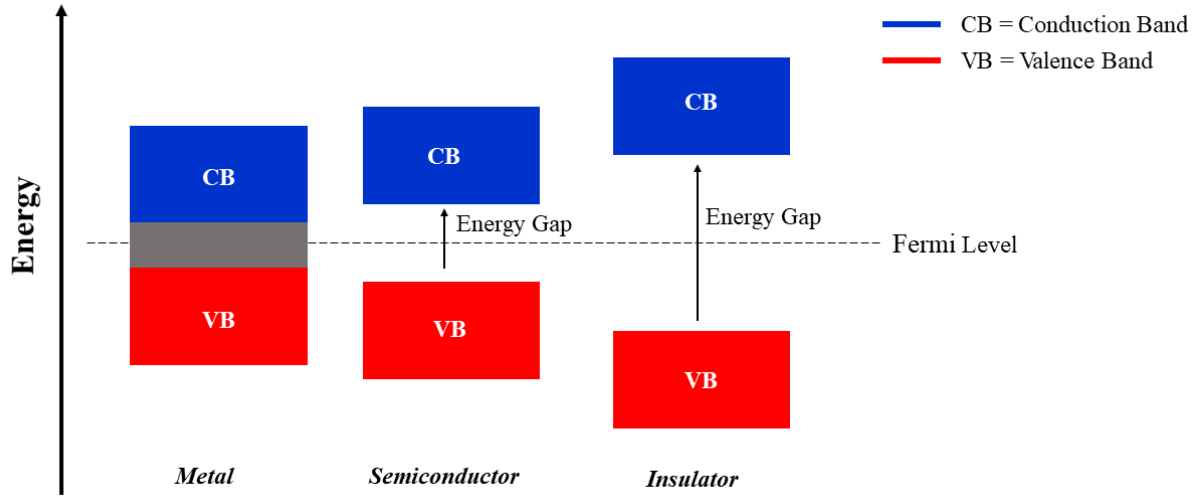

Figure 1.2: Schematic representation of Valence Band and Conduction Band for (a) Metals, (b) Semiconductors and (c) Insulators in terms of band theory

The difference between these two levels, called Energy gap (E_g), determines the properties of the material. In the case of a metal, the conduction band is partially filled or overlapped with the valence band. Electrons are free to move in an electric field and their large number results in a high conductivity (10^4-10^6 $\Omega^{-1}cm^{-1}$) of the material. In an insulator the valence band is fully filled, the conduction band is empty, and no net motion of charge follows the application of an electric field. A semiconductor can be described similarly, but in this case, electrons can be thermally or optically promoted from VB to CB, resulting in a lower conductivity compared to the metals one due to the smaller number of current carriers. The promotion of an electron to the Conduction Band leaves a vacancy, an occupied electron position, namely hole that can move through the material by transferring an electron to the vacancy and so results movable. Another essential concept is the Fermi Level, **eq. 1.1** represents the Fermi Dirac distribution:

$$f(E) = \frac{1}{1+e^{\frac{(E-E_F)}{K_B T}}} \qquad \textbf{eq. 1.1}$$

where f(E) represents the probability that a state of energy E is occupied, E_F the Fermi energy, K_B the Boltzmann's constant ($1.380649 \times 10^{-23} JK^{-1}$) and T the absolute temperature. The E_F corresponds to the energy level for which f(E) = 1/2, so this level is virtual, and it has a 50% probability to be filled by electrons. In the case of intrinsic semiconductors (such as Si and Ge), the Fermi Level is equidistant with respect to the valence and to the conduction band. An extrinsic semiconductor is created by adding electron rich or electron deficient impurities into the lattice of a semiconductor. Considering for example the case of Si, it is possible to generate an *n-type* semiconductor when an electron reach element as As is introduced in the system, because of the occupied molecular orbitals of Si are filled, the introduction of electron excess fill a new level close to the conduction band, called donor band (DB) (**Figure 1.3**). Otherwise, a *p-type* semiconductor is generated when an electron deficient element as Ga leads to create an acceptors band (AB) close to the valence band (**Figure 1.3**).

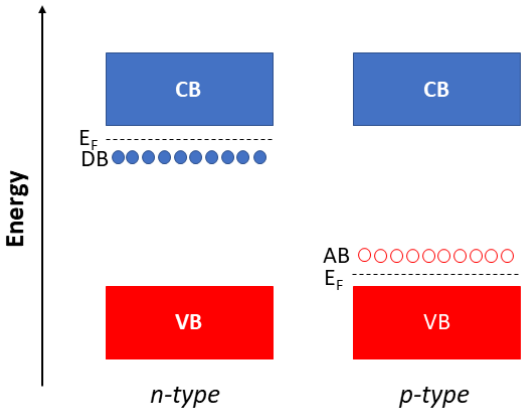

Figure 1.3: Schematic representation of donor band and acceptor band for an *n-type* and *p-type* semiconductor

1.1.1 Semiconductor-electrolyte interface

For a one-electron redox couple, the Nernst equation can be used to describe the electrochemical potential of electrons, or the redox potential or Fermi level as described in the **eq. 1.2**[19]

$$E_{F,redox} = E^{\circ}_{F,redox} + K_B T ln\left[\frac{C_{ox}}{C_{red}}\right] \qquad \textbf{eq. 1.2}$$

where C_{ox} and C_{red} are respectively the concentration of the oxidized and reduced form of the redox couple in the electrolyte, E°_{Redox} is the formal redox energy and K_B is the Boltzmann's constant. In the case of a nondegenerate semiconductor, the Fermi Level follows the **eq. 1.3**:

$$E_F = E_C + K_B T ln\left[\frac{n_c}{N_c}\right] \qquad \textbf{eq. 1.3}$$

where E_c is the energy of the conduction band evaluated on its edge (with respect to vacuum, it is obtained by the electron affinity E_A), n_c is the density of the electrons in the CB and N_c is the effective density of conduction band states. When a semiconductor is in contact with an electrolyte, if their Fermi Level does not lie at the same energy, a net motion of charge is expected until the equilibration of these two phases. In the case of an n-type semiconductor, the Fermi level is higher in energy with respect to the redox potential of the electrolyte and electrons are transferred to the solution, this results in a positive space charge region in the semiconductor and a consequent upward band bending as shown in **Figure 1.4a**. An opposite situation can be found in the case of a p-type semiconductor, the

electrons are transferred from the solution to the semiconductor substrate with a consequence negative space charge and a downward band bending (**Figure 1.4b**). In both these two situations, because the majority carrier is removed, the depletion region term can be used.

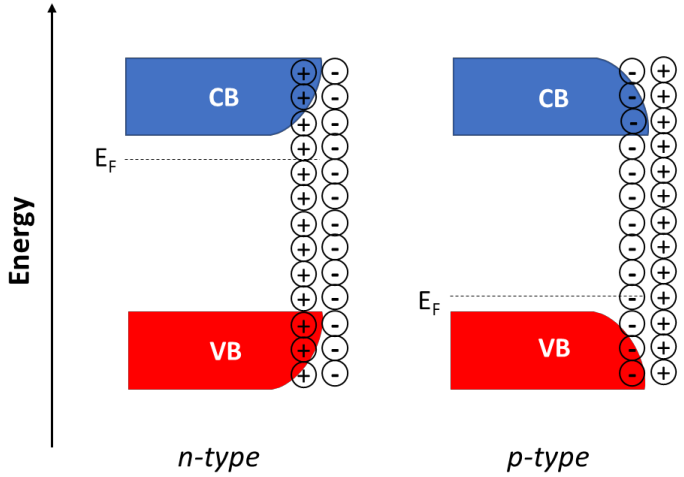

Figure 1.4: (a) Upward band bending for an n-type semiconductor in contact with an electrolyte and (b) downward band bending for a p-type semiconductor in contact with an electrolyte

In the case of nanocrystalline semiconductors, used in this thesis work, these terms above described cannot be used due to the small dimension of the nanoparticles that are comparable to the depletion layer width.[20]

1.1.2 Mesoporous semiconductors

Since the first work of Grätzel and O'Regan on mesoporous TiO_2,[9] nanocrystalline semiconductors have started to be widespread due to the advantage of a large surface area if compared to single or multiple crystal substrates. Particularly, in the field of DSSCs, the increase of the surface area is of a 1000 factor that makes possible to collect a larger number of sensitizer molecules. The main used nanocrystalline semiconductor is TiO_2 in the anatase form, many efforts to try to synthesize other materials such as ZnO,[21-24] SnO_2,[25, 26] Nb_2O_5,[27, 28] ternary oxides such as $SrTiO_3$[29, 30] and Zn_2SnO_4[31-34] and core-shell structures like ZnO-coated SnO_2[35, 36] were also made.

TiO_2 is a wide-band gap semiconductor characterized by an energy gap of 3.2 eV that makes it transparent to the visible light (ca. $\lambda > 380$ nm), which is slightly higher than the rutile form, allowing less competition with the absorption of photons by the dye. Anatase and rutile are characterized by different dye absorption and electronic transport.[37, 38] Furthermore, the conductivity and the CB position are higher in the case of the anatase TiO_2, instead the rutile one results in better stability and can be obtained from the anatase form at 600 °C temperature.[39] Via Sol-gel preparation,[40] it is possible to get a mesoporous layer starting from nanoparticles with an average diameter of 10-20 nm, **Figure 1.5a** shows a Scanning Electron Microscope (SEM) image of a sintered electrode characterized by a porous network of nanoparticles homogeneously distributed for all the substrate with a dimension of the order of ca. 20 nm. In **Figure 1.5b** a cross-section of the same electrode having a thickness of ca. 7 µm is shown.

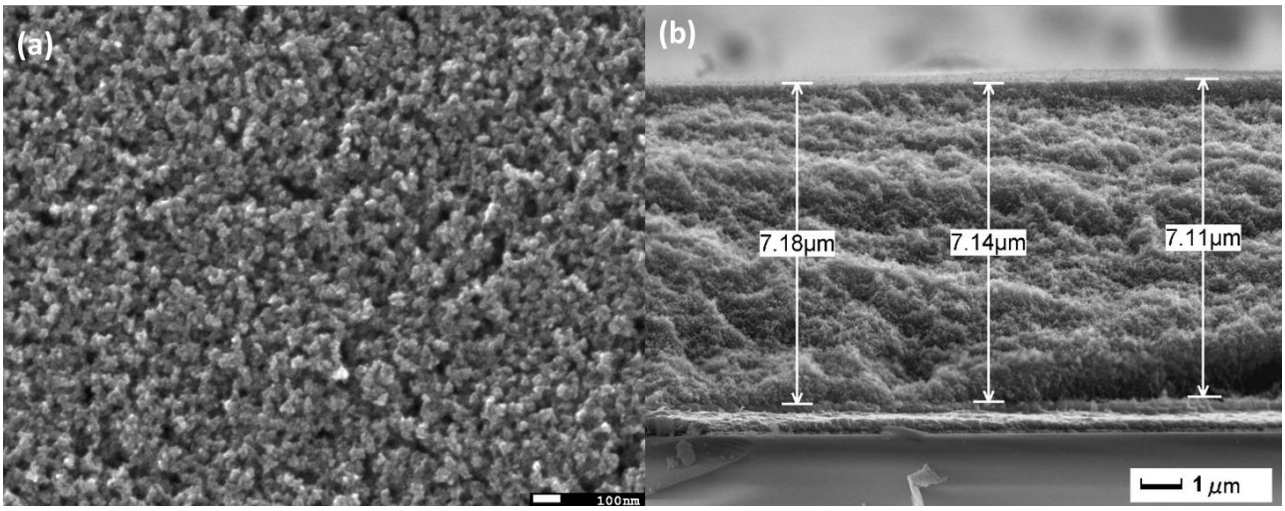

Figure 1.5: (a) Top view SEM image of a TiO_2 mesoporous electrode, (b) Cross-section of the same substrate

1.1.3 Sensitizers

To collect visible light, (TiO_2 absorbs light with $\lambda < 380$ nm) the sensitizer needs to be anchored to the semiconductor. This field is probably one of the main studied in the past and a myriad of compounds were synthesized including metal complexes, porphyrins, phthalocyanines and metal-free organic dyes. Some requirements must be met:

1) ideally the dye should have a panchromatic absorption from the ultraviolet to the NIR ($\lambda < 920$ nm)
2) the sensitizer should not aggregate but create a monolayer on the surface
3) the excited state of the dye must be higher in energy than the conduction band edge of the semiconductor to enable electron injection
4) the oxidation potential of the sensitizer should be more positive of the redox potential of the electrolyte to allow an efficient regeneration
5) the dye should be electrochemically and thermally stable and photostable
6) it should have a strong anchoring group like carboxylic acid (COOH), sulfonic acid (SO_3H), alkoxysilyl [$Si(OR)_3$] or phosphoric acid (H_2PO_3).

Dye-TiO_2 interaction employs principally covalent bonds to ensure strong coupling, a homogeneous dye distribution, and device stability. Hydrogen bonds are also possible because the superficial area is rich of defects and hydroxyl groups. In the case of the prototypical benchmark carboxylic acid anchoring group, six major types of possible anchoring modes have been identified: a monodentate ester, bidentate chelating, bidentate bridging, monodentate and bidentate H-bonding, as well as monodentate coordinating mode through a C=O group (Scheme in **Figure 1.6**).[41, 42] Due to the intimate contact between carboxylate anchoring-based dyes and the metal oxide surface, the structures with bidentate modes (chelating or bridging), usually exhibit superior stability compared to other types of anchoring modes.[10]

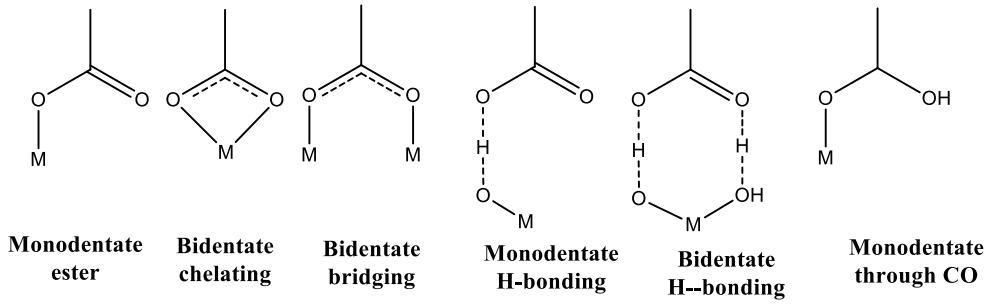

Figure 1.6: Schematic chelating bonds for carboxylic acid anchors onto a metal oxide as titanium

1.1.3.1 Ruthenium based complexes

Substituted polypyridine based Ruthenium (II) complexes were the first dyes able to generate appreciable efficiency (many examples are reported in **Figure 1.7**), **N3** ($Ru(H_2DCB)_2(NCS)_2$)) (H_2DCB is the 4,4' dicarboxy 2,2' bipyridine)[43] and the double deprotonated form **N719**,[44] are rare examples of molecules able to reach a broad absorption in the visible spectra (up to the NIR), a low deactivation via radiative or nonradiative pathway, irreversible interactions with the TiO_2 surface, an excited state oxidation potential negative enough (-0.77 V)[10] to inject electrons in the CB and a ground state oxidation potential positive enough (+1.09 V) to be intercepted by the redox potential of the redox couple and stability. Their absorption spectra are characterized by intense metal to ligand charge transfer (MLCT) transitions, the electrons are mainly localized on the ligand in a region close to the surface and the holes on the metal. Starting from these complexes, different substituents on the ancillary polypyridine ligands were introduced, for example the introduction of 3-methoxystyryl and 2-(3,6-dimethoxyphenyl)ethenyl in **Z910** and **N945**, respectively, extends the conjugation to increase the molar extinction coefficient.[45, 46] **Z907** are characterized by the introduction of two hydrophobic alkyl chains on the bipyridyl ligand able to shield the titania surface and reduce the recombination processes.[47] Also black dye (**BD**) or **N749** (tri(isothiocyanato)(2,2';6',2''-terpyridyl-4,4',4''-tricarboxylic acid)ruthenium(II), is well known for its high efficiency due to a bathochromic shift of the MLCT transition that results in a broad absorption spectrum (up to 920). This is obtained thanks to the decrease of the π^* level of the terpyridine ligand and to the increase in the energy of the t_{2g} metal orbitals. The NIR absorption spectrum extension leads to a decrease in the LUMO energy with consequence decreasing in injection driving force.[48] To date, the best efficiencies were obtained with triiodide/iodide-based redox mediator, with values close to 11-15% depending on the fine tuning of the cell substrates.[49]

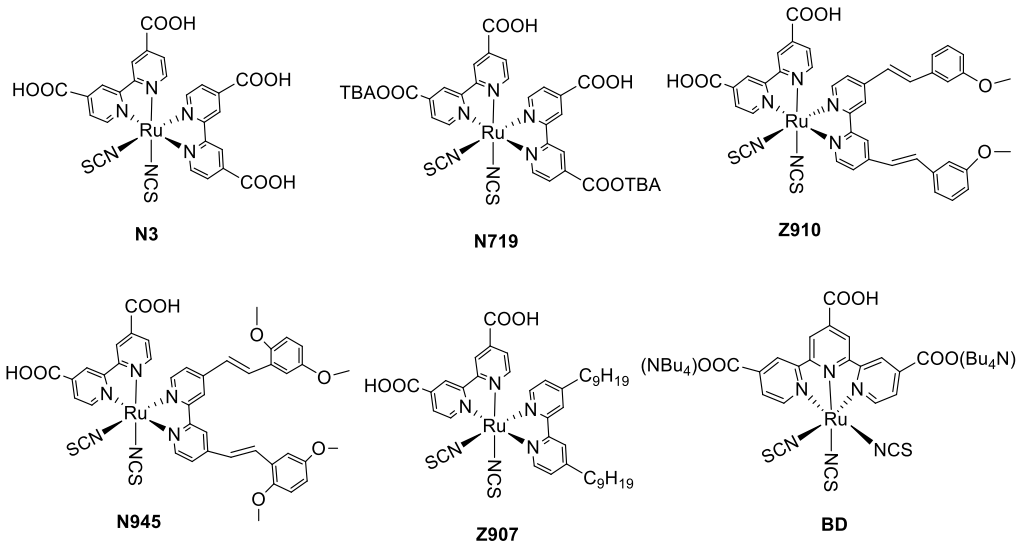

Figure 1.7: Examples of some of the most important Ruthenium dyes: **N3**, **N719**, **Z910**, **N945**, **Z907** and **BD**

Many efforts have also been spent designing sensitizers with other metal ions, such as Os,[50, 51] Re,[52] Pt,[53] and Cu[54] but they will not be discussed in this thesis.

1.1.3.2 Metal-free organic dye

A sustainable solution was found in the metal-free organic dyes characterized by a straightforward design and synthesis, a lower cost than the noble metal-based sensitizers and an extinction molar coefficient generally higher than that found for the ruthenium complexes. As drawback needs to be mentioned the multi-step involved in the synthesis. Typically, these molecules are characterized by a donor-(π bridge)-acceptor (D-π-A), where moieties like indoline,[55-57] triarylamine,[58-60] and coumarin,[61-63] are employed as electron donor units, whereas carboxylic acid, cyanoacrylic acid, and rhodamine units are employed as electron accepting groups. The linking between the donor and the acceptor is done by adding π spacers such as polyene and oligothiophene.[64, 65] These systems are characterized by an efficient electron transfer from the donor unit to the acceptor one constituted of anchoring moieties able to interact with the surface. Triarylamine (**Figure 1.8**) is one of the most promising metal-free organic dyes thanks to the good electron transporting capability and distribution of π–π stacking that leads to an improvement of the performance of the cell by reducing the charge recombination, minimizing the dye aggregation, and enhancing the molar extinction coefficient.[66-68] Structural modifications could be performed by introducing alkyl chains or donating groups.[69-71] **D35**, synthesized in 2009 by Hagberg et al.[58] is characterized by a para substituted amine with a phenyl moieties functionalized with p,o-butoxy groups that in the same years, gave excellent efficiency close to 7% in conjunction with a Co(II/III) based electrolyte,[59] this organic compound harvest sunlight below 620 nm. For this reason, in 2011 Grätzel's group synthesized **Y123**[60] by introducing cyclopentadithiophene[72] bridging unit in the D-π-A structure that allows the extension of the spectral response up to 700 nm and permitted to reach 40% higher photocurrent density compared to **D35**. A further improvement in the red response and in the molar extinction coefficient was achieved by the same group synthesizing **XY1** which is characterized by a relatively high potential and long alkyl side chains able to work properly also in the case of demanding redox mediator.[73]

To date, one of the best efficiencies achieved for a DSSC-based device is of 29.2% (under 1000 LUX intensity) obtained combining the latter described sensitizer (**XY1**) and a Cu(I)/(II) redox mediator. This value increases to 30% considering a co-sensitization (**XY1** + **5T**)[12], the PCE% of the same cell, is close to 10% under AM1.5G illumination. Considering only the case of AM1.5G illumination, 14% was obtained combining **LEG4** and another organic dye together with a cobalt-based electrolyte.[74]

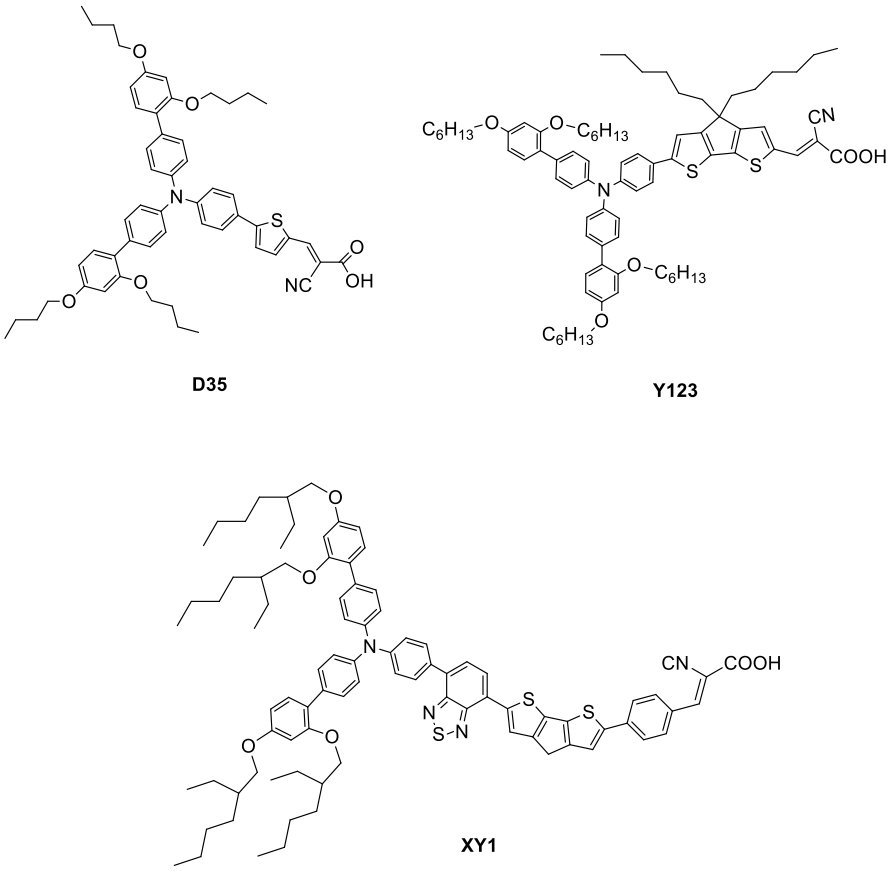

Figure 1.8: Some of the most relevant triarylamine based metal-free organic dye: **D35**, **Y123** and **XY1**

1.1.3.3 Iron sensitizers

The relative low natural abundance of Ruthenium (≈ 0.001 ppm in the Earth's crust)[75] and its consequent higher cost required to investigate Earth abundance metals, mainly the first-row d-block such as iron, cobalt, nickel, copper and zinc. These elements are characterized by an earth-crustal abundance of ≈ 41,000, 20, 80, 50 and 75 ppm respectively, where iron exhibits up to 800-folder the availability shown by the other metals. Since the first report of Ferrere and Gregg[76] on $[Fe(dcbpy)_2(CN)_2]$ (dcbpy = 4,4'-dicarboxy-2,2'-bipyridine) substituted polypyridine complex, iron sensitizers revealed the possibility to give photocurrent once they have grafted onto the semiconductor substrate, although the low efficiency recorded < 0.1%. The reason of the low performance needs to be found on their energy levels and a comparison with the ruthenium complexes should be made. Analyzing the standard $[Ru(bpy)_3]^{2+}$ complex, well known for its spectroscopic features, after having assumed an octahedral geometry (the actual is lower), all the six valence electrons are paired in the t_{2g} orbitals leaving the relatively high e_g orbitals empty, as shown in **Figure 1.9a**, resulting in a low spin d^4 electron configuration. The strong t_{2g} - e_g separation allows the π^* orbitals to be energetically below the metal e_g. The lower excited state is a metal to ligand charge

transfer (MLCT) type, and it is generated by the promotion of one t_{2g} electron into the π* orbital. Considering both the energy gap and the small horizontal shift along the Ru-N normal coordinate between the ^{3}MLCT lowest excited state and the $^1A_{1g}$ ground state,[77] a radiative excited state deactivation is possible. This process is in competition with the non-radiative deactivation. Considering the (MC) $^3T_{1g}$ excited state, a significant shift along the Ru-N normal coordinate is present because one electron has moved from a nonbonding to an antibonding orbital. This horizontal shift (from the ^{3}MLCT state) allows a partial overlap of these two potential curves that leads to the population of the ^{3}MC states over a certain barrier of energy and from here to the $^1A_{1g}$ ground state.[78] Decreasing the ligand field strength such as in the case of $[Ru(tpy)_2]^{2+}$ (where tpy = 2,2':6',2''-terpyridine), the $^3T_{1g}$ is significantly lower resulting in a faster MLCT deactivation. Considering now the case of the iron complexes and for comparison the $[Fe(bpy)_3]^{2+}$ analog to the ruthenium one, the metal centered state is significantly lower because the radial distribution of the six 3d electrons is closer to the metal core than that of the 4d electrons in Ru(II). For this reason, there are two MC states lower than the ^{3}MLCT state ($^3T_{1g}$ and $^5T_{2g}$) and other three close in energy ($^3T_{2g}$, $^1T_{1g}$, $^1T_{2g}$).[79] The ^{3}MLCT deactivation is recorded in only 50 fs without any energy barrier followed by vibrational cooling that occurs in few ps.[80]

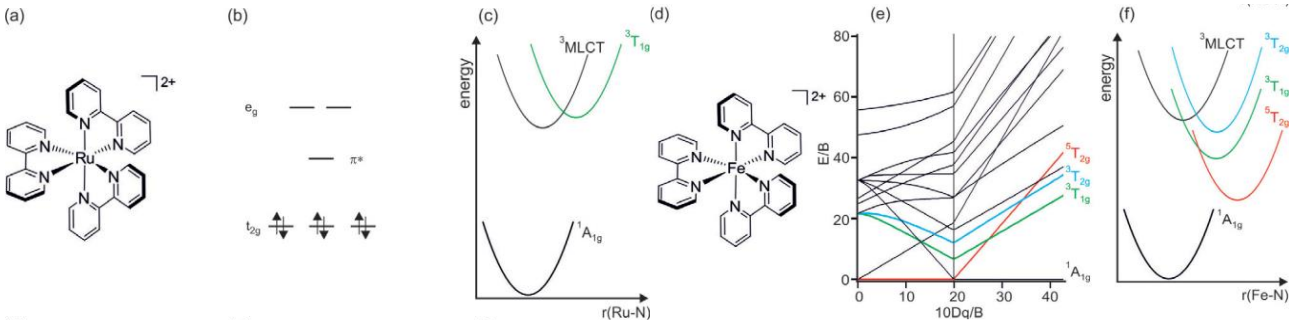

Figure 1.9: $[Ru(bpy)_3]^{2+}$ (a) structure, (b) t_{2g}, e_g and π* orbitals representation, (c) simplified potential energy curves for ground and excited states. $[Fe(bpy)_3]^{2+}$ (d) structure, (e) Tanabe and Sugano diagram, (f) simplified potential energy curves for ground and excited states. From ref 81

Commonly, when the complexes are functionalized with anchoring groups the injection in the semiconductor substrate occurs from the ^{1,3}MLCT, but it is now clear that the fast deactivation in the case of Fe(II) leads to an injection quantum yield $\Phi_{inj} << 1$. In a recent review,[81] Wenger summarized some of the possible strategies employed to try to stabilize the ^{1,3}MLCT states (within the limit of the energy gap law[82] where the decreasing in energy of the lower excited states leads to a more efficient non-radiative deactivation) or destabilized the MC levels:

1) Use of highly symmetric ligand fields[83]
2) Use of push–pull ligand set with high simmetry[84]
3) Use of highly strained complexes giving access to ^{5}MLCT states[85, 86]
4) Stabilization of MLCT States/Destabilization of MC States with Cyclometalating σ- and π-Donor Ligands[87-89]
5) Use of mesoionic carbenes to combine σ donor and π acceptor[90]
6) Enhancement of Ligand Field Strength with σ-Donating NHC Ligands[91-93]

Based on this latter way, Gros and co-workers employed a Fe(II)NHC (NHC=N-Heterocyclic-Carbene) based sensitizer[6] (structure reported like an insert in **Figure 1.10**) characterized by a strong NHC σ-donating groups combined with a pyridine π acceptor functionalized with a carboxylic moiety, this latter functional group is needed to be anchored to the surface and also because otherwise

the MLCT state would be too high in energy. Gros recorded a lifetime of 16 ps.[94] The PCE% recorded for **C1** (Initially called **C2**) was of 0.13% obtained combining the commercially available TiO_2 with a platinum counter electrode and a standard Solaronix triiodide/iodide electrolyte (see photocurrent density-voltage (J-V) reported in **Figure 1.10**). This suggests the possibility of higher photovoltaic performances by fine-tuning the electrolyte and the photoanode configuration.

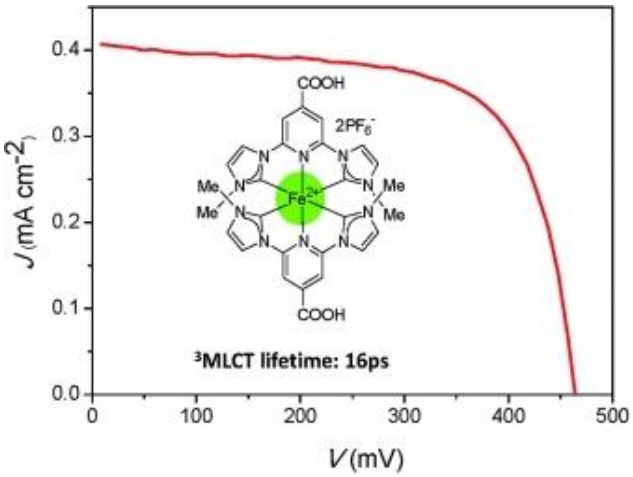

Figure 1.10: Photocurrent density-voltage recorded for **C1**, and its chemical structures reported as insert. From ref 6

1.1.4 Counter electrode

The counter electrode (CE) covers another crucial DSSC component necessary to regenerate the reduced form of the redox mediator. The main feature required is a high catalytic activity to enhance the charge transfer at the counter electrode-electrolyte interface. Another characteristic, but less critical, is the conductivity of the material. The charge transfer at this interface plays an important role in the overall series resistance influencing the cell's fill factor (FF) and the overall power conversion efficiency.[95, 96] The bare FTO, despite the high conductivity, is a very poor counter electrode that leads to the resistance at the electrolyte interface on the order of 10^6 Ωcm^2 in a standard triiodide/iodide electrolyte.[97] From the beginning, platinum-based CE represents one of the most widespread materials. To prepare this counter electrode, the easiest way is to spread an alcoholic chloroplatinic acid solution on a pre-cleaned FTO followed by thermal annealing to obtain nanosized Pt granules.[98] It is required just a small loading of platinum (<5 $\mu g/cm^2$) to keep low the charge transfer resistance (<1 Ω/cm^2)) and to guarantee the transparency of the substrate that otherwise it would be a limitation for the natural application of DSSCs. Other strategies to achieve platinum-based CE were analyzed such as electrodeposition[98] and vapor-deposition[99] but these methodologies have revealed a dissolution of the deposited platinum forming complexes like $PtI_4^{2-}$and PtI_6^{2-} when the electrodes are in contact with a triiodide/iodide based electrolyte. Other drawbacks of Pt materials are their low natural availability and consequent high cost. Alternative Pt free counter electrodes such as carbon material and conductive polymers have been investigated.[10] The main advantages of the former typology are their low cost, high surface area and high electronic conductivity.[100] Kay and Grätzel[101] realized a combination of graphite and carbon black to regenerate the reduced form of the electrolyte, the role of the former component was to give at the material good electronic conduction and catalytic activity instead, the role of the carbon was to obtain a high surface area and so to increase the catalytic behavior of the synthesized substrate. It was observed a better adhesion increasing the number of layers, Pettersson[102] prepared a two-layer substrate achieving an enhanced catalytic effect thanks to the Pt doping and higher electronic conductivity. Using alternative redox couples such as

cobalt and copper-based electrolyte, need to be also highlighted mass transport limitations linked to the use of platinum. With these new monoelectronic redox shuttles, but also with the classical triiodide/iodide electrolyte, the use of conductive polymers has shown an excellent catalytic activity. This class of compounds includes Poly(3,4-ethylenedioxythiophene) (PEDOT), polyaniline and polypyrrole as well. PEDOT represents the most widespread polymeric CE, it was synthesized by Jonas and Kirchmeyer by chemical oxidation of EDOT in the presence of polystyrenesulfonic acid obtaining a water dispersion of PEDOT:PSS.[103] The same material can be electropolymerized on an electrode surface. **Figure 1.11a** summarizes the starting monomer and the final polymer; the reaction consists of a first monoelectronic oxidation, followed by a C-C coupling of two radical cations, proton losses and re-aromatization until a certain length of the formed PEDOT oligomers.[104] During the chemical or electrochemical polymerization, further oxidation of the neutral oligomers to obtain the oxidized form of the PEDOT occurs, the main charge carrier across the polymer in its doped state are polarons and bipolarons[104] (**Figure 1.11b**). The exact ratio between EDOT and dopant depends on the capability of this latter to stabilize the positive charge on PEDOT (namely *dopant ratio* in the case of monomeric dopants).

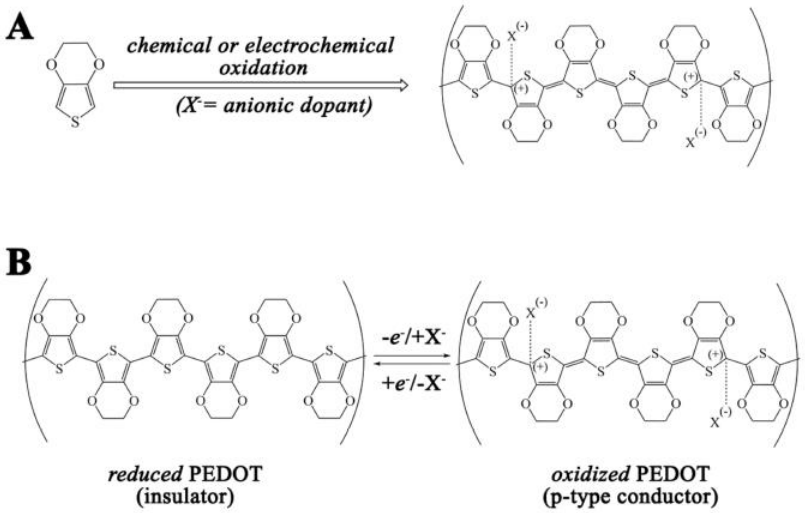

Figure 1.11: (a) General representation of chemical or electrochemical oxidation of EDOT to obtain PEDOT:X and (b) Switch between reduced insulator and oxidized (p-type conductor) forms of PEDOT. From ref 105

A very recent review,[105] published by us, retraces the historical steps behind the use of PEDOT as a counter electrode for DSSCs. One of the first reports was published by Prof. Yanagida[106] for cells assembled in combination with triiodide/iodide electrolyte. They were encouraged by the preliminary observation of Inganas et al. who observed that PEDOT can improve of the charge transfer between a metal oxide and the I^-/I_3^- redox couple. To date, a considerable number of dopants were tested such as PSS (polystyrene sulfonate), TsO (tosylate), ClO_4^- (perchlorate), TFSI (Bis(trifluoromethane)sulfonimide) and Cl^- (chloride), obtaining comparable cell efficiencies of those obtained with the platinum-based counter electrode. In 2013 Carli[107] published a comparative study concerning the main cobalt(II)/(III) based redox couples in combination with PEDOT in the presence of different dopants such as PSS, ClO_4^- and SDS (sodium dodecyl sulfate). PEDOT outperformed the platinum standard CE, where PEDOT/ClO_4 was the best substrate with the best electrocatalytic behavior thanks to the higher porosity that led to a more elevated contact surface between the material and the electrolyte, with consequent lower diffusional and charge transfer resistances. This was also confirmed in other studies where the use of PEDOT decreased the cell series resistance such an extent

to mitigate the mass transport which generally affects the alternative redox couples.[96] PEDOT CEs were also tested in combination with the new promising copper(I)/(II) based electrolyte achieving some of the best results for a DSSC, with PCE close to 10% and 30% under 1 SUN and in indoor conditions (1000 LUX) respectively.[12, 108]

1.1.5 Redox mediator

Ideally the electrolyte should provide an efficient charge transport in a non-corrosive environment without absorbing a significant portion of the visible spectrum, it must regenerate the dye after having injected electrons in the conduction band of the semiconductor and then itself at the counter electrode. Since the first contributions of Grätzel and O'Regan[9] on DSSC, triiodide/iodide appeared like an efficient redox couple displaying a fast regeneration and slow recombination kinetics despite a very basic organic electrolyte. In solution iodine interacts with iodide to form the triiodide species with K_1 equilibrium constant:[109]

$$I_2 + I^- \overset{K_1}{\Leftrightarrow} I_3^- \qquad \textbf{eq. 1.4}$$

The redox potential of the electrolyte (E_{redox}) will be given by the Nernst equation reported in **eq.1.2**, where $C_{ox} = I_3^-$ and $C_{red} = I^-$. Several one-electron redox reactions can occur and some of these are of importance for the DSSC functioning as:

$$2I^{\cdot} \overset{K_2}{\Leftrightarrow} I_2 \qquad \textbf{eq. 1.5}$$

$$I^{\cdot} + I^- \overset{K_3}{\Leftrightarrow} I_2^{-\cdot} \qquad \textbf{eq. 1.6}$$

Considering now the regeneration of the Dye, it can be simplified as:

$$D^+ + I^- \xrightarrow{regeneration} D + I_3^- \qquad \textbf{eq. 1.7}$$

The following steps provide the pathways of dye reduction:

$$D^+ + I^- \rightarrow [D \cdots I] \qquad \textbf{eq. 1.8}$$

$$[D \cdots I] + I^- \rightarrow D + I_2^{-\cdot} \qquad \textbf{eq. 1.9}$$

$$2I_2^{-\cdot} \rightarrow I_3^- + I^- \qquad \textbf{eq. 1.10}$$

The cycle is concluded when I_3^- is reduced to I^- at the counter electrode. In order to have an efficient dye regeneration, the electrolyte requires a high concentration of iodide or otherwise its diffusion should be fast. Higher the viscosity of the solvent and higher the concentration of the reduced form contained in the electrolyte should be.[110] Concerning the transport of triiodide to the counter electrode, this step can be the limiting process when the concentration of triiodide is low or when high viscous solvents are used.[111] When the depletion of triiodide is reached at the CE, the voltage output of the solar cell decrease due to overpotential. A yellowish/brownish color characterizes the iodine-based electrolyte, and this means a partial visible light absorption in competition with the sensitizer: a study revealed that a concentration of 1M of triiodide leads to a 13% loss in the photocurrent when cells are assembled with **N719** dye.[112] Another drawback of using these types of electrolyte is the high metal corrosivity, in fact, an incorrect sealing of the cells can result in irreversible collectors damage.[109] Mainly for this latter peculiarity, scientists have been spending their effort to try to replace the efficient triiodide/iodide redox couple with inexpensive and available metals such as the first-row elements. The great advantage of the application of complex-based redox couple is the possibility to tune the electrochemical potential through the correct choice of the coordination sphere. Cobalt has been showing a great interest since the first promising reports date back to 2000s.[113] This element is characterized by a high reorganization energy related to the electron

transfer process for the implication of an antibonding e_g metal orbital, the oxidation leads from a high spin Co(II) $t_{2g}^5e_g^2$ to low spin Co(III) t_{2g}^6 configuration,[114] this explains the typical low self-exchange rate constants (i.e. $4x10^{-2}$ $M^{-1}s^{-1}$ for $[Co(Phen)_3]^{3+/2+}$).[114]

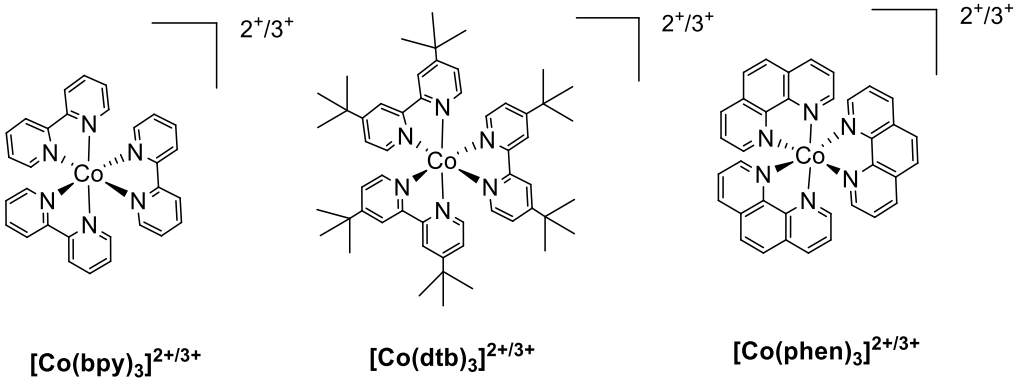

Figure 1.12: Example of cobalt-based complexes namely: **$[Co(bpy)_3]^{2+/3+}$**, **$[Co(dtb)_3]^{2+/3+}$** and **$[Co(phen)_3]^{2+/3+}$**

Cobalt-based electrolytes are characterized by a low extinction molar coefficient (≈100 $M^{-1}cm^{-1}$) leading a negligible competition with the sensitizer in absorbing the visible light. Compared to the triiodide/iodide redox couple, the more positive quasi-reversible oxidation potential can be adjusted with the correct choice and synthetic modification of the ligands. In **Figure 1.12** some examples of the main cobalt complexes synthesized are reported. The one-electron redox couples have shown good electron transfer kinetics with the drawback to suffer of back electron transfer with consequent faster recombination dynamic if compared to the iodine systems. This trend is more evident in the case of **$[Co(bpy)_3]^{2+/3+}$** which is characterized by a smaller steric hindrance, less in the case of **$[Co(phen)_3]^{2+/3+}$**and even less in the case of **$[Co(dtb)_3]^{2+/3+}$**. A report published in 2014[74] showed one of the best efficiencies ever reported combining **$[Co(phen)_3]^{2+/3+}$** and a co-absorption of organic dyes with a resulting efficiency close to 14% as mentioned above. Despite this remarkable result, the high internal reorganization energy to switch from the high spin d^7 to low spin d^6 configuration limits the driving force for the dye regeneration.[115] It was reported at least 230 mV required driving force in order to obtain a regeneration on the order of 93%[116] which still shows a substantial potential loss.[117, 118] The cobalt redox shuttles, characterized by an octahedral geometry with six ligands that form a bulky system, suffer of mass transport limitations in the mesoporous layer.[119-121] Other issues concerning their stability and toxicity lead to some troubles connected to industrialization and mass production.[122] Copper complexes have shown great interest as redox shuttles for DSSCs application. **$[Cu(dmp)_2]^{1+/2+}$** was the first Cu-based complex to achieve a high efficiency close to 8%,[123, 124] this molecule is composed by a couple of phenanthroline substituted in position 2 and 9 for each ligand with methyl groups, which has a distorted tetragonal shape providing relatively low reorganization energy.[125]

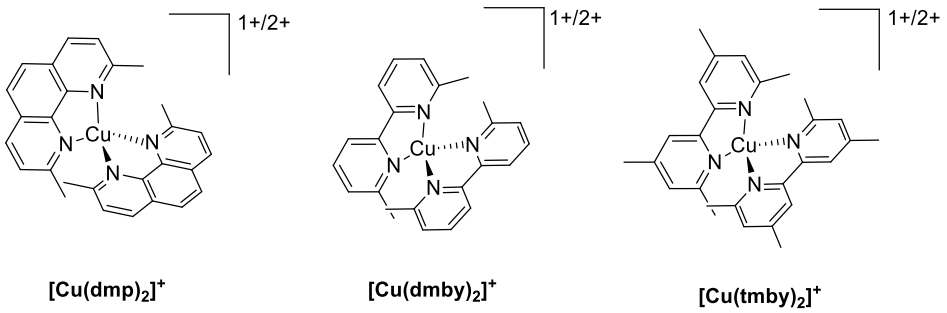

Figure 1.13: Example of copper-based complexes namely: **[Cu(dmp)$_2$]$^{1+/2+}$**, **[Cu(dmbp)$_2$]$^{1+/2+}$** and **[Cu(tmby)$_2$]$^{1+/2+}$**

Starting from this structure, in 2016 Freitag[126] published a report with **[Cu(dmbp)$_2$]$^{1+/2+}$** and **[Cu(tmby)$_2$]$^{1+/2+}$** compared to the standard **[Cu(dmp)$_2$]$^{1+/2+}$**, the phenanthroline was replaced by a substituted bipyridine which has kept the methyl groups in 2,9-positions. In the case of **[Cu(tmby)$_2$]$^{1+/2+}$**, the introduction of methyl substituents also in 4,6-position cover the role of electron donating groups (see **Figure 1.13**) with a consequent cathodic shift of the redox potential that leads to a higher dye regeneration driving force. Due to the small reorganization energy, also in the case of a small driving force, the copper-based electrolyte has been showing a unitary dye regeneration efficiency.[126] In this contribution Freitag achieved more than 10% PCE observing a high open circuit photovoltage (above 1 V) also decreasing the light illumination to 0.2 SUN. Thanks to this preliminary result, in these last years the same group has been obtaining PCE% close to 30% under indoor conditions (1000 LUX) with the co-absorption of organic dyes to achieve a panchromatic light harvesting.[6]

1.1.5.1 Electrode passivation methodologies

To reduce the recombination pathways between the photoinjected electrons and the one-electron redox couple, a myriad of strategies has been studied such as the design of organic dyes with a significant steric hindrance to shield the electrode surface as well as electrode passivation technique including the introduction of basic additives, preparation of a blocking underlayer (BUL), tuning of the film thickness and co-adsorbers. The basic additives play several roles when added to the electrolyte mixture such as modification of the redox couple potential, band shift of the semiconductor material, effects on surface shielding, or surface dye organization.[10] Grätzel in 1993 has added 4-tert-butyl pyridine (4-TBPy) to the electrolyte mixture obtaining a significant increase in the open circuit photovoltage in combination with lithium cations.[127] A detailed study attributed the role of this cation in shifting the titania band edge toward higher energy,[128] other study confirm the role of 4-TBPy and Li^+ in fine-tuning the TiO_2 conduction band and trap levels.[129] Thanks to the lone electron pair located in the nitrogen of the 4-TBPy, it works as a Lewis base and it can interact with the surface covering the defects and blocking the recombination pathways. Another efficient additive was found in guanidinium thiocyanate (GuNCS) where the cation can interact with the surface covering the defects and so blocking the recombination.[130] The BUL resulted in having a crucial role in blocking the recombination when cells are assembled in combination with one-electron redox couples,[121, 131] this layer can be fabricated starting by the deposition of a $TiCl_4$ or a Ti(IV)isopropoxide solution with the aid of a spin coater or a spray pyrolysis technique,[132, 133] followed by a sintering process under 500°C in a preheated oven. The resulting film requires a thickness on the order of a few nanometers, it

increases the resistance at the FTO/electrolyte interface decreasing the recombination pathway between the photoinjected electron and the oxidized form of the redox mediator. Concerning the co-adsorbers as a strategy to clock the recombination, Gregg et al.[134] introduced a post dye absorption treatment to passivate the semiconductor surface and block the recombination by covering the TiO_2 sites not occupied by the sensitizer. Later Carli et al.[135] published a detailed study concerning the application of a TiO_2 treatment with different silanes characterized by a different steric hindrance, in combination with Co(II)/Co(III) redox mediator. He obtained a 600% cell efficiency improvement in comparison with the untreated electrode.

1.2 Excited state and electron transfer theory

As mentioned above, the electron transfer from the sensitizer to the semiconductor's conduction band occurs from the excited state (ES). When a molecule absorbs light, an electronic transition happens, and the molecule's excited state is obtained. Different energy and electronic distribution characterize this new generated species compared to the ground state (GS) and it can be defined as a new chemical identity.[136] This perturbated state, created by an external perturbation, has a transitory character and it can undergo deactivation by interacting with other molecules. Otherwise, it will decay with an overall first-order rate constant that defines the excited-state lifetime τ (see **paragraphs 2.2.1.2** and **2.2.2**). The excited state results as a better reducing and oxidant agent than the GS as a consequent as the lower ionization potential (IP) and the higher electronic affinity (AE). The change in shape, size, and solvation of the new perturbated state leads to a shift between the absorption and emission spectra (*Stokes shift*) with respect to the ground state. When this value is small, the mentioned changes and also the entropy content of the ES and GS are negligible. The redox potential of the excited state so can be approximated to **eq. 1.11** and **eq 1.12** as follow:

$$E^0(A^+/{}^*A) = E^0(A^+/A) - E^{00}({}^*A/A) \qquad \textbf{eq. 1.11}$$

$$E^0({}^*A/A^-) = E^0(A/A^-) + E^{00}({}^*A/A) \qquad \textbf{eq. 1.12}$$

where $E^{00}({}^*A/A)$ represents the one-electron potential related to the zero-zero spectroscopic energy of the excited state and $E^0(A^+/A)$ and $E^0(A/A^-)$ represent the oxidation and reduction potential respectively of the ground state. The $E^{00}({}^*A/A)$) parameter generally is evaluated by the crossing point of the absorption and emission spectra, in the case of a non-emissive species it can be estimated by the onset of the absorption spectrum (considering ca. 5% of the maximum intensity). **Figure 1.14** schematizes the excited state deactivation pathways, generally *A can undergo to three unimolecular ways i) chemical deactivation with the formation of a new product P, ii) radiative deactivation (with consequent emission of a photon) and iii) radiationless deactivation (the absorbed energy is dissipated in the form of heat) with k_p, k_r and k_{nr} respectively the kinetic constants of the processes.

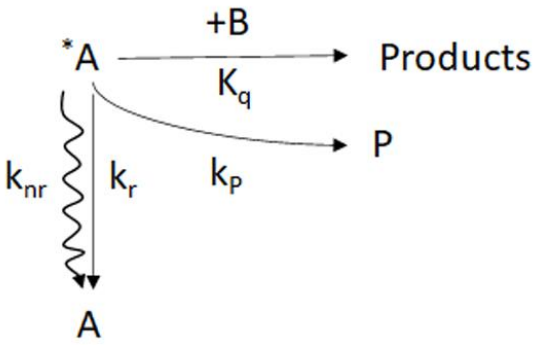

Figure 1.14: Simplified Excited state deactivation pathway. In the scheme the possible intersystem crossing are not reported

If $^*A$ interacts with a B species, the excitation energy can be transferred to the second molecule in the form of electron or energy as described by **eq. 1.13**, **eq. 1.14** and **eq. 1.15** as follow:

$$^*A + B \rightarrow A^+ + B^- \qquad \textbf{eq. 1.13}$$

$$^*A + B \rightarrow A^- + B^+ \qquad \textbf{eq. 1.14}$$

$$^*A + B \rightarrow A + {}^*B \qquad \textbf{eq. 1.15}$$

where **eq. 1.13**, **eq. 1.14** represent the oxidative and reductive quenching pathways of the electron transfer processes. The main common way of electron injection in the semiconductor's conduction band in DSSCs involves the processes described in **eq. 1.13** (under certain conditions $^*A$ can interact with I^- undergoing to a reductive quenching followed by the injection in the TiO_2 or recombination with the redox couple) [137, 138]. The Marcus model[139] describes the rate constant for an electron transfer process according to the **eq. 1.16** as follow:[140]

$$k_{el} = \nu_N \kappa_{el} e^{\left(\frac{\Delta G^{\neq}}{RT}\right)} \qquad \textbf{eq. 1.16}$$

where ν_N is the average nuclear frequency factor, κ_{el} is the electronic transmission coefficient, and $\Delta G^{\neq}$ is the free activation energy. After having assumed parabolic potential energy curves for reactants and products along the reaction coordinate, $\Delta G^{\neq}$ can be defined according to the following Marcus quadratic relationship (**eq. 1.17**):

$$\Delta G^{\neq} = \frac{1}{4\lambda}(\Delta G^0 + \lambda)^2 \qquad \textbf{eq. 1.17}$$

where ΔG^0 represents the standard free energy variation of the considered reaction and λ the nuclear reorganizational energy. This latter parameter is characterized by the sum of a couple of terms: λ_i which is the inner contribution related to the molecule's nuclear coordinate variation and λ_o, the outer contribution, related to the solvent repolarization. Based on **eq. 1.16** and **eq. 1.17** it is possible to define three distinct kinetics regions, illustrated by the potential energy curves reported in **Figure 1.15**:

i) Normal Region: $-\lambda < \Delta G^0 < 0$, an increase in the driving force leads to a favorable electron transfer kinetics reducing the activation energy necessary for the process

ii) Activationless Region: $-\lambda = \Delta G^0$, a small perturbation in the driving force related to the electron transfer process, doesn't lead to an important change in the reaction rate

ii) Inverted Region: $-\lambda > \Delta G^0$, the increase of the driving force leads to a decrease of $\ln k_{el}$

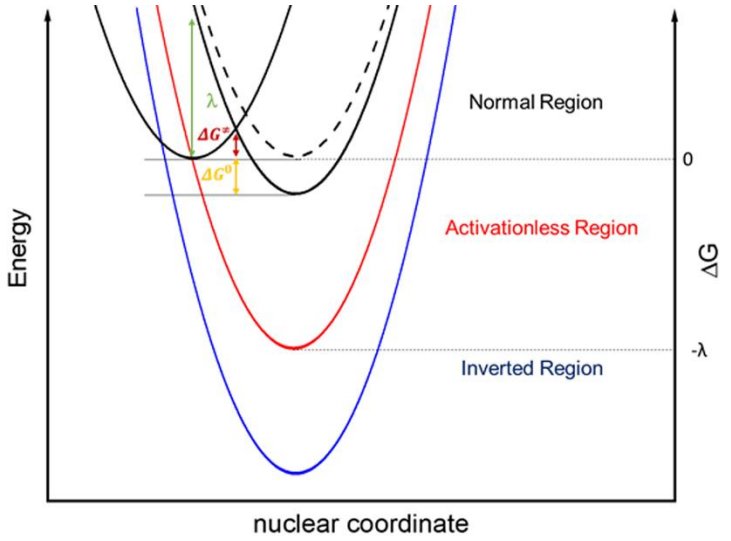

Figure 1.15: Potential energy curves for a process in the normal region (the dashed line represents the final step for an isoergonic reaction) with the description of the main terms of the Marcus equation. In the same picture the other two kinetics regions namely Activationless and Inverted Region are also depicted

From a quantum mechanical point of view, the rate constant of the electron transfer reaction can be written as reported in **eq. 1.18**:

$$k_{et} = \frac{2\pi}{\hbar}\left(H_{AB}^{el}\right)^2 FCWD \qquad \textbf{eq. 1.18}$$

where FCWD represents the Franck-Condon factor weighted for the Boltzmann population of the energy levels and H_{AB}^{el} the electronic coupling factor between the two electronic states, A and B, involved in the process.

1.3 Electron transfer processes

This paragraph will describe the different electron transfer steps that occur at the FTO/dye/electrolyte interfaces involved in the DSSC functioning, depicted in **Figure 1.16** together with the relative kinetics rate and the energetic levels.[141]

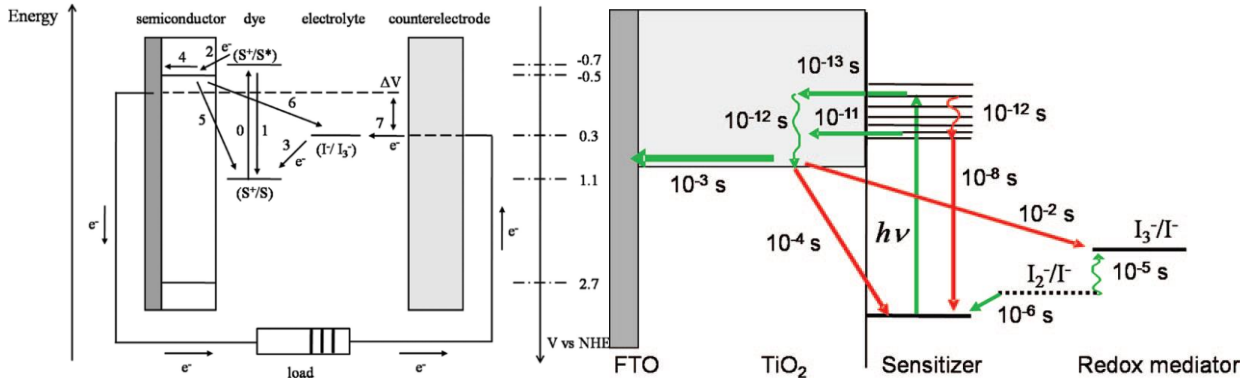

Figure 1.16: (a) Electron transfer processes in DSSC devices and (b) their relative kinetics rate. From ref 10

1.3.1 Reactions 1 and 2: electron injection and excited state decay

The ultrafast injection of the photoexcited electron from the sensitizer's ES (excited state) represents one of the main involved steps necessary for the functioning of the DSSC devices (*reaction 2*). This electron transfer step needs to be faster or at least comparable to the excited state deactivation (*reaction 1*) which, in the case of the standard Ru complexes, occurs on the order of ca. 20-40 ns. Instead, as above described, in the case of the Fe(II) systems the ES deactivation is much faster and so leads to a higher competition with the electron injection. It has been found that electron injection into the TiO_2 conduction band follows a nonexponential kinetic for the heterogeneity of the sites surface, dye aggregation, distribution of sensitizer binding modes and strengths and molecule aggregation.[10] The theoretical electron injection description at the solid/liquid interface into the semiconductor substrate was postulated by Marcus and Gerischer in the late 60's [142, 143] and then perfected for the case of DSSCs,[144] the resulting electron injection rate constant can be written as reported in **eq. 1.19:**

$$k_{inj} = A \int V^2 \left(1 - f\left(E, E_f\right)\right) \rho(E)\, exp\left(\frac{-(E - E^*_{ox} + \lambda)^2}{4\pi\lambda k_B T}\right) dE \qquad \textbf{eq. 1.19}$$

where E is the absolute energy of the semiconductor's accepting states Vs NHE, V is the average electronic coupling between the dye excited state and the semiconductor states that lie at the same energy E, f(E,E_f) term represents the Fermi occupancy factor for all the semiconductor acceptor states, ρ(E) the acceptor states density at E Vs NHE and λ the total reorganization energy for the injection charge process. ρ(E) is one of the critical parameters that affects the rate constant[145] which is assumed as an ideal semiconductor conduction band states density that quadratically increase above the conduction band edge ($\rho(E) \propto E\text{-}E_{CBE})^2$).[141, 146-148] In most experimental measurements conducted in the presence of an organic electrolyte, ρ(E) is assumed to increase exponentially: $\rho(E) \propto exp(E/E_0)$.[149-152] Because the injection proceeds from the excited dye into the semiconductor acceptor states, the injection rate should also have the same exponential trend to change in the relative energetics of the dye and acceptor states. For example, the injection process is found seven times efficient in the presence of Li^+ cations.[153] Also the excited state oxidation potential (E^*_{ox}) is found determining the electron injection: considering the electron transfer into an exponential increasing density of acceptor states with for example E_0 equal to 100 meV, the 100 meV increase of the E^*_{ox} leads to increase the states density and, as a consequence, also the K_{inj} that, in this case, will be three times higher.[145] The electron injection rate K_{inj} is used to derive the efficiency of this injection step as written in the following **eq. 1.20**:

$$\varphi_{inj} = \frac{k_{inj}}{k_{inj} + \sum k_i} \qquad \textbf{eq. 1.20}$$

where k_{inj} represents the rate constant for the electron injection and $\sum k_i$ the summatory of all the deactivation pathways of the excited state. To obtain φ_{inj} close to the unit, the rate constant of the injection process should be at least 100 folders $\sum k_i$. When a basic additive is added to the electrolyte mixture to increase in energy the semiconductor conduction band position, the electron transfer efficiency could be slow down due to the decrease of the electron injection driving force (ΔE_{inj}), this parameter is defined as the difference between the injecting states of the dye and the conduction band of the TiO_2. In this way the resulting open circuit voltage (V_{OC}) increases and the J_{sc} decreases, a compromise needs to be achieved to gain the best performances of the cell. The injection dynamic is also affected by the distance between the dye and the acceptor, when the anchoring function and the metal center are separated by a bridge, the injection efficiency can decrease in the case of a non-conjugated spacers.

1.3.2 Reaction 3: Dye regeneration

After the charge injection (*reaction 2*) the oxidized sensitizer should be efficient reduced by the reduced form of the electrolyte (*reaction 3*), this process occurs in a microsecond time scale.[10, 110] The efficiency of the process can be described as follow (**eq. 1.21**):

$$\varphi_{reg} = \frac{k_{reg}}{k_{reg}+k_{rec}} \qquad \textbf{eq. 1.21}$$

where k_{reg} and k_{rec} represent the time constant for the regeneration and recombination processes respectively. The main experiments involved in the regeneration investigation are based on the transient absorption analysis. [154-156] Considering the case of the well-known iodine/iodide based electrolyte, several mechanism has been hypothesized, Durrant[145] revealed a possible oxidized sensitizer-iodide complex, in particular, transient absorption experiments showed a fast formation of this system. The next meeting between a second I^- and the formed complex, to release the regenerated sensitizer and the $I_2^{\cdot-}$ species (followed by its disproportionation), resulted in the rate determining step of the regeneration reaction.[157] The regeneration kinetic is influenced by several factors such as the electrolyte viscosity,[158, 159] the nature of the cation of the iodide salt (in the case of small high density species they can intercalate in the TiO_2 mesoporous layer resulting in a higher local concentration of the negative iodide species[156]) and the steric hindrance of the sensitizer. This latter factor is found slow down the regeneration when the dye is equipped with a long alkyl chains as consequence of the nonpolar shielding effect offered to the oxidized metal center.[160]

1.3.3 Reaction 4: electron transport in mesoporous oxide film

The mesoporous semiconductor thin films are characterized by different physical features compared to the compact one with lower inherent conductivity of the film, impossibility to create a build-in electrical field due to the small nanoparticles and by a huge contact area at the electrolyte/oxide nanoparticles pores interface. Electrons can percolate in the network by hopping between two nanoparticles close each other. The gradient of electron concentration results to be fundamental in transport in the TiO_2 layer, electrons are moved by diffusion.[161-163] These negative charges are compensated by ions in the electrolyte mixture leading to a coupling through a weak electric field, the **eq. 1.22** describes the ambipolar diffusion model that describe the electron diffusion:[164, 165]

$$D_{amb} = \frac{n+p}{\frac{n}{D_p}+\frac{p}{D_n}} \qquad \textbf{eq. 1.22}$$

where D_{amb} describes the ambipolar diffusion coefficient, n and p are electrons and cations in the DSSC device and D_p and D_n describe the diffusion coefficient of n and p. Yanagida found a strict influence of the cation absorption in the electron transport.[166, 167] Some studies have revealed a cation nature dependance in the electron transport[168] but also a negligible effect of some anions.[169] 4-tert-butylpyridine in combination with LiI has shown a decreased electron transport times.[170] The electron diffusion depends also indirectly on the incident light intensity because it depends on electron concertation and on the semiconductor's Fermi Level position. Generally, the diffusion coefficient is lower compared to that determined for single-crystalline TiO_2 anatase,[171] the solution of this discrepancy is found in the multiple trapping model (MT).[172-176] Electrons are trapped below the conduction band in localized states from which they can be escape by thermal activation. Considering a small perturbation method, the chemical diffusion coefficient (D_n) can be written by a quasi-static approximation in the MT model as follow in **eq. 1.23**:[174, 176]

$$D_n = \left(1 + \frac{\partial n_t}{\partial n_c}\right)^{-1} D_0 \qquad \textbf{eq. 1.23}$$

where n_t and n_c describe the electron concentration in the trap states and in the conduction band respectively and D_0 represents the conduction band diffusion coefficient.

1.3.4 Reactions 5 and 6: electron recombination pathway

The parasite back-electron transfer process that occur from the conduction band of the semiconductor to the oxidized form of the dye, follow a multiexponential time law in a microsecond to millisecond time scale. This process is in competition with the dye regeneration which generally occurs in the microsecond time scale and follows a first-order kinetics; it can be studied in detail via nanosecond laser spectroscopy.[177-179] Durrant found a stretch exponential function as fitting function for the transient absorption (ΔA) kinetics[129, 180] described by the **eq. 1.24**:

$$\Delta A_t = A + be^{\left(-\frac{t}{\tau}\right)^d} \qquad \textbf{eq. 1.24}$$

where d (often found as α) is the exponential dispersion parameter related to the distribution of the trap states in the semiconductor that depend both on the electrolyte employed[180] and on the dye characteristics.[181]

The *electron lifetime* terminology is about the charge recapture with an electron acceptor in the electrolyte mixture and it can be studied via open circuit photovoltage decay experiments as described by Bisquert,[182] this process can happen both at TiO_2/electrolyte and at the TCO/electrolyte interfaces. This second pathway can be reduced introducing a thin titania blocking underlayer interposed between TCO and the active semiconductor layer.[183]

1.3.5 Reaction 7: Electrolyte diffusion and regeneration

After the dye regeneration, the oxidized form of the redox couple need to diffuse to the catalytic counter electrode, in fact, the high conductivity and ionic strength make the electric field and transport by migration practically negligible. The viscosity of the selected solvent plays a crucial role, more it is higher more the diffusion coefficient is too low to keep constant the redox couple flux, with consequent limitation in the photocurrent recorded.[184] The transport of the redox couple between the two electrodes leads to a new series resistance. The diffusional impedance depends both on the redox couple concentration and on the thickness of the spacer between the photoanode and the counter electrode.[97]

As previously described, the counter electrode should have an efficient catalytic behavior to ensure a fast electron transfer process with a low overpotential. This charge transfer pathway generates another series resistance R_{CT} (charge transfer resistance) that at low overpotential (η) (where η and the density photocurrent J are liner), it can be written as reported in the following eq. **1.25**:

$$R_{CT} = \frac{\eta}{J} = \frac{RT}{nFJ_0} \qquad \textbf{eq. 1.25}$$

where n depends on the exchanged electrons (two in the case of iodine-based electrolyte and one in the case of copper and cobalt mixture) and J_0 the exchange current density.

CHAPTER 2: Experimental techniques

This chapter will describe all the experimental techniques employed to characterize new species, devices, and material such as electrochemical, photoelectrochemical, as well as photophysical. The Dye Sensitized Solar Cell characterization together with some physical aspects will be also described.

2.1 Electrochemical methods

Scientists employ electrochemical techniques on a chemical system for several scopes like obtaining a thermodynamic information regarding a process or, for example, to generate a transient unstable species to study its decay. In this thesis, these methods were employed to characterize new species in solution or when anchored to a semiconductor, to deposit a layer on a conductive substrate or to record the characteristic photocurrent density-voltage curves for the analyzed photovoltaic devices. Electrochemical instrumentations are generally composed by a potentiostat necessary to control the applied voltage to a working electrode (WE) along with a function generator to produce the desired perturbation with consequent signal registration.[185] The instrument carefully controls the counter electrode potential against the working electrode (WE) to have the desire difference potential between the WE and the reference electrode (RE) as user set. An example of a potentiostat that employed a negative feedback mechanism to carefully check and control the specified parameters is reported in **Figure 2.1**.

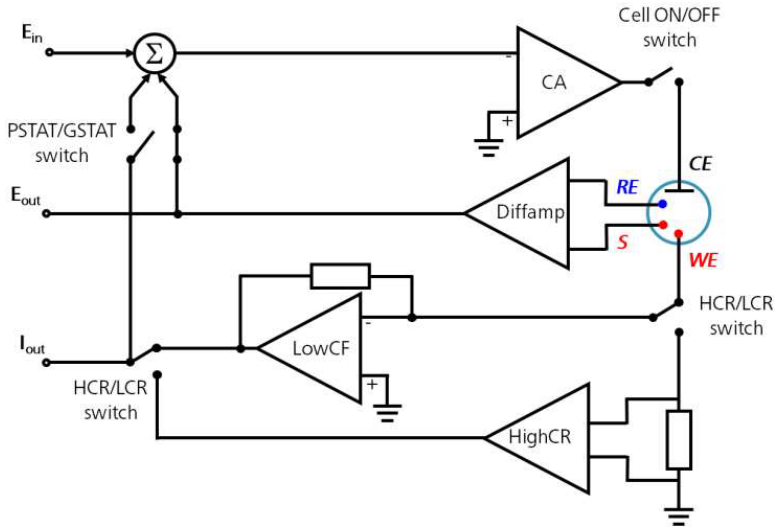

Figure 2.1: A simplified potentiostat scheme of a PGSTAT potentiostat

The CE is located at the end of a control amplifier that forces the current to flow along the cell. The value is measured with a current flower (LowCF) or a shunt (HighCR) for high and low values respectively. The differential amplifier is used to measure the potential difference between RE and S. The signal that is then sent to the summation point (∑) along with the waveform set by the digital-to-analog converter (E_{in}), will be used as a control amplifier input. The standard instrument setup is the three-electrode configuration where the potential difference is controlled between the WE and CE and checked among RE and S. In this configuration S and WE are short-circuited and because this latter electrode is kept at a fixed and stable potential thanks to the control of the CE polarization, also the potential difference between the RE and WE is controlled at any time.

2.1.1 Cyclic voltammetry

Cyclic voltammetry (CV) analysis is a classical electrochemical method employed to characterize processes at the electrode/electrolyte interface. The voltage is swept in a cyclic way from V_1 to V_2 and back to V_1, so it follows a triangular diagram scheme. **Figure 2.2** represents the classical voltammogram in which the potential is scanned from negative to positive values, it is possible to observe an anodic peak characterized by a positive current (IUPAC convention) associated to the oxidation of a species under analysis, in correspondence of a potential E_p^a (Red → Ox + e^-). Upon reverse scan, a negative peak is recorded ascribed to the reduction of the species before generated in correspondence of a potential E_p^c (Ox + e^- → Red).

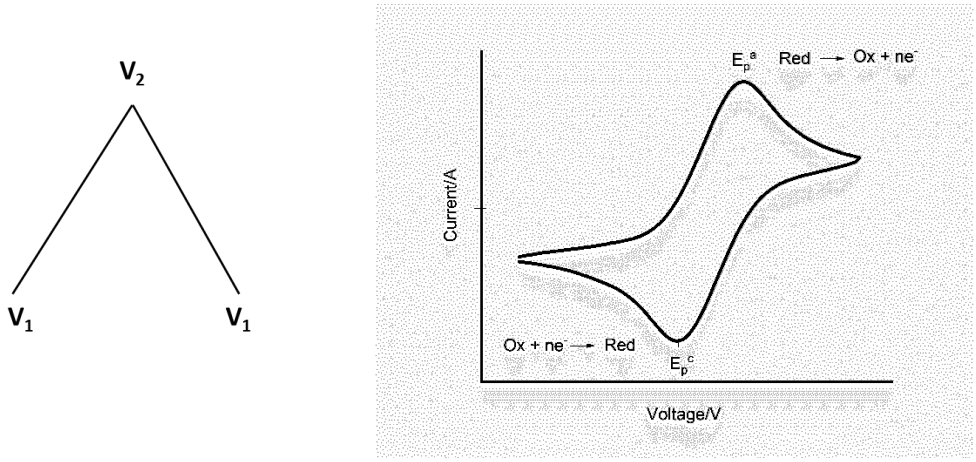

Figure 2.2: (a) Triangular diagram scheme of the applied voltage. (b) Example of a voltammogram for one-electron reversible process

Cyclic voltammetry is an important tool to gain thermodynamic information, in the case of a reversible process, the difference between E_p^a and E_p^c is given by the **eq. 2.1**:

$$\Delta E = E_p^a - E_p^c = \frac{59}{n} mV \qquad \textbf{eq. 2.1}$$

where n is related to the electrons involved in the electrochemical process. The reversibility decrease increasing the peak separation. The oxidation potential of a given species, namely $E_{1/2}$ or E_{ox} is reported in the **eq. 2.2** as follow:

$$E_{1/2} = \frac{E_p^a + E_p^c}{2} \qquad \textbf{eq. 2.2}$$

The peak current depends on several parameters and follow the Randles-Sevcik equation[186] as reported in the following **eq. 2.3**:

$$i_p = 0.0446 nFAC^0 \sqrt{\frac{nF\upsilon D_0}{RT}} \qquad \textbf{eq. 2.3}$$

where n is the number of electrons involved in the reaction, F the Faraday constant, A the working electrode area reported in cm^2, C^0 the bulk concentration of the species under investigation, D_0 the diffusion coefficient, T the absolute temperature and ν the scan rate. The peak current linearly increases with the root square of the scan rate. Results evident that rearranging the Randles-Sevcik equation it is also possible to extrapolate the diffusion coefficient of a given species.

2.1.2 Electronic impedance spectroscopy

Electronic impedance spectroscopy (EIS) is characterized by the application of an AC voltage to a system and to the analysis of the AC current response as a frequency function.[187] A small DC perturbation of few mV is applied to the AC signal, in order to maintain the pseudo-linearity of the

system. The frequency spans from some MHz to few mHz. As consequence of the application of a sinusoidal voltage $V(\omega,t)=V_0\sin(\omega t)$ with a frequency $f = \frac{\omega}{2\pi}$ (ω represents the angular frequency) to a given system, a response current $I(\omega,t)$ is recorded at the same *f*. The associated impedance $Z(\omega,t)$ follows the Ohm's Law and it can written as reported in the following **eq. 2.4**:

$$Z(\omega,t) = \frac{V(\omega,t)}{I(\omega,t)} \qquad \textbf{eq. 2.4}$$

For each ω values, the current can be *in-phase* or *out-of-phase* and so it can be written as $I(\omega,t)=I_0\sin(\omega t-\theta)$ (I_0 represents the current signal amplitude and θ the phase angle between V and I).[188] By applying the complex number notation, V and I can be rearranged in $V(\omega,t)=V_0e^{j\omega t}$ and $I(\omega,t)=I_0e^{j(\omega t-\theta)}$ (where j is the imaginary unit) and the resulting impedance follows the **eq. 2.5**:

$$Z(\omega,t) = \frac{V(\omega,t)}{I(\omega,t)} = \frac{V_0}{I_0}e^{j\theta} = |Z(\omega)|e^{j\theta} \qquad \textbf{eq. 2.5}$$

with |Z| the module impedance and θ the impedance phase. A further rearrangement is obtained after the application of the Eulero's relationship as reported in **eq. 2.6**:

$$Z(\omega,t) = |Z(\omega)|(cos\theta + jsin\theta) = Z'(\omega) + jZ''(\omega) \qquad \textbf{eq. 2.6}$$

where Z' = |Z|cosθ represents the real part of the impedance and Z'' = |Z|sinθ the imaginary one. **Figure 2.3** shows two possible representations of the ESI data for a DSSC recorded under open circuit conditions, the Nyquist plot reports Z'' as function of Z' in the complex plane instead the Bode reports log|Z| or the phase angle against the log*f*.

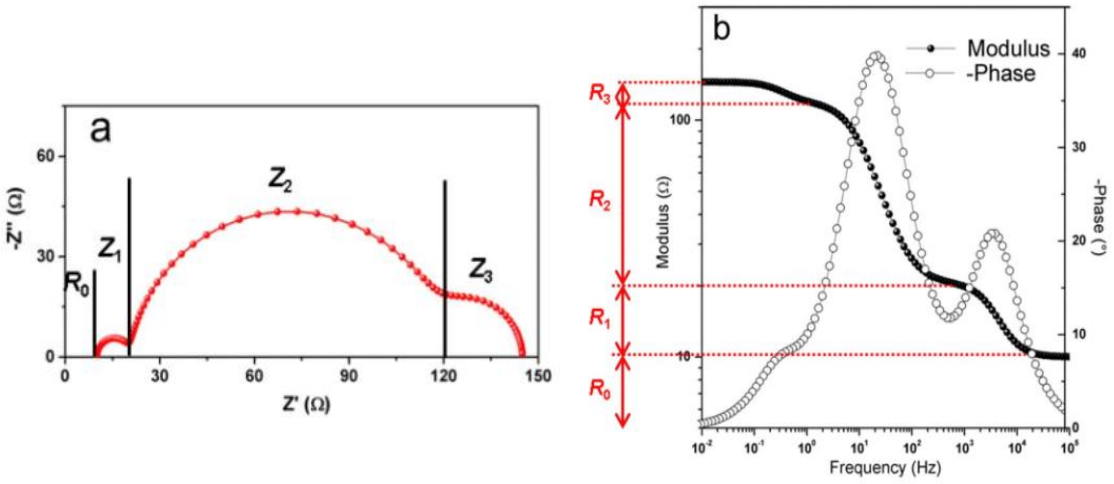

Figure 2.3: (a)Nyquist and (b) Bode representations of a DSSC under open circuit condition. From ref 187

An electrochemical cell can be approximated considering an impedance to a small sinusoidal perturbation and so its performances can be fitted with the aid of equivalent circuits composed of a resistors and capacitors in which pass current with the same amplitude and phase of the cell in the real condition.[185] **Table 2.1** summarizes the main elements used to the interpretation of the EIS experiments regarding solar cells and their relative impedance values:

Table 2.1: The main elements employed in the EIS interpretation and their relative impedance

Element	Symbol	Impedance
Resistor	R	R
Capacitor	C	$\frac{1}{j\omega C}$
Constant Phase element	Q	$\frac{1}{Q(j\omega)^{\beta}}$
Warburg short	Ws	$R_d\sqrt{\frac{\omega_d}{j\omega}}\tanh\left(\sqrt{\frac{j\omega}{\omega_d}}\right)$

In the **Paragraph 2.3.3** a detailed discussion about the model to be employed in the EIS analysis of a Dye Sensitized Solar Cell depending on the applied voltage will follow.

2.2 Spectroscopic techniques

2.2.1 Steady-state techniques

2.2.1.1 Absorption spectroscopy

The absorption spectrum is the consequence of the electronic transitions generated by the absorption of photons from the ground states of a molecule. The double beam configuration of a spectrophotometer (see **Figure 2.4**) can be summarized by Deuterium and Xenon light sources respectively for the UV and Visible part of the spectrum, a monochromator to select the desired wavelength, a beam-splitter to send the light both trough the sample and the reference, and a final photodiode detector.

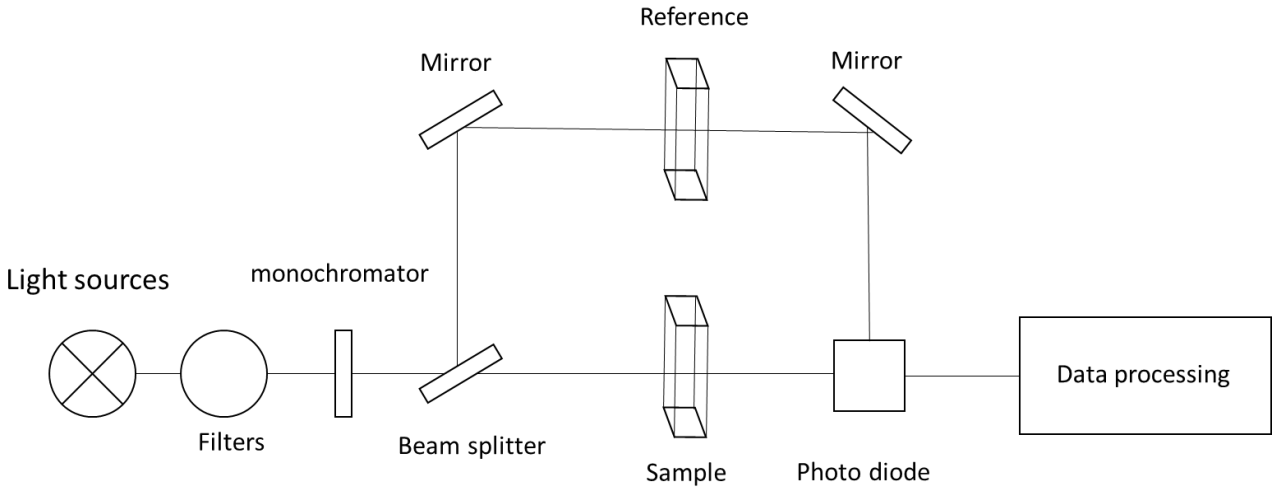

Figure 2.4: Block diagram of a double beam spectrophotometer

The absorbance is defined as reported in **eq. 2.7** as follow:

$$A(\lambda) = \log_{10}\left(\frac{1}{T(\lambda)}\right) \qquad \textbf{eq. 2.7}$$

where T(λ) is the transmittance of the sample, and it depends on the ratio between I and I_0 and after rearrangement gives **eq. 2.8**:

$$A(\lambda) = \log_{10}\left(\frac{I_0}{I}\right) \qquad \textbf{eq. 2.8}$$

where I_0 and I are the incident and the measured intensity after passing through the sample respectively. The absorbance can be related to the molar concentration of a species through the Lambert-Beer Law as reported in the **eq. 2.9**:

$$A(\lambda) = \varepsilon(\lambda)cl \qquad \textbf{eq. 2.9}$$

where l is the optical pathlength and ε is the molar extinction coefficient ($M^{-1}cm^{-1}$) which represents the absorbance of a 1 M solution with a 1 cm optical pathlength. The linearity of this relationship is kept under 1 of absorbance. In this thesis work, this technique has also been applied to determinate the surface concentration Γ ($molcm^{-2}$) of a given species when it was anchored to the semiconductor substate, as follow in the **eq. 2.10** and **eq. 2.11**:

$$A(\lambda) = 1000\varepsilon(\lambda)\Gamma \qquad \textbf{eq.2.10}$$

$$\Gamma = \frac{A(\lambda)}{1000\varepsilon(\lambda)} \qquad \textbf{eq. 2.11}$$

In the case of opaque materials, the spectra need to be acquired in diffuse reflectance mode (R% = 100 - A% - T%, where A% is the absorptance of the sample) employing an integrative sphere and generally it is reported in Kubelka-Munk units as follow in **eq. 2.12**:

$$F(R_\infty) = \frac{K}{S} = \frac{(1-R_\infty)^2}{2R_\infty} \qquad \textbf{eq. 2.12}$$

2.2.1.2 Emission spectroscopy

The presence of luminescence is important to the understanding of the emitting excited states.[189] These types of experiments are generally performed with a spectrofluorimeter, schematized in **Figure 2.5**. The source of light is typically represented by a continuous xenon arc lamp ranging between the UV to the NIR, a first monochromator is needed to select the excitation wavelength, another one is required to select the wavelength of the emitted photons analyzed by the detector, generally a PMT is employed. To make the excitation contribution negligible, the emitted light is sampled from the center at 90° with respect to the incident light. For emission experiments, it is necessary to use a very diluted solutions to avoid a strong absorption of the first layers that would make negligible the quantity of light able to reach the center of the cuvette.

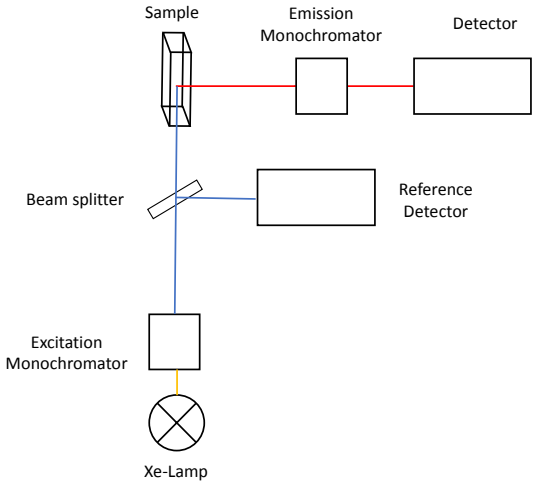

Figure 2.5: Schematic representation of a spectrofluorimeter

To record an emission spectrum, it is required to set the excitation wavelength inside the absorption spectra, generally to the wavelength of the maximum at low energy. The resulted plot should be corrected for the variation of the emission intensity of the light source, for the transmission efficiency of the emission monochromator and for the detector response.[189] After having recorded the emission spectrum, the same apparatus can be employed to perform excitation measurements, in this case the emission monochromator is fixed to the emission wavelength of the sample and the excitation one is used to scan the energy range corresponding to the absorption spectrum of a given species. This latter technique was not used in this thesis. The emission technique is characterized by a liner response over a wide range of concentration when diluted solutions are used, the absorbance needs to be lower than 0.05. The loss of linearity is originated by two main factors, mathematical and geometric. Concerning the former point, it is required to analyze the relationship of the luminescent intensity and the concentration as described by the **eq. 2.13**:

$$I_{em} = \phi I_{abs} = \Phi I_0(1 - 10^{-A}) \qquad \textbf{eq. 2.13}$$

where I_{em} represents the luminescent intensity, ϕ the emission quantum yield, I_{abs} the number of absorbed photons, I_0 the intensity of the incident light and A the absorbance of the solution. The exponential dependence between I_{em} and A can be considered linear when A<0.05 because the exponential term can be expanded in series and after the simplification of all the terms, except for the first, **eq. 2.13** can be rearranged in **eq. 2.14**:

$$I_{em} = \Phi I_0(2.303A) \qquad \textbf{eq. 2.14}$$

The geometric contributions can be divided in solution absorbance at the excitation and at the emission wavelength. In the former case, if the solution results too concentrate, the first part of the cuvette is characterized by a stronger absorption and only a small portion of the excitation light will reach the center of the cuvette (the monitored region by the detector), resulting in a loss of the signal. Regarding the latter geometric factor, when a given species is characterized by a small Stoke shift between the absorption and emission spectra, the emitted light can be reabsorbed by the solution before being revealed by the detector. This phenomenon is more accentuated more the solution is concentrated.

2.2.2 Transient absorption and emission spectroscopy

Transient absorption spectroscopy (TAS) is based on the analysis of species characterized by a very short lifetime enable to be detected with the classical experimental methods. In this work thesis the TA spectra were recorded via nanosecond resolution experiment covering a window ranging from 10^{-9} to 10^{-1} s.

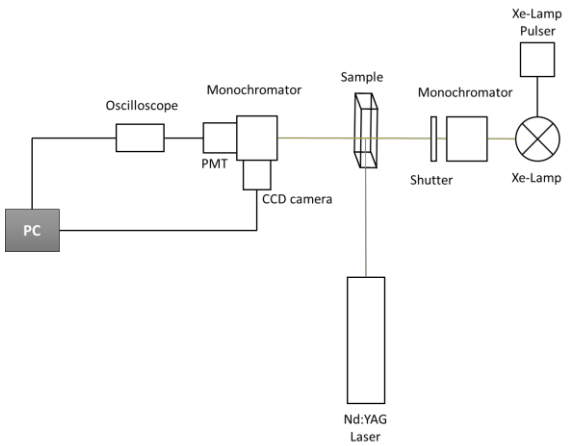

Figure 2.6: Schematic setup of Nanosecond Laser flash photolysis

In **Figure 2.6** a schematic representation of a Nanosecond Laser flash photolysis apparatus is reported. The xenon lamp (which can be used also as monochromatic source) is generally employed as analysis source which is generally pulsed enhancing the output intensity by 5-100 folders for few μs[190] improving so the signal to noise ratio (S/N) but losing temporal resolution. The most used laser is the Nd:YAG with a fundamental 1064 nm wavelength tuned by prisms to achieve 2nd (532 nm), 3rd (355 nm) and 4th (266 nm) harmonics. A photomultiplier tube (PMT) is the main detector employed, and it is coupled with a monochromator. The newest PMTs span from 200 nm to the near Infrared (NIR). The measurement is based on the difference of absorbance of a sample before (A_0) and after (A(t)) the laser excitation as described by the following equations:

$$A_0 = \varepsilon_G C l \qquad \textbf{eq. 2.15}$$

$$A(t) = \varepsilon^* C^* l + \varepsilon_G (C-C^*) l = \varepsilon^* C^* l + \varepsilon_G C l - \varepsilon_G C^* l \qquad \textbf{eq. 2.16}$$

$$\Delta A(t) = A(t) - A_0 = \varepsilon^* C^* l + \varepsilon_G C l - \varepsilon_G C^* l - \varepsilon_G C l = (\varepsilon^* - \varepsilon_G) C^* l = \Delta\varepsilon C^* l \qquad \textbf{eq. 2.17}$$

where ε_G and ε^* represent the molar extinction coefficient of the ground and excited state respectively. As shown in **eq. 2.17** the ΔA(t) depends on the concentration of the ES and on the difference in the molar extinction coefficient. Plotting the ΔA(t) against t it is possible to extrapolate the lifetime of the species under analysis. To obtain ΔA against wavelength profile it is required to collect the traces every 10-20 nm and to report the transient spectra at any given delay time after the laser pulse. To increase the S/N ratio it is necessary to shoot several times to the sample for every wavelength. The laser power can be adjusted by tuning the laser voltage and by interposing neutral filters. The output signal can be also amplified by selecting the appropriate oscilloscope input impedance (keeping in mind the resolution loss due to its time constant $\tau = RC$). The same apparatus can be employed to emission lifetime measurements avoiding the illumination of the sample with the xenon Lamp and recording the emission of the compound after the laser excitation which must be shorter than the lifetime and power enough to generate an appreciable excited state quantity. This technique is based on the measure of the excited state concentration as function of the time, considering a decay described by a first-order kinetics, the emission intensity follows an mono-exponential law as reported in **eq. 2.18**:

$$I(t) = I_0 e^{\frac{-t}{\tau}} \qquad \textbf{eq. 2.18}$$

where I(t) is the intensity of the transmitted light as function of the time, I_0 is intensity of the incident light and τ represents the lifetime of the species. When more species are involved in the decay, the process follows a multiexponential function. In this thesis the transient spectroscopy was employed mainly to analyze sensitized solid substrate and for the non-homogeneity of the surface sites, multi exponential or a Stretched exponential functions, as described in the previous and in the next chapters, have been used.

2.3 Solar Cells

2.3.1 Relevant parameters of DSSCs

Figure 2.7a reports the classical photoresponse for a Dye Sensitized Solar Cell recorded under AM 1.5G irradiation. The Power Conversion Efficiency, which represents the most important parameters that reflects the performances of the device, it can be written as follow in **eq. 2.19**:

$$PCE\% = \frac{P_{MAX}}{P_{inc}} x\ 100 \qquad \textbf{eq. 2.19}$$

where P_{MAX} is the point of maximum power and P_{inc} is the power of the incident light generally set to 1 SUN (100 mW/cm^2), the **eq. 2.19** can be rearranged as follow:

$$PCE\% = \frac{V_{OC}J_{SC}FF}{P_{inc}} x\ 100 \qquad \textbf{eq. 2.20}$$

where V_{OC} is the open circuit photovoltage (V) obtained when the flowing current is zero, J_{sc} is the short circuit photocurrent density reported in A/cm^2 which corresponds to the zero applied voltage point and FF is the fill factor which is the ratio between the maximum power and the product of V_{oc} and J_{sc}. Graphically the fill factor shows how rectangular the J-V is and it indicates the quality of the device, it increases with the increases of the shunt resistance, and it decreases with the series one. **Figure 2.7b** reports an Incident to Current Conversion Efficiency spectrum (IPCE) or External Quantum Efficiency which is described by the ratio between the number of electrons collected in the external circuit and the number of photons at a given wavelength as reported in **eq. 2.21**:

$$IPCE(\lambda) = \frac{n_e}{n_{h\nu}} = \frac{hc}{e}\frac{J}{\lambda P} \qquad \textbf{eq. 2.21}$$

where h represents the Planck's constant, c the speed of light, e the electron charge, J the photocurrent density, λ the selected wavelength and P the radiant power density. IPCE can be rearranged as reported in **eq. 2.22** to obtain information about injection quantum yield (Φ_{inj}) and the efficiency of electron collection at the photoanode (η_c).

$$IPCE(\lambda) = LHE(\lambda)\Phi_{inj}\eta_c \qquad \textbf{eq. 2.22}$$

where LHE is the Light Harvesting Efficiency that describes the portion of incident light absorbed by the sensitizer anchored to the mesoporous semiconductor and follow the Lambert Beer Law (**eq. 2.23**):

$$LHE(\lambda) = 1 - 10^{-A(\lambda)} \qquad \textbf{eq.2.23}$$

where A is the absorbance of the film at the net of the semiconductor contribution. η_c can be obtained according to **eq. 1.21** by laser flash photolysis experiments. IPCE matches the absorption spectrum of a given dye, possible shift can be observed as a consequence of a Stark effect[191], and it indicates the possible harvestable energy. Most of the synthesized sensitizers don't absorb significantly the near infrared portion of the sun light spectrum. Dividing IPCE by LHE it is possible to extract the Absorbed Photon to Current Conversion Efficiency (APCE), a λ independent parameters which is described by **eq. 2.24**:

$$APCE = \frac{IPCE(\lambda)}{LHE(\lambda)} = \Phi_{inj}\eta_c \qquad \textbf{eq. 2.24}$$

it results now clear the possibility to extrapolate the injection quantum yield by dividing the APCE for η_c. Φ_{inj} can be adjusted by tunning the electrolyte composition, increasing for example the small high-density cation such as Li^+ and Mg^{2+} that lead to an improvement of the injection driving force.

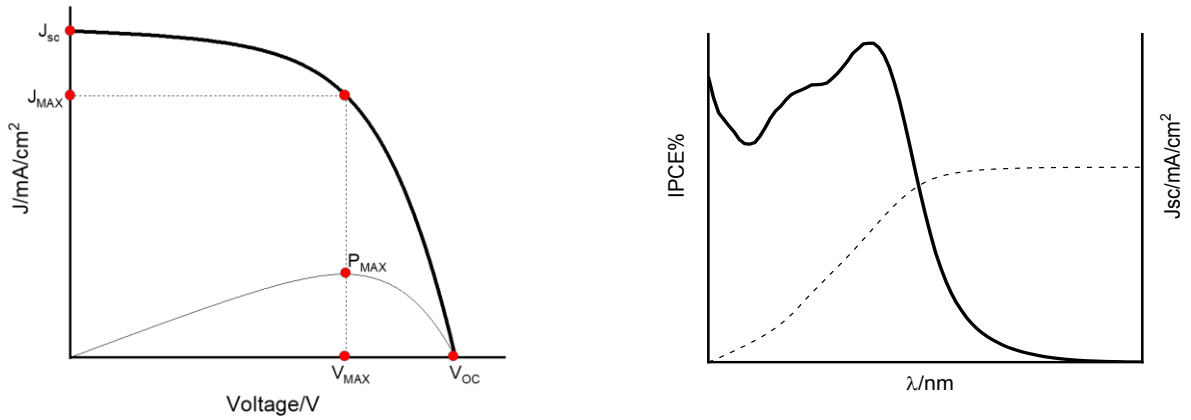

Figure 2.7: (a) Photocurrent density Voltage (J-V) curve together with the power curve. (b) Incident-Photon-to-current-conversion-efficiency and its relative integrated photocurrent density

2.3.2 One-diode equation

The general shape of the characteristic photocurrent density-voltage of a DSSC is well approximated by the Shockley diode equation (the associated circuit is reported in **Figure 2.8**) considering additional resistive loss pathway as follow:

$$I_{ext} = I_{ph} - I_D - I_{sh} \qquad \textbf{eq. 2.25}$$

where I_{ph} is the photogenerated current, I_D the diode current, and I_{sh} the shunt current associated with the recombination processes or the leakage current. **eq. 2.26** represents the I_D that leads to I_{ext} written as follow in **eq. 2.27**:

$$I_D = I_0 \left[e^{q\frac{V+I_{ext}R_S}{nkT}} - 1 \right] \qquad \textbf{eq. 2.26}$$

$$I_{ext} = I_{ph} - I_0 \left[e^{q\frac{V+I_{ext}R_S}{nkT}} - 1 \right] - \frac{V+I_{ext}R_S}{R_{sh}} \qquad \textbf{eq. 2.27}$$

where I_0 is the diode reverse saturation current, n is the diode quality factor, k the Boltzmann constant, T the absolute temperature, R_s and R_{sh} the series and shunt resistances respectively.

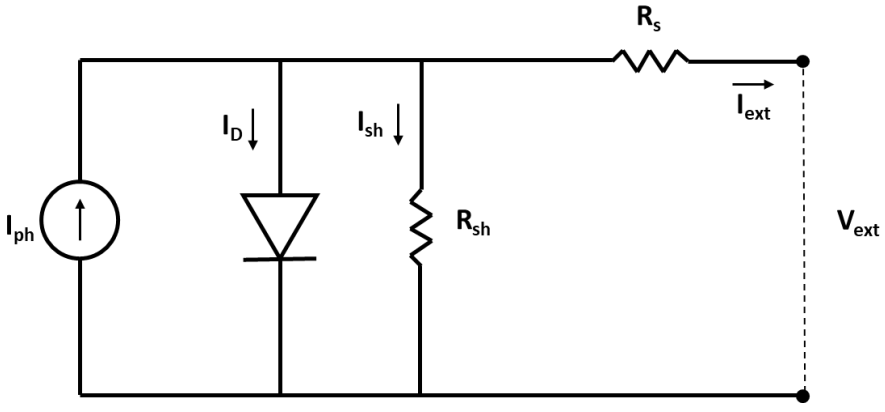

Figure 2.8: One-diode equivalent circuit model for DSSCs

The **eq.2.27** can be rearranged to approximate several parameters such as J_{sc}, V_{oc}, J_{max} and V_{max}, when the net current trough the cell is zero, the resulting open circuit potential can be written as follow:

$$V_{OC} = \frac{nkT}{q} ln\left(\frac{I_{ph}}{I_0}\right) \qquad \textbf{eq. 2.28}$$

2.3.3 EIS equivalent circuits

The one-diode equivalent circuit is considered a simplified representation of the transmission line model proposed by Fabregat et al.[192] employed to the interpretation of the impedance spectroscopy data related to DSSCs. This articulated circuit which consider transport, accumulation, and electron recombination was adopted because the simplified model works only in certain conditions.[97, 193-195] **Figure 2.9** represents the Nyquist plots for a DSSC device in different applied voltage situations fitted with the transmission line model reported in **Figure 2.10a**.

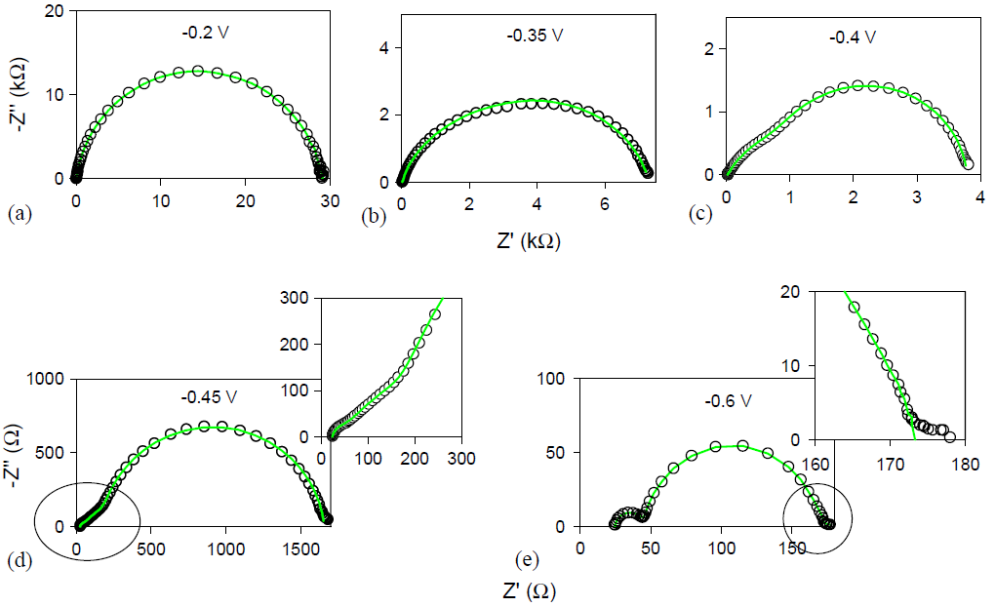

Figure 2.9: Nyquist plot for the different applied potential, from -0.2 V to V_{oc}. From ref 192

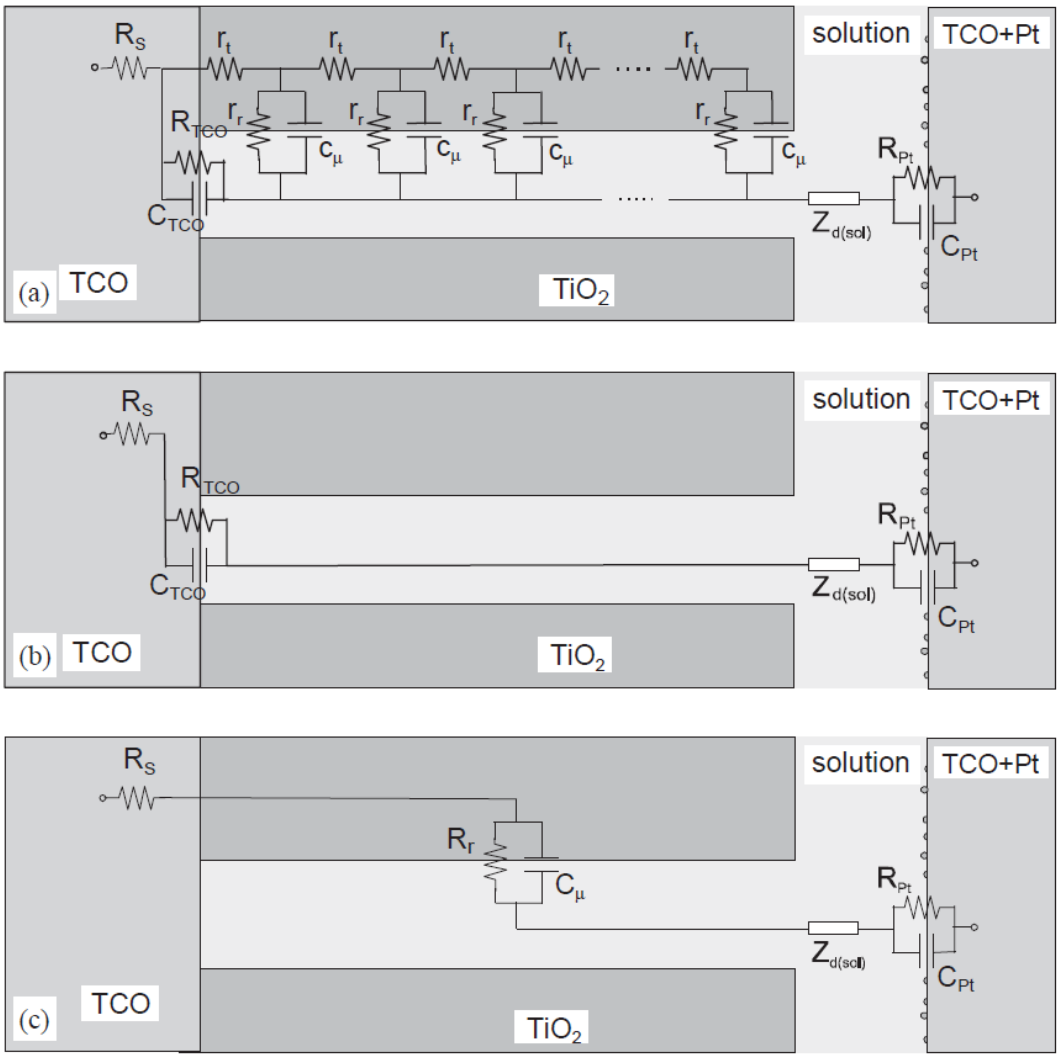

Figure 2.10: (a) Equivalent circuit for a complete solar cell. (b) Simplified circuit for insulating TiO_2 (potentials around 0 V). (c) Simplified circuit for TiO_2 in the conductive state. From ref 192

From the **Figure 2.10**, R_S and R_{TCO} represent the transport series resistance of the TCO and the charge transfer resistance related to the back electron recombination between uncovered TCO and electrolyte respectively; C_{TCO} the capacitance of the TCO/TiO_2/electrolyte interface;[196] $C\mu$ ($=c_\mu L$) the chemical capacitance related to the change of electron density as Fermi Level's function;[197] R_t ($=r_t L$) and R_r ($=r_r/L$) the resistances associated to the electron transport and to the charge transport for the electron recombination at the TiO_2/electrolyte interface; $Z_{d(sol)}$ the impedance associated to the redox couple diffusion[97, 195] and R_{pt} and C_{pt} the charge transfer resistance and the interfacial capacitance at the counter electrode/electrolyte interface.[193, 194] This reported network can be associated with the diffusion and reaction impedance[198-200] which can be written as reported in **eq 2.29:**

$$Z = \sqrt{\frac{R_t R_r}{1+i\omega/\omega_k}}\, coth\left(\sqrt{\frac{\omega_k}{\omega_d}}\sqrt{1+\frac{i\omega}{\omega_k}}\right) \qquad \textbf{eq. 2.29}$$

where $\omega_d = D_n/L^2 = 1/R_t C_\mu$ represents the characteristic frequency of diffusion in a finite layer, $\omega_k = 1/R_r C_\mu$ the rate constant associated to the recombination, ω the angular frequency and i the imaginary unit ($i = \sqrt{-1}$). The **eq. 2.29** can be rearranged[199, 201] in the case of *low recombination* ($R_t < R_r$ or $\omega_k < \omega_d$) to a semicircle at the low frequency as reported in the **eq 2.30**:

$$Z = \frac{1}{3}R_t + \frac{R_r}{1+i\omega/\omega_k} \quad \textbf{eq. 2.30}$$

and to a straight diffusion line at high frequency as reported in **eq. 2.31**:

$$Z = R_t\sqrt{i\frac{\omega}{\omega_d}} \quad \textbf{eq. 2.31}$$

where ω_d represents the frequency value of transition between the two behaviors. The opposite situation can be found in the case of *high recombination* so where $R_t >> R_r$ that leads the **eq. 2.29** to be written as follow in the **eq. 2.32**:

$$Z = \sqrt{\frac{R_t R_r}{1+i\omega/\omega_k}} \quad \textbf{eq. 2.32}$$

which is reported in literature like a diffusion and reaction in semi-infinite space[201] and also in this case it is characterized by a diffusion line at high frequency. The state of the semiconductor at the different applied potential, controls the shape of the spectra reported in **Figure 2.9**. In particular, at (a) *low applied potential*, to fit the spectrum in **Figure 2.9a** that shows a simple semicircle, the transmission line model can be simplified in that one reported in **Figure 2.10b** described by a mesh composed by a R_{TCO} in parallel with C_{TCO}, in series with Rs (in this potential region the TiO_2 is insulator). Also the counter electrode contribution can be extrapolated by an RC mesh. Z_d can be ignored.

In the case of (b) *intermediate applied potential* (**Figure 2.9d** with $R_t < R_r$), the impedance spectra are well fitted by the transmission line model with the associated impedance reported in the **eq. 2.29**. It is clearly visible the diffusion line at the high frequency characterized by a slope close to 1and, at the low *f* values, a semicircle originated by the meshes $C_\mu R_r$ along the semiconductor, Z_d can be neglected.

In the case shown in **Figures 2.9b** and **2.9c** the complete model, without any simplification, is required to fit the impedance and to try to extrapolate the contribution given by the TCO, TiO_2 and counter electrode which lying at the same frequency domain.

In the last situation (c) *more negative applied potential,* the Fermi Level of the TiO_2 is closed to the CB energy and for the high electron density, R_t and R_r become smaller, the semiconductor is now highly conductive, R_t is negligible and $C_\mu >> C_{TCO}$. The transmission line circuit can be now simplified to that one reported in **Figure 2.10c** characterized by two RC meshes, the former related to TiO_2 contribution (composed by R_r and C_μ) and the latter related to the CE, these couple of RC are separated by the diffusion contribution Z_d.

CHAPTER 3: New examples of Ru(II)-tetrazolato complexes as thiocyanate-free sensitizers for Dye Sensitized Solar Cells

3.1 Introduction

This first experimental chapter of my thesis was realized in collaboration with the Professor Stefano Stagni's group of the University of Bologna, that addressed the design and the synthesis of the complexes reported in **Figure 3.1**. This work is related to the analysis of the photoanode compartment trough the characterization of a new series of Ruthenium based complexes for Dye Sensitized Solar Cells. Over the past decade, intense research efforts have been devoted to study the coordination chemistry of tetrazole and tetrazolato based compounds, which have found application as building blocks for metal organic frameworks (MOFs)[202, 203] as well as nitrogen rich molecules for energetic materials[204] and polytopic ligands for the construction of luminescent metal and lanthanide-based complexes.[205, 206] In very recent times, the applicative scenario of these synthetically versatile nitrogen-rich heterocycles has been extended to the third generation photovoltaic technologies with the incorporation of tetrazolato based chelates, such as the 2-pyridyl tetrazolato anion,[207-209] within the structure of Ru(II) photosensitizers for dye sensitized solar cell application (DSSCs). It will be reported the preparation and characterization of new examples of Ru(II)-tetrazolato complexes, which differ both in nature and in the coordinating mode adopted by the tetrazolato ligands (**Figure 3.1**). The first structure is based on a Ru(II) tetrazolato dye reported by Dragonetti et al.,[207] (complex **D2**, **Figure 3.1**), by replacing the 2-pyridyltetrazolato ligand with the 2-pyrazinyl tetrazolato anion (complex **D1**, **Figure 3.1**). Further modifications were related to the replacement of the classical thiocyanate (NCS) units adopted in the well performed Ru(II) complexes by introducing a class of tetrazolato-based ligands, such as 5-(4-cyanophenyl)-1H-tetrazole in the case of complex **D3** as well as 5-(4-bromophenyl)-1H-tetrazole in the case of complex **D4** (**Figure 3.1**). The excited state nature and the charge transfer dynamics of **D1**, **D3**, **D4** together with the standard **N719** on TiO_2, were obtained by combining TD-DFT calculations with transient absorption spectroscopy (TAS) in the ns-ms region and DC/AC photoelectrochemical measurements with a commercial and a homemade I^-/I_3^- based electrolytes.

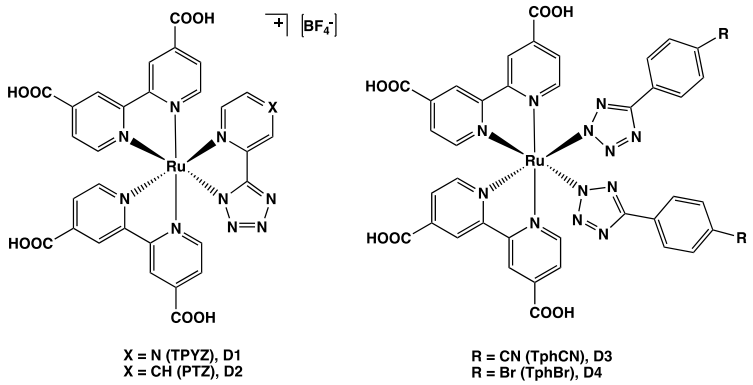

Figure 3.1: Ru(II) based complexes and relative labels described in this chapter. From ref 210

3.2 Experimental

3.2.1 Materials

All the reagents and solvents used by Professor Stagni's group were obtained commercially (e.g Alfa-Aesar) and used as received without any further purification unless otherwise specified. Alconox, Ti(IV)isopropoxide, EDOT, 1-methyl-3-propylimidazolium iodide (PMII) ≥ 98%, iodine > 99.8% and solvents (1-butanol, Absolute ethanol, 2-propanol, ACS grade methanol and anhydrous acetonitrile (ACN)) were purchased from Sigma Aldrich. $LiClO_4$ ≥99%, was bought from Acros. Magnesium iodide > 99% was obtained from Fluka. Tetrabutylammonium hexafluorophosphate ($TBAPF_6$) ≥ 98% and 1M Tetrabutylammonium hydroxide (TBAOH) were bought from Alfa Aesar. Surlyn 25 and Iodolyte Z100 were purchased from Solaronix, Switzerland. 18-NRT TiO_2 pasta was supplied from Greatcell Solar. The standard **N719** was prepared according to literature procedure.[211]

3.2.2 Methods

ESI-mass spectra were carried out with a Waters ZQ-4000 instrument (ESI-MS, acetonitrile as the solvent).

Nuclear magnetic resonance spectra (consisting of ^1H, and ^{13}C experiments) were always recorded using a Varian Mercury Plus 400 instrument (^1H, 400.1) at room temperature.

Absorption spectra of the dyed films or the solutions were recorded at room temperature using a Jasco V50 or a PerkinElmer Lambda 35 UV/Vis spectrometer respectively. The recorded spectra were corrected with an undyed TiO_2 or proper solvent.

Steady-state emission and excitation spectra were recorded using an Edinburgh FLSP920 spectrometer equipped with a 450 W xenon arc lamp, double excitation and single emission monochromators, and a Peltiercooled Hamamatsu R928P photomultiplier tube (185–850 nm).

Cyclic voltammetry measurements were performed using an Autolab PGSTAT302N potentiostat using a glassy carbon or a platinum disk as working electrode and a Standard Calomel Electrode (SCE) as reference electrode at the scan rate of 100 mV/s. The experiments were carried out in degassed ACN/CH_3OH 1:1 (v:v) solutions containing 0.1 M $TBAPF_6$. The recorded potentials have been referred to the redox couple Fc^+/Fc (ferricenium|ferrocene), which displayed E_{ox} = 0.33 V Vs SCE under the same experimental conditions.

Photocurrent density–voltage curves were carried out with a PGSTAT 302N potentiostat in cyclic voltammetry mode at 20 mV/s under AM 1.5G illumination setting the spectral irradiance to 100 mW/cm^2 (1 SUN) provided by an ABET sun simulator.

Incident Photon to Current Conversion Efficiency spectra were collected under monochromatic illumination obtained by coupling a 300 W Luxtel xenon lamp with a Newport Cornerstone CS-260 monochromator. Illumination was orthogonal to the DSSCs via a Newport liquid light guide, illuminating a spot size of ca. 1.5 cm^2. A National Instruments PXI 4130 Source Measure Unit in a PXI-1033 chassis recorded the photocurrent from the cell under test, while a PXI-4065 Digital Multimeter simultaneously measured the voltage from a Thorlabs PDA100A-EC Si amplified detector monitoring part of the irradiating light reflected by a quartz beam splitter.

Transient absorption spectroscopy in the ns–ms time scale on dyed TiO_2 thin films or methanolic dye solutions was carried out with a nanosecond Nd:YAG laser (Continuum Surelite II) by exciting the sample with the 532 nm harmonic attenuated to ca. 3.3 mJ/cm^2 /pulse by using a defocusing lens and neutral filters. Sensitized TiO_2 thin films in contact with the selected electrolytes (*CFE*, *Z100 Iodolyte*

or 0.1 M $LiClO_4$/ACN) were oriented at an angle of ca. 45° with respect to the laser beam, in order to reflect scattered laser light away from the detector. A stack of two 532 nm notch filters placed at the entrance of the detector further eliminated residual 532 nm radiation scattered by the sample. The white light probe beam generated by a 150 W Xe lamp was orthogonal with respect to the laser source. Pulsing of the Xe lamp was optional and could be exploited within a time window lower than 400 μs in order to improve the S/N ratio of the transient signals. The probe light was filtered through a 380 nm cut off filter in order to remove most of the high frequency UV radiation before being focused into the sample by means of a cylindrical lens and being collected. Depending on the time frame to be explored, in order to optimize the S/N ratio of the oscillographic traces, various oscilloscope impedances were used, ranging from 50 Ω to 10 kΩ. Usually, 10–30 laser shots at a frequency of 0.2 Hz at each sampled wavelength were averaged.

The geometry optimization of the dye structures was performed with Gaussian 09 A2[212] at the restricted DFT-pbe0/DGDZVP level in vacuo with tight convergence criteria. Time depending density function theory (TD-DFT) spectra were computed in CH_3OH according to the polarizable dielectric continuum model (IEFCPM). Kohn Sham (KS) molecular orbitals were visualized as isodensity surfaces with Gaussview 5. Wavefunction analysis and EDDM of the optical transitions were obtained with Multiwfn 3.3.9.[213] The oxidation potential of the lowest singlet excited state, whose $^{S}E^{00}$ spectroscopic energy is not experimentally accessible from steady state emission spectroscopy, was calculated from the lowest computed vertical excitation energy according to $^{S}E_{ox}^{*} = E_{ox} - {}^{S}E^{00}$. The triplet excited state potential was calculated in a similar fashion by using the spectroscopic energy $^{T}E^{00}$ from the onset of the emission spectrum according to the 10% intensity criterion (**Figure A3.5**).[214]

3.2.3 Synthesis

The synthetic part of this project was realized by the University of Bologna with the following procedures.

3.2.3.1 Ligand synthesis

TphCN, **TPYZ** and **PTZ** were obtained by following the literature procedures reported by Finnegan and co-workers.[215]

TphCN (Y = 66%). ^{1}H-NMR: (400 MHz, DMSO-d_6, δ ppm) = 8.06 (d, 2H, $J_{H\text{-}H}$ = 3.99 Hz), 8.31 (d, 2H, $J_{H\text{-}H}$ = 7.99 Hz);

TPYZ (Y = 64%), ^{1}H-NMR: (400 MHz, DMSO-d_6, δ ppm) = 9.37 (d, 1H, $J_{H\text{-}H}$ = 4.6 Hz), 8.85 (m, 2H);

PTZ (Y = 62%), ^{1}H-NMR: (400 MHz, DMSO-d_6, δ ppm) = 8.76 (d, 2H, $J_{H\text{-}H}$ = 3.99 Hz), 8.19 (d, 1H, $J_{H\text{-}H}$ = 4.6 Hz) 8.04 (m, 1H), 7.59 (m, 1H).

TphBr was obtained by following the procedure from Koguro and co-workers (Yield = 84%).[216]

^{1}H-NMR: (400 MHz, DMSO-d_6, δ ppm) = 7.98 (d, 2H, $J_{H\text{-}H}$ = 5.99 Hz), 7.81 (d, 2H, $J_{H\text{-}H}$ = 5.99 Hz);

3.2.3.2 Preparation of the *cis*-$[Ru(N^N)_2(L)]^+[BF_4]^-$-Type Complexes

cis-$[Ru(dcbpy)_2Cl_2]$ (0.066 g, 0.10 mmol) was dissolved in 60 mL of methanol in a round-bottom flask protected from light. A slight excess (2.2 eq) of $AgBF_4$ was added, and the mixture was stirred at reflux for 3 h. The reaction mixture was filtered out through Celite, and the filtrate was added dropwise to a methanolic solution of the appropriate tetrazolato ligand (1.6 eq). Once the addition was complete, the deep-red solution was stirred at reflux overnight. The mixture was then cooled to room temperature, concentrated and precipitated with a large amount of diethyl ether. The crude product was collected by filtration.

1) D1 ^{1}H-NMR: (400 MHz, CD_3OD, δ ppm) = 9.5 (s, 1H), 9.17 (m, 2H), 9.12 (m, 2H), 8.42 (d, 2H), 8.2 (d, 1H), 8.15 (d, 1H), 8.05 (m, 2H), 7.95 (m, 3H), 7.9 (m 1H), 7.43 (m, 1H,) (see **Figure A3.1**). **ESI-MS** (m/z) CH_3CN: $[M]^+$ = 823, $[M]^-$ = 87. Anal. Calcd. For $C_{29}H_{19}N_{10}O_8B_1F_4Ru_1$ (823.41) C 42.3, H 2.33, N 17.01. Found: C 42.5, H 2.36, N 17.03.

2) D2 ^{1}H-NMR: (400 MHz, CD_3OD, δ ppm) = 9.17 (m, 2H), 9.12 (m, 2H), 8.42 (d, 2H), 8.1 (m, 3H), 8.05 (d, 1H), 7.99 (m, 3H), 7.89 (m, 2 H), 7.68 (m 1H), 7.43 (t, 1H) (see **Figure A3.2**). **ESI-MS** (m/z) CH_3CN: $[M^+]$ = 823, $[M^-]$ = 87. Anal. Calcd. For $C_{30}H_{20}N_9O_8B_1F_4Ru_1$ (822.43) C 43.8, H 2.45, N 15.33. Found: C 44.1, H 2.48, N 15.36.

3.2.3.3 Preparation of the neutral *cis*-$[Ru(N^N)_2(L)_2]$-Type Complexes

cis-$[Ru(dcbpy)_2Cl_2]$ (0.046 g, 0.07 mmol) was dissolved in 80 mL of methanol in a round-bottom flask protected from light. A slight excess (2.2 eq) of $AgBF_4$ was added, and the mixture was stirred at reflux for 3 h. The reaction mixture was filtered through celite and the filtrate was added dropwise to a methanolic solution of the appropriate tetrazolato ligand (2.2 eq). Once the addition was complete, the deep-red solution was stirred at reflux temperature overnight. The mixture was then cooled to room temperature, concentrated and precipitated with a large amount of diethyl ether. The crude product was collected by filtration.

3) D3 ^{1}H-NMR: (400 MHz, CD_3OD, δ ppm)) = 10.04 (d, 2H, $J_{H\text{-}H}$ = 3.9 Hz), 9.02 (s, 2H), 8.90 (s, 2H), 8.18 (m, 2H), 8.02 (m, 2H), 7.97 (d, 4H, $J_{H\text{-}H}$ = 7.9 Hz), 7.74 (m, 2H), 7.70 (d, 4H, $J_{H\text{-}H}$ = 7.9 Hz) (see **Figure A3.3**). **ESI-MS** (m/z) CH_3CN: $[M+Na]^+$ = 952. Anal. Calcd. For $C_{40}H_{24}N_{14}O_8Ru_1$ (929.8) C 51.67, H 2.60, N 21.09. Found: C 51.75, H 2.68, N 21.1.
4) D4 ^{1}H-NMR: (400 MHz, CD_3OD, δ ppm) = 10.03 (d, 2H, $J_{H\text{-}H}$ = 7.9 Hz), 8.98 (s, 2H), 8.85 (s, 2H), 8.12 (m, 2H), 7.78 (m, 2H), 7.70 (d, 4H, $J_{H\text{-}H}$ = 7.9 Hz), 7.53 (m, 2H), 7.48 (d, 4H, $J_{H\text{-}H}$ = 7.9 Hz) (see **Figure A3.4**). **ESI-MS** (m/z) CH_3CN: $[M+Na]^+$ = 1058. Anal. Calcd. For $C_{38}H_{24}N_{12}O_8Br_2Ru_1$ (1037.57) C 43.99, H 2.33, N 16.2. Found: C 44.05, H 2.39, N 16.4.

3.2.4 DSSC assembly and characterization

The FTO slides were cleaned in Alconox and in 2-propanol solutions for 10 min under sonication each time, followed by an annealing step at 450 °C for 20 min. A thin blocking underlayer was deposited by spin coating a 0.3 M Ti(IV)isopropoxide /1-butanol solution with the following program steps: 10 sec at 1000 RPM and 20 sec at 2000 RPM followed by 15 min a 500 °C. The active TiO_2 layer was cast by doctor blade technique and annealed in an oven with the following temperature program: RT-120 °C in 10 min, 120 – 450 °C in 20 min, 30 min at 450 °C, 450 - 500°C in 10 min

and a final rest step at 500 °C for 10 min. The resulting slides were cooled down to room temperature (RT). A final top layer with a 0.4 M $TiCl_4$ solution was down in a closed chamber for 16 h and annealed at 450 °C for 30 min. The electrodes were then dipped for 16 hours in 0.2 mM ethanol solution of each dyes and of the standard **N719**. The dyed photoanodes were assembled in an open configuration. 0.25 cm^2 electrocatalytic PEDOT films for use as counter electrodes were fabricated by potentiodynamic electropolymerization on the FTO surface delimited by surlyn 25 masks. EDOT electropolymerization occurred between the working (FTO) and counter electrode (Ti sheet, 4 cm^2) facing each other at a distance of ca. 3 mm by exploiting 2 potential sweeps in cyclic voltammetry mode (0 – 1.6 V vs. SCE at 50 mVs^{-1}) in an electrolyte made of 10^{-2} M EDOT/0.1 M $LiClO_4$/ACN.[107] Different electrolytes were employed, consisting of either a custom formulated electrolyte (*CFE*) comprised of 0.1 M LiI, 0.6 M 1-methyl-3-propylimidazolium iodide (PMII), 0.05 M MgI_2 and 0.1 M I_2 in ACN or with a commercial optimized electrolyte for NCS containing dyes (*Iodolyte Z100*, Solaronix, Switzerland). The active area of the solar cells was fixed at 0.25 cm^2.

3.3 Results and Discussions

3.3.1 Synthesis, ESI-MS and NMR spectroscopy

The tetrazole ligands preparation routes were obtained by following two slightly different methods involving the 1,3 dipolar cyclization of the azide anion (N_3^-) onto the appropriate nitrile precursor. The procedure adopted by Finnegan[215] has been employed to prepare the 2(1,H tetrazol-5yl) pyridine (H-**PTZ**), 2(1,H tetrazol-5-yl) pyrazine (H-**PYTZ**) and 5-(4-cyanophenyl)-1H-tetrazole (H-**TphCN**) ligands with a quasi-quantitative yield. The 5-(4-bromophenyl)-1H-tetrazole (H-**TphBr**) was instead realized via Koguro method.[216] The complexation employed to synthesized the **D-**series was realized following multistep procedures that involved at first halide extraction from cis-[$Ru(dcbpy)_2Cl_2$] (dcbpy = 2,2'-bipyridine-4,4'-dicarboxylic acid) with a molar excess of $AgBF_4$ methanol under reflux. The removal of AgCl afforded a red filtrate that was then combined with the desired tetrazolate anion. After being heated at the reflux temperature overnight, the resulting mixtures were cooled down to room temperature. The precipitation of the desired Ru(II) complexes were realized by adding a large amount of diethyl ether to the reaction. The obtained compounds did not require any further purification step. The identity of all the Ru(II) complexes was deduced by ESI-Mass spectrometry and confirmed by ^{1}H-NMR experiments.

3.3.2 Electrochemical characterization

The thermodynamic properties of all the synthesized Ru(II) complexes **D1**-**D4** were evaluated by cyclic voltammetry analysis performed in CH_3OH/ACN 1:1 solution, the parameters are listened in **Table 3.1**.

Table 3.1: Redox properties of all the Ru(II) species presented in this work at 25 °C, CH_3OH/ACN 1:1

Complex	E / V		E_{HOMO}[c]	E_{LUMO}[c]
	oxidation[a,b] (E^*_{ox})	reduction[a,b] (E^*_{red})	(eV)	(eV)
D1	+1.31 (0.98)	-1.01 (-1.34)	-5.91	-3.59
D2	+1.02 (0.69)	-1.01 (-1.34)	-5.62	-3.59
D3	+1.30 (0.97)	-1.36 (-1.69)	-5.90	-3.24
D4	+1.07 (0.74)	-1.59 (-1.93)	-5.67	-3.01
N719	+1.07 (0.74)	-1.46 (-1.79)		

[a] In a 0.1 M $TBAPF_6$/ CH_3OH/ACN 1:1 solution, [b] E_{ox} vs SCE, (vs. Fc+/Fc); E_{ox} (Fc^+/Fc) = 0.33 V vs SCE. [c] calculated with E_{HOMO} =-(e∗E_{ox} + 4.6 [eV]) and E_{LUMO} = -(e∗E_{red} + 4.6 [eV]),[217] where e is the unitary charge [1C]

All the species are characterized by a single oxidation Ru(II)→Ru(III). **D1** exhibited a more positive oxidation potential (1.31 V Vs SCE) compared to **D2** (1.02 V Vs SCE) (**Figure 3.2a** and **c**) due to the stronger electron withdrawing effect of the pyrazine ring (**TPYZ**) with respect to the pyridyl tetrazolato (**PTZ**) moiety. A similar trend was obtained in the case of the neutral complexes **D3** and **D4**, where the stronger effect provided by the cyanide group (**TphCN**) compared to that one given by the bromide analogue, leads to a more positive oxidation potential of 1.30 V against 1.07 V Vs SCE. (**Figure 3.2e** and **g**).

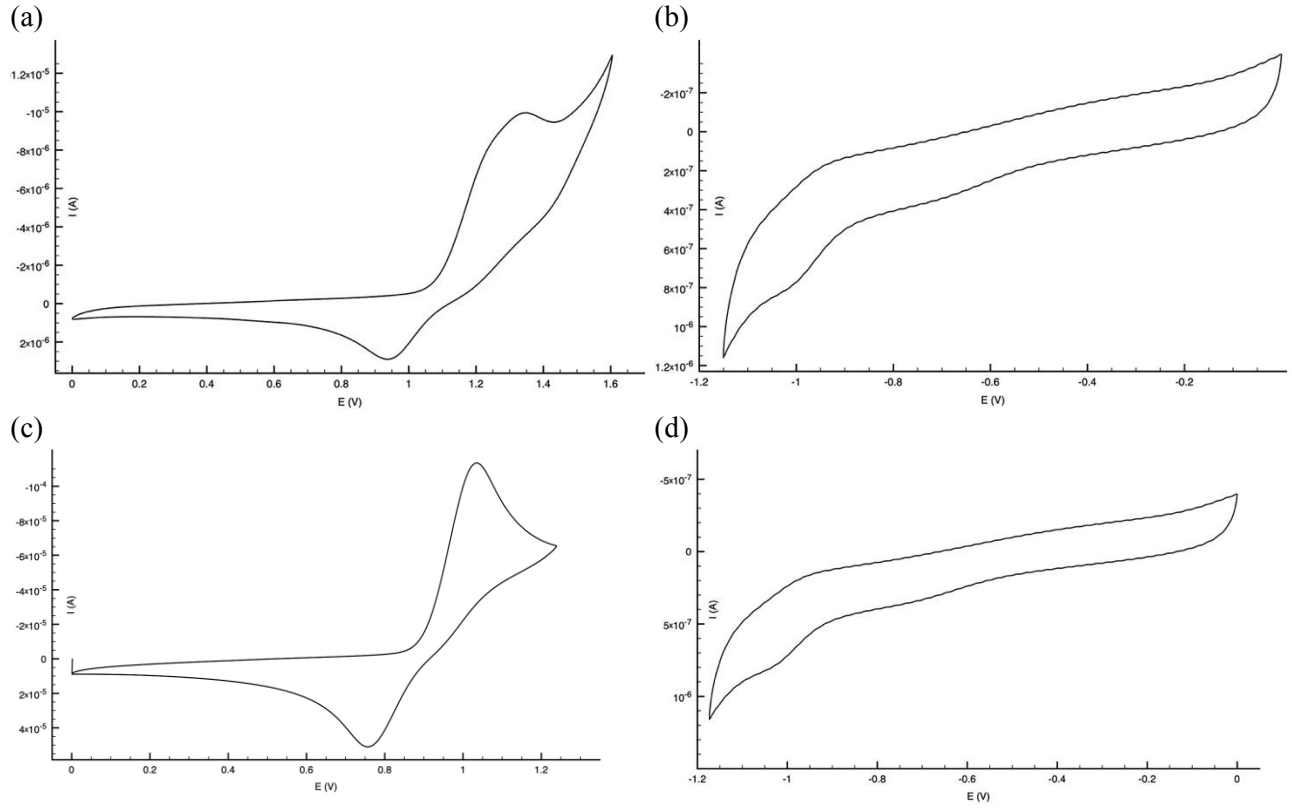

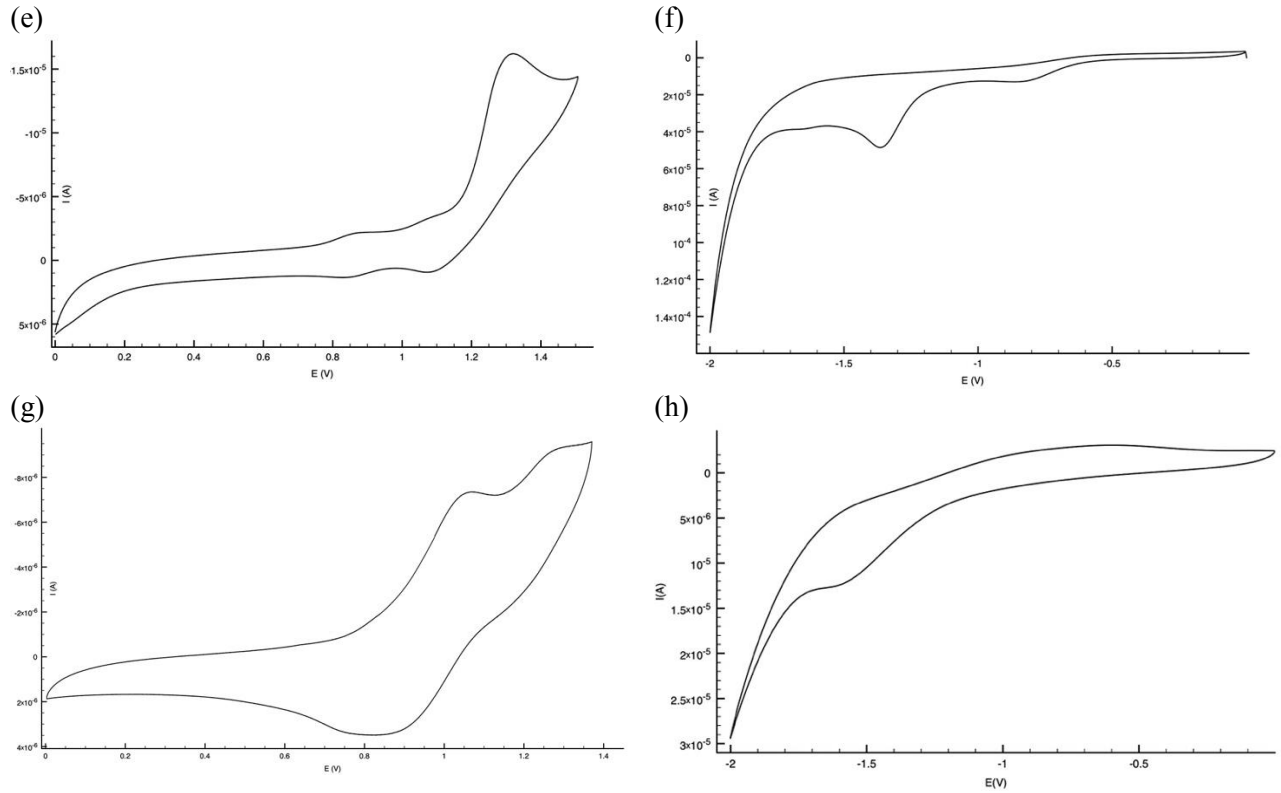

Figure 3.2: Cyclic voltammogram plots recorded in CH_3OH/ACN 1:1; (sx) oxidation, (dx) reduction for **D1** (a and b), **D2** (c and d), **D3** (e and f) and **D4** (g and h). The first two compounds were analyzed on Pt working electrode and the last two on glassy carbon. From ref 210

The reduction potential for the positively charge complexes **D1** and **D2** was found at -1.01 V in both the cases, instead for the neutral species the reduction processes are localized at -1.36 V for **D3** and -1.56 V for **D4** in agreement with the electronic effects provided by the bromine substituent. The standard Ruthenium **N719** exhibited the oxidation potential at +1.07 V and the reduction, centered on the ligand species, at ca. -1.46 V.

3.3.3 Electronic Spectroscopy

Figure 3.3a shows the absorption spectra of the methanolic solutions of the Ruthenium-based series, characterized by ligand centered transitions (π-π^*) in the UV region between 200 and 350 nm. The lower energy portion of the spectra, ranging between 450-510 nm, are characterized by weaker MLCT-type transitions involving the Ru metal center and both the dcbpy- and the tetrazolato-based ligands. The assignment was possible thanks to the TD-DFT calculations described in the next paragraph.

(a) (b)

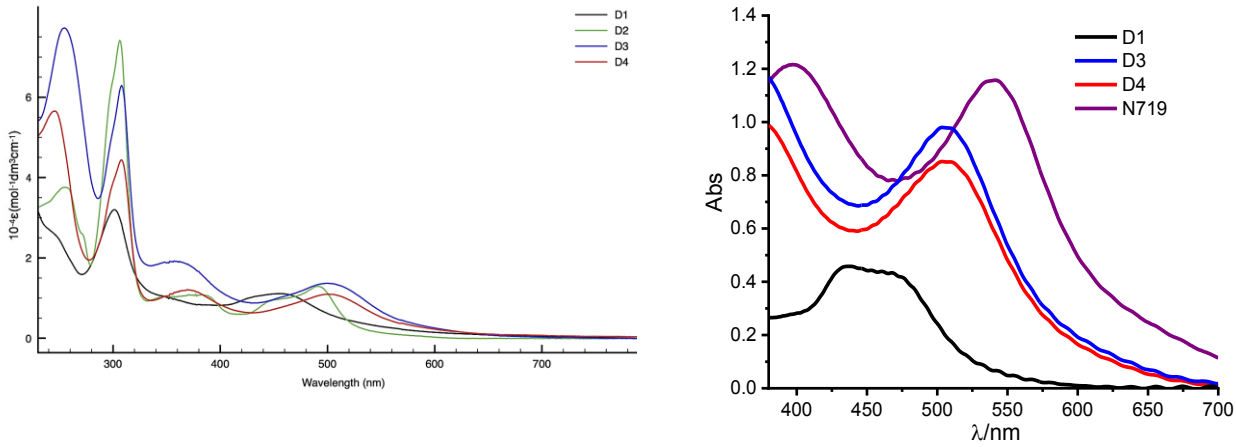

Figure 3.3: Absorption spectra of the **D**-series complexes (a) in methanolic solution and (b) absorbed onto TiO_2. From ref 210

All the series exhibited a hypsochromic shift of the main visible band compared to the standard **N719**, more pronounced in the case of **D1**($\Delta\lambda$ = ca.70 nm) and less for the other complexes ($\Delta\lambda$ = 20-30 nm), as reported in **Table 3.2**.

Table 3.2: Relevant parameters extrapolated by the absorption spectra reported in **Figure 3.3**

Complex	**Abs** λ_{max}/**nm**, $\varepsilon/10^{-4}$
D1	302 (3.19), 454 (1.11)
D2	256 (3.57), 305 (7.40), 384 (1.07), 493 (1.28)
D3	254 (7.71), 308 (6.29), 362 (1.91), 500 (1.37)
D4	247 (5.64), 307 (4.42), 370 (1.20), 501 (1.09)

In particular, the 40 nm shift of the maximum in the case of **D1** and **D2** was assigned to the more electron withdrawing effect provided by the pyrazine ring. Once absorbed onto TiO_2, **D3** and **D4** harvest up to 90% of the incident visible light on the maximum around 500 nm, **D1** exhibited a less harvest capability due to both the lower solubility in the selected solvent that leads to a lower uptake, and to the smaller absorptivity (ε). The profile recorded on thin film (**Figure 3.3b**) is coherent with those reported in solution, also in this case, a hypsochromic shift of the visible MLCT transition compared to the standard has been observed, which is characterized by the maximum of absorption around 550 nm and a tail up to beyond 700 nm, this allows to collect the low energy photons, negligible in the case of our new dyes.

3.3.4 TD-DFT calculations

The frontier orbitals involved in the main transitions are depicted in **Figure 3.4** for the ruthenium series and for the standard **N719**.

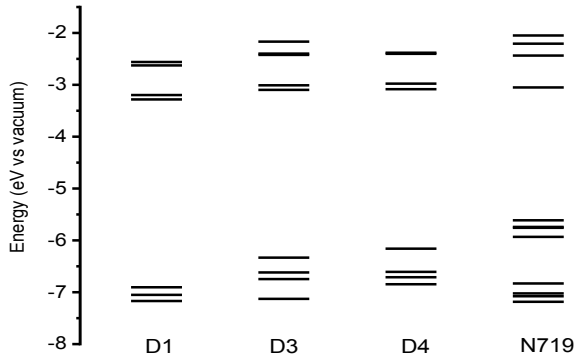

Figure 3.4: Energy levels of the KS orbitals of **D1**-**D4** complexes compared with **N719** computed at the TDDFT/PBE0/DGDZVP level in CH_3OH. The energy of the orbitals involved in the 25 lowest optical transitions are represented. From ref 210

As reported in literature, the PBE0 has been selected to reproduce the equilibrium geometry of the ruthenium complexes,[218] the DGDZVP basis set was employed to analyze the optical and electronic properties[219, 220] instead, the bulk solvation properties were described in the framework of the continuum polarization model.[221] The experimental HOMO energy trend, extrapolated via cyclic voltammetry analysis, was well reproduced by the performed calculations as follow: **D1** > **D3** > **D4**. The obtained energy resulted deeper of that one of the standard **N719**, coherent both with the experimental data and with the electron withdrawing effect provided by the tetrazolato ligands. The predicted LUMO's energy was obtained quite similar in the case of **D3**, **D4** and **N719**, being mainly localized on the same dcbpy units, while in the case of **D1**, it appeared ca. 300 meV lower. The trend is in agreement with the reduction potentials reported in **Table 3.2** but, the comparison with the absolute values should be done with some cautions for the irreversible behavior provided by the first reduction process localized on the dcbpy moieties. The lowest 25 transitions reproduce, with a good approximation, the absorption spectra of the complexes in solutions, as reported in **Figure 3.5**. The main transitions are localized around 2.5 and 3.5 eV in good agreement with the visible transitions of the experimental spectra, in particular, the most intense computed vertical transition overlap well with the lowest band found in the experimental absorption spectra, around 2.74 eV in the case of **D1** and around 2.5 eV for **D3** and **D4**. This selected TD-DFT basis set, less reproduces the tail of the spectra that are also characterized by spin forbidden excitations to triplet states because it considers only excitations with the same multiplicity. In the case of the standard **N719**, the vertical transitions (centered around 3.25 and 2.2 eV) reported in **Figure 3.5d** appear red shifted coherently with the experimental absorption spectra.

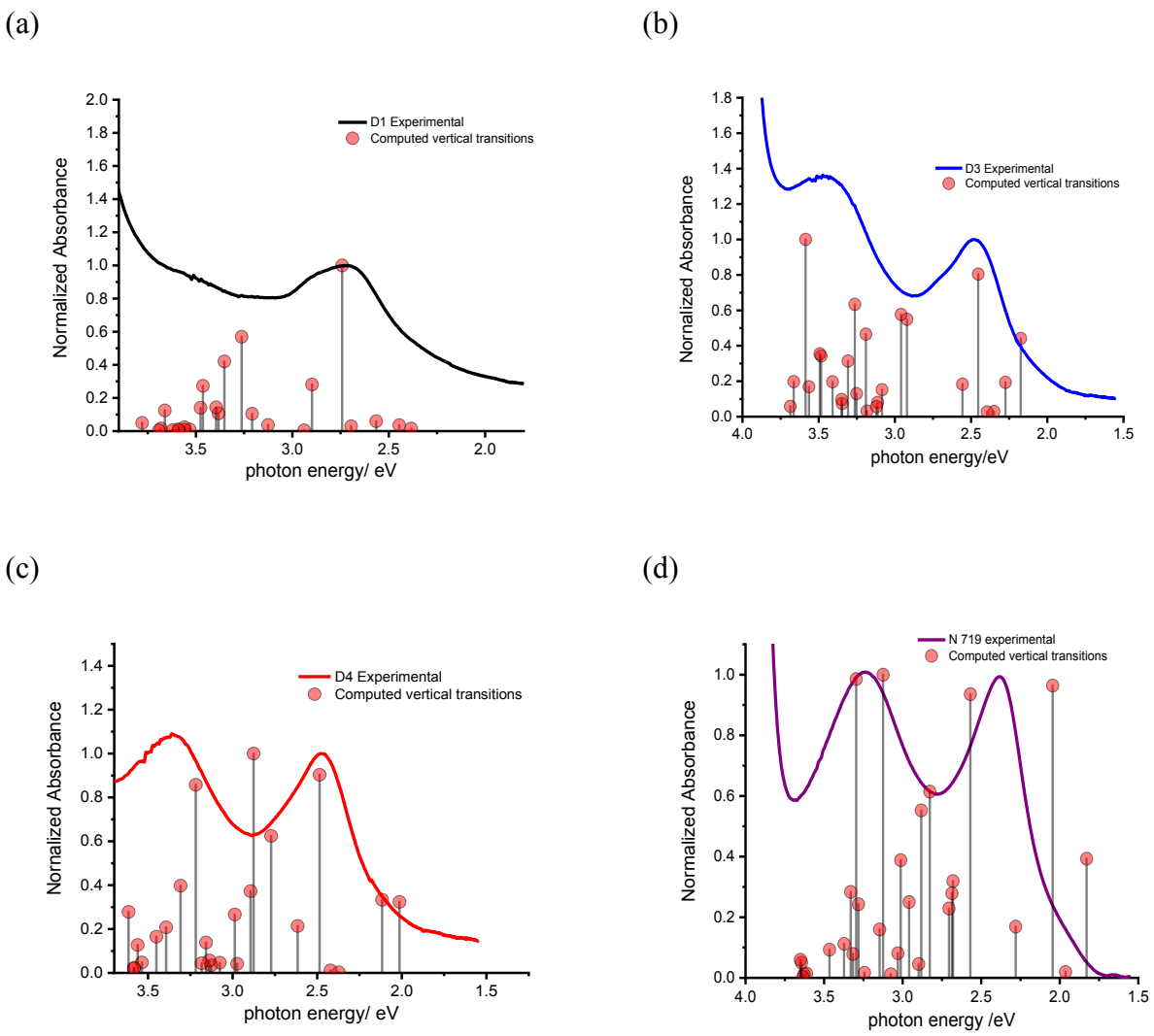

Figure 3.5: Experimental (black, blue, red and purple) vs TDDFT/PBE0/DGDZVP computed optical transitions (vertical grey lines surmounted by red circles) in the complexes **D1**-**D4** (from (a) to (c)) compared to (d) **N719**. Experimental spectra were normalized to the lowest absorption band, while vertical transitions were normalized to the most intense one. From ref 210

The main optical transitions are characterized by mixed excitations from the frontier orbitals HOMO, HOMO-1, HOMO-2 to LUMO, LUMO+1, LUMO+2 as reported by the energy diagram of **Figure 3.4** and the respective isodensity maps of **Figure 3.6**. In the case of **D4**, also the HOMO-3 and LUMO+3 orbitals are involved in the main optical transitions.

(a) D1

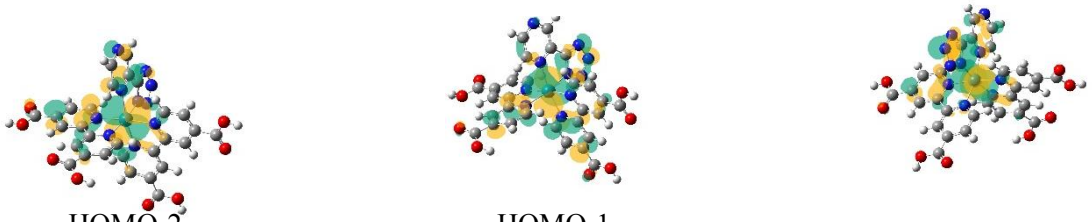

HOMO-2 HOMO-1 HOMO

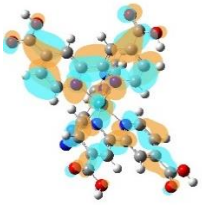

LUMO

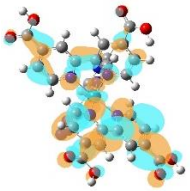

LUMO+1

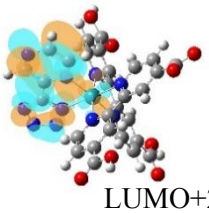

LUMO+2

(b) D3

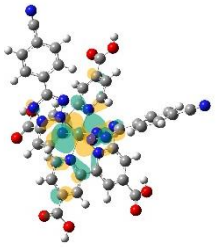

HOMO-2

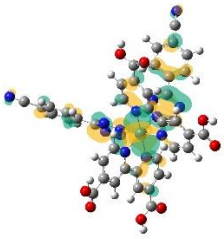

HOMO-1

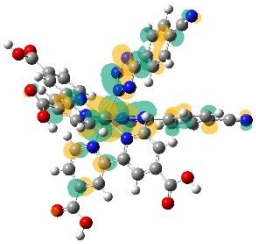

HOMO

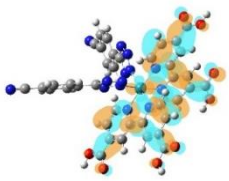

LUMO

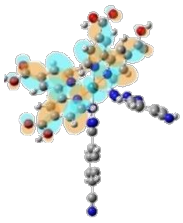

LUMO+1

LUMO +2

(d) D4

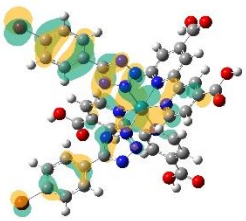

HOMO-3

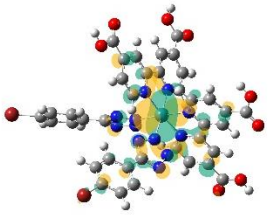

HOMO-2

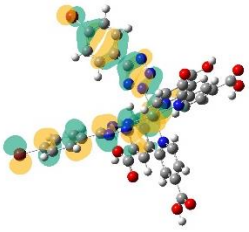

HOMO-1

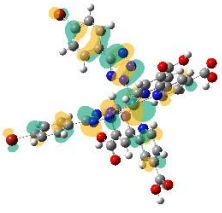

HOMO

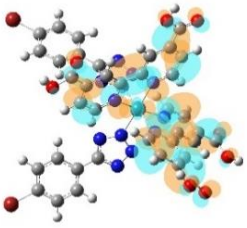

LUMO

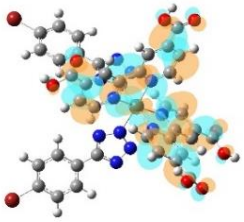

LUMO+1

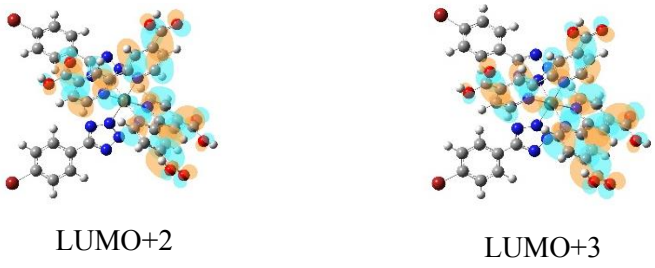

LUMO+2 LUMO+3

(d) **N719**

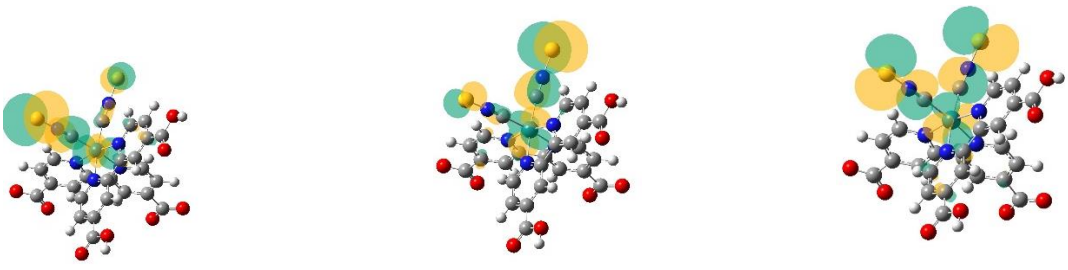

HOMO-2 HOMO-1 HOMO

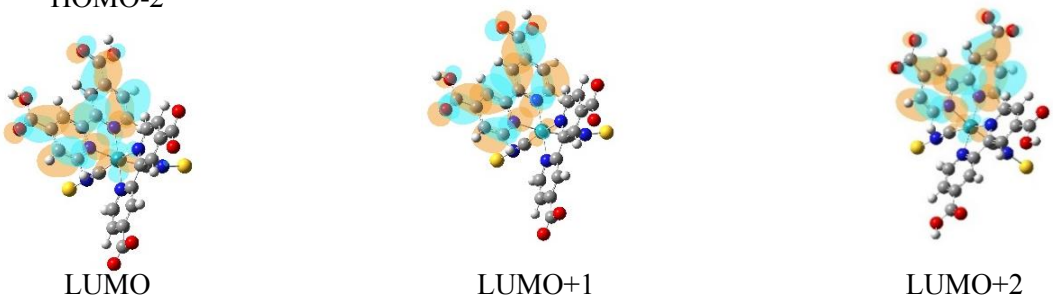

LUMO LUMO+1 LUMO+2

Figure 3.6: Isodensity surfaces of the KS orbitals contributing to the vertical transitions reported in **Figure 3.5** for (a) **D1**, (b) **D3,** (c)**D4** and (d) **N719**. From ref 210

For all the complexes, the lowest virtual orbitals are mainly localized on the dcbpy moieties whose energy is thus nearly the same for all whole **D**-family. The occupied orbitals bear contributions from the atomic orbitals of the Ru(II) metal center, which may mix both the σ and π systems of the ancillary ligands. As expected,[222] **N719** is characterized by a strong mix with the π system of the NCS groups, where the sulfur atoms contributed up to 45% to the amplitude of the highest occupied orbital. In fact, if in the case of the standard, the visible absorption bears the contribution from mixed MLCT and LLCT states, for the **D**-series the transitions appear like a classical MLCT. This behavior is corroborated by the EDDMs (electron density difference maps) of the lowest visible excitation which represent the electrons and holes distribution in the lowest excited state (**Figure 3.7**).

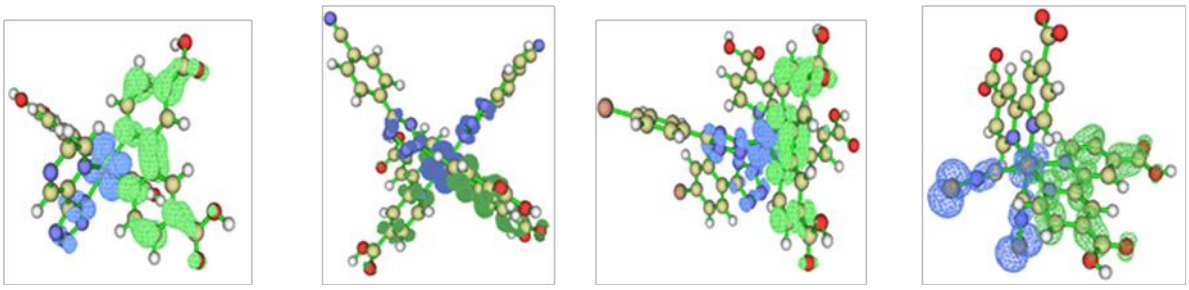

Figure 3.7: EDDMs resulting from the lowest energy optical excitation of complexes **D1**, **D3** and **D4** compared to **N719** (left to right). The green surfaces depict increased electron density (*i.e.* electron localization) while blue surfaces indicate regions of depleted electron density (*i.e.* hole localization). From ref 210

From the EDDMs it is clear that the electrons are mainly localized on the dcbpy moiety, involving the -COOH anchoring group allowing a favorable coupling for the electron transfer to TiO_2 necessary for an efficient charge injection. Substantially the hole density is mainly localized on the Ru(II) core for **D1** while in the case of **D3** and **D4**, also a significant mixing with the orbitals of the 5-aryl-tetrazolato moieties are present. The lower extinction coefficient of **D1** can be explained by the shorter transition dipole moment compared to **D3** and **D4**. The molecular mechanics model illustrates the spatial charge separations that occurs after electron injection in the TiO_2 surface where the holes are directed far from the semiconductor favoring the long-lived charge separation by decupling the positive and negative charge (**Figure 3.8**).

(a) (b)

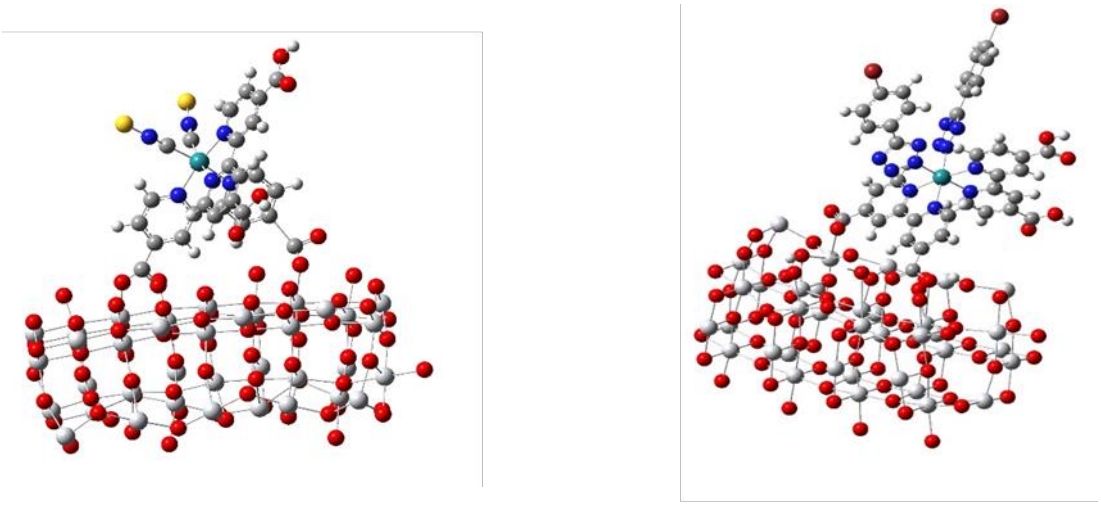

Figure 3.8: MM models of (a) **N719** and (b) **D4** right interacting with a TiO_2 surface slab optimized at the MM-UFF level. Equilibrium geometries were optimized at the DFT/PBE0/DGDZVP level. Bonding to the TiO_2 was modeled at the MM level, by freezing the internal coordinates of the dyes. In both cases the ancillary ligands point outwards with respect to the surface, but the hole density on the NCS groups is more substantial than in the case of the **TphBr** moieties. From ref 210

Unrestricted PBE0/DGDZVP calculations performed on the oxidized species (basically on Ru(III)), introduce the orbital relaxation effect due to the origin of a positive charge on the complex as a consequence of the electron injection. These analyses show a stronger involvement of the tetrazolate ligand despite that shown by the EDDMs. The involvement of the non-chromophoric ligands in the HSOMO (Highest Singly Occupied Molecular Orbital, **Figure 3.9**), which essentially describes the spatial hole distribution, varies in the order **N719** (NCS) > **D4** (**TPhBr**) > **D3** (**TphCN**) > **D1** (**TPYZ**). **Table A3.1** reports the single atom contribution to the HSOMOs for the **D**-series and for **N719** as

comparison, showing that the amplitude of such wave function on the Ru atoms decreases in the order **D1** > **D3** > **D4** > **N719**, in agreement with the increasing extent of delocalization on the ancillary ligand. Besides retarding back recombination, hole delocalization on the ancillary ligands can be crucial in accelerating the regeneration kinetics by the electrolyte, by exposing most of the hole density to diffusing iodide ions acting as electron donors in solution.

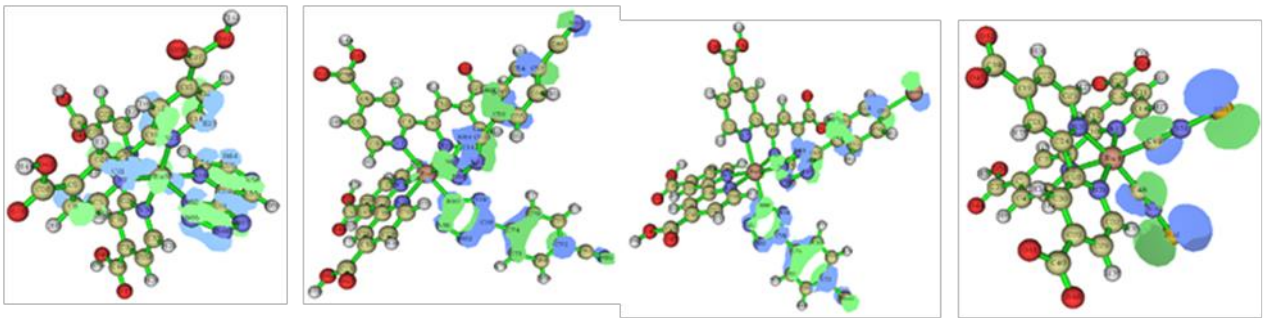

Figure 3.9: HSOMO isodensity surfaces for the **D1**, **D3** and **D4** dyes in the oxidized form compared with **N719** (left to right respectively). From ref 210

3.3.5 Time-resolved spectroscopy

The transient absorption spectra of the methanolic solutions of the **D**-series are reported in **Figure 3.10**, in the case of **D1**, it was necessary to deprotonate the -COOH groups with few drops of TBAOH for the low solubility in the selected medium.

(a) (b)

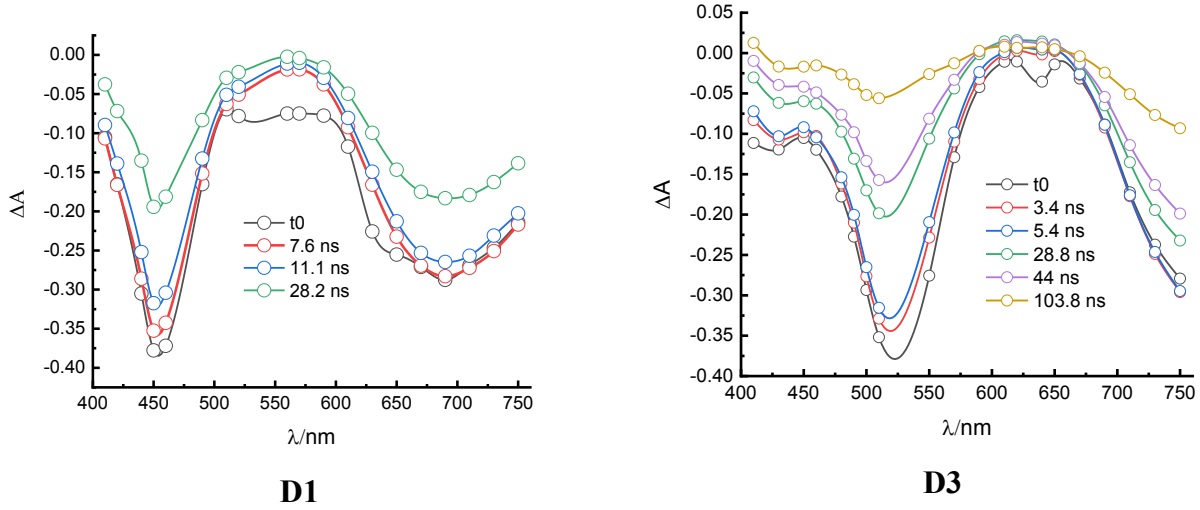

D1 **D3**

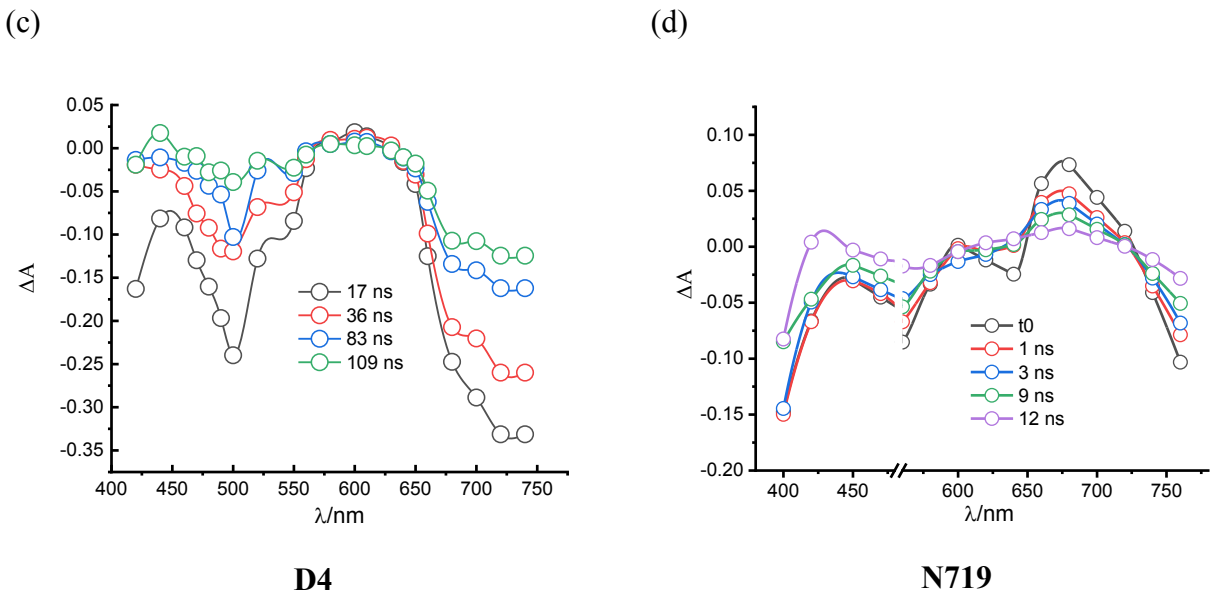

Figure 3.10: Transient absorption spectra recorded in Ethanol solution (aerated conditions) upon 532 nm pulsed (FWHM ca. 8 ns) laser excitation for (a) **D1**, (b) **D3**, (c) **D4** and (d) **N719**. Due to low solubility, **D1** was measured in methanol/TBAOH. From ref 210

All the dyes displayed a mono-exponential excited state decay with a lifetime, in aerated conditions, that follow the trend: **D4** (108 ns) > **D3** (60 ns) > **D1** (33 ns) > **N719** (ca. 8 ns). All the TA spectra exhibited the classical broad bleaches ranging between 400 - 600 nm that perfectly mirror the main visible bands of the absorption spectra. In the case of the standard dye, the spectrum is short-lived and partially convolved with the instrumental response of our spectrophotometer. Nevertheless, the bleach of the MLCT/LLCT is well defined followed by the triplet absorption ranging between 650 and 750 nm and then by the stimulated emission. The positive signal is less evident in the case of the **D**-series due to the blue shifted emission rising up at $\lambda > 600$ nm coherently with the emission spectra reported in the appendix in **Figure A3.5**. The energy gap law[82, 223] is necessary to explain the longer lifetime shown by the **D**-family together with the coordination sphere of the standard **N719** which is characterized by two anionic NCS ligands that facilitate vibrational funneling of the electronic energy and collisional relaxation via the establishment of stronger second sphere solvation. The benchmark **N719** is characterized by a more negative excited state oxidation potential (E^*_{ox}) compared to the semiconductor's conduction band edge and good excited state directionality. It is characterized by an efficient injection that occurs in a fs time scale from the lowest singlet state S_1, while, the injection from the lowest triplet states is reported to occurs in the 1-100 ps time frame[224] that, in the case of DSSCs devices seems to be the dominant one.[225] The E^*_{ox} extrapolated for the **D**-family is comparable to that one exhibited by the ruthenium standard and range between -1.07 V for **D1** and -0.87 V for **D3**, while the triplet states oxidation potential ($^TE^*_{ox}$) is at least 200-300 mV lower. **Figure 3.11** summarizes the relevant energetic levels necessary for the functioning of the new complexes-based Dye Sensitized Solar Cells (DSSCs) together with the benchmark **N719**, in good agreement with the data reported in literature.[127, 225] The flat band potential (EF) for the TiO_2 semiconductor is reported at -0.7 V Vs SCE as commonly used when it is in contact with an organic electrolyte along with the density of states (DOS) according to $DOS \propto e^{\frac{E}{E_0}}$,[226] where E_0 is an experimental potential parameter ranging between 50 and 100 mV. For all the complexes the singlet excited states are quite aligned with that one obtained for **N719** and the triplet states, with the only exception of **D3**, are comparable or slightly better reductants.

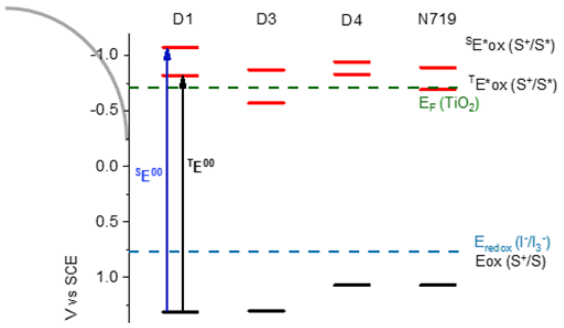

Figure 3.11: Ground and excited state oxidation potentials of the dyes under consideration (Data from **Table 3.1** and **Figure A3.3**) compared to the TiO_2 flat band potential in an organic solvent and to the equilibrium potential of a typical iodide-based electrolyte. From ref 210

The extrapolated parameters and the good excited state directionality obtained, suggest a favorable coupling with the acceptor states of the semiconductor and so an efficient injection from the singlet or triplet excited states. The **D**-family exhibited a better driving force for the regeneration process mediated by the reduce form of the electrolyte compared to the ruthenium standard, this could lead to an efficient regeneration also having a less favorable HSOMO localization with respect to **N719**.[227] **Figure 3.12** reports the transient absorption spectra for the dyed TiO_2 in contact with 0.1 M Li^+/ACN, which are characterized by a strong bleach that match the MLCT/LLCT transitions followed by the cation absorption together with the electron absorption from the TiO_2 trap states, starting from $\lambda >$ 600 and > 650 nm respectively. This positive signal is less evident in the case of **D1** and more pronounced for **D3**, **D4** and **N719**. The formation of the long lived charge separated state (Ru(III)/e^- (TiO_2)) occurs inside the laser pulse at the best resolution of our spectrophotometer (FWHM ca. 7 ns) and it is incomplete in the 5 ms time scale selected for these experiments.

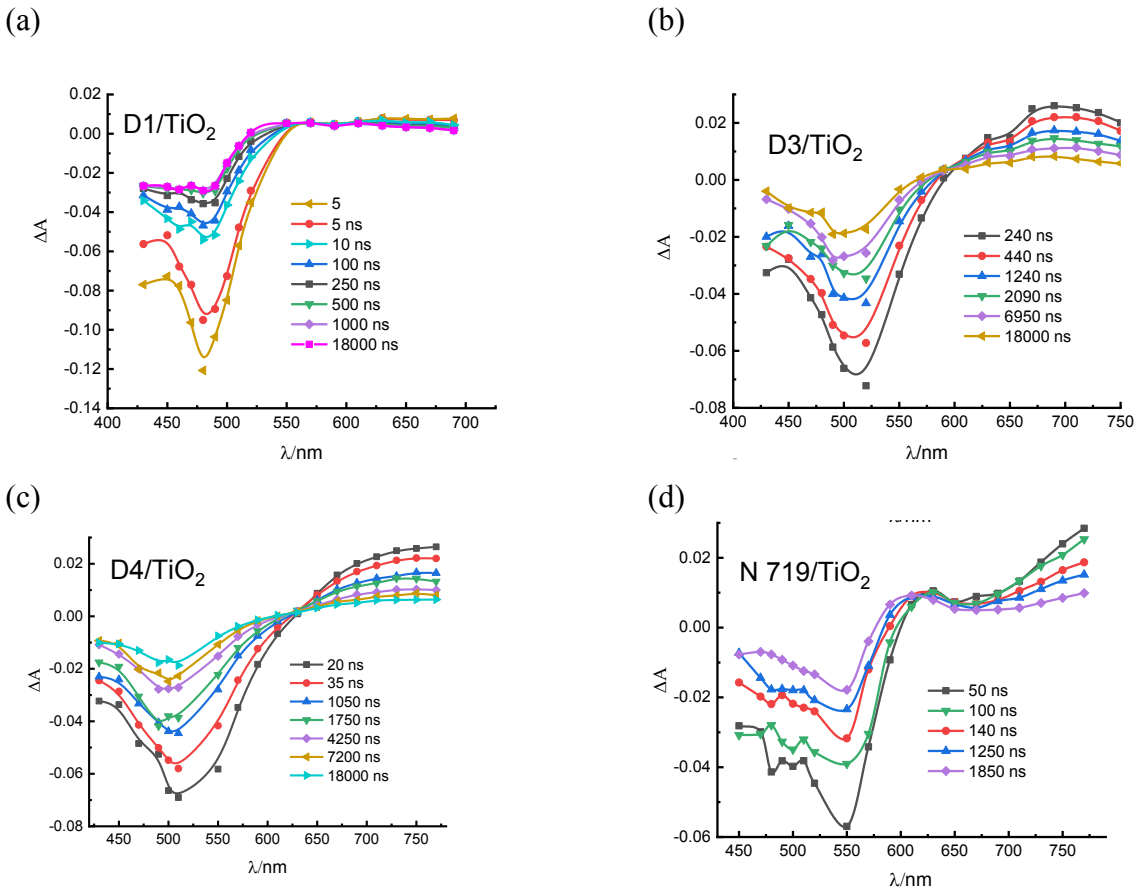

Figure 3.12: ns-µs transient absorption spectra of the **D**-dyes loaded on transparent TiO_2 thin films in contact with 0.1 M $LiClO_4$/ACN. Oscilloscope input impedance 350 Ω. **N719** is included as a comparison. From ref 210

The charge recombination between the photoinjected electron and the oxidized sensitizer follow a multiexponential kinetic for the non-homogeneity of the surface sites while the regeneration (see the regeneration kinetics reported in **Figure 3.13**) mediated by the iodide was obtained faster, being mostly complete within 10^{-5} - 10^{-4} s time scale. This leads to a regeneration efficiency stands at 98% for **D3** and **D4** and around 80% for **D1**. The faster regeneration recorded for the former dyes is related to the better delocalization of holes on **TphBr** and **TphCN** tetrazolato moieties that leads to a favorable electronic coupling with I^- species. Also in the case of **N719** the regeneration is quantitative and occurs within the instrumental response (FWHM ca. 1µs) of our instrument when the signal is pre-amplified by 10 kΩ input impedance.

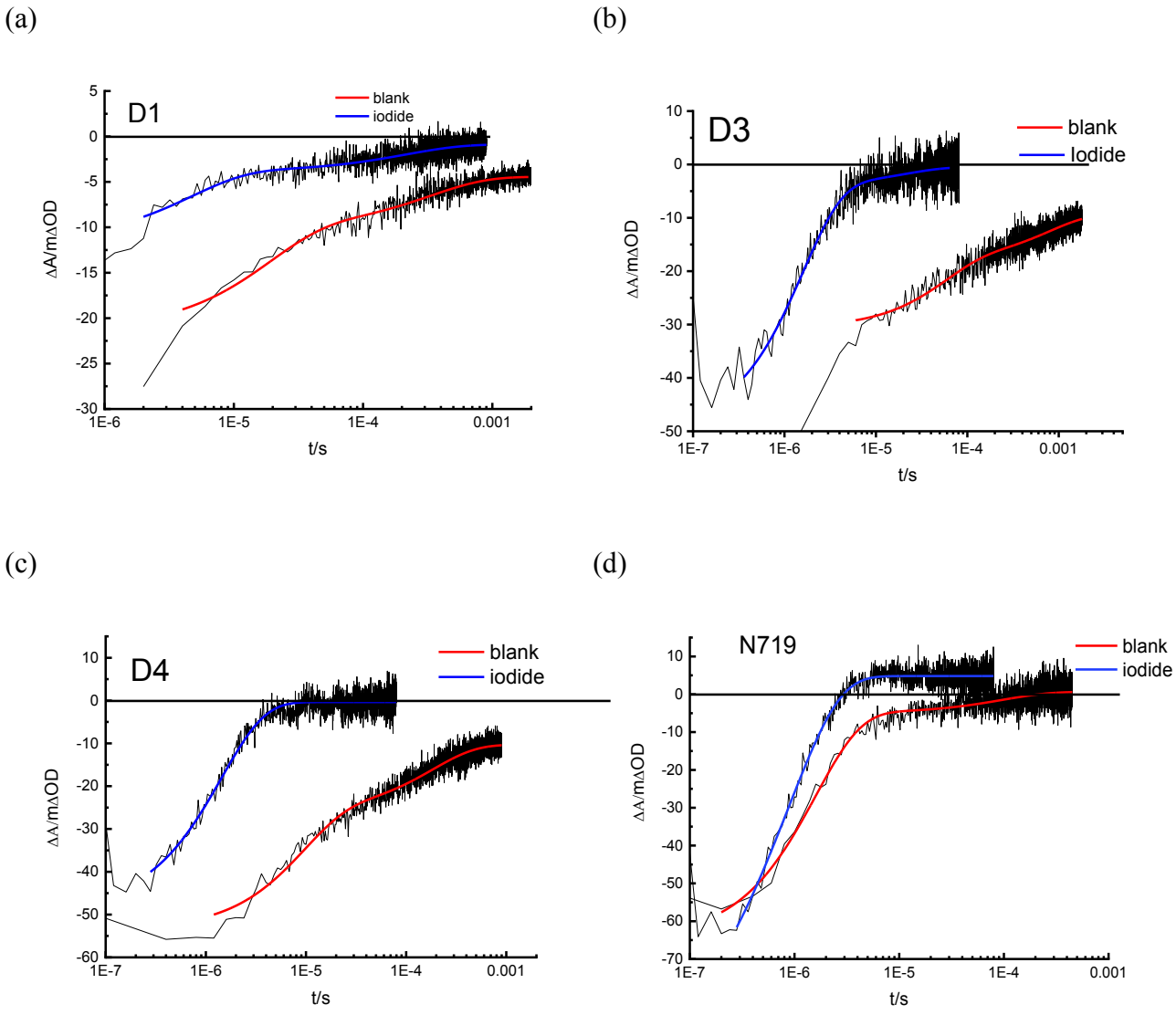

Figure 3.13: μs-ms regeneration and recombination kinetics of the Ru(III)/e$^-$(TiO_2) state probed at 510 nm. The iodide containing electrolyte was 0.1 M LiI, 0.6 M PMII, 0.05 M MgI_2 in ACN). The TA signal was amplified by a factor of 200 with a 10 KΩ impedance. Most of the **N719** regeneration occurs within the instrumental response of the spectrometer, resulting in a positive Stark absorption, after Ru(III) is completely consumed, leaving electrons inside the mesoscopic film[191]. From ref 210

3.3.6 Photoelectrochemistry

Figure 3.14 reports the J-Vs curves together with the Incident Photon to Current Conversion Efficiency and the Absorbed Photon to current Conversion Efficiency spectra. The performances of the **D**-family shown by the J-Vs under AM 1.5G illumination follow the trend **D4** > **D3** > **D1** where **D3** exhibited the best photocurrent density close to 8 mA/cm^2 and **D4** the best open circuit photovoltage but both these two complexes exceed the photovoltage recorded for the benchmark. This is confirmed in the absence of light (dark J-Vs) where the current varying in the order **D3** ≈ **D4** < **N719** < **D1** (see the Table of **Figure 3.14b** for the relevant parameters). The explanation can be found in the shielding effect provided by **TphBr** and **TphCN** that partially screen the semiconductor surface from the approach of I_3^- electron acceptor. The lower efficiency achieved by **D1** was ascribed to the lower surface protection achieved by the lower steric hindrance of the **TPYZ** combined with

the lower solubility of the complex that led to a lower surface loading. The lower photocurrent density recorded in the case of the **D**-series appears to be mainly motivated by the lower light harvesting, in fact, the IPCE% spectra, reported in **Figure 3.14c**, clearly show a broader photoaction spectrum in the case of **N719** that collects photons up to 770 nm while in the case of **D3** and **D4** up to $\lambda < 700$ nm and in the case of **D1** just to 600 nm coherently with the blue shifted absorption spectra.

(a)

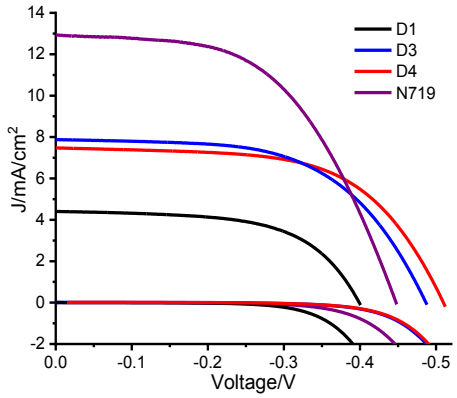

(b)

Dye	Jsc/ mA/cm^2	Voc/ V	FF%	PCE%
D1	4.40	0.40	58	1.03
D3	7.87	0.49	57	2.19
D4	7.47	0.51	59	2.27
N719	12.9	0.45	53	3.09

(c)

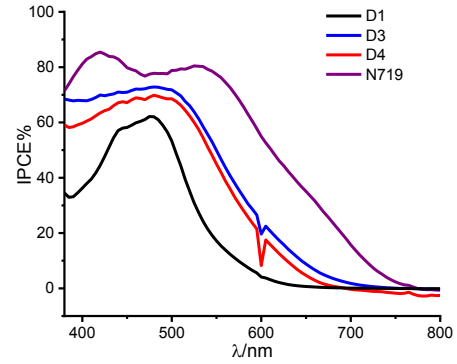

(d)

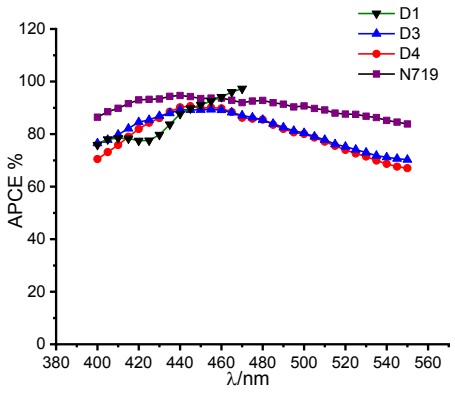

Figure 3.14: (a) J-V curves collected under AM 1.5G illumination and under dark conditions, (b) relevant parameters extrapolated by the J-V curves (c) IPCE spectra under short circuit and (d) APCE spectra (APCE=IPCE/LHE) computed from data in **Figure 3.14c** and **Figure 3.3b**. The APCE spectra were restricted to the spectral region enclosing the visible band maximum, where the error in the estimation of the LHE is the smallest. Cells were in contact with *CFE* electrolyte. From ref 210

After the normalization of the IPCE% spectra, for the Light Harvesting Efficiency (LHE (λ) = $1 - 10^{-A(\lambda)}$, where A is the absorbance of the film after correction for an undyed TiO_2 film), the resulted APCE% spectra range between 80 to 90% in good agreement with the η_{reg} estimated from the TAS and they are consistent with good injection yields (80 – 90%) for the **D**-family, as expected on the basis of their excited state oxidation potential. The information provided by the APCE plots confirms that the low performance exhibited by **D1** can be also attributable to the poor light harvesting and blue shifted response together with the lowest η_{reg}. **D3** and **D4** have shown a lower APCE% compared to **N719** for the lower injection efficiency from the excited states that, as already discussed, are less sensitive to the solvent environment that the benchmark, able to establish second sphere interactions

with the solvent medium thanks to the NCS groups. In fact, when **N719** is in contact with the CFE electrolyte become a significant better reductant, owing to a cathodic shift of ca. 200 mV of the Ru(II)/(III) potential. This peculiarity can be exacerbated when the dyed semiconductors are in contact with electrolyte formulated with a lower amount of small and highly polarizable cations such as Li^+ and Mg^{2+}. The cells were so assembled with commercial materials and filled with a high stability electrolyte formulated for **N719** ("Iodolyte Z-100"-Solaronix) containing basic additives to increase the photovoltage. The photoelectrochemical characterization is reported in **Figure 3.15** and the relevant parameters are summarized in the Table of **Figure 3.15e**. As expected, all the complexes exhibited a decreased photocurrent, less in the case of **N719** and more accentuated in the case of the **D**-family. In contrast, an increase in the photovoltage has been recorded, particularly in the case of the benchmark, instead, this increment is less evident for the **D**-series due to the significantly lower photocurrent which suggests a lower injection efficiency and lower regeneration that was obtained incomplete in 0.1 ms in the TAS experiments (see **Figure 3.15f**). Also in the presence of this commercial electrolyte, **D4** is the best sensitizers of among the tetrazolato series owing the best combination of ground and excited state oxidation potentials and light harvesting, as confirmed by electrochemical impedance spectroscopy analysis (see **Figure 3.16**).

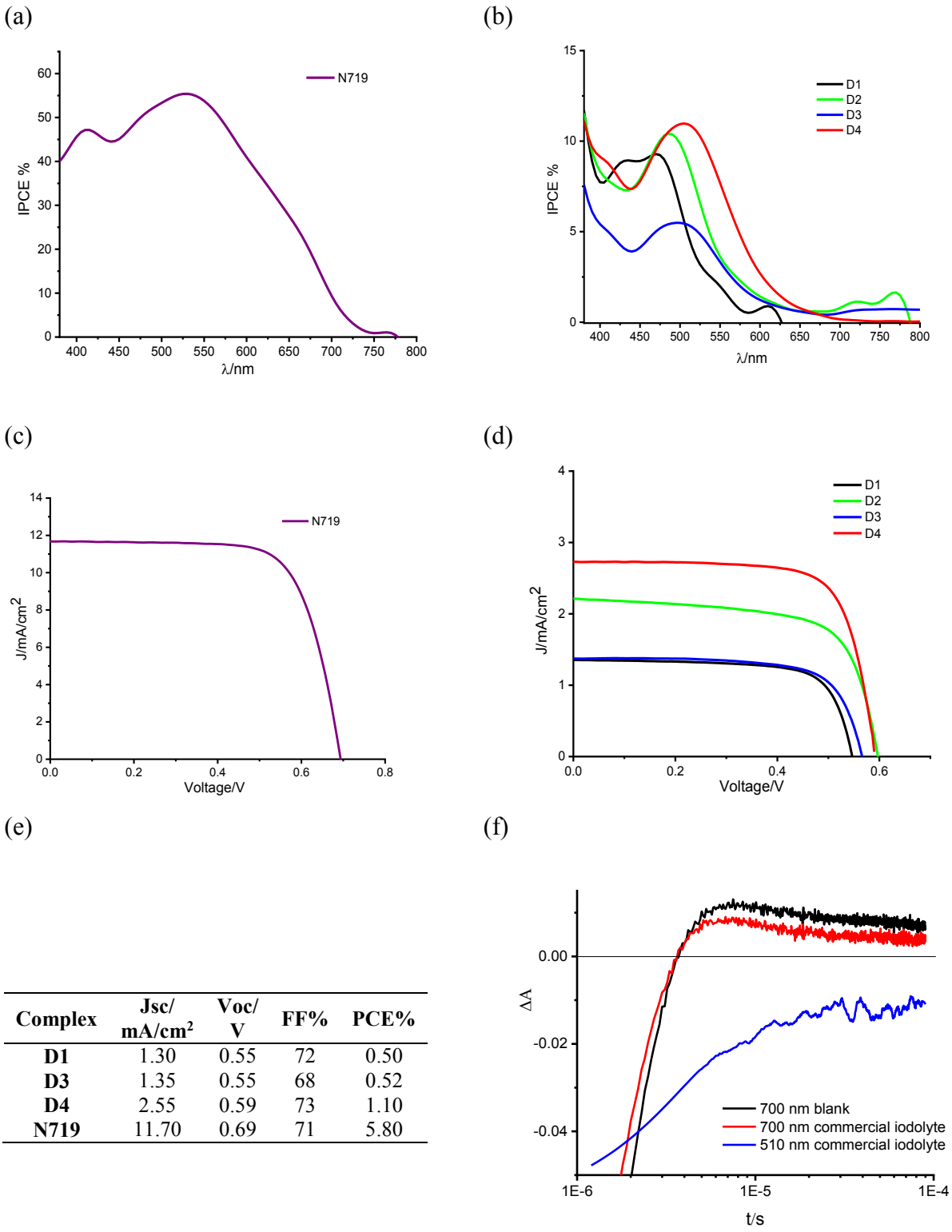

Complex	Jsc/ mA/cm^2	Voc/ V	FF%	PCE%
D1	1.30	0.55	72	0.50
D3	1.35	0.55	68	0.52
D4	2.55	0.59	73	1.10
N719	11.70	0.69	71	5.80

Figure 3.15: IPCE% for (a) the standard **N719** and (b) all the **D**-series in contact with the Iodolyte Z-100" electrolyte. Photocurrent density-voltage curves for (c) **N719** and the (d) the synthesized **D**-family and (e) their relevant parameters. (f) Regenerations kinetics for **D4** in contact with Iodolyte Z-100" electrolyte. From ref 210

The EIS provides the negative of the imaginary part of Z (-Z'') vs log(ω) plot from which one can obtain the TiO_2 electron lifetime (τ) defined by $\tau = \frac{1}{\omega_{max}}$ (**Figure 3.16a**),[228, 229] where ω_{max} is the angular frequency at which the –Z'' peak is observed. This time constant depends on the charge recombination rate that occurs between TiO_2 sensitized films and the oxidized form of the redox

couple contained in the "Iodolyte Z-100" electrolyte.[230] In agreement with the results obtained from the photoelectrochemical characterization, the calculated electron lifetime values (**Figure 3.16b**) suggest that **D3** and **D4** are the most suitable Ru(II) complexes for DSSC fabrication in the **D**-series described herein.

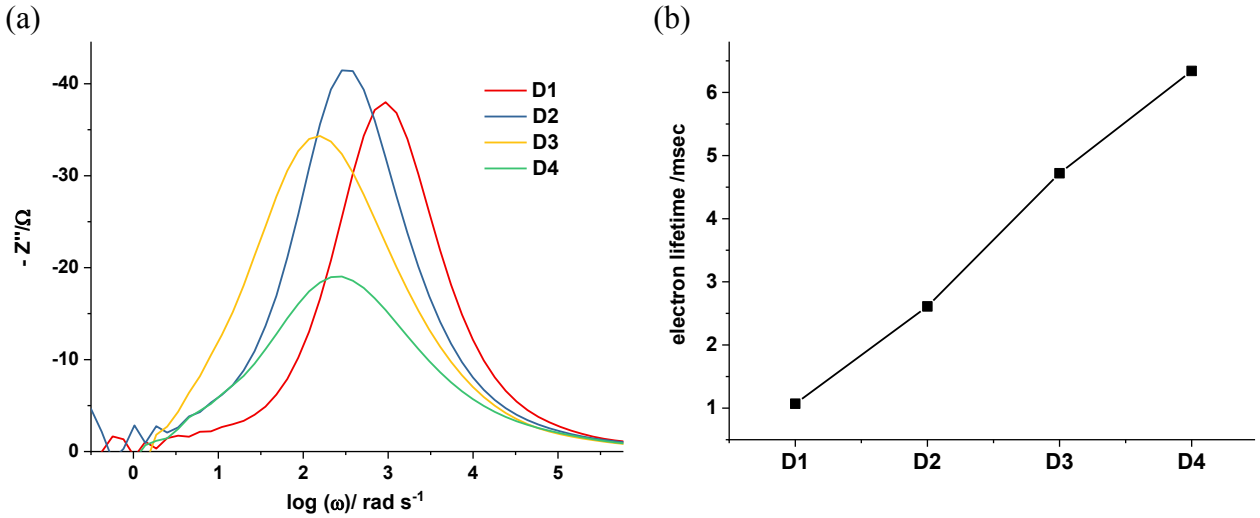

Figure 3.16: (a) Imaginary impedance plot of the EIS analyses and (b) calculated electron lifetime. Cells were in contact with Iodolyte Z-100" electrolyte. From ref 210

3.4 Conclusions

In this chapter of my thesis we have reported the synthesis and the characterization of a new series of Ru(II) sensitizers realized with 5 aryl-tetrazolato ligands with the aim to investigate their structure-related electronic properties and charge transfer dynamics when employed for n-type sensitization. The TD-DFT calculations revealed that all the complexes have a MLCT excited state character with a favorable directionality for n-type sensitization, while the combination with the electrochemical and spectroscopic analyses have shown a ground and excited states thermodynamic properties suitable for efficient interfacial charge separation. This point was corroborated with the nanosecond transient absorption spectroscopy and with the external quantum yield of photon to electron conversion higher than 80% in a Li^{+}/Mg^{2+}-based electrolyte. The best performances have been recorded in the case of **D4** thanks to the combinations of the broader harvesting, efficient regeneration, and electron injection. The new compounds were tested in the presence of the well-known **N719** that, compared to **D**-series, exhibited a broader and red shifted absorption spectrum. The origin of the higher energy shift of the new compounds is provided by the stronger stabilization of the d_{π} orbitals of the metal center induced by the tetrazolato moieties, which limits photoconversion at $\lambda < 700$ nm.

CHAPTER 4: Iron(II)NHC-based sensitizers

This second experimental chapter of my thesis is still about the photoanode optimization trough the employment of abundant first row d-block elements, in particular iron (II) complexes as photosensitizers. Three subparagraphs will describe the different way employed to try to increase the Power Conversion Efficiency of this abundant and not toxic material. All the synthetic parts of these projects were addressed by Dr. Gros Group's of the University of Lorraine and most of the computational characterization by Dr. Mariachiara Pastore's group of the same University. Our first study was about the investigation of charge transfer dynamics that occurs in photoelectrochemical cells in the presence of **C1**, a homoleptic complex characterized by σ-donating carbene and σ-donating and π-accepting pyridine, synthesized with the aim to try to stabilize the ^{1,3}MLCT states below the MC levels. This dye was synthesized and employed for n-type sensitization, for the first time, by Dr. Gros that led to an unprecedented 0.13% of cell efficiency with a commercial substrate and electrolyte. After the optimization of all the components (photoanode, electrolyte and counter electrode) we achieved 1% of Power Conversion Efficiency with an external quantum yield of photon to electron conversion around 50%. In the second project, we decided to try to increase the excited state directionality with heteroleptic complexes designed with similar features but with and without spacers between the pyridine-based ligand and the carboxylic anchoring group. In particular, **ARM13**, the heteroleptic analogue of the **C1,** led to 1.5% of Power Conversion Efficiency. A further improvement was obtained introducing an electron-donating group to the ancillary ligand not involved in the interaction with the semiconductor surface. **ARM130** led to 1.83% of efficiency after the optimization of the substrate. **Figure 4** shows the structures of the three best sensitizers employed in our different projects.

(a) (b) (c)

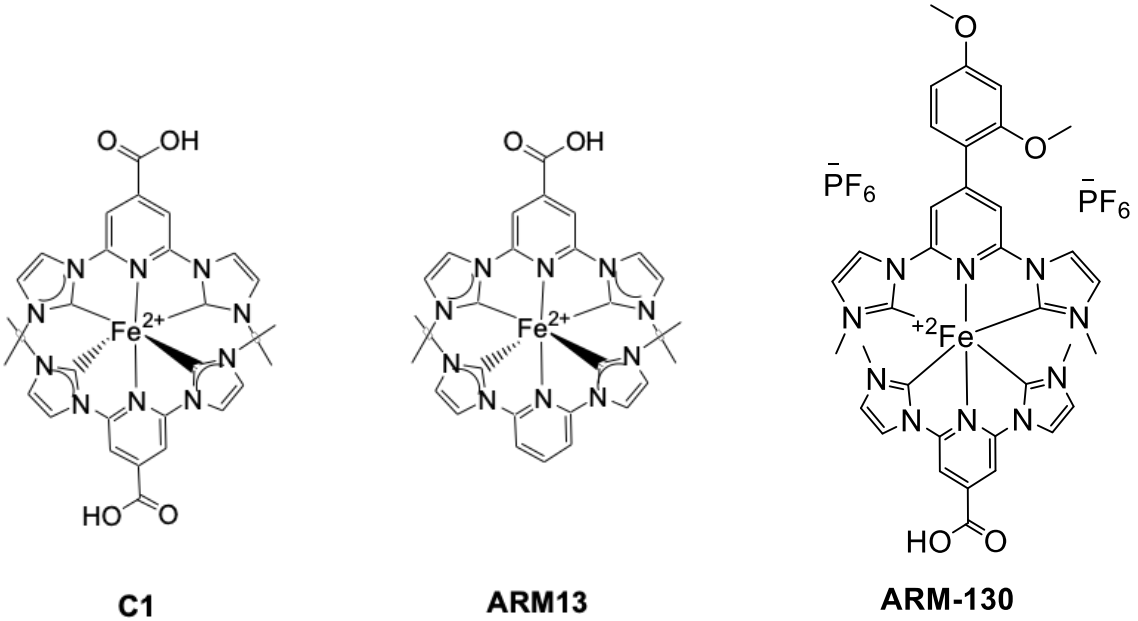

Figure 4: Structures of (a) the homoleptic **C1**, (b) the heteroleptic **ARM13** and (c) the heteroleptic **ARM130**

a) Recombination and regeneration dynamics in Fe(II)NHC-sensitized solar cells

4.1a Introduction

Fe(II) polypyridine complexes are characterized by an ultrafast deactivation of the MLCT manifold to metal centered states,[81, 231-233] significant advances have been recently reported by Dr. Gros[6] with the employment of pyridyl-N-heterocyclic carbenes (NHC)[6, 91, 94, 234, 235] leading to a significant improvement in the ^{3}MLCT lifetime, reaching 16 ps in the case of the complex **C1**. This great result was achieved combining σ-donating NHCs and π-accepting carboxylic groups as anchoring moieties. Dr. Gros in 2016 obtained an unprecedent PCE% of 0.13% with commercially available materials. The aim of this first projects on Fe(II)-sensitized solar cells was to investigate the bottlenecks of these photovoltaic devices through the investigation of recombination and regeneration dynamics involving **C1** adsorbed on either n-type TiO_2 and SnO_2 in contact with I^-/I_3^- optimized electrolyte. After all the optimization, we obtained 1% of PCE.

4.2a Experimental

4.2.1a Materials

PMII ≥ 98%, ACS grade I_2 ≥ 99.8%, GuNCS ≥ 97%, EDOT 97%, Alconox, Titanium(IV) isopropoxide ($Ti(OiPr)_4$), 4-TBPy 96%, $SnCl_2$ 98% and solvents (anhydrous ACN 99.8%, ACS grade 2-propanol ≥ 99.8%, ACS grade absolute Ethanol (EtOH), 99.9% 1-butanol) were purchased from Sigma-Aldrich and used as received. Ultra dry LiI 99.999% and MgI_2 > 99% were bought from Fluka, $LiClO_4$ ≥ 99% was purchased from Acros organics. FTO TEC-7 was bought from NSG, 18NR-T and 18NR-AO TiO_2 pastes were purchased from Greatcell Solar, the high stability electrolyte (HSE) was bought from Dyesol. Surlyn 25 was supplied from Dyepower Consortium. **N 719** was synthesized according to previous directions.[211] SnO_2 paste was prepared according to published procedures.[236] The Fe(II)NHC complex **C1** was prepared according by Dr. Gros's group as previously reported.[6]

4.2.2a Methods

Absorption spectra of the sensitized films were recorded with an agilent Cary 300 UV-Vis spectrophotometer at RT against a reference constituted by an undyed photoanode belonging to the same preparative batch.

The CVs were obtained with a PGSTAT 302N potentiostat in a standard three electrode cell on the dyed TiO_2 thin film as working electrode, a Pt as a counter electrode and double jacketed SCE as a reference in 0.1 M $LiClO_4$/ACN.

The photocurrent density - Voltage curves were collected by a PGSTAT 302N potentiostat, in cyclic voltammetry mode, coupled with an ABET technologies AM 1.5G sun simulator. The lamp irradiance was set to 100 mW/cm^2 (1 SUN). Incident photon-to-current efficiency spectra were recorded under the monochromatic illumination generated by an air-cooled Luxtel 175 W Xe lamp coupled to an Applied Photophysics monochromator.

Transient absorption spectroscopy was carried out on the sensitized thin films in contact with various electrolytes using the 532 nm harmonic of a nanosecond Nd:YAG laser (Continuum Surelite II) and a monochromatic probe beam. Various neutral filters were used to set the laser fluence at the desired

value and appropriate input impedances, varying from 50 to 1 MΩ were used to amplify the transient signals on the appropriate time scales.
AFM images of the different electrodic substrates were collected with a Digital Instruments Nanoscope III scanning probe microscope (Digital Instruments, CA). The instrument was equipped with a silicon tip (RTESP-300 Bruker) and operated in tapping mode. Surface topographical analysis of raw AFM images was carried out with NanoScope analysis 1.5 program.
FT-IR were measured on a Bruker Vertex 70 FT-IR in diffuse reflectance mode by using either **C1** dispersed in KBr or loaded on Degussa P25 TiO_2 powder. In order to avoid saturation, the dyed P25 was disperded in KBr until obtaining a good S/N ratio without showing saturated bands. Frequency calculations were performed by DFT on the optimized structures of **C1** in fully protonated, anionic and coordinated to Ti(IV) forms. Optimization was carried in vacuo at the B3LYP/LANL2DZ level by using Gaussian 09 A 02.

4.2.3a DSSC assembly and characterization

The FTO slides were cleaned in Alconox and in 2-propanol solutions for 10" under sonication each time, followed by an annealing step at 450 °C for 20 min. A thin blocking underlayer was deposited by spin coating a 0.3 M Ti(IV)isopropoxide /1-butanol solution with the following program steps: 10 sec at 1000 RPM and 20 sec at 2000 RPM followed by 15 min a 500 °C. The TiO_2 colloidal paste (18-NRT and 18-NRAO) was cast by doctor blade technique and annealed in an oven with the following temperature program: RT-120 °C in 10 min, 120 – 450 °C in 20 min, 30 min at 450 °C, 450-500°C in 10 min and a final rest step at 500 °C for 10 min. The resulting slides were cooled down to RT. A final top layer with a 0.4 M $TiCl_4$ solution was down in a closed chamber for 16 h and annealed at 450 °C for 30 min. The electrodes were stained by immersion in a 0.2 mM of acetonitrile solution of **C1** with 0.04 mM of chenodeoxycholic acid. Similar adsorption conditions were used for **N719** adsorption from ethanolic solution. The dyed photoanodes were assembled in an open configuration with PEDOT as counter electrode (prepared according to the directions reported in the previous chapter) and Surlyn 25 as spacer. The active area of the solar cells was fixed at 0.25 cm^2. Other FTO substrates were first treated by spin coating a 0.3 M $SnCl_2$ in EtOH according to the same protocol described above. Following heating at 500 °C for 15 min the SnO_2 blocking underlayer was obtained. Mesoporous SnO_2 was obtained by blade casting an aqueous SnO_2 paste[236] on top of the compact SnO_2 layer, followed by sintering at 500 °C. A final treatment with $TiCl_4$ in order to improve the adsorption capability of these photoanodes was performed, as described above. Redox electrolytes were prepared according to the following formulations, *electrolyte 1 (el1):* 0.1 M LI, 0.6 M PMII, 0.1 M I_2, 0.05 M MgI_2 in acetonitrile; *electrolyte 2(el2):* 0.1 M LI, 0.6 M PMII, 0.1 M I_2, 0.1 M MgI_2, 0.1 M GuNCS in acetonitrile; *basic electrolyte:* 0.1 M LI, 0.6 M PMII, 0.1 M I_2, 0.05 M MgI_2, 0.2 M 4-TBPy in acetonitrile; commercial HSE (High stability electrolyte).

4.3a Results and Discussions

4.3.1a General characterization

In order to employ the optimal substrate for the cell efficiency, a screening of the semiconductor morphology was performed. A first commercial transparent TiO_2 paste was analyzed with and without blocking underlayer, its surface is characterized by a network of ca. 20 nm nanoparticles

homogenously distributed (**Figure 4.1a**). A similar configuration was tested in the case of a semi-opaque films that are characterized by 20 nm active nanoparticles together with larger light scattering particles in the 100 nm range (**Figure 4.1b**). When **C1** is loaded on TiO_2 (**Figure 4.1c**), its absorption spectrum is characterized by a narrow well-defined MLCT band centered around 500 nm that, in this wavelength, collects quasi-quantitatively the incident photons. The same profile was recorded when the Fe(II) sensitizer is anchored on SnO_2 (**Figure 4.1d**), also in this conditions, similar harvesting efficiency is found. **C1** does not emit in fluid solution, its spectroscopic energy (E^{00} = 2.26 eV) was evaluated from the onset of the MLCT band at 550 nm, point where the absorption intensity is ca. 5% of that one recorded at the maximum value.

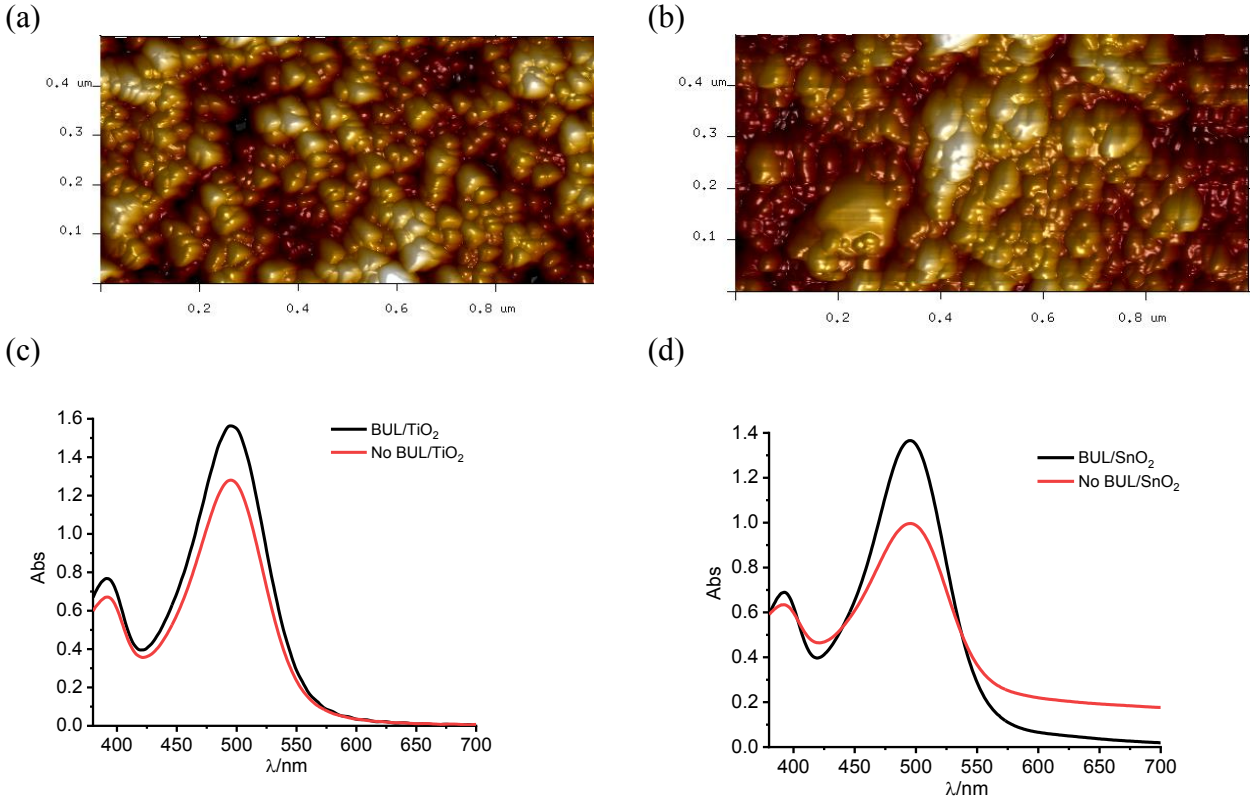

Figure 4.1: 3D map of (a) the transparent TiO_2 (18NR-T) nanoparticles and (b) the opaque TiO_2 film (18NR-AO). Absorption spectra of **C1** recorded with and without blocking underlayer on (c) TiO_2 or (d)SnO_2 substrates. From ref 237

Figure 4.2 reports the cyclic voltammetry plots carried out on dyed film as working electrode which are characterized by a quasi-reversible Fe(II)/(III) oxidation process with an E_{ox}= 0.67 V Vs SCE and a $\Delta E_{peak} \approx$ 100 mV. Combining the spectroscopic energy and the oxidation potential, the resulting excited oxidation potential was found at -1.6 V leading to an ample driving force (ca. 900 meV) for the electron injection in the TiO_2 conduction band, that is commonly reported at -0.7 V Vs SCE in an organic medium.

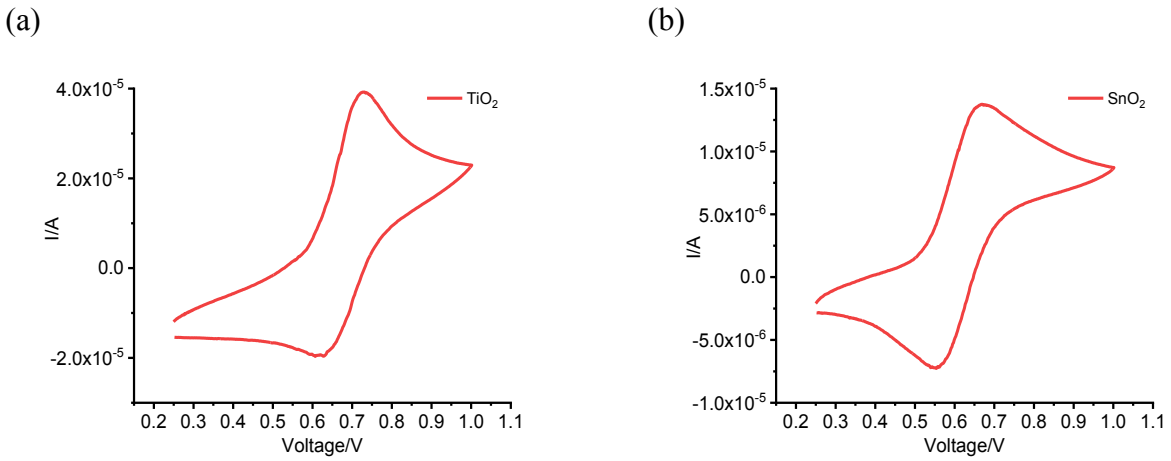

Figure 4.2: Cyclic voltammetry of **C1** loaded on (a) TiO_2 and (b) SnO_2. From ref 237

4.3.2a FT-IR

FT-IR analysis were carried out to estimate the degree of deprotonation of **C1** onto TiO_2. **Figure 4.3a** reports the shift of the COOH stretching band of **C1** from 1701 cm^{-1} to 1739 cm^{-1}, this frequency is coherent with the calculated one found at 1725 cm^{-1} (**Figure 4.3b**) when no deprotonation occurs. The obtained shift can be assigned to the ester type COO-Ti anchoring mode.[238] The computed spectrum of the fully anionic form (**Figure 4.3c**) is characterized by the normal modes of the COO^- groups around 1610 and 1618 cm^{-1} having a low intensity. These agree experimentally with the presence of a relatively broad band at 1624 cm^{-1} (**Figure 4.3d**) when the dye is loaded on TiO_2, suggesting the partial formation of the fully anionic form. Chelation of COO^- to Ti(IV) also results in a band at 1336 cm^{-1}, predicted by the calculations, which is found in the experimental spectrum at 1340 cm^{-1}. When **C1** interacts with Ti(IV) another collective mode bearing the contribution of the COO^- uncoordinated to Ti(IV) is found at 1370 cm^{-1}, clearly observed when **C1** is loaded on TiO_2, but absent when the same dye is dispersed in the KBr matrix. This spectral evidence suggests that deprotonation of both carboxylic groups may occur upon interaction of the Dye with TiO_2.

(a)

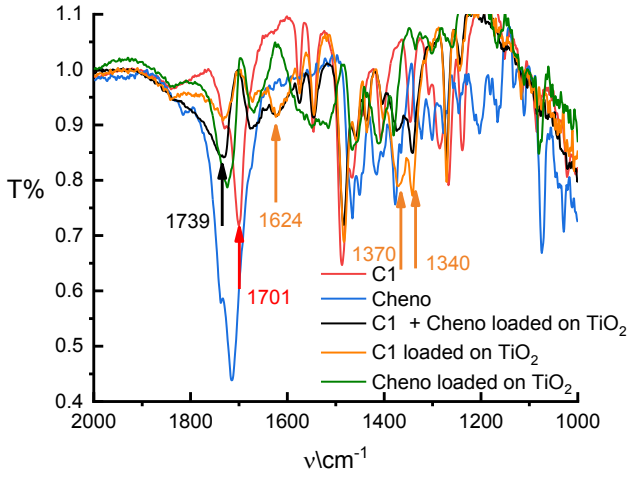

(b)

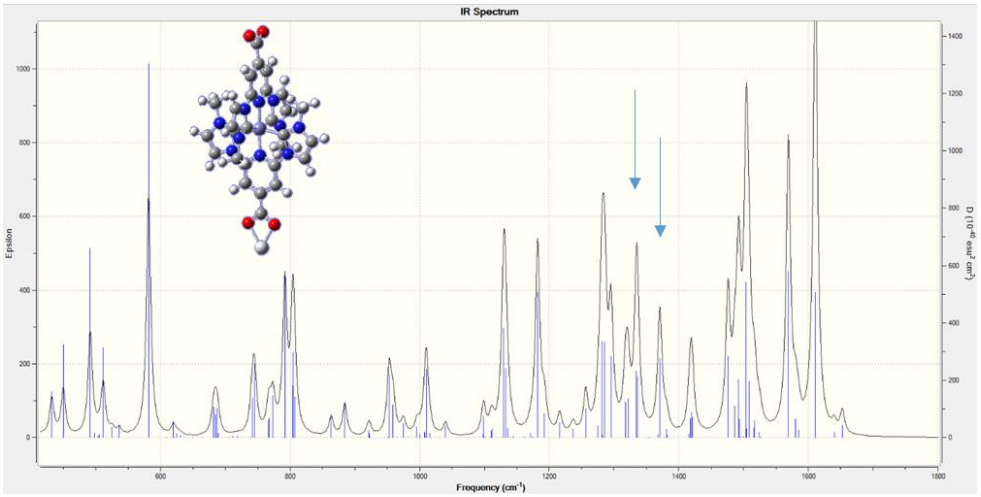

(c)

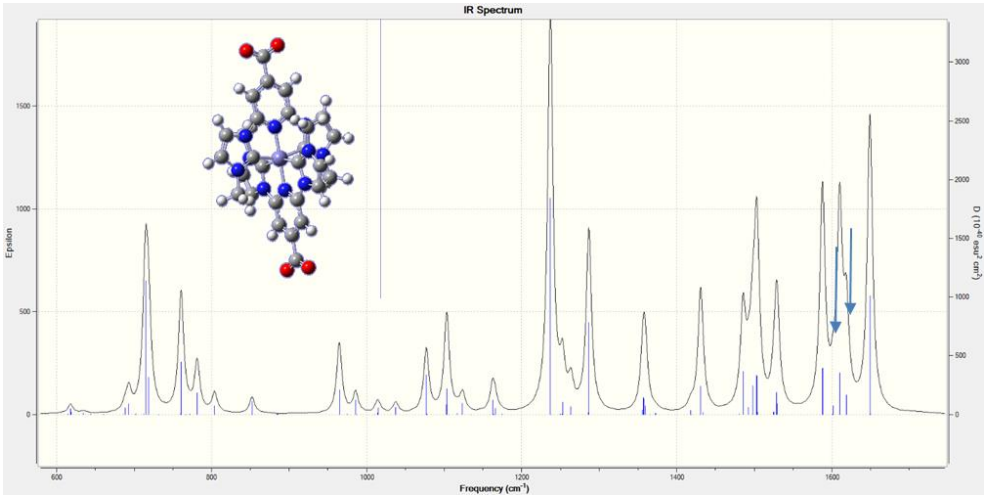

(d)

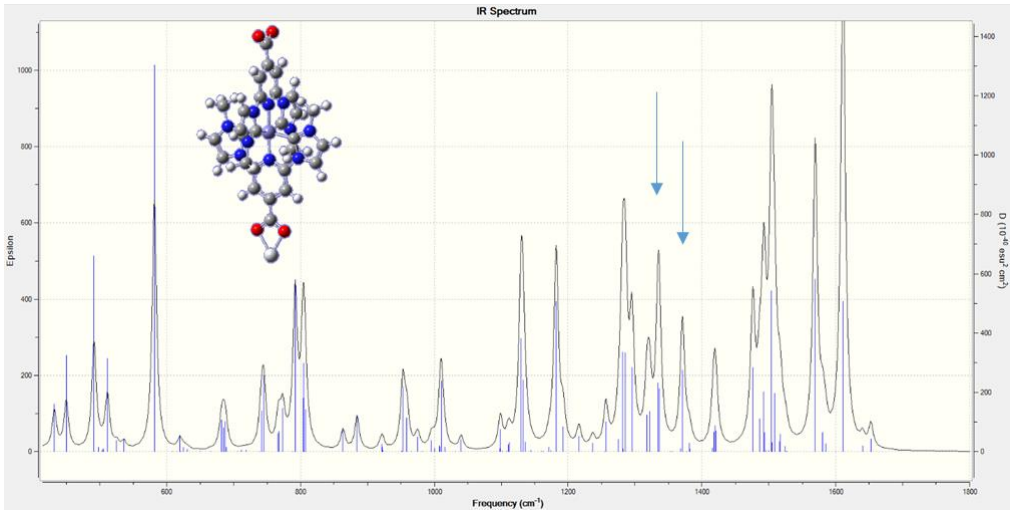

Figure 4.3: (a) FT-IR spectra of **C1** loaded on TiO_2 (orange) compared to **C1** dispersed in KBr (red), **C1** loaded on TiO_2 in the presence of Chenodeoxycholic acid (black), Chenodeoxycholic acid loaded on TiO_2 (green) and Chenodeoxycholic acid dispersed in KBr matrix (blue). Computed (B3LYP-LANL2DZ) IR spectrum of **C1** in (b) protonated form, (c) anionic form and (d) in anionic form coordinated to a Ti(IV) ion. From ref 237

4.3.3a Photoelectrochemical characterization

Figure 4.4a reports the photocurrent density – voltage curves that show a significant improvement in the photoconversion efficiency when cells are equipped with blocking underlayer. The PCE% increase from 0.49% to 0.75% in the presence of *el 1*, this enhancement of the photovoltaic performances is attributable to the increment of the shunt resistance (R_{sh}) that leads to a decreasing in the dark current flowing between -0.1 and -0.3 V. A further improvement was reached by adding GuNCS to the electrolyte mixture (*el 2*) and increasing the concentration of MgI_2 to 0.1 M. The role of the former additive was ascribed to increase the fill factor and open circuit voltage by blocking the recombination while, the role of magnesium, being a small high-density cation that may absorb on the TiO_2 surface, was attributable to induce a surface excess of I^-, speeding up the regeneration. This electrolyte led to a J_{sc} = 3.3 $mAcm^{-2}$, V_{oc} = 0.44V, FF% = 63% and PCE% ≈ 1% that, at the time of this project, was the highest value reported in literature. By introducing the opaque titania paste as semiconductor, a slight increase in the photocurrent, but a marginally lower open circuit photovoltage, led to ca. the same PCE% of 1%. The relevant parameters for the functioning of the DSSCs devices are summarized in **Table 4.1**

(a) (b)

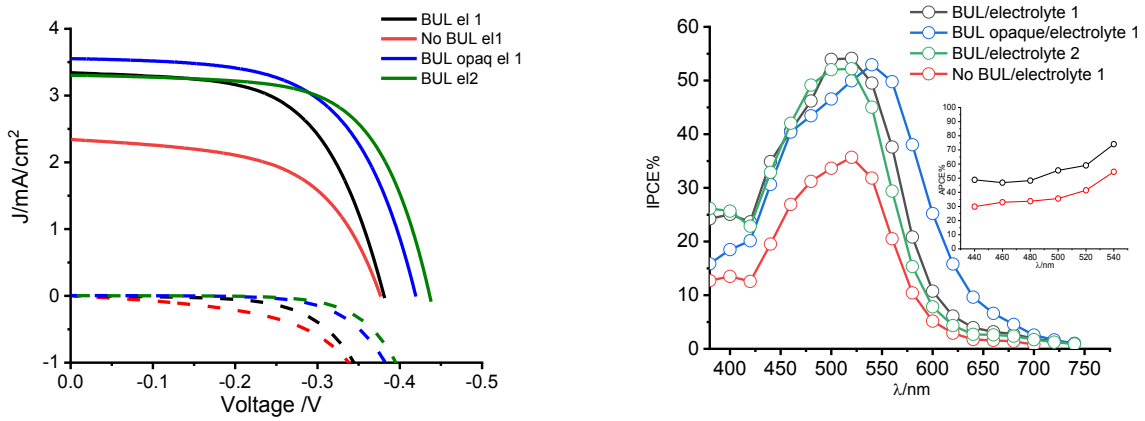

Figure 4.4: (a) Photocurrent density – voltage curves for **C1** in the presence of different substrates and electrolytes. (b) Incident Photon to Current Conversion Efficiency spectra and the relative Absorbed Photon to Current Conversion Efficiency spectra as insert of **C1** in the same conditions described in the point (a). From ref 237

The Incident Photon to Current Conversion Efficiency spectra, reported in **Figure 4.4b**, show a maximum of photoconversion of 50% in all the cases, but slightly broader in the case of the opaque substrates thanks to the scattering properties of the 18NR-AO paste.

Table 4.1: Cell efficiency parameters from **C1**/TiO_2 sensitized solar cells in the presence of different electrolytes and semiconductor substrates. As a comparison, results from **N719** sensitized solar cells assembled with *BUL-el1* are given in entry 5

Fe(II)	**Jsc (mA/cm^2)**	**Voc (V)**	**FF%**	**PCE%**
BUL el1	3.34	0.38	59	0.75
No *BUL el1*	2.34	0.38	55	0.49
BUL Opaque titania *el1*	3.55	0.42	60	0.89
BUL el 2	3.30	0.44	63	0.92
N719	**Jsc (mA/cm^2)**	**Voc (V)**	**FF%**	**PCE%**
BUL *el1*	12.9	0.45	53	3.09

The standard **N719** was tested under comparable conditions so in the absence of basic additives that as reported by Housecroft et al.[239] greatly depressed the photocurrent in iron-sensitized solar cells. This behavior was confirmed with the commercially available High Stability Electrolyte (HSE) and with the *basic electrolyte* as reported in **Figure A4.1**. Cells were also tested in the presence of SnO_2 semiconductor which is characterized by ca. 300 meV larger driving force for the charge injection, we obtained a lower photocurrent, ca. half that observed with *BUL-el1*, corresponding to an IPCE of ca. 25% and APCE ≈ 30% (**Figures A4.2**). This suggested no thermodynamic limitation for charge injection in to TiO_2 with respect to SnO_2 and the existence of fast recombination channels from SnO_2,[240] where the blocking underlayer had basically no effect on the resulting J-Vs characteristics (**Figure A4.3**). After the normalization of the IPCE for the LHE, the resulted Absorbed Photon to Current Conversion Efficiency is around 50/60%. Under short circuit conditions, considering the slow bielectronic triiodidide reduction and the low intensity of the employed lamp, the η_{coll} could be unitary leading to ϕ_{inj} of only 50/60 as discussed in the next paragraph.

4.3.4a Transient absorption spectroscopy

The transient absorption spectrum of **C1**/TiO_2 in the ns/s time scale is reported in **Figure 4.5a**. At the best resolution of our spectrophotometer (FWHM = 7/9 ns), the oxidized species of **C1** is generated inside the laser pulse. After a careful analysis of the TA spectrum, the first 43 ns are characterized by a spectral evolution that are substantially convolved with the laser pulse which appears in a narrowing and in a slight blue shift of the MLCT bleaching together with the disappearance of the weak absorption signal for $\lambda > 650$ nm. **Figure 4.5b** shows the first 4 ns after the laser pulse which are characterized by a narrowing from 91 to 73 nm and a blue shift of few nanometers. This spectral changing could be assigned to the relaxation of the residual population of the lowest triplet state (T1). The T1 deactivation can proceed via non radiative pathway to the ground state level or by electron injection into the conduction band of the TiO_2. The low extrapolated ϕ_{inj} suggests the deactivation via non radiative pathway. After ca. 40 ns, no further changes in spectral shape are present. The lower limit of the electron injection rate is set to ca. 10^8 s^{-1}. The spectroscopic signature of the Fe(III) species can be summarized by a strong blech around 500 nm that mirrors the ground state absorption band and by a weak and featureless absorption from 600 nm originated by the cations absorption together with the electrons in the TiO_2 trap states.

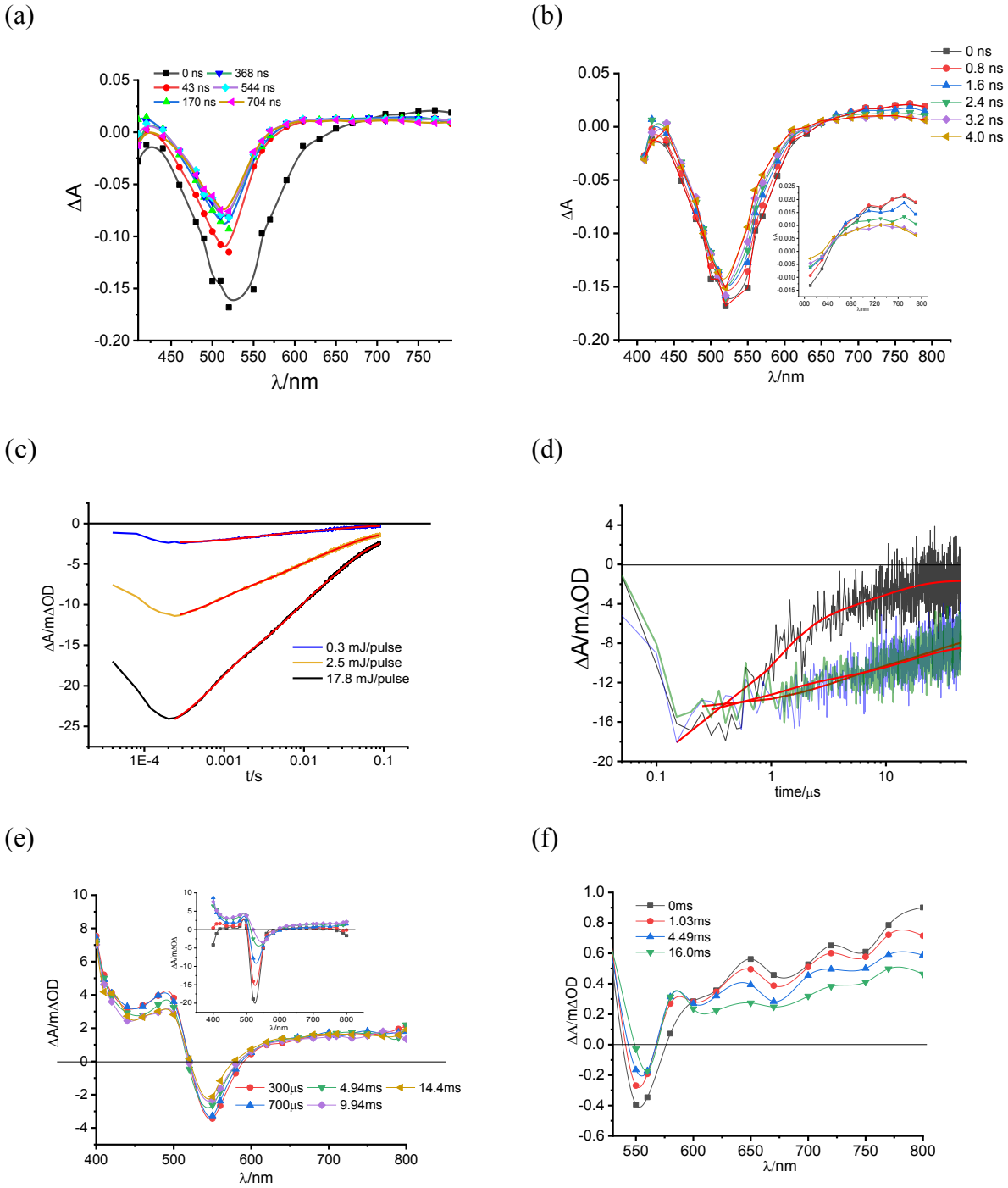

Figure 4.5: (a) TA spectra of **C1** loaded on TiO_2 in contact with 0.1 M $LiClO_4$/ACN upon 532 nm excitation and (b) their spectral evolution during the first 4 ns starting from the maximum of the laser pulse. Inset, magnification of the spectral region for $\lambda > 600$ nm (c) 500 nm charge recombination kinetics in **C1**/TiO_2 photoanodes measured under different excitation energy decreasing from 17.8 mJ/cm^2/pulse (black) to 0.3 mJ/cm^2/pulse (blue). (d) 500 nm recovery kinetics with (black) and without (blue (0.1 M $LiClO_4$/ACN), green (0.1 M $LiClO_4$/0.2 M 4-TBPy/ACN)) the presence of *el 2* deprived of the oxidized form of the mediator (I_2). TA spectra (10 kΩ input impedance) of **C1**/TiO_2 in contact with (e) *el2* deprived of I_2. The inset shows the evolution of the transient spectrum during the first 300 ms from excitation (0 ms (black), 20 ms (red), 60 ms (blue), 180 ms (green), 300 ms (purple)) and (f) in the presence of the full electrolyte 2 (containing 0.6 M PMII, 0.1 M LiI, 0.1 M GuNCS, 0.1 M MgI_2 and 0.1 M I_2). From ref 237

In a blank electrolyte, the recovery of Fe(III) is power dependent and multiexponential (**Figure 4.5c**): at low laser energy (300 μs/cm^2/pulse) the decay was fitted with a bi-exponential function and it is characterized by a two components with equal amplitude, with time constant on the order of $2x10^{-3}$ s and $2x10^{-2}$ s, respectively. At higher laser pulse intensity, a third component need to be taken into

account for the faster electron/hole recombination with a time constants on the order of 10^{-4} s. Also in the conditions employed in our study (ca. 18 mJ/cm^2/pulse), the decay of the charge separated state is less than 80% complete on a time scale of 0.1 s. After the introduction of the reduced form of the redox couple (**Figure 4.5d**) in the electrolyte, 75% of the regeneration occurs on a time scale of 10 µs. A residual amplitude of the 500 nm bleaching (ca. 4 mΔOD) however doesn't recover in this time scale. The complete transient absorption spectra of **C1**/TiO_2 in contact with the electrolyte 2 deprived of I_2, is reported in **Figure 4.5e**. To amplify the residual signal for t > 10 µs, it was necessary to employ 10 kΩ input impedance, which increases the signal of 200 folder. The first 300 µs are practically convolved with the laser pulse and are characterized by a fast recovery accompanied by a red shift of ca. 40 nm with consequent formation of an absorption band in the blue region with the maximum localized around 490 nm followed by a steep increase for λ < 450 nm. The red portion of the TA spectrum shows a flat absorption originated by the photoinjected electrons (herein, it is possible to assume no LMCT states of Fe(III) for the fast regeneration of Fe(II)). These spectral features remain constants in the hundreds of µs to s range, just a slightly reduction in the amplitude is observed due to the charge recombination. The initial fast bleach recovery is due to the iron regeneration by iodide, which results in the formation of I_3^-, that absorbs in the blue region and particularly, it is responsible for the steep band rising for λ < 420 nm.[191] After the dye regeneration, electrons are free to accumulate in the conduction band of the substrate, where in the absence of I_3^- (except the locally generated one) they persist for several of ms. This long-lived bleach is incompatible with the fast regeneration, and it is thus assigned to a Stark Effect,[191] generated by the electron accumulation in the semiconductor. The TA data have been corroborated with the spectro-electrochemical measurements (**Figure 4.6**) which are characterized, upon negative polarization of the photoanode in dark, of a blue shift that leads, in the difference spectra, to a narrow bleach with the minimum around 530 nm together with an absorption band peaking around 480 nm. These observations agree with the absorption band reported in **Figure 4.5e**.

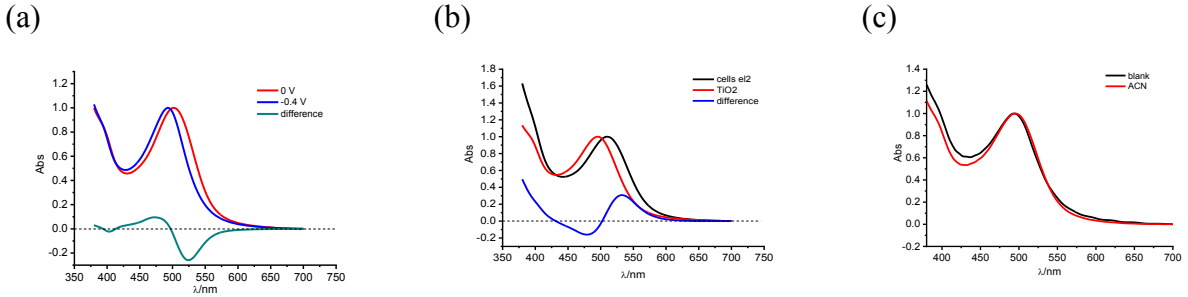

Figure 4.6: Absorption spectra of **C1**/TiO_2 measured in (a) a three electrode spectroelectrochemical cell containing in 0.1M $LiClO_4$ /ACN. Spectra taken at open circuit (disconnected wires) (red line) and at -0.4V vs Ag (blue line) and the resulting difference spectrum (green line) are shown, in (b) contact with air (red line) and in contact with the reduced form of the *el 2* (black line) and the resulting difference spectrum (blue line) and in (c) contact with and without acetonitrile. From ref 237

The transient difference spectrum of **C1** in contact with the complete electrolyte 2 (**Figure 4.5f**) appears quite noisy due to the strong absorption originated in the blue arising from the presence of I_3^- but, nevertheless, it was possible to confirm the presence of the Stark Effect. These traces, compared to the previous case (*el2* deprived of I_3^-), gave us information about the electron recapture by the oxidized form of the redox mediator. **Figure 4.7a** shows the kinetic of the 750 nm absorption in the absence of the triiodide which is practically constant (just 6% of recovery) on a time scale of 20 ms. When the film was in contact with the complete electrolyte, a decay with a time constant of 5.6 ms was recorded (**Figure 4.7b**) setting the apparent electron recapture rate constant around $2x10^2$ s^{-1}.

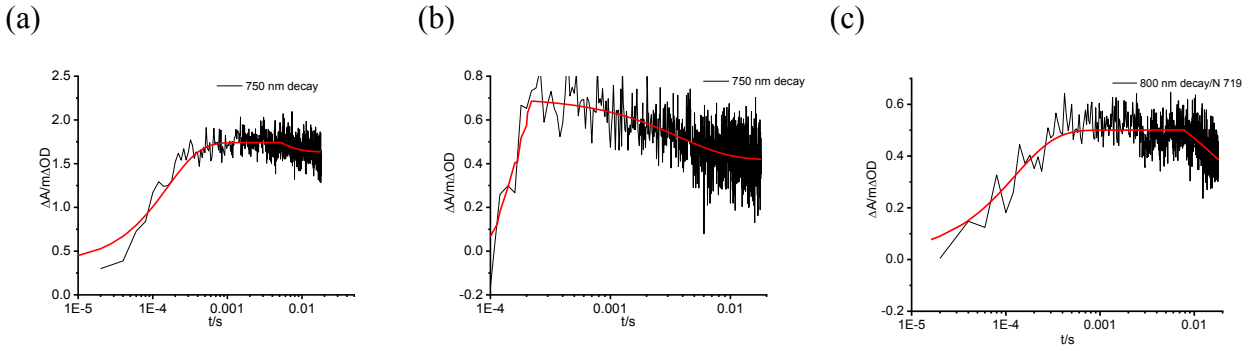

Figure 4.7: 750 nm electron absorption decay in **C1**/TiO_2 in the presence of (a) the reduced form of the electrolyte 2 (without I_3^- initially present) and (b) in the presence of the complete electrolyte. (c) 800 nm electron absorption decay in **N719**/TiO_2 in presence of complete electrolyte 2. From ref 237

In the same conditions, **N719** showed a time constant of ca. 18 ms (**Figure 4.7c**), indicating a slower electron recombination with the oxidized form of the redox mediator. The different time constant recorded could be due to a different surface potential of the semiconductor generated by the absorption of the positive **C1** and by the negative standard **N719**. In fact, the positive charge (see FT-IR characterization) of **C1** could attract the reduce form of the redox mediator increasing the efficiency of the regeneration process but also attract the I_3^- form which contributes to the electron recombination together with a non-optimal shield imparted at the surface by **C1**. This could be coherent with the significant improvement on the PCE% obtained when cells are equipped with the blocking underlayer. The transient data recorded for **N719** (**Figure 4.8a**) show a life time of 0.5 ms (Ru(III)) shorter than the lifetime recorded for Fe(III) but doesn't influence the solar performances, since in both the cases the regeneration occurs in a μs time scale with a consequent unitary regeneration efficiency.

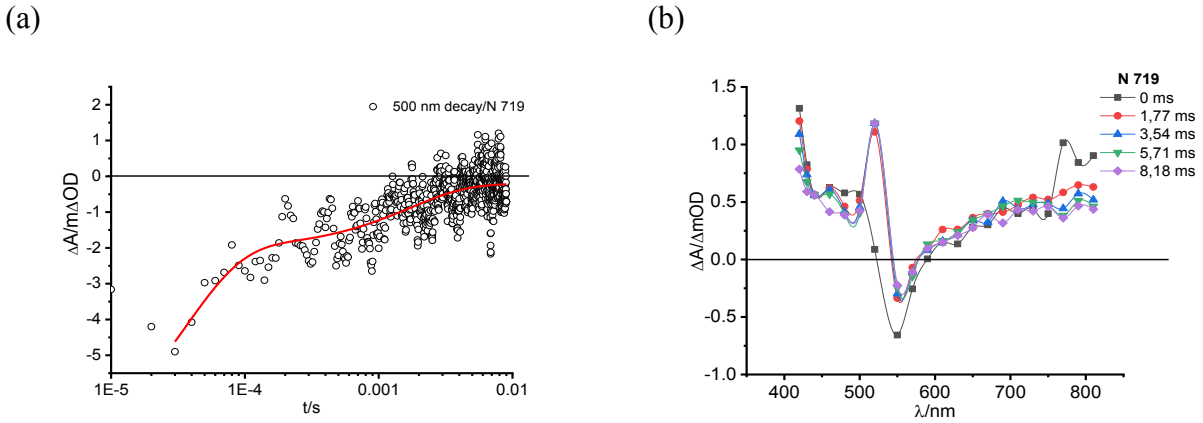

Figure 4.8: (a) 500 nm charge recombination kinetics measured with **N719** loaded on TiO_2 in contact with 0.1 M $LiClO_4$/ACN. (b) 800nm electron absorption decay in **N719**/TiO_2 in presence of complete electrolyte 2. From ref 237

4.4a Conclusions

This second experimental chapter of my thesis has shown that despite the shorter lifetime of the iron complexes (the decay occurs in a ps time scale), after the electron injection in the conduction band of the semiconductor substrate, **C1** gave a long lived charge separated state ($e^-(TiO_2)$/Fe(III)) that lives several milliseconds in a blank electrolyte (similar trend was recorded using SnO_2 but with worse performances). The regeneration was found unitary, and this leads to consider, from the APCE

spectrum, a quantum yield of injection close to 50%. From this study it is possible to find out some crucial factors affecting the photoelectrochemical performances of **C1**: i) the composition of the electrolyte leads to the best performances ever recorded so far. ii) The recombination of the photoinjected electrons with the I_3^- due to the positive surface together with a non-optimal electrode passivation. iii) incomplete injection of only 50% that is in competition with the fast deactivation of the excited state. In consideration of the excited state energetics, this could be due to a non-optimal electronic coupling arising from the symmetric design of the homoleptic **C1**. In the next sections of my thesis asymmetric complexes with the aim to increase the excited state directionality will be presented.

b) Record power conversion efficiencies for iron(II)-NHC-sensitized DSSCs from rational molecular engineering and electrolyte optimization

4.1b Introduction

Significant improvement in the Fe(II) complexes lifetime has been obtained by Dr. Gros's group for the complex **C1**, reaching a lifetime of 16 ps that opened the possibility to obtain high performing iron-based solar cells. In the **Chapter 4a** we have recorded a significant improvement in the Power Conversion Efficiency (ca. 1%) after the fine-tuning of the electrolyte and the photoanode configuration. However the recorded efficiency resulted the highest reported in literature at the time of the project, **C1** exhibited a relatively low performances. This is mainly related to the low injection quantum yield due to the competition with the excited state deactivation and to a wrong directionality of the charge flow connected to its symmetric structure. Continuing our strong collaboration with the University of Nancy, we decided to synthesize and characterized heteroleptic complexes, one of them is the asymmetric analogue of **C1** namely **ARM13**, the other molecules are instead characterized by spacers between the anchoring moieties (COOH) and the pyridine linked to the metal center. In the case of **ARM7** we introduced a thiophene and in the case of **ARM11** a phenyl ring. The role of the spacer was to increase the distance between the TiO_2 surface and the metal center increasing the electron-hole separation as well as to increase the light harvesting capability. We have significantly increased the previous result obtained for **C1** obtaining a PCE close to 1.5% in the case of its heteroleptic analogue. **ARM13** overcame the other complexes thanks to the higher electron concentration localized in the anchoring moieties.

4.2b Experimental

4.2.1b Materials

Lithium trifluoromethanesulfonate (LiOTf) 99.995%, PMII ≥ 98%, ACS grade I_2 ≥ 99.8%, GuNCS ≥ 97%, EDOT 97%, Alconox, $Ti(OiPr)_4$), Tetrabutylammonium iodide (TBAI) ≥ 98, Magnesium trifluoromethanesulfonate (MgOTf), Silver trifluoromethanesulfonate (AgOTf) ≥ 99%, and solvents (anhydrous ACN 99.8%, ACS grade 2-propanol ≥ 99.8%, ACS grade absolute EtOH, 99.9% 1-butanol) were purchased from Sigma-Aldrich and used without further purification. $TBAPF_6$ ≥ 98% was bought from Alfa Aesar. Ultra-dry LiI 99.999% and MgI_2 > 99% were purchased from Fluka, $LiClO_4$ ≥ 99% was purchased from Acros organics. FTO TEC-7 was bought from NSG, 18NR-T TiO_2 paste was purchased from Greatcell Solar. Surlyn 25 was supplied by Dyepower Consortium. **N719** was synthesized according to literature procedures.[211] 1-Methyl-3-propylimidiazolium trifluoromethanesulfonate (PMIOTf) was prepared by reacting AgOTg and PMII in acetonitrile and filtering off the AgI precipitate. The solvent was removed decreasing the pressure using a rotavapor. **ARM13** was prepared according to literature procedure.[241]

4.2.2b Methods

^{1}H (400 MHz) and ^{13}C NMR (100 MHz) spectra were recorded on a DRX400 Bruker spectrometer at room temperature.

High-resolution mass spectrometry (HRMS) data were collected by using a Bruker micrOTOF-Q spectrometer.

UV-Vis spectra of the complexes in solution were recorded in a 1 cm path length quartz cell on a LAMBDA 1050 (Perkin Elmer) spectrophotometer. The absorption spectra of the Fe(II)NHC sensitized electrodes were obtained in transmission mode with an Agilent Cary 300 UV-Vis spectrophotometer. These spectra were collected against the background constituted by an undyed TiO_2.

Electrochemical data for complexes in solution were obtained using a Radiometer PST006 potentiostat. A single compartment cell was used with Ag/AgCl as the reference electrode, glassy carbon as the working electrode and Pt wire as the counter electrode, and the supporting electrolyte was 0.1 M $TBAPF_6$/dry acetonitrile. All $E_{1/2}$ values were calculated from (Epa + Epc)/2 at a scan rate of 100 mVs^{-1}. All potentials were reported versus SCE. Cyclic voltammetry of the Fe(II)NHC-sensitized films used as working electrodes was carried out with a PGSTAT 302N potentiostat at a scan rate of 50 mV s^{-1} in acetonitrile/0.1 M $LiClO_4$ solution, using a three electrode cell with a platinum wire as the counter electrode and a double jacketed SCE as a reference.

SEM imaging of the anatase mesoporous films was carried out at the Department of Physics in the University of Trento with a JEOL JSM-7001F FEG-SEM. Surface morphology images were acquired in top-down and tilted mode whereas cross sectional analysis was performed by placing the films on a 90° stub.

Nanosecond laser experiments on Fe(II)NHC sensitized TiO_2 films were performed with previously described spectrometric apparatus (see **Chapters 3** and **4a**) In the ms-s region, the laser energy was adjusted to 500 mJ per cm^2 per pulse by acting on the Q switch and laser power supply and by interposing various optical elements to defocus and attenuate the beam in order to achieve a homogeneous excitation of the whole sensitized surface in the optical path of the monochromatic probe beam. Various oscilloscope input impedances were used to amplify the S/N of the trace (from 50 Ω to 1MΩ) in a given temporal window and each oscillographic trace was averaged over ca. 100 laser shots at a repetition rate of 1 Hz. Experiments carried out at the maximum time resolution of our spectrometer (FWHM ca. 7 ns) were conducted with a 10 mJ/cm^2/pulse to obtain a better S/N ratio without pre-amplification. Sensitized TiO_2 films supported on FTO were held at 45° degrees with respect to both the excitation and probe beam to reflect the scattered laser away from the detector. The electrolyte could fill the gap between the mesoporous film and a microscope slide pressed against it by capillarity.

Photo-electrochemical experiments were performed with a PGSTAT 302N potentiostat equipped with an Abet sun simulator (AM 1.5G filter) setting the lamp irradiance at 0.1 W cm^{-2}. The JV curves were collected in cyclic voltammetry mode by linear sweeping an applied potential at 20 mV s^{-1} from 0 V to slightly larger potentials than the measured V_{oc} of each cell. The IPCE spectra were obtained with custom-made apparatus composed of a Xe lamp (Ceralux CL300BF) source focused into the entrance slit of a motorized Newport Cornerstone monochromator coupled to an optical fiber to provide monochromatic illumination of the sandwich solar cell. Incident irradiance, recorded with a calibrated silicon photodiode, and the photocurrent output of the cell, collected under short circuit conditions, were acquired via a National Instruments PXI 1033 system. To avoid collecting an excess

of scattered light into the solar cell photoactive layer, cells were framed with a black tape mask having an active area of 0.25 cm^2. The APCE spectra were obtained according to APCE = IPCE/LHE where LHE (λ) = 1– $10^{-A(\lambda)}$ was computed using the absorbance (A(λ)) of each sensitized TiO_2 film in contact with the blank electrolyte.
EIS measurements were obtained with a PGSTAT 302N potentiostat by applying a 10 mV perturbation in the 10^5 to 10^{-1} Hz range to solar cells under dark conditions and probing the forward potential region from the onset of the dark current onwards.

4.2.3b Synthesis

Dr. Gros's group of the University of Lorraine realized the synthetic part of this thesis work in the following way:

Synthesis of *aminopyridine 1.* In a clean and dry 100 mL two-neck flask charged with imidazole (4.18 g, 61.35 mmol) and KOH (3.44 g, 61.35 mmol) flakes and heated at 250 °C under high vacuum and cooled to ambient temperature gave potassium salt of imidazole. Then added 4-amino-2,6-dichloropyridine (1.0 g, 6.13 mmol) in diglyme (20 mL) by vigorous stirring under Argon atmosphere at 150 °C for 18 h. The mixture was poured into water and the precipitate that formed was filtered and dried to isolate desired compound **1** (1.25 g, 93% yield). ^{1}H NMR (400 MHz, DMSO-d_6, δ ppm): 8.43 (s, 2H), 7.78 (s, 2H), 7.02 (s, 2H), 6.62 (bs, 2H), 6.61 (s, 2H) (**Figure A4.4**). ^{13}C NMR (100 MHz, DMSO-d_6, δ ppm): 159.6, 148.9, 135.65, 130.3, 117.0, 94.8. (Fi**gure A4.5**) ESI-HRMS calcd for $C_{11}H_{11}N_6$ m/z = 227.1040. Found: 227.1038.

Synthesis of bromopyridine 2. To a solution of **1** (0.7 g, 3.09 mmol) in 15 mL HBr 48% in H_2O, a solution of $NaNO_2$ (0.213 g, 3.09 mmol) in 3.0 mL of H_2O was slowly added at 0 °C. The mixture was stirred for 15 min and added to a solution of $CuBr_2$ (0.345 g, 1.55 mmol) in 5.0 mL HBr 48%. The resulting mixture was stirred and refluxed for 1 h. The reaction mixture was quenched with 2M NaOH until pH ≈ 8. The suspension thus obtained was extracted with ethyl acetate (3 X 100 mL). The organic layer was washed with aqueous NaCl, dried over Na_2SO_4 and concentrated to dryness. The desired creamy color compound **2** was obtained without purification and used directly for next step (0.48 g, 53% yield). ^{1}H NMR (400 MHz, $CDCl_3$, δ ppm): 8.36 (s, 2H), 7.62 (s, 2H), 7.44 (s, 2H), 7.24 (s, 2H) (**Figure A4.6**). ^{13}C NMR (400 MHz, $CDCl_3$+CD_3OD, δ ppm): 152.5, 141.3, 139.1, 134.4, 120.4, 117.4. (**Figure A4.7**). ESI-HRMS calcd for $C_{11}H_9N_5Br$ m/z = 290.0036. Found: 290.0082.

Compound 3. To a solution of **2** (0.2 g, 0.69 mmol) in toluene (5 mL), a solution of 5-carboxy-2-thiophene-boronic acid pinacolester (0.175 g, 0.69 mmol) and K_2CO_3 (0.285 g, 2.07 mmol) in methanol (5 mL) was added. The mixture was degassed with argon for 30 min and then $PdCl_2$(dppf) (0.050 g, 0.069 mmol) was added, and the solution was refluxed at 80 °C for 8 h. After completion of the reaction, the reaction mixture was filtered through Celite powder and washed with 10% MeOH in DCM. After evaporation of solvents, the residue was purified by column chromatography over silica gel using a DCM/methanol/triethylamine (TEA) (9/1/0.1) mixture as the eluent to give the product as a grey solid (0.21 g, 90% yield). ^{1}H NMR (400 MHz, $CDCl_3$ + TEA, δ ppm): 8.33 (s, 2H), 7.61 (s, 2H), 7.54–7.55 (m, 1H), 7.48 (d, J = 3.8 Hz, 1H), 7.36 (s, 2H), 7.17 (s, 2H) (**Figure A4.8**). ^{13}C NMR (101 MHz, DMSO-d_6 + TEA, δ ppm): 163.0, 149.15, 147.0, 145.2, 137.5, 136.6, 134.4,

130.7, 129.5, 117.7, 106.5 (**Figure A4.9**). ESI-HRMS calcd for $C_{16}H_{12}N_5O_2S$ m/z = 338.0706. Found: 338.0686.

Compound 4. To a solution of **2** (0.18 g, 0.62 mmol) in toluene (5 mL), a solution of 4-carboxy-benzene-boronic acid (0.093 g, 0.56 mmol) and K_2CO_3 (0.258 g, 1.86 mmol) in methanol (5 mL) was added. The mixture was degassed with argon for 30 min, and $PdCl_2$(dppf) (0.046 g, 0.062 mmol) was added and refluxed at 80 °C for 8 h. After completion of the reaction, the reaction mixture was filtered through Celite powder and washed with 10% MeOH in dichloromethane (DCM) (50 mL). After solvent evaporation, the residue was purified by column chromatography over silica gel using a DCM/methanol/TEA (9/1/0.1) mixture as the eluent to yield a grey solid (0.19 g, 92% yield). ^{1}H NMR (400 MHz, DMSO-d_6 +TEA, δ ppm): 13.22 (bs, 1H), 8.88 (s, 2H), 8.28 (s, 2H), 8.21 (d, J = 8.47 Hz, 2H), 8.12–8.14 (m, 4H), 7.19 (s, 2H) (**Figure A4.10**). ^{13}C NMR (100 MHz, DMSO-d_6 + pyridine-d_5 + TEA, δ ppm): 167.46, 153.56, 148.94, 140.50, 132.72, 130.67, 130.36, 128.31, 117.56, 108.25 (**Figure A4.11**). ESI-HRMS calcd for $C_{18}H_{14}N_5O_2$ m/z = 332.1142. Found:332.1161.

Ligand precursor L1. Compound **4** (0.18 g, 0.543 mmol) was charged in a 25 mL round bottomed flask and dissolved in 1mL of DMF. Then methyl iodide (0.069 mL, 1.11 mmol) was added and the mixture was heated at 130 °C for 1 h. The desired compound was precipitated upon addition of diethyl ether. The solid was collected by filtration and washed three times with diethyl ether and dried under vacuum. Then the solid was dissolved in a minimum amount of DMSO (ca. 2 mL) and saturated NH_4PF_6 solution was added followed by 2 M HNO_3 until the solution became acidic (pH ≈ 2). The mixture was stirred until the product was precipitated. Ligand **L1** was collected by vacuum filtration and washed 3 times with water and then diethyl ether (0.25 g, 71% yield). ^{1}H NMR (400 MHz, CD_3CN, δ ppm): 9.52 (s, 2H), 8.28–8.30 (m, 4H), 8.20 (s, 2H), 8.07 (d, J = 9.2 Hz, 2H), 7.67 (s, 2H) (**Figure A4.12**). ^{13}C NMR (101 MHz, DMSO-d_6, δ ppm): 167.95, 155.14, 146.53, 137.59, 137.34, 137.13, 130.49, 127.90, 125.40, 119.76, 111.93, 37.08 (**Figure A4.13**). ESI-HRMS calcd for $C_{20}H_{19}N_5O_2$ m/z = 180.5764. Found: 180.5804[M-2PF_6].

Ligand precursor L2. Compound **3** (0.1 g, 0.296 mmol) was charged in a 25 mL round bottomed flask and dissolved in 1 mL of DMF. Methyl iodide (0.038 mL, 0.607 mmol) was added, and the mixture was heated at 130 °C for 1 h. The desired compound was precipitated upon addition of diethylether. The solid was collected by filtration and washed three times with diethylether and dried under vacuum. Then the solid was dissolved in a minimum amount of DMSO (ca. 2 mL) and a saturated NH_4PF_6 solution was added followed by 2 M HNO_3 until the solution became acidic (pH ≈ 2). The mixture was stirred until precipitation and after vacuum filtration and washing three times with water and then diethyl ether, **L2** was obtained as a pale brown solid (0.137 g, 70% yield). ^{1}H NMR (400 MHz, DMSO-d_6, δ ppm): 10.32 (s, 2H), 8.78 (s, 2H), 8.46 (s, 2H), 8.12 (d, J = 3.8 Hz, 1H), 8.01 (s, 2H), 7.90 (d, J = 3.8 Hz, 2H), 3.98 (s, 6H) (**Figure A4.14**). ^{13}C NMR (101 MHz, DMSO-d_6, δ ppm): 162.8, 148.15, 146.7, 143.7, 138.7, 136.9, 134.7, 130.7, 125.4, 119.7, 11.4, 37.2 (**Figure A4.15**). ESI-HRMS calcd for $C_{18}H_{17}N_5O_2S$ m/z =183.5546, Found: 183.5642 [M-2PF_6].

ARM7. To a solution of **L2** (0.078 g, 0.118 mmol) and **L3** (synthesized using the literature procedure[242]) (0.063 g, 0.118 mmol) in 2 mL of anhydrous DMF, $FeCl_2$ (0.015 g, 0.118 mmol) was added and the mixture was degassed with argon for 10 min. Then t-BuOK (0.053 g, 0.473 mmol) was

added to the above mixture and stirred at room temperature for 20 min. A saturated solution of NH_4PF_6 was added (10 mL), followed by 2 M HNO_3 until the solution became acidic (pH ≈ 2) and the precipitate was collected by filtration. Then the crude product was further purified by silica gel column chromatography using an acetone/H_2O/KNO_3 (sat) = 10 : 3 : 0.5 mixture. The reddish fraction was collected and after the evaporation of acetone, and the remaining solution was treated with a saturated solution of NH_4PF_6 followed by 2 M HNO_3 until the solution became acidic (pH ≈ 2). After the precipitation of the complex, it was then filtered, washed with distilled water, and dried under vacuum. The isolated **ARM-7** was obtained in a reddish color (0.012 g, 11% yield). ^{1}H NMR (400 MHz, CD_3CN, δ ppm): 8.19 (t, J = 8.2 Hz, 1H), 8.12 (d, J = 2.18 Hz, 2H), 8.05 (s, 2H), 8.00 (d, J = 2.18 Hz, 2H), 7.96 (d, J = 3.99, 1H) 7.90 (d, J = 3.99, 1H), 7.74 (d, J = 8.18, 2H), 7.01 (d, J = 2.19, 2H), 7.00 (d, J = 2.19, 2H), 2.57 (s, 6H), 2.51 (s, 6H) (**Figure A4.16**). 13C NMR (100 MHz, CD_3CN, δ ppm): 200.67, 200.56, 162.69, 154.87, 154.45, 146.61, 142.73, 139.20, 135.13, 128.70, 127.19, 127.12, 117.08, 116.97, 105.97, 102.35, 35.27, 35.03 (**Figure A4.17**). ESI-HRMS calcd for $C_{31}H_{28}FeN_{10}O_2S$ m/z = 330.0728, found: 330.0814 (M-2PF_6).

ARM11. To a solution of Ligand **L1** (0.092 g, 0.142 mmol) and **L3** (synthesized using the literature procedure[242]) (0.075 g, 0.142 mmol) in 2 mL of anhydrous DMF, $FeCl_2$ (0.018 g, 0.142 mmol) was added and the mixture was degassed with argon for 10 min. Then t-BuOK (0.064 g, 0.568 mmol) was added to the above mixture and stirred at room temperature for 20 min. A saturated solution of NH_4PF_6 was added (10 mL) followed by 2 M HNO_3 until the solution became acidic (pH ≈ 2) and the precipitate was collected by filtration. Then the crude product was further purified by silica gel column chromatography using an acetone/H_2O/KNO_3 (sat) = 10 : 3 : 0.5 mixture. The orange fraction was collected and after the evaporation of acetone, the remaining solution was treated with a saturated solution of NH_4PF_6 followed by 2M HNO_3 until the solution became acidic (pH ≈ 2). After the precipitation of the complex, it was then filtered, washed with distilled water and dried under vacuum. The isolated **ARM-11** was obtained in an orange color (0.016 g, 12% yield). ^{1}H NMR (400 MHz, CD_3CN, δ ppm): 8.27 (d, J = 8.32 Hz, 2H), 8.19 (t, J = 8.12 Hz, 1H), 8.15 (d, J = 8.32 Hz, 2H), 8.11 (d, J = 2.02 Hz, 2H), 8.10 (s, 2H), 8.01 (d, J = 2.02 Hz, 2H), 7.74 (d, J = 8.15, 2H), 7.02 (d, J = 2.00 Hz, 2H), 7.00 (d, J = 2.02 Hz, 2H), 2.56 (s, 6H), 2.52 (s, 6H) (**Figure A4.18**). ESI-HRMS calcd for $C_{33}H_{30}FeN_{10}O_2$ m/z = 327.0946, found: 327.1075 (M-2PF_6).

4.2.4b DSSC fabrication

The FTO slides for electrode fabrication were cleaned by sequential ultra-sonication in Alconox/water and 2-propanol for 10 min each. After drying at room temperature the resulting slides were heated at 450 °C for 20 min to remove residual organic contaminants. The blocking underlayer was fabricated by spin coating (10 s at 1000 rpm followed by 20 s at 2000 rpm) a 0.3 M titanium tetraisopropoxide solution in 1-butanol followed by heating at 500 °C for 15 min. Ca. 16 µm thick transparent TiO_2 was obtained by repeating the blade casting of 18NR-T paste twice according to the classical scotch tape method. Each casting was followed by a sintering process in an oven according to the following temperature program: 25–120 °C (10 min), 120–450 °C (30 min), 450 °C (20 min), 450–500 °C (10 min), 500 °C (10 min). Cooling at RT was accomplished by removing the electrodes from the oven and storing them at RT in a desiccator. $TiCl_4$ treatment was performed by drop casting a 0.4 M aqueous $TiCl_4$ solution on top of the TiO_2 film followed by overnight hydrolysis at room temperature in a closed case. Later, after removing the excess $TiCl_4$ solution by rinsing with deionized

water, a final annealing stage was carried out at 450 °C for 30 min. After optimizing the dye adsorption process, the following conditions were deemed to be the best for optimal light harvesting: **C1** and **ARM13** were chemisorbed on a TiO_2 film by using 0.2 mM dye/0.04 mM chenodeoxycholic acid (CDCA) acetonitrile baths; **ARM7** and of **ARM11** were chemisorbed from a more concentrated 0.5 mM acetonitrile solution in the absence of CDCA. **N719** was adsorbed from 0.2 mM ethanolic baths. 0.25 cm^2 electrocatalytic PEDOT films for use as counter electrodes were fabricated by potentiodynamic electropolymerization on the FTO surface delimited by surlyn 25 masks. EDOT electropolymerization occurred between the working (FTO) and counter electrode (Ti sheet, 4 cm^2) facing each other at a distance of ca. 3 mm by exploiting 2 potential sweeps in cyclic voltammetry mode (0 – 1.6 V vs. SCE at 50 mVs^{-1}) in an electrolyte made of 10^{-2} M EDOT in 0.1 M $LiClO_4$ in acetonitrile. Cells were prepared in an open configuration using surlyn 25 as a spacer. Redox electrolytes were prepared according to the following formulation: electrolyte 2 (*el2*): 0.1 M LI, 0.6 M PMII, 0.1 M I_2, 0.1 MgI_2, and 0.1 M GuNCS in acetonitrile (ACN). A further formulation conceived for enhancing photocurrent was named electrolyte 3 (*el3*) and consisted of 0.1 M LI, 0.6 M PMII, 0.1 M I_2, 0.1 M MgI_2, 0.1 M GuNCS, and 0.1 M TBAI in acetonitrile.

4.2.5b Computational analysis

Dr. Mariachiara Pastore's group of the University of Lorraine performed the computational analysis, on the synthesized complexes, in the following way:

Isolated dye molecules. Theoretical calculations were performed at the Density Functional Theory (DFT) level, within the modified B3LYP* functional (with a 15% Hartree–Fock exchange–correlation fraction) and 6-311G(d) basis set. This functional was chosen since it has been tuned to properly describe the optical properties of Fe(II) complexes,[243] and its success has largely been documented in the literature.[88, 244, 245] The implicit effect of the methanol solvent environment was considered by employing the Polarizable Continuum Model (PCM).[246] In all cases, the dye complexes were considered in their low spin (singlet) state in view of their larger stability with respect to the high spin (triplet and quintet) configurations. For instance, the low spin ground state (GS) energy of **C1** was found to be 1.76 and 1.57 eV more stable compared to the same energy in its triplet and quintet spin states, respectively. The ground state oxidation potential (E_{ox}) has been estimated here as minus the Kohn–Sham (KS) energy of the highest occupied molecular orbital (HOMO) in solution. The approximate method to obtain an experimental estimate of the excited state oxidation potential (E^*_{ox}) is to subtract the adiabatic lowest excitation energy (E_{00}) from the E_{ox}. Here it was compared these experimental estimates with the calculated E^*_{ox} obtained as $E^*_{ox} = E_{ox} - E_{max}$, where E_{max} is the maximum of the calculated absorption band. This approximation will provide slightly overestimated E^*_{ox}, but with the expectation that the trend within the series of Fe complexes will be reliably reproduced. The ground state (GS) geometries of the considered dyes were fully optimized and, in the Frank–Condon approximation, the vertical excitation energies were calculated by means of Time-Dependent DFT (TD-DFT). The simulated absorption spectra were built by convoluting the 50 lowest energy vertical transitions with the Gaussian function of half-width at full-length of 0.17 eV. The character of the MLCT transitions has been analysed on the basis of the transition density matrices performed by using the TheoDORE package.[247] All sets of calculations for the isolated dyes were carried out within the Gaussian 09 suite of programs.[212]

TiO_2/dye cluster models. The optimized GS structure of the **C1** and **ARM13** dyes was adsorbed in a bidentate fashion, after having transferred the carboxylic proton to one surface oxygen, to a $(TiO_2)_{82}$ cluster having dimensions of about 2 x 2 nm. This cluster model was obtained by exposing the anatase bulk phase to the (101) surface and it has been successfully employed to reproduce the dye/TiO_2 opto-electronic properties in previous work.[248, 249] Despite the fact that this model was initially tested to reproduce the correct TiO_2 band edge and relative dye-semiconductor energy levels by employing the standard B3LYP functional, the calculated interfacial energetics is very similar for both B3LYP and B3LYP* functionals (see the calculation for **C1** in **Figure A4.19**). The B3LYP* results were thus employed for the discussion. The optimized **C1**/TiO_2 and **ARM13**/TiO_2 geometries were obtained by performing DFT calculations with the Perdew–Burke-Ernzerhof (PBE) functional, COnductor-like Screening MOde (COSMO) solvation model,[250] and D2 Grimme's dispersion correction[251] for treating the van der Waals interactions, as they have been implemented in the Amsterdam Density Functional (ADF) package.[252] In addition, Double/Triple Zeta Polarized (DZP/TZP) basis sets were used for C, N, H, S, O, Mg/Fe, and Ti atoms, respectively. To rationalize the effect of the MgI_2 electrolyte on the dye/TiO_2 interface properties, the **C1**/Mg-TiO_2 and **ARM13**/Mg-TiO_2 systems have been studied by placing the Mg^{2+} cation between two O atoms of the TiO_2 surface close to the dye and following the procedure detailed above for the geometry optimization. For the sake of consistency with the isolated dye calculations, the electronic structure of the dye/TiO_2 system was calculated using the same level of theory (functional, basis set and solvent environment description) as the one described in the previous section. Even though the photovoltaic properties were measured in an acetonitrile solvent, a methanol solvent was used as the continuum medium for both relaxation and electronic structure calculations. In spite of this, in a continuum-medium description, the results will be almost identical for both solvent environments in view of their similar dielectric constants (ε = 32.613 for methanol and ε = 35.688 for acetonitrile). The interface charge injection properties were estimated by following the diabatic-like scheme developed by Thoss and coworkers.[253] Within this method, the diabatic couplings are calculated by resorting to a Fermi golden rule framework, where the charge injection rates k_{inj} are calculated as follows:

$$k_{inj} = \frac{2\pi}{\hbar}\sum_k |dk|^2 \rho(\varepsilon_k) \qquad \textbf{eq. 4.1}$$

where k_{inj} represents the sum over the manifold of *k* TiO_2 acceptor states of interest, whereas d is the dye donor state, $|Vdk|^2$ is the square of the coupling elements, ρ(εk) is the semiconductor partial density of states (DOS), and their product $|Vdk|^2\rho(\varepsilon k)$ defines the so-called probability distribution Γ(εk). The diabatic states for donor (dye) and acceptor (TiO_2) moieties were extracted by the localization of the MOs of the entire complex into the donor and acceptor species, thus ending up in a Fock matrix where the diagonal elements display the energies of the localized states, while the off-diagonal blocks include the coupling elements V_{kd}. In the final step, the corresponding hole/electron injection rates were calculating by applying the formula:

$$\tau(fs) = \frac{658}{\Gamma(meV)} \qquad \textbf{eq. 4.2}$$

It is important to highlight that although all previous work involving dye/TiO_2 diabatic analysis was conducted with the B3LYP functional,[248, 249] the results obtained with B3LYP* are comparable to those obtained with the B3LYP (**Figures A4.20** and **A4.21** and **Table A4.1**).

4.3b Results and Discussions

4.3.1b Synthesis

The scheme in **Figure 4.9** summarizes the synthetic steps involved in the preparation of the complexes followed by Dr. Gros's group. The Suzuki cross coupling was employed to synthesize the ligand precursors **L1** and **L2** and was performed between the pyridine **2** and the appropriate arylboronic acids. The desired complexes were realized reacting $FeCl_2$ with the appropriate ligands (**L1**, **L2**, **L3** and **L4**)[6, 242] in the presence of t-BuOK as base.

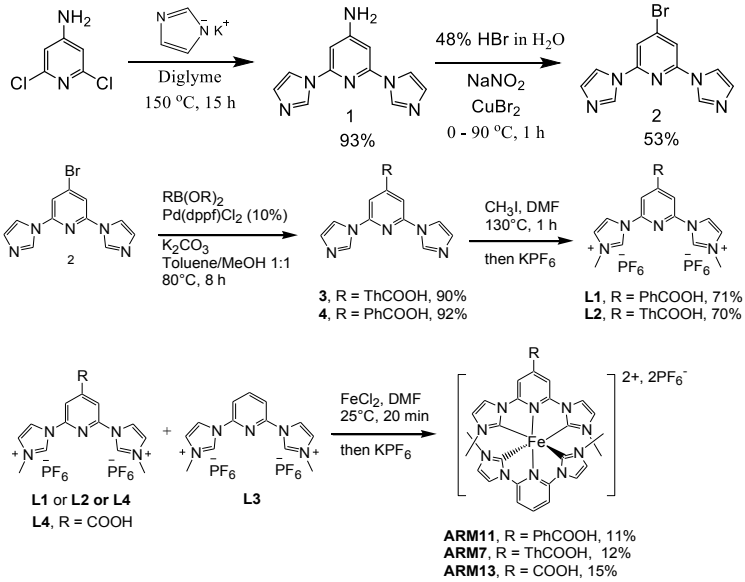

Figure 4.9: Synthetic scheme of the ligand precursors and complexes. From ref 254

4.3.2b Electronic and electrochemical properties

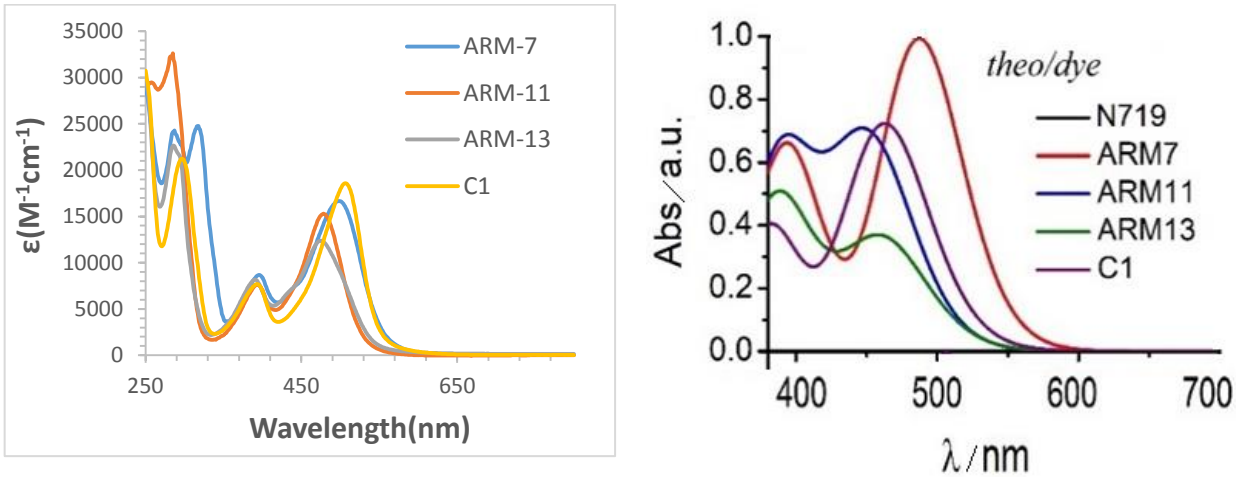

Figure 4.10: Absorption spectra for the Fe(II)NHC (a) in methanolic solutions and (b) the calculated ones. From ref 254

Figure 4.10a reports the absorption spectra of the complexes in methanol medium (the extrapolated parameters are summarized in **Table 4.2**). The spectra are characterized by an intense band at higher energy (250 - 330 nm) assigned to π-π^* transition and two bands in the lower energy region. The former corresponds to Fe-carbene transitions (340 - 420 nm) and the latter to Fe-pyridine MLCT transitions (420 - 600 nm). Passing from **C1** to the heteroleptic analogue **ARM13**, the lowest-energy MLCT band is blue shifted and less intense. **ARM7** (thiophene linker) and **ARM11** (phenyl linker)

are characterized by an intense molar extinction coefficient due to the extended π-conjugation. The thiophene-based complex exhibited a higher and red shifted band (λ_{max} = 499 nm, ε = 16719 $M^{-1}cm^{-1}$) with respect to the phenyl-based analogue (λ_{max} = 479 nm, ε = 15306 $M^{-1}cm^{-1}$).

Table 4.2: Optical properties of **C1**, **ARM7**, **ARM11** and **ARM13** dyes: absorption maximum in MeOH, absorption edge energies (E^{00},), absorption maxima on TiO_2 ($E_{max}(TiO_2)$), calculated E_{max} with relative oscillator strengths and nature of the main single particle transitions contributing to these excited states (percentage for each transition)

	Experimental			Calculated	
Dye	**λ_{max} (ε ($M^{-1}cm^{-1}$))**	**E_{00}**	**λ_{max} (TiO_2)**	**E_{max} (Oscillator strength)**	**Transition (%)**
C1	507 (18582)	551	496	463 (0.309)	H-2→ L+1 (45.4%) H-1→ L (45.1%)
ARM13	475 (12375)	528	478	461 (0.148)	H-2→ L (63.4%)
ARM11	478 (15306)	541	481	454 (0.271)	H-1→ L (64.4%)
ARM7	499 (16725)	551	502	487 (0.371)	H-1→ L (67.1%)

(a)

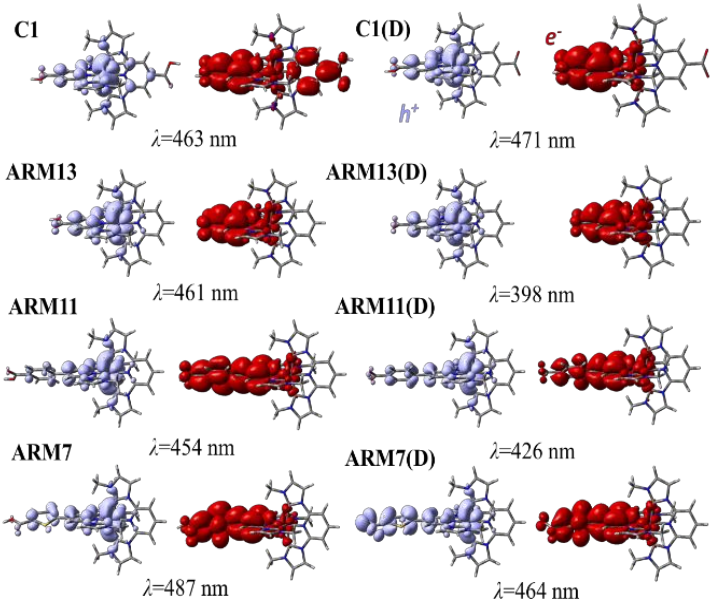

(b)

	n	E_x (eV)	λ (nm)	*f* (a.u.)	*Transition*	%
C1	1	2.1	591	0	H→ L	66.6
	5	2.68	463	0.308	H-2→ L+1	45.4
	9	3.23	384	0.155	H→ L+3	69.4
ARM13	1	2.04	607	0	H→L	70
	4	2.69	461	0.148	H-2→ L	63.4
	9	3.22	385	0.15	H→ L+3	55
ARM11	1	2.23	555	0	H→L	69.1
	4	2.73	454	0.271	H-1→ L	64.4
	9	3.2	388	0.209	H-2→ L+1	58.8
ARM7	1	2.04	607	0	H→L	69.5
	3	2.54	487	0.371	H-1→ L	67.1
	9	3.17	391	0.135	H→ L+3	50.2

Figure 4.11: (a) NTOs for the main transition forming the MLCT excitations of the Fe(NHC) complexes both in their protonated (left) and deprotonated (right) forms. Purple/red colors are employed to display hole/electron isodensity plots. (b) State Number (*n*), excitation energies (E_x), wavelengths (λ), oscillator strengths (f), major contributions and related percentage (%) of the main transitions in the visible region for the protonated dyes. Transitions related with MLCT excitations are marked with orange color. From ref 254

The TD-DFT calculations were performed with the aim to better assign the nature and topology of the MLCT bands. The computed spectra (**Figure 4.10b**) confirm the increase in the molar extinction coefficients in the case of **ARM7** and **ARM11** and the blue shift of **ARM13** with respect to **C1**. **Table 4.2** reports the composition of the main excitation of the MLCT bands, while the associated natural transition orbitals are depicted in **Figure 4.11a**. Interestingly, the lowest energy transitions

(H→L) are dark for all dyes (**Table** in **Figure 4.11b**), and the main MLCT transitions, composing the lowest-energy band, involve HOMO-1, and HOMO-2 and LUMO levels (in the case of **C1** the LUMO and LUMO+1 levels are degenerated for the presence of two anchoring carboxylic groups). The cyclic voltammetry analysis was initially carried out in acetonitrile solutions, **Figure 4.12a** depicts the extrapolated and computed oxidation potential values against SCE together with the TiO_2 conduction band edge and the redox potential of the electrolyte. The introduction of the spacer reduced the redox potential (0.74V for **ARM7** and 0.70 V for **ARM11** against 0.82 V for **ARM13** and 0.85 V for **C1**) probably due to the extension of the π-conjugation arising from the spacers. The ground state oxidation potential of the dyes is positive enough than the redox couple potential indicating a favorable driving force for the regeneration.

Table 4.3: Experimental and calculated ground/excited state oxidation potentials in eV versus SCE of **C1**, **ARM7**, **ARM11** and **ARM13**

	Experimental		Calculated	
Dye	E_{ox}/ V	E^*_{ox} ($E_{ox} - E^{00}$)/ V	E_{ox}/ V	E^*_{ox} ($E_{ox} - E_{max}$)/ V
C1	0.85	-1.40	1.08	-1.60
ARM13	0.82	-1.47	1.00	-1.69
ARM11	0.70	-1.65	0.92	-1.81
ARM7	0.74	-1.51	0.93	-1.61

The excited state oxidation potentials are negative enough than the TiO_2 conduction band to have an efficient electron injection. The computed levels are slightly overestimated but provided the correct trend, validating so the employed level of theory for reproducing the electronic structure of the sensitizers in solution (**Table 4.3**). The ground and the excited state oxidation potentials were also carried out on thin film to include the perturbation of the electronic levels of the dye when anchored to the semiconductor substrate. The cyclic voltammetry analysis perform on the film immersed in 0.1 M $LiClO_4$/ACN revealed a quasi-reversible Fe(II)/(III) oxidation potential for all the series, with a $\Delta E \approx 100$ mV indicating a fast electron transfer kinetics (**Figure 4.12b**). We obtain a systematic cathodic shift in the E_{ox} with respect to the solution data of the order of 100 - 150 mV that could be assigned to a decreased back bonding caused by the deprotonation of the carboxylic group upon binding of the complexes to the TiO_2 surface. In particular, we recorded an oxidation potential of 0.56 V, 0.55 V and 0.6 V for **ARM7**, **ARM11** and **ARM13** respectively. **ARM13** exhibits the strongest anodic potential (coherently with the data obtain for the acetonitrile solutions) probably for the stronger electron withdrawing effect provided by the carboxylic group directly bonded to the NHC ligand. Furthermore, the cathodic shift of ground state potentials makes the ES of the dye slightly better reductants than in solution. It was obtain at least 900 meV driving force for the electron injection from the excited state of the dye onto the CB of the TiO_2 (considering -0.7V vs SCE the lower edge of the accepting band in organic solvents containing lithium cations).[10]

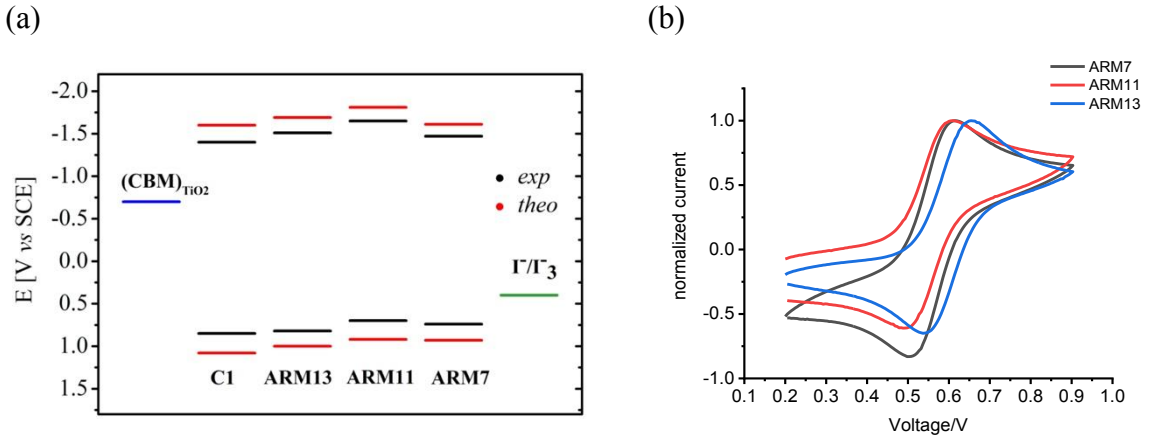

Figure 4.12: (a) Schematic energy levels vs SCE of **C1**, **ARM13**, **ARM11** and **ARM7** as estimated by means of absorption and electrochemical measurements (black), and DFT/TDDFT calculations (red). The TiO_2 conduction band minimum (CBM) and the potential of the I^-/I_3^- electrolyte are also plotted. (b)Normalized cyclic voltammetry recorded on TiO_2 for **ARM7**, **ARM11** and **ARM13** (black, red, and blue line respectively). The voltage is referred to double jacket SCE. From ref 254

4.3.3b Steady state and transient absorption spectroscopy of thin films

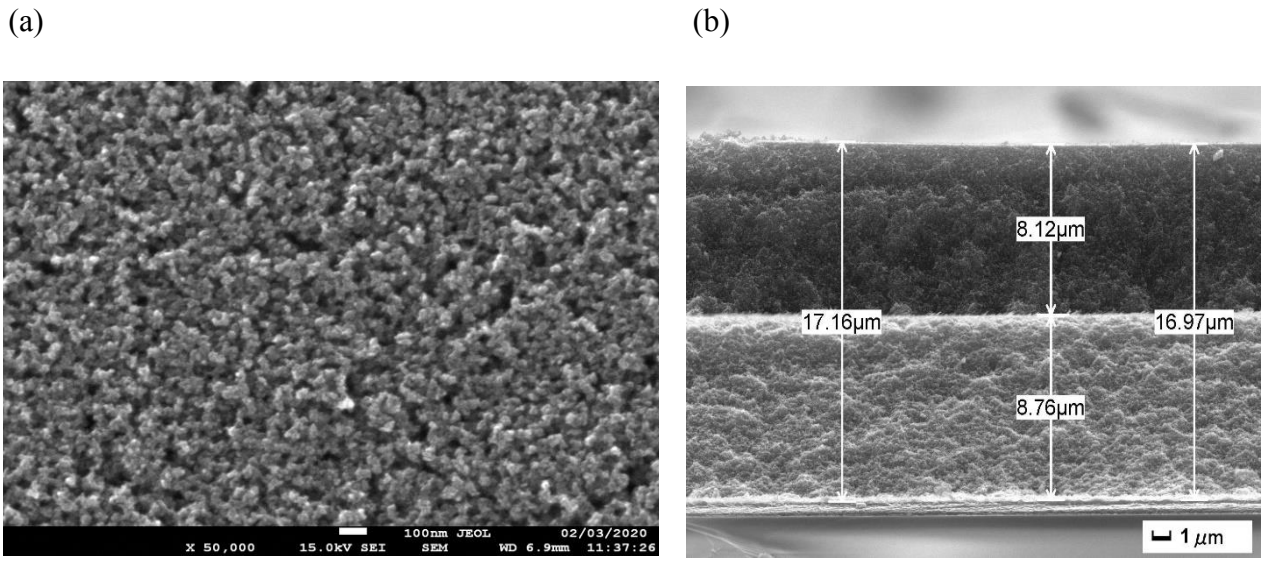

Figure 4.13: SEM (a) cross-section and (b) top view of a two-layered TiO_2 electrode. From ref 254

We have prepared relatively thick semiconductor films in order to optimize the light harvesting, at least at the MLCT maximum. As already reported in the **Section 4a**, the films (**Figure 4.13a**) are characterized by a homogenous network of nanoparticles having an approximate size of ca. 20 nm. The cross section shows a thickness of about 17 µm (**Figure 4.13b**). **Figure 4.14a** reports the absorption spectra of the sensitized electrodes for all the Fe(II)NHC series together with the standard **N719**, recorded in transmittance mode. All the iron species exhibited an intense MLCT band between 480 and 500 nm, followed by a weaker band centered around 400 nm. On the maximum, the light harvesting is larger than 90% for all the Fe(II)NHC series, with the best efficiency for **ARM7** and **C1**, which are characterized by a maximum of absorbance ≥ 2 and in the case of the former complex, a spectral extension up to 650 nm in agreement with the computational and solution data. **N719** still displays the best red response, with two MLCT bands covering most of the visible spectrum extending

beyond 700 nm. From $A(\lambda) = 1000\ \Gamma\ \varepsilon(\lambda)$, where A is the absorbance of the dyed films measured in transmission mode and Γ and $\varepsilon(\lambda)$ are the surface concentration ($molcm^{-2}$) and the extinction coefficient ($M^{-1}cm^{-1}$), it was possible to calculate the superficial loading that is quite similar in all the cases, in the order of 0.12±0.10 µmol cm^{-2}, indicating that the lower absorbance of **ARM13** is only related to its lower ε.

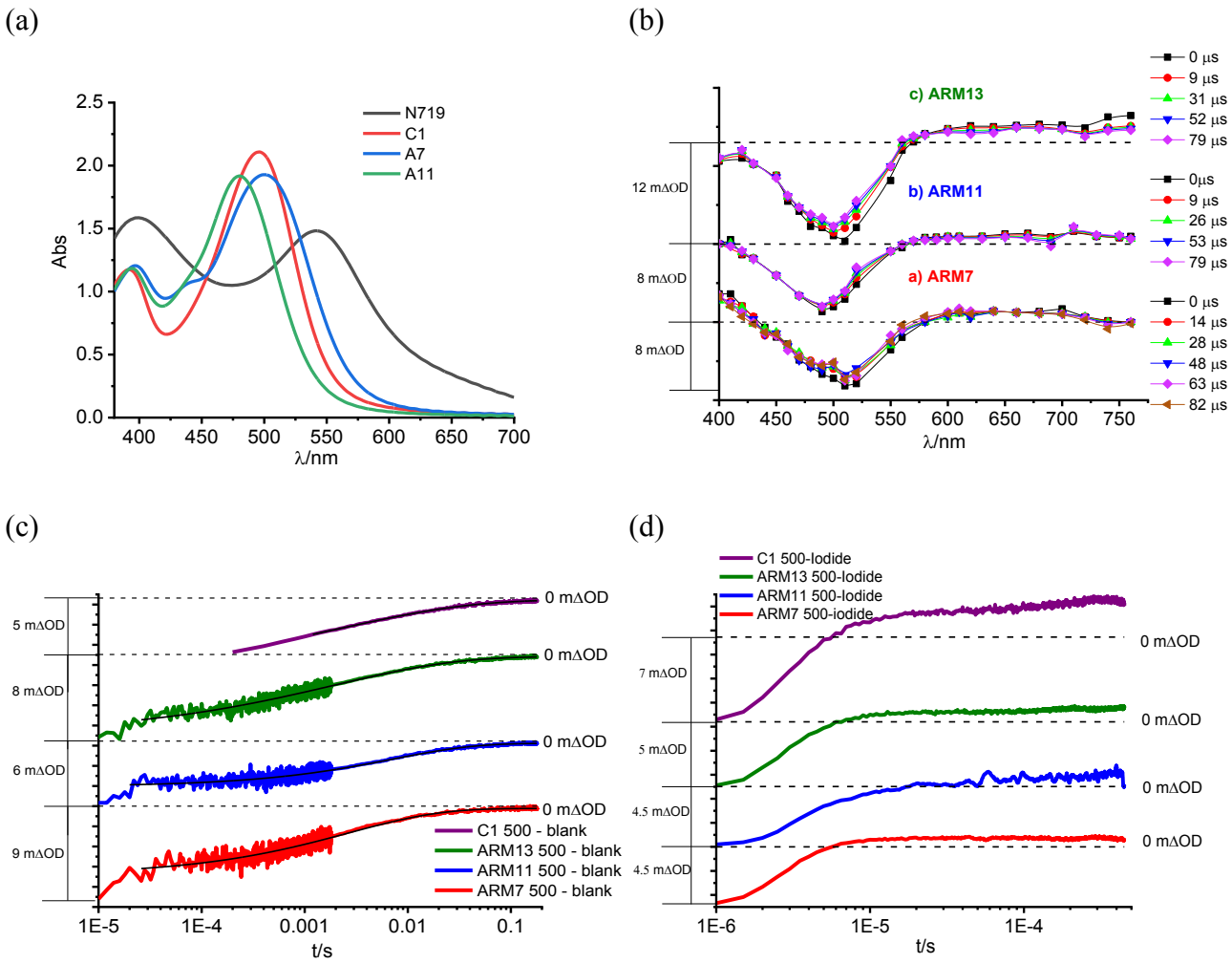

Figure 4.14: (a) Absorption spectra of the Fe(II)NHC-sensitized film, (b) Transient absorption spectra recorded for **ARM7**, **ARM11** and **ARM13** with 0.1MLiClO4/ACN. Input impedance is 350 Ω. (c) 500 nm recombination kinetics of the Fe(III)/e^-(TiO_2) charge separated state with blank electrolyte 3 (deprived of iodine/iodide). The kinetics were constructed by joining traces recorded within different time windows, spanning the 10 ms to 2 ms interval (10 kΩ amplifier impedance) and 2–200 ms (1 MΩ amplifier). (d) Positive absorption at 500 nm due to the Stark effect, as a consequence of Fe(II) regeneration inside the laser pulse for **ARM7** (red line), **ARM11** (blue line), **ARM13** (green line) and **C1** (purple line). Electrolyte 3 (without I_2). From ref 254

Recombination and regeneration dynamics on the sensitized electrodes were obtained via transient absorption spectroscopy (TAS) in the ns-ms time scale. **Figure 4.14b** displays the TA spectra from the new synthesized complexes on TiO_2 in contact with 0.1 M $LiClO_4$/ACN, the charge separated state (Fe(III)/e^-(TiO_2)) is generated within the instrumental response function (300 ns with a 350 Ω pre-amplifying impedance). All the spectra are characterized by similar features, an intense bleaching of the MLCT ground state absorption centered around 500 nm and an isosbestic point around 570 nm followed by a flat band associated to the contribution of the LMCT transitions together with the absorption of the photoinjected electrons in the TiO_2 trap states. The spectra are practically constant in the 100 µs time window selected for the experiments and are consistent with the date reported for

C1 in the previous section. This indicates that the recombination occurs slowly, and it is largely incomplete after ca. 80 µs. With respect to the ground state, the bleaching of the MLCT is red shifted (ca. 10/20 nm) due to a Stark shift[191] induced by the surface adsorption of small high-density cations when films are in contact with Li^+ and Mg^{2+} based electrolyte, as already observed in the previous work on **C1**.

When the electrodes are in contact with the electrolyte 3 (**Figure 4.14c**), deprived of the iodine/iodide redox couple, the complete decay of the charge-separated states (with initial amplitude in the order of 5-7 mΔOD) occurs in a time window, which extends up to 200 ms with 500 µJ/cm^2/pulse. These recombination kinetics follow a stretched exponential function (see **eq 4.3**),[226], and span from ns to ms, originated from an energy distribution of semiconductor/electrolyte states from which recombination occurs according to an ample range of different rate constants:

$$y = a + be\left(-\frac{x}{\tau}\right)^c \qquad \textbf{eq. 4.3}$$

Coherently with the literature data,[226] the exponential parameters c is in the 0.34 - 0.54 range. Lifetimes of 2.7 ms, 7.1 ms, 2.0 ms and 2.3 ms were obtained for **ARM7**, **ARM11**, **ARM13** and **C1** respectively, with consequent K_{rec} in the 10^{-3} to 10^{-2} s^{-1} range. After the introduction of the reduced form of the redox couple in the electrolyte mixture (**Figure 4.14d**), a fast recovery of the bleach in the 10^{-6} to 10^{-5} range was recorded, which is largely confined in the instrumental response function (10 KΩ pre-amplifier), suggesting a regeneration efficiency close to the unit. The fast recovery is followed by a flat absorption coherent with the Stark effect generated by the charging of the TiO_2 films with electrons, which are no longer compensated by Fe(III) centers at the interface. As previously described, all the TA spectra are characterized by Stark characteristics (**Figure 4.15**) which blue shift the GS absorption and leads to a broad absorption around 500 nm, dominant in the ms to s time scale. This behavior is stronger for **C1** and less intense in the case of the other iron complexes.

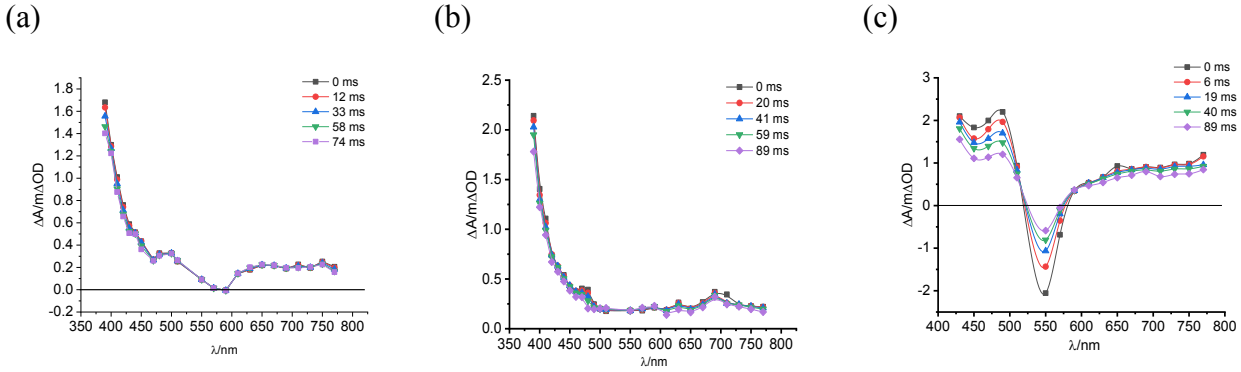

Figure 4.15: ms-time scale TAS (1 MΩ input impedance) of Fe(II)NHC sensitized films for **ARM7** (a), **ARM11** (b) and **C1** (c) in contact with electrolyte 3 deprived of I_2. All the spectra are characterized by general features like absorption of I_2 generated upon Fe(II) regeneration at 420 nm, stark absorption at 500 nm, bathochromic shifted bleach and absorption of electrons in TiO_2 trap states starting from 600 nm. From ref 254

The presence of the Stark absorption as consequent of the fast regeneration confirms that the recovery occurs within a time scale of 3 µs, setting the lower limit of the time constant for this process in the order of $3.3x10^5$ s^{-1}. With respect to the recombination, the regeneration rate is from hundred to thousand times faster leading to the regeneration efficiency η_{reg} by the reduce form of the electrolyte, practically quantitative. To better evaluate the competition between the recombination and regeneration dynamics, we have evaluated the processes at the best resolution of our

spectrophotometer (50 Ω pre-amplifying impedance and a FWHM of ca. 7 ns of the instrumental Gaussian response) increasing the energy of the laser pulse to 10 mJ/cm-^{2}/pulse to record traces with a good signal-to-noise ratio S/N (**Figures 4.16a** and **b**). We decided to employ an empiric pseudo-first order time constant, the time at half amplitude of the decay ($\tau_{1/2}$),[181] to fit the traces because the recombination kinetic is highly non-monoexponential and was less than 50% complete in 500 ns. We extrapolated the k_{reg} according to **eq. 4.4**:

$$k_{reg} = k_{app} - k_{rec} \qquad \textbf{eq. 4.4}$$

where k_{app} corresponds to $1/\tau_{1/2app}$ and k_{rec} corresponds to $1/\tau_{1/2rec}$ and were calculated from the time constants extrapolated when the films were in contact with an I^-- and a blank-based electrolyte respectively. In these experimental conditions, we extrapolated a kinetic constant of the order of 1.5 x 10^7 s^{-1}, which leads to a regeneration efficiency (η_{reg}) of ca. 80%. By combining the result estimated at long- and short-time window, we can affirm that the regeneration is in the order of 80-90%. Then we analyzed the effect of high-density cations in the electrolyte, since a large improvement in photoconversion performance was reported in the previous section, compared to the previous study.[6] Although the charge injection was recorded within the instrumental response of our spectrophotometer at the best resolution ($K_{inj} < 1.5x10^8$ s^{-1}), we found that the amplitude of the charge separated state is double in the presence of 0.1 M Li^+/0.1 M Mg^{2+} (**Figure 4.16c**). This is explained with a larger fraction of excited dye undergoes injection on ultrafast time scales. Our observation is consistent with the positive shift in the TiO_2 density states of ca. 400 meV recorded in cyclic voltammetry in an inert electrolyte (0.6 M PMIOTf/0.1MTBAPF$_6$/0.1 M GuNCS (**Figure 4.16d**). We also observed a large increase in film conductivity, which leads to a ca. 4 times increase in the current associated with the electroactivity of the substrate thanks to the charge compensating capability of Li^+ and Mg^{2+} (it was reported to increase the ambipolar electron diffusion coefficient in the TiO_2 films, favoring the charge collection). However, such an effect, while beneficial in increasing cell performance, cannot influence the magnitude of the charge-separated states observed at early time scales.

(a) (b)

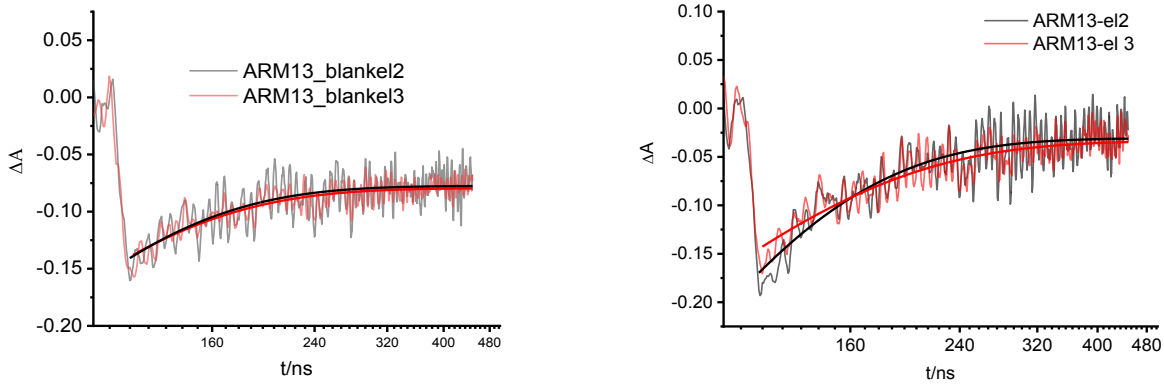

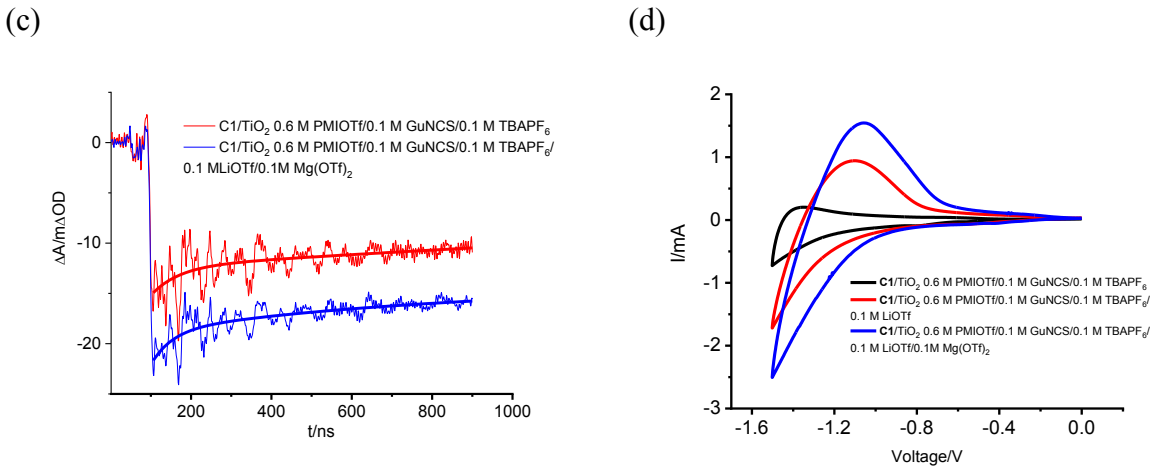

Figure 4.16: (a) Recombination dynamics recorded at 500 nm for **ARM13** dyed film in contact with blank electrolyte 2 (0.6 M PMIOTf + 0.1 M LiOTf + 0.1 M GuNCS + 0.1 M $MgOTF_2$ in acetonitrile) and blank electrolyte 3 (blacnk *el2* + 0.1 M $TBAPF_6$). (b) Regeneration dynamics of **ARM13** in presence of the reduced form of electrolyte 2 (0.6 M PMII + 0.1 M LiI + 0.1 M GuNCS + 0.1 M MgI_2 in acetonitrile) and 3 (*el2* + 0.1 M TBAI). (c) 500 nm kinetics for **C1** dyed film in contact with 0.6 M PMIOTf + 0.1 M GuNCS + 0.1 M $TBAPF_6$ and with 0.6 M PMIOTf + 0.1 M GuNCS + 0.1 M $TBAPF_6$ + 0.1 M LiOTf + 0.1 M $Mg(OTf)_2$. (d) Cyclic voltammetry of **C1** dyed film in contact with 0.6 M PMIOTf + 0.1 M GuNCS + 0.1 M TBAPF6, with 0.6 M PMIOTf + 0.1 M GuNCS + 0.1 M $TBAPF_6$ + 0.1 M LiOTf and with 0.6 M PMIOTf + 0.1 M GuNCS + 0.1 M $TBAPF_6$ + 0.1 M LiOTf + 0.1 M $Mg(OTf)_2$. From ref 254

4.3.3b Photoelectrochemical characterization

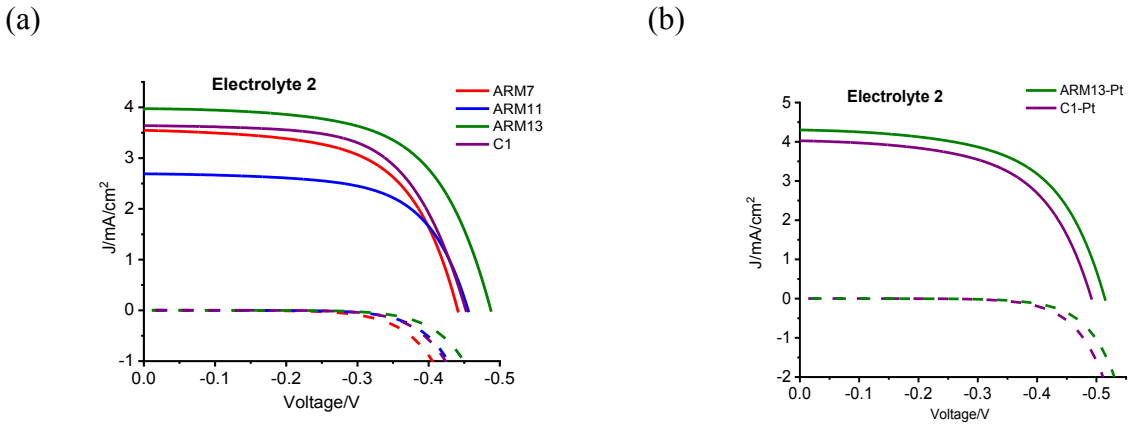

Figure 4.17: (a) J-V curves obtained with *el2* under AM 1.5G illumination (solid lines) and in the dark (dashed lines). (b) **C1** and **ARM13** sensitized solar cell equipped with a Pt coated FTO counter electrode in the presence of *el2* under AM 1.5G illumination (solid lines) and in the dark (dashed lines). From ref 254

The photoelectrochemical performances were initially tested in the presence of the Mg-based electrolyte formulated for the optimization of **C1** (namely *el 2*) in the previous section. In **Figure 4.17a** the averaged J-Vs for all the Fe(II)NHC series are reported. The performances of **ARM7**, **ARM13** and of the standard **C1** resulted quite align with photocurrent density varying between 3.5 mA/cm^2 to 4 mA/cm^2, while the V_{oc} was around 0.45 V. In detail, **ARM7** exhibited a J_{sc}=3.55 mA/cm^2, a V_{oc}=0.44V, a FF=60% and a PCE=0.94%. **ARM11** showed the lowest PCE of the series of 0.74% with J_{sc}=2.69 mA/cm^2, V_{oc}=0.46 and FF=60%. The best PCE% of 1.2% was recorded in the case of the heteroleptic analogue of **C1**, **ARM13**, due to the best combination of photocurrent (3.95 mA/cm^2), photovoltage (0.49) and FF (61%). This asymmetric compound exhibited the lowest dark current which explains the best V_{oc} among this Fe(II)NHC series. The overall PCE% (1%) obtained in the case of the standard **C1** is quite align with the result obtained previously (0.92%), just slightly higher for the introduction of a thicker substrate. Despite the lower light harvesting of

ARM13, it performed better than **C1**. Based on their similarity in regeneration efficiency and excited state energetics, the reason could be explained by its asymmetric design, which leads to a better electronic coupling for charge injection. The standard ruthenium dye **N719** exhibited a higher efficiency (3.57%) due to the combination of the higher photocurrent density (12.8 mA/cm^2) and the higher V_{oc} (ca. 0.5 V). The reason of the superior open circuit photovoltage was attributable to the higher current density, this was confirmed by placing neutral filter to reduce the J_{sc} to 4 mA/cm^2 with consequent V_{oc} comparable to those obtained for the Fe(II)NHC family. The photovoltaic performances are listened in **Table 4.4**.

Table 4.4: Photovoltaic parameters of **ARM7**, **ARM11** and **ARM13** compared with **C1** and **N719** with blocking under layer after double annealing

Dyes	Electrolyte	Jsc/ mA/cm^2	*V*oc/ V	FF%	PCE%
N719	*el2*	12.84	0.48	58	3.57±0.34
ARM7	*el2*	3.55	0.44	60	0.94±0.11
ARM11	*el2*	2.69	0.46	63	0.78±0.08
ARM13	*el2*	3.95	0.49	61	1.18±0.10
C1	*el2*	3.64	0.45	62	1.02±0.11
N719	*el3*	12.87	0.50	57	3.68±0.52
ARM7	*el3*	3.89	0.43	57	0.95±0.09
ARM11	*el3*	2.90	0.45	62	0.81±0.10
ARM13	*el3*	4.44	0.45	64	1.27±0.12
C1	*el3*	4.38	0.43	59	1.11±0.17

The replacement of the PEDOT films with a transparent Pt coated counter electrodes (**Figure 4.17b**) allowed a partial light reflection which led to better performances. In detail, the photocurrent density recorded increased from 3.95 to 4.26 mA/cm^2 and from 3.64 to 4.02 mA/cm^2 for **ARM13** and for **C1** respectively.

We considered the reasons behind the lower performances recorded for the Fe(II)NHC family with respect to the standard ruthenium, because of the regeneration efficiency resulted at least around 80%, we took into account other possible losses originating from the recombination of the photoinjected electrons with I_3^-. This kind of recombination was analyzed with EIS in the dark at various forward voltages, the Nyquist plot are reported in **Figure 4.18**. The total resistance can be written as follow:

$$R_{TOT} = R_{\Omega} + R_{CT} \qquad \textbf{eq. 4.5}$$

where R_{Ω} represents the constant contact resistance (20 /25 Ω) and R_{CT} represents the charge transfer resistance ascribed to recombination with I_3^- at the TiO_2/electrolyte interface. The overall resistance (**Figure 4.18f**) varied according to **N719** < **ARM7** < **ARM11** ≈ **ARM13** ≈ **C1** where the major differences are observed at the threshold of the dark current processes (e.g. around -0.3 V), while the dark response of all sensitized electrodes becomes quite aligned when the applied potential is more negative than -0.4 V. These results, obtained in a complete cell configuration, provided as a more reliable estimation of the recombination dynamics than those one obtained via spectroscopic analysis (see previous chapter), and show that the recombination between the photoinjected electrons and the reduced form of the redox couple in the *el 2* formulation, is not a critical issue with respect to **N719**. This, combined with the regeneration efficiency η_{reg} calculated through the spectroscopic analysis, leads to consider the main limitation of Fe(II)-based solar cells in the charge injection process that is in competition with the excited state deactivation that occurs in a ps time scale.

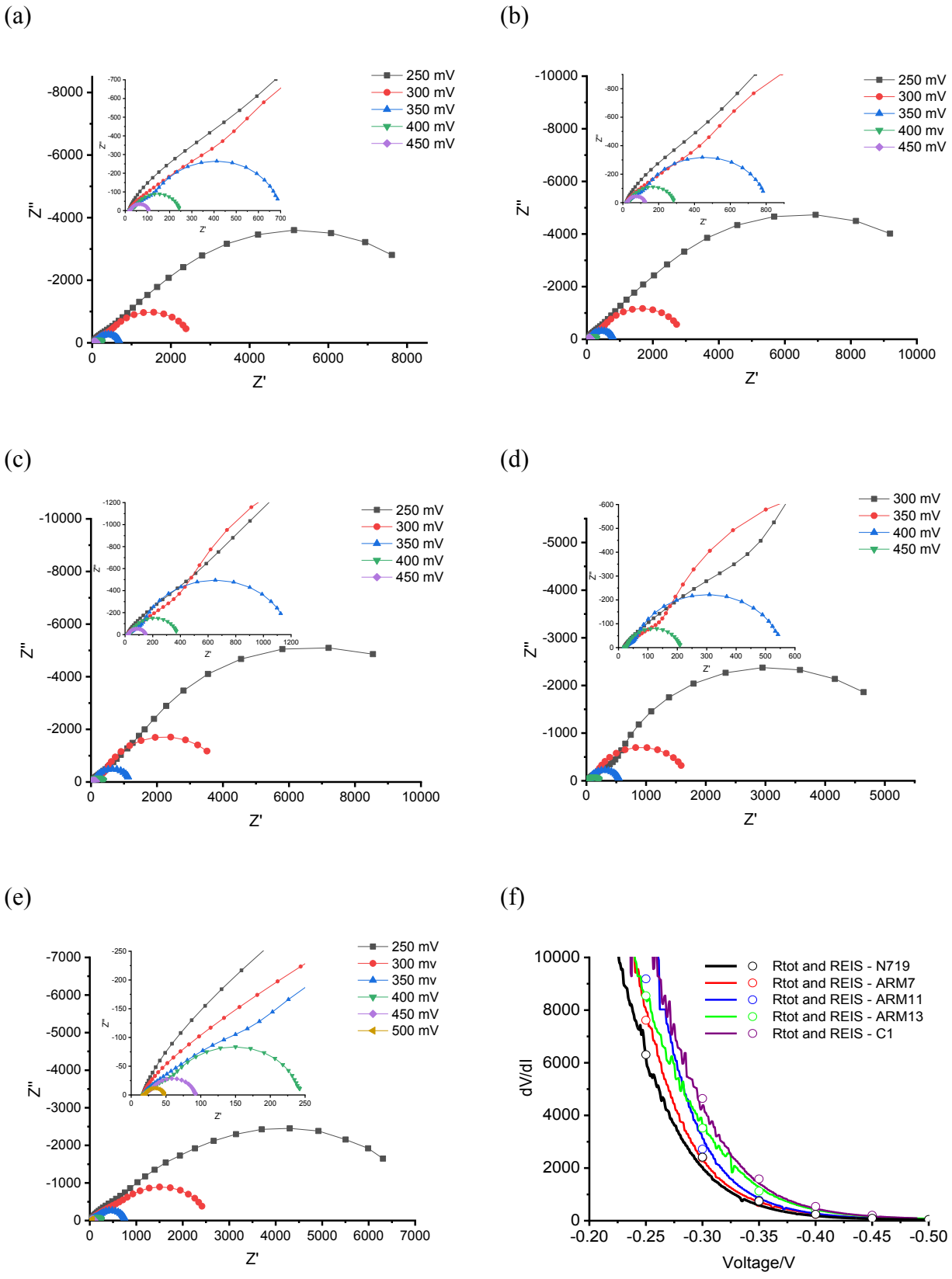

Figure 4.18: (a)-(e) Complex plane (Nyquist) plots of Fe(II)NHC-based solar cell in the presence of electrolyte 2. (f) $R_{TOT} = \frac{\partial V}{\partial J}$ showing a good agreement with R_{TOT} extracted from the fitting of EIS data obtained by sampling the forward voltage at 50 mV intervals under dark conditions. From ref 254

We observed also that injection is possible in the absence of small high-density cations, consistent with the strong reducing capabilities of the iron-based family excited states and with what was previously discussed in the TA characterization, but the resulting IPCE is reduced to 5-6%, associated with a maximum photocurrent density of 0.54mA/cm^2 (**Figure 4.19**).

(a) (b)

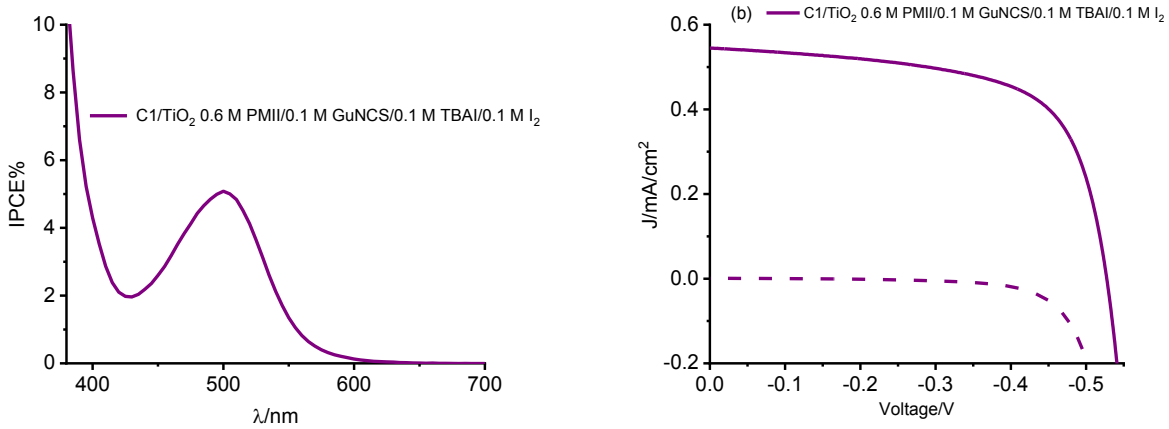

Figure 4.19: (a) IPCE and (b) J-V curves obtained for **C1** sensitized cells with electrolyte 3 deprived of Li^+ and Mg^{2+}. From ref 254

The IPCE spectra of the Fe(II)NHC in contact with *el 2* series are reported in **Figure 4.20a**, the absorbed dyes exhibited a bathochromic shift when are in contact with small high density cations like Li^+ and Mg^{2+}, as already discussed in the previous section. All the spectra are characterized by similar features: their maximum of conversion is consistent with the main visible MLCT band and ranges between 450 to 700 nm and peaks around 500 - 520 nm in all the cases. The IPCE% maximum varies between 30% in the case of **ARM11** to 40% in the case of **ARM13** and it is consistent with the photocurrent density trend. After the normalization of the IPCE for the LHE, the resulted APCE is around 40% in the case of the best sensitizer **ARM13** (**Figure 4.20b**). By matching this datum with the estimated η_{reg} of 85±5%, it suggests a quantum yield of injection of 47±4% and consists with the data obtained in the case of **C1**.

(a) (b)

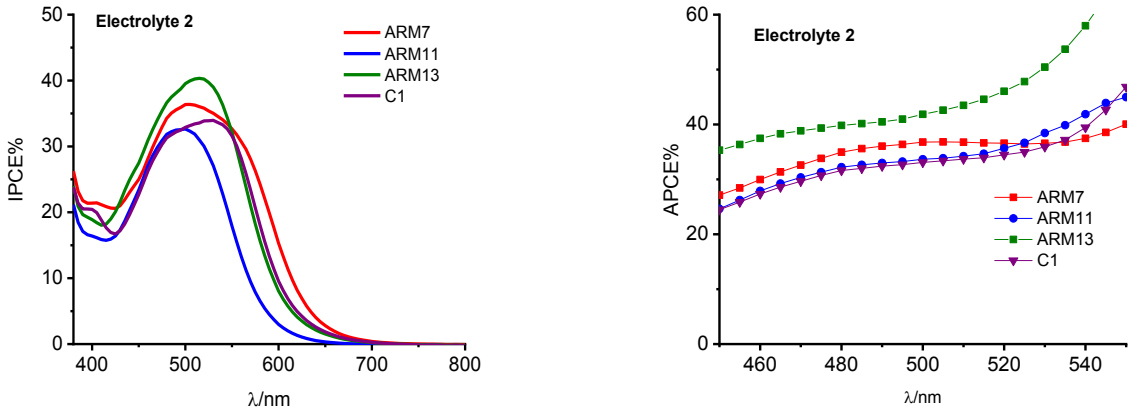

Figure 4.20: a) IPCE spectra obtained with *el2* in Fe(II)NHC sensitized cells. (b) APCE curves obtained from **Figure 4.14a**. The tendency to diverge at low λ is generated by errors in a proper estimation of the optical density of the electrode when the absorbance decreases sharply from the maximum around 500 nm. From ref 254

We tried to optimize the electrolyte mixture by adding 0.1 M TBAI in the electrolyte 2 obtaining the *el 3*, in all the case we recorded a slight improvement in the power conversion efficiency. In particular, **ARM13** was the dye that most benefited of this electrolyte, the resulted IPCE and APCE exceeded 40% (**Figures 4.21a** and **b**). Under AM 1.5G illumination the photocurrent density increased to 4.44 mA/cm^2 with a PCE% of 1.27%. Under the same conditions, the standards **C1** and **N719** increased from 1.03% to 1.11% and from 3.57 to 3.68%. Also with this electrolyte we have decided to replace our PEDOT-based CE with a partly reflective platinum counter electrode (**Figure 4.21d**), the photocurrent density of **ARM13** further increased to 5 mA/cm^2 leading to a PCE of 1.44% that, at the time of this work, was the highest efficiency recorded for a Fe(II)NHC sensitized solar cell. The role of the additive TBAI is not fully understood, we didn't record a reduced recombination in the dark current plot (**Figure 4.21e**) (just in the case of **N719**) and we didn't reveal an increased regeneration efficiency at the best time resolution of our spectrophotometer. From the J-V curves it is possible to affirm that the overall cell resistance is reduced when TBAI is introduced in the electrolyte mixture and could be attributable to a reduced resistance either at the TiO_2/electrolyte interface or in the diffusional resistance of the electrolyte.

(a)

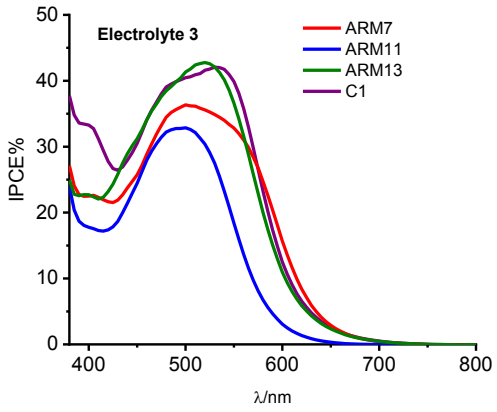

(b)

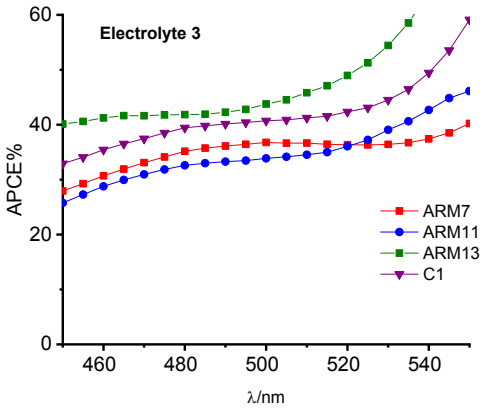

(c)

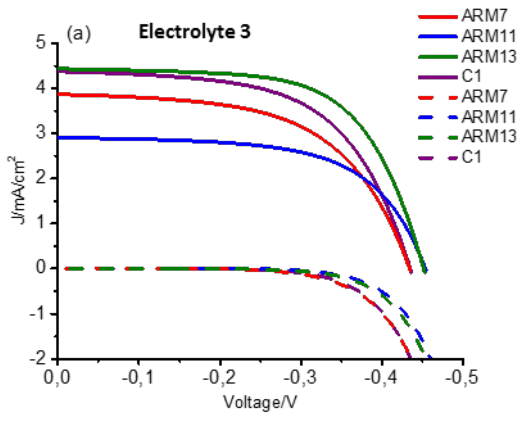

(d)

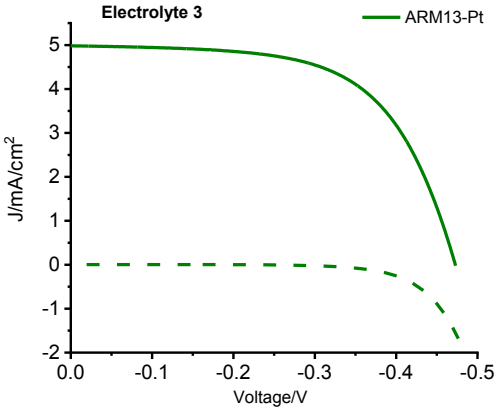

(e)

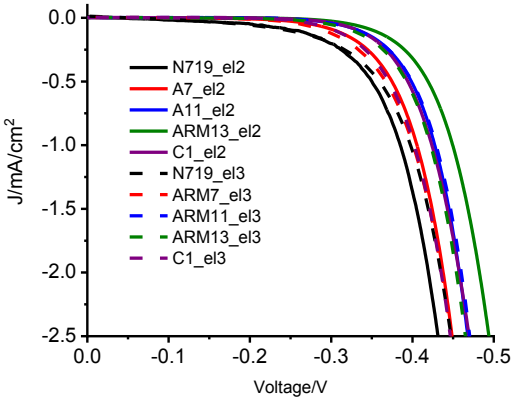

(f)

Pt-based CE

Dyes	Electrolyte	Jsc (mA/cm^2)	Voc (V)	FF%	PCE%
C1	*el2*	4.02	0.49	58	1.14±0.07
ARM13	*el2*	4.26	0.51	59	1.29±0.09
ARM13	*el3*	4.98	0.47	62	1.44±0.07

Figure 4.21: (a) IPCE, (b)APCE, (C) J-V curves for Fe(II)NHC complexes in contact with electrolyte 3 (TBAI based electrolyte). (d) J-V curve for **ARM13** in contact with electrolyte 3, and a platinum based Counter electrode. (e) Comparison of the dark currents of Fe(II)NHC sensitized TiO_2 in contact with electrolyte 2 (solid line) and electrolyte 3. (f) Photovoltaic parameters for cell assembled with platinum counter electrode. From ref 254

4.3.4b Computation characterization

As already reported in the experimental section, these analyses were conducted by Dr. Mariachiara Pastore's Group of the university of Lorraine to tray to better understand the role of Mg^{2+} at the **C1**/TiO_2 interface that allows electron injection, the possibility of Mg^{2+} in justifying the higher photocurrent of **ARM13** despite its quite low and slightly blue-shifted absorption spectrum and to try to understand the worse performances recorded in the case of the spacer-based complexes despite their higher light harvesting.

Effect of MgI_2 electrolyte. Following a computational approach similar to the one used to model the effect of Li^+ cations at the indoline D102/TiO_2 interface reported in literature,[255] it was simulated the adsorption of a Mg^{2+} cation at the **C1**/TiO_2 and **ARM13**/TiO_2 interfaces and analysed the interfacial electron transfer kinetics. The realistic model of the dye/TiO_2 interfaces should include several cations adsorbed on the surface at different positions but, nevertheless, as has been shown for Li^{+}[255] and H^{+}[256] cations adsorbed on the $(TiO_2)_{82}$, there is an almost linear effect as the number of positive charges increases on the energy shift of the TiO_2 CB and dye's LUMO levels, as well as on the gain in the injection rates. Thus, since the main target was to examine the qualitative impact of the cation on the dye/TiO_2 electronic structure, the model was limited to a single cation model, stably interacting close to the dye's anchoring group.[255]

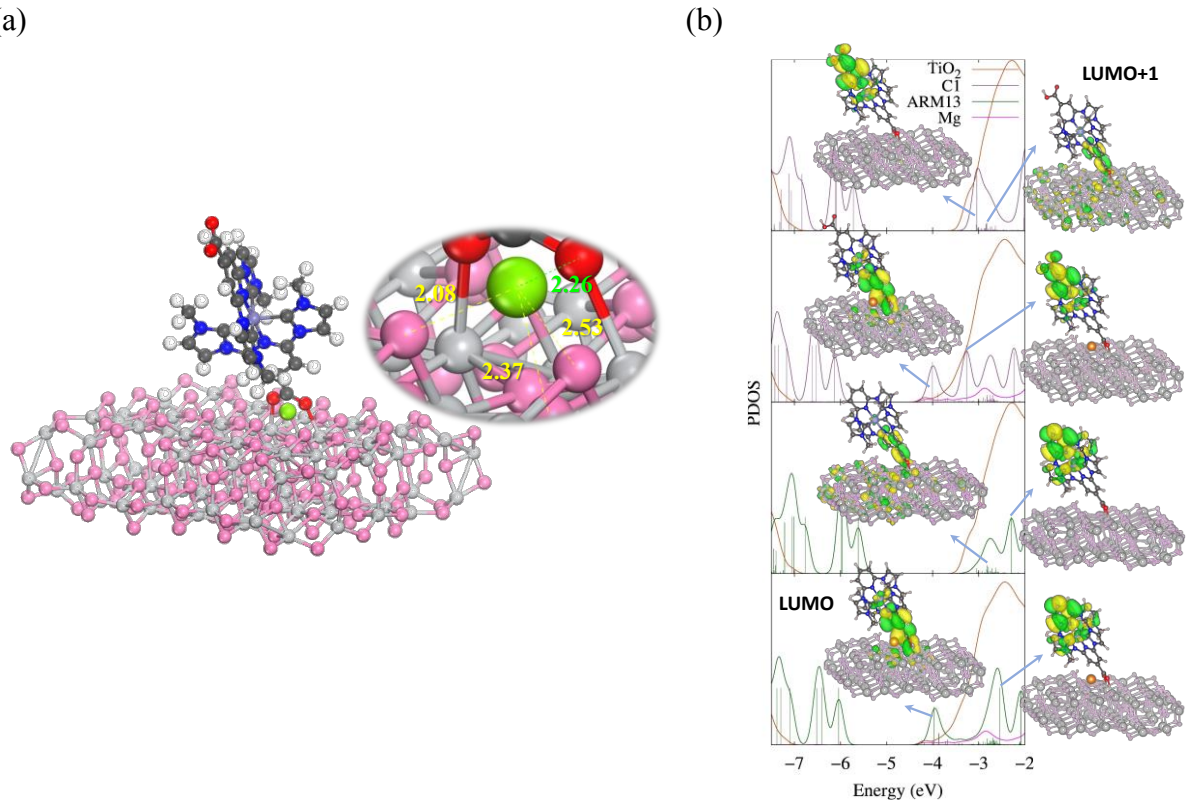

Figure 4.22: (a) Optimized structure of the **C1**/Mg-TiO_2 system; a zoomed-in image of the Mg^{2+} cation (green colored atom) and its closest O neighbor atoms is displayed in the inset of the perspective view as well. (b) Projected Density of States (PDOS) of the **C1**/TiO_2/**C1**/Mg-TiO_2 (top) and **ARM-13**/TiO_2/**ARM-13**/Mg-TiO_2 (bottom) systems over the atoms belonging to the dye (red), TiO_2 surface (blue) and Mg^{2+} cation (magenta) as calculated by Mulliken population analysis. For visualization purposes, only the vertical bars of the dye's PDOS are represented here and the TiO_2 DOS intensity has been divided by a factor of 10. The isodensity plots (isovalue 0.02 a.u.) of the dye unoccupied MOs indicated by the grey arrows are displayed in the insets of the PDOS plots. From ref 254

As is apparent in **Figure 4.22a** for the **C1** dye, the Mg^{2+} cation lies close to three oxygens of the TiO_2 surface in a hollow fashion (distances to the nearest neighbor O atoms of TiO_2 of about 2.0 Å, 2.5 Å and 2.4 Å), as well as to one of the anchoring O atoms of the dye (Mg–O distance of 2.3 Å). As shown by the Projected Density of States (PDOS) plots in **Figure 4.22b**, the main energetic effect of the presence of the cation at the surface is the expected negative shift for all the unoccupied interfacial energy levels in both **C1** and **ARM13**-sensitized TiO_2. A deeper look at the localization of the frontier MOs, however, reveals that the adsorption of Mg cations on the semiconductor surface in proximity to the dye induces a striking and more pertinent consequence for **C1** (top panels in **Figure 4.22b**). In **C1**/TiO_2, indeed, the dye's LUMO is localized in the unbound ligand with essentially no electronic coupling with the semiconductor CB states (99% localization on the dye): the metal-to-ligand charge transfer goes in the opposite direction with respect to TiO_2 and electron injection is impeded. This is a consequence of the destabilization of the CT toward the deprotonated-anchored ligand. When the Mg cation is present at the interface, on the other hand, its localized positive charge in proximity to the anchoring unit stabilizes the CT toward the surface-adsorbed ligand, where the dye's LUMO is now localized (**Figure 4.22b**): the lowest-energy bright MLCT transition recovers the correct directionality and electron injection is now possible, thus explaining the measured photocurrents. On the other hand, the shape, and relative energies for the highest occupied levels of the dyes remain

very similar upon Mg^{2+} adsorption, since their localization on the top and central part of the dye, far from the surface, significantly weakens their interaction with the cation (**Figure 4.23**).

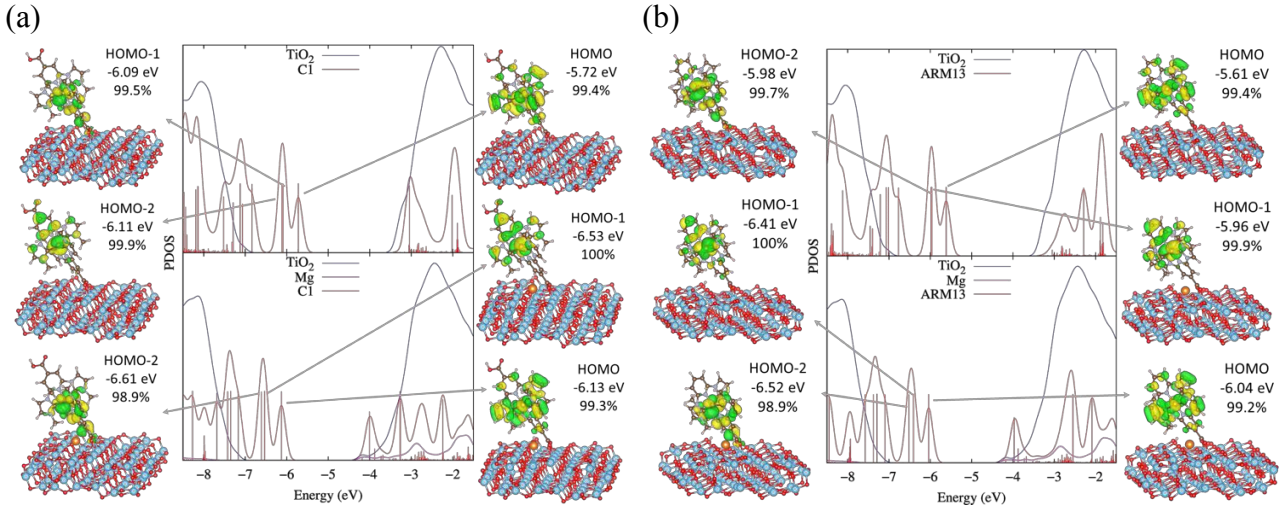

Figure 4.23: (a) Projected Density of States of the **C1**/TiO_2 (top) and **C1**/Mg-TiO_2 (bottom panel) systems over the atoms belonging to the **C1** dye (red), TiO_2 surface (blue) and Mg^{2+} cation (magenta) moieties as calculated by Mulliken population analysis. Note that for the sake of a better visualization, only the vertical bars conforming the **C1** DOS are represented here and the TiO_2 DOS intensity has been divided by a factor of 10. The isodensity plots of the relevant dye occupied MOs indicated by the grey arrows are displayed in the onsets of the PDOS plot. The energies and weight percentages for each plotted MOs are reported as well. The isovalue used in the isodensity plots was 0.02 a.u. (b) Projected Density of States of the **ARM13**/TiO_2 (top) and **ARM13**/Mg-TiO_2 (bottom panel) systems over the atoms belonging to the **ARM13** dye (red), TiO_2 surface (blue) and Mg^{2+} cation (magenta) moieties as calculated by Mulliken population analysis. Note that for the sake of a better visualization, only the vertical bars conforming the **ARM13** DOS are represented here and the TiO_2 DOS intensity has been divided by a factor of 10. The isodensity plots of the relevant dye occupied MOs indicated by the grey arrows are displayed in the onsets of the PDOS plot. The energies and weight percentages for each plotted MOs are reported as well. The isovalue used in the isodensity plots was 0.02 a.u. From ref 254

To obtain a more quantitative picture, the diabatic couplings between the levels of the dyes and the ones of the TiO_2 slab was calculated, with the aim of evaluating how the Mg^{2+} cation affects the interfacial electron transfer kinetics (injection/recombination times). The diabatic energy levels for the dye's frontier molecular orbitals and TiO_2 conduction and valence bands are reported in **Table A4.2**, while the diabatic electronic couplings are plotted in **Figures A4.22-A4.25** (Appendix). The results relative to the electron injection process, by considering the electronic coupling for both the LUMO/LUMO+1 and the CB states are gathered in **Table 4.5** for the **C1**/TiO_2, **C1**/Mg-TiO_2, **ARM13**/TiO_2 and **ARM13**/Mg-TiO_2 systems, while the data for the recombination between the injected electrons (TiO_2 VB) and the oxidized dye (HOMO/HOMO-1/HOMO-2) are listed in **Table A4.3** in the Appendix. It is important to stress that the electron transfer efficiency results from the interplay of two factors, the extent of the electronic coupling between the donor's and the acceptor's states and the density of available acceptor's (TiO_2) states; their product gives the probability distribution G(3), that, evaluated at the energy of the donor state, provides the injection rates. The injection times of 4.6 and 3.9 fs (**Table 4.5**) calculated for the LUMO+1 and LUMO in **C1**/TiO_2 and **C1**/Mg-TiO_2, respectively, clearly show the recovery of the correct CT direction in the homoleptic complex when Mg^{2+} is at the interface and the possibility of injecting electrons from the LUMO, as indicated by the increased amplitude of the charge separate state (dye(+)/e^-TiO_2) in **Figure 4.16c** and the consequent increase in the IPCE spectra, discussed in the **Paragraph 4.3.3b**. Moreover, the sizeable increase in the electronic coupling between the LUMO and the surface localized TiO_2 CB edge state (**Figures A22 and A24)** largely compensates for the detrimental shift of the dye's LUMO at lower energies, yielding a decrease of TiO_2 empty acceptor states (second and fourth panels in **Figure 4.21b** starting from the top). Similar considerations apply for **ARM13**, for which an increase

in the injection probability GL is calculated when Mg^{2+} is at the interface and the injection time decreases from 4.3 to 3.7 fs. Notably the predicted interfacial electron injection kinetics perfectly match the photocurrent values recorded for **C1** and **ARM13** (**Table 4.4**), indicating slightly superior injection efficiency for the heteroleptic complex, despite its inferior light harvesting capability (**Figure 4.14a**). Regarding the recombination rates, as shown by the data in **Table A4.3** and **Figure A23 and A25,** the addition of Mg^{2+} is translated to a slight increase in the couplings of TiO_2 the highest occupied levels of the dye. Nevertheless, this increase is not so significant to expect a big change in the recombination rates and the device efficiencies.

Table 4.5: Probability distributions, $G(\varepsilon_k)$ (eV) extracted at the dye's LUMO (Γ_L) and LUMO+1 (Γ_L+1) diabatic energies (**Table A4.2b**) and associated injection times, s (fs)

System	Γ_L (eV)	τ_L (fs)	Γ_{L+1} (eV)	τ_{L+1} (fs)
C1/TiO₂	1.12E-05	58530	0.142	4.6
C1/Mg-TiO₂	0.167	3.9	7.54E-05	8723
ARM13/TiO₂	0.152	4.3	3.07E-05	21428
ARM13/Mg-TiO₂	0.179	3.7	4.43E-05	14840

Effect of the conjugated spacer. A fast and reliable way to estimate the electron injection capability of a dye sensitizer is by looking at the extent of localization of the LUMO on the anchoring COOH unit.[256] Nevertheless, a qualitative evaluation of the spatial localization of holes and electrons in the lowest energy bright MLCT transitions as it appears in the Natural Transition Orbitals (NTOs) depicted in **Figure 4.11a,** although capable of providing a rough idea, is not sufficient. A more quantitative and accurate analysis of the charge and hole localization characterizing the lowest bright excited state has been obtained here by employing the transition density matrix manipulation tools implemented in TheoDORE.[247] The calculated percentages are reported in **Figure 4.24**. The relevant data here are the percentages of electrons localized on the anchoring moiety (COOH): 16.3%, 8.3% and 6.7% for **ARM13**, **ARM7** and **ARM11**, respectively. These values directly correlate with the corresponding measured photocurrents of 3.95 (**ARM13**), 3.55 (**ARM7**) and 2.69 mA/cm^2 (**ARM11**) reported in **Figure 4.20f**. It is now evident that, despite inducing an overall improvement of the optical properties, the introduction of a conjugated thiophene or phenyl spacer results in a markedly decreased CT toward the anchoring group, with reduced injection efficiencies.[255] Although the presence of Mg^{2+} cations at the dye/TiO_2 interface will increase the localization on the anchoring unit and thus the coupling with the CB states as shown for **ARM13**, it is not expected a differential effect within the series and thus a change in the order of the predicted photocurrents.

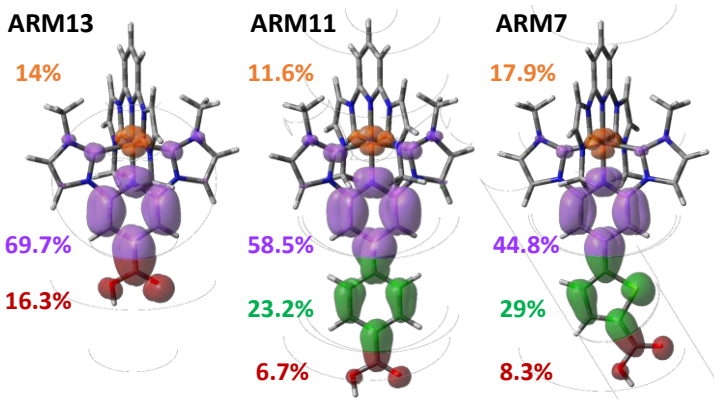

Figure 4.24: Electron Natural Transition Orbitals (NTOs) in **ARM13**, **ARM11** and **ARM7** with the percentages of delocalization for each fragment. The colours employed to plot the isodensities correspond to the unbound pyridylNHC ligand and iron (orange), anchoring ligand: pyridylNHC (purple), spacer (green) and carboxylic group (red) moieties. The isovalue used for this plot was 0.03 a.u. From ref 254

4.4b Conclusions

With this interdisciplinary project we have obtained an important step forward in the development of more efficient Fe(II)NHC-based DSSC obtaining, at the time of the work, the highest power conversion efficiency close to 1.5% (1.44%). This great result was obtained by combining all the acquired knowledge of every one of us, in particular, the chemical design rules required to improve the dye-to-TiO_2 electron injection,[94] as well as on the optimization of the electrolyte composition and substrate tuning (see the previous section). In this work we realized heteroleptic complexes, for which the lowest energy MLCT has the desired topology and we employed Mg^{2+}-based electrolyte with the aim to improve the photovoltaic performances. We prepared a new heteroleptic family composed of **ARM13**, the heteroleptic analogue of **C1**, and **ARM7** and **ARM11** characterized by a thiophene and phenyl spacers between the metal center and the anchoring group to try to increase the charge separation and reduce the recombination processes. By combining the APCE% data with the recombination and regeneration dynamics, we obtained that the injection process is still the main limiting factor for iron sensitized solar cells due to a competition with the excited state deactivation, while the recombination dynamic is not a crucial parameter as reported in the previous section.
We combined the photovoltaic performances with the computational analysis to better understand the resulted trend. We obtained that the presence of Mg^{2+} cations adsorbed at the dye/TiO_2 interface stabilized the CT toward the surface adsorbed carbene ligand allowing for a quite efficient electron injection in the case of or standard homoleptic **C1** and for an improved injection rate in the case of its heteroleptic analogue **ARM13**. We also better understood the reason behind the lower performances of the complexes characterized by the conjugated spacer despite the broader light harvesting. The problem was found in the local π-π* character of the MLCT excitations introduced by the aromatic spacers, which significantly lowers the charge separation within the dye and the injection of electrons into the semiconductor.

c) A Series of Iron(II)-NHC Sensitizers with Remarkable Power Conversion Efficiency in Photoelectrochemical Cells

4.1c Introduction

In our previous studies, we have demonstrated the possibility to increase the photovoltaic performances of the iron-based Solar Cells by fine-tuning the electrolyte composition as well as the substrate configuration. In particular, we obtained 1% cell efficiency with **C1** by coupling a TiO_2 equipped with a blocking layer and a Mg^{2+} based electrolyte. In a second study, we have designed, synthesized and analyzed the performances of heteroleptic complexes with the aim to increase the excited state directionality. In our series, we have also screened the effect of the introduction of spacer between the metal center and the carboxylic group showing a lower electron localization on the anchoring moieties (COOH) when the spacers were present, and consequent reduced injection efficiencies. With the acquired knowledge, we decided to study the impact of the electronic modifications of the ancillary ligand on the photovoltaic properties of the corresponding devices. Dr. Gros's group synthesized new six asymmetric complexes (**Figure 4.25**) characterized by ancillary ligands bearing electron withdrawing or donating substituents and we have performed the photophysical, electrochemical and photoelectrochemical investigation obtaining an unprecedent 1.83% record efficiency combining the **ARM130** sensitizer, Mg^{2+}-based electrolyte and a relative thick TiO_2 photoanode.

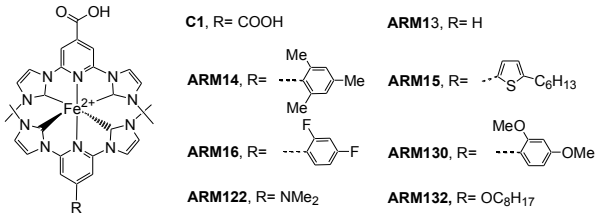

Figure 4.25: Chemical structures of Fe(II)NHC sensitizers studied in this work, the counter ion is PF_6^- in every case. From ref 257

4.2c Experimental

4.2.1c Materials

PMII ≥ 98%, ACS grade I_2 ≥ 99.8%, GuNCS ≥ 97%, EDOT 97%, Alconox, $Ti(OiPr)_4$, TBAI ≥ 98 and solvents (anhydrous ACN 99.8%, ACS grade 2-propanol ≥ 99.8%, 99.9% 1-butanol) were purchased from Sigma-Aldrich and used without further purification. Ultra-dry LiI 99.999% and MgI_2 > 99% were purchased from Fluka, $LiClO_4$ ≥ 99% was bought from Acros organics. FTO TEC-7 was obtained from NSG, Ti-nanoxideT/SP (transparent titania) and Tinanoxide R/SP (scattering titania) pastes were purchased from Solaronix. Surlyn 25 was supplied by Dyepower Consortium. ZrO_2 colloidal paste was prepared following the literature.[258]

4.2.2c Methods

^{1}H (400 MHz) and ^{13}C NMR (100 MHz) spectra were taken on a DRX400 Bruker spectrometer at ambient temperature.

High-resolution mass spectrometry (HRMS) data was obtained by using Bruker micrOTOF-Q spectrometer. UV-vis spectra were recorded in a 1 cm path length quartz cell on a LAMBDA 1050 (Perkin Elmer) spectrophotometer.

Absorption spectra of the Fe(II)NHC sensitizers loaded on transparent thin films were obtained in transmission mode with an Agilent Cary 300 UV-Vis spectrophotometer, against an identical undyed TiO_2 film as a reference. Diffuse reflectance absorption spectra of the titania photoanodes equipped with a scattering layer were recorded with a JASCO V-570 spectrophotometer with an integrating sphere. Spectra were acquired by illuminating through the transparent FTO side with a band pass of 10 nm.

FTO supported TiO_2 or ZrO_2 films modified with Fe(II)NHC dyes were used as working electrodes for cyclic voltammetry in nitrogen purged three electrode electrochemical cells equipped with a platinum counter electrode (A= 4 cm^2) placed in front of FTO, while a standard calomel electrode (SCE) served as a reference. CVs were carried out at a scan rate of 20 mV/s with a PGSTAT 302N potentiostat in 0.1 M $LiClO_4$/ACN

J-Vs curves were recorded with a PGSTAT 302N potentiostat coupled with an ABET sun simulator equipped with an AM 1.5G filter. The irradiance was adjusted to 100 mW/cm^2 (1 SUN). The IPCE spectra were recorded with a homemade apparatus described in detail elsewhere; it is composed by a Xe lamp (Ceralux CL300BF) and a National Instruments PXI 1033 measurement system. Photocurrent was registered under short circuit condition.

APCE were computed according to IPCE/LHE, where LHE was calculated from the Absorbance of the thin films measured in transmission mode using an undyed titania film as a reference. For the LHE calculation relevant to APCE, UV-Vis spectra were corrected for the red shift observed in the presence of Li^+, by using a spectral shape factor obtained from the normalized ratio of the absorption spectra of thin films in the absence and in the presence of lithium ions.

EIS were carried out with a PGSTAT 302N potentiostat under the illumination generated by an ABET AM1.5 G sun simulator (1 SUN irradiance) by applying a sinusoidal 10 mV perturbation while sampling the forward potential interval corresponding to the discerning branch of the J-V characteristic. Perturbation frequency decreases from 10^5 to 10^{-1} Hz when moving from left to right. Data were fitted with ZView software by using the circuit model reported in **Figure 4.33h**. Non ideal interfacial capacitances of porous films were described by constant phase elements (CPE) defined as:

$$Z_{CPE} = \frac{1}{T(j\omega)^P} \qquad \textbf{eq. 4.6}$$

(where z_{CPE} is the CPE impedance, T is the CPE admittance (CPE-T in ZView) and P is a coefficient (CPE-P in Zview) which normally varies between 1 and 0.8). The equivalent capacitance can be calculated according to:

$$C_{max} = T(j\omega_{max})^{P-1} \qquad \textbf{eq. 4.7}$$

In the case the CPE of titania films in the investigated cells, P was in all cases close to 0.96 hence $C_{max} = C_\mu$ and T were practically coincident.

Transient absorption spectroscopy on Fe(II)NHC sensitized TiO_2 were carried out with a Nd:YAG laser (Continuum Surelite II) and a monochromatic probe beam. Suitable input impedances (varying

from 350 Ω to 1 MΩ) were used to amplify the signals on the appropriate time scale. To increase the ratio S/N multiple shots were accumulated.

4.2.3c Synthesis

Dr. Gros's group of the University of Lorraine realized the synthetic part of this thesis work in the following way:

***2,6-di(1H-imidazol-1-yl)-4-mesitylpyridine (2*).** To a solution of **1** (0.130 g, 0.448 mmol) in toluene (5 mL) was added a solution of 2,4,6-trimethylphenyl boronic acid (0.088 g, 0.537 mmol) and K_2CO_3 (0.186 g, 1.34 mmol) in methanol (5 mL). The mixture was degassed under Argon for 20 min then $PdCl_2$(dppf) (0.033 g, 0.044 mmol) was added, and the solution was refluxed at 80 °C for 8 h. After completion of reaction, the mixture was filtered through a celite pad and washed with dichloromethane. After evaporation, the residue was purified by column chromatography over silica gel using 4-6% methanol in dichloromethane as the eluent to give the product as a white solid (0.100 g, 68 % yield). ^{1}H NMR (400 MHz, $CDCl_3$) δ ppm: 8.39 (brs, 2H), 7.67 (brs, 2H), 7.24 (s, 2H), 7.09 (s, 2H), 7.01 (brs, 2H), 2.36 (s, 3H), 2.09 (s, 6H) (**Figure A4.26**). ^{13}C NMR (100 MHz, $CDCl_3$) δ ppm: 156.8, 148.7, 138.7, 135.1, 134.8, 134.7, 131.2, 128.7, 116.1, 110.5, 21.1, 20.5 (**Figure A4.27**). ESI-HRMS calcd for $C_{20}H_{20}N_5$ m/z = 330.1713. Found: 330.1889.

***4-(5-hexylthiophen-2-yl)-2,6-di(1H-imidazol-1-yl)pyridine (3)*.** To a solution of **2** (0.200 g, 0.689 mmol) in toluene (5 mL) was added a solution of 5-hexylthiophene boronic acid pinacolester (0.223 g, 0.758 mmol) and K_2CO_3 (0.285 g, 2.07 mmol) in methanol (5 mL). The mixture was degassed with Argon for 20 min then $PdCl_2$(dppf) (0.050 g, 0.069 mmol) was added, and the solution was refluxed at 80 °C for 8 h. After completion of reaction, the mixture was filtered through celite powder and washed with dichloromethane. After evaporation, the residue was purified by column chromatography over silica gel using 2-4% methanol in dichloromethane as the eluent to give the product as white solid (0.222 g, 85 % yield). ^{1}H NMR (400 MHz, $CDCl_3$) δ ppm: 8.39 (s, 2H), 7.68 (s, 2H), 7.46 (d, *J*= 3.72 Hz, 1H), 7.34 (s, 2H), 7.24 (s, 2H), 6.88 (d, *J*= 3.66 Hz, 1H), 2.88 (t, *J*= 7.58 Hz, 2H), 1.77-1.69 (m, 2H), 1.44-1.31 (m, 6H), 0.90 (t, *J*= 6.98 Hz, 3H) (**Figure A4.28**). ^{13}C NMR (100 MHz, $CDCl_3$) δ ppm: 150.6, 149.0, 148.1, 136.4, 135.1, 131.1, 126.9, 126.0, 116.2, 105.4, 31.5, 31.4, 30.4, 28.7, 22.5, 14.0 (**Figure A4.29**). ESI-HRMS calcd for $C_{21}H_{24}N_5S$ m/z = 378.1747. Found: 378.1780.

4-(2,4-difluorophenyl)-2,6-di(1H-imidazol-1-yl)pyridine (4). To a solution of **1** (0.3 g, 1.03 mmol) in toluene (5 mL) was added a solution of 2,4-difluorophenyl boronic acid (0.196 g, 1.24 mmol) and K_2CO_3 (0.429 g, 3.10 mmol) in methanol (5 mL). The mixture was degassed with Argon for 20 min then $PdCl_2$(dppf) (0.076 g, 0.103 mmol) was added, and the solution was refluxed at 80 °C for 8 h. After completion of reaction, the reaction mixture was filtered through celite powder and washed with DCM. After evaporation of solvents, the residue was purified by column chromatography over silica gel using 2-4% methanol in dichloromethane as the eluent to give the product as grey solid (0.27 g, 81% yield). ^{1}H NMR (400 MHz, $CDCl_3$) δ ppm: 8.42 (s, 2H), 7.70 (s, 2H), 7.60-7.52 (m, 1H), 7.39 (s, 2H), 7.26 (s, 2H), 7.11-7.01 (m, 2H) (**Figure A4.30**). ^{13}C NMR (100 MHz, $CDCl_3$) δ ppm: 165.3, 165.2, 162.8, 162.6, 161.3, 161.2, 158.8, 152.7, 149.2, 148.8, 135.2, 131.6, 131.3, 131.3,

131.1, 131.1, 131.05, 131.0, 128.3, 128.2, 121.3, 121.3, 121.2, 121.2, 116.2, 112.8, 112.8, 112.6, 112.6, 109.6, 109.5, 105.6, 105.3, 105.0, 74.0, 73.9, 73.5, 73.4 (**Figure A4.31**). ^{19}F NMR (400 MHz, $CDCl_3$) δ ppm: -105.79 (q, 1F), -111.55 (qt, 1F) (**Figure A4.32**). ESI-HRMS calcd for $C_{17}H_{11}F_2N_5$ m/z = 324.1055. Found: 324.1073.

4-(2,4-dimethoxyphenyl)-2,6-di(1H-imidazol-1-yl)pyridine (5). To a solution of 1 (see ref) (0.13 g, 0.448 mmol) in toluene (5 mL) was added a solution of 2,4-dimethoxyphenyl boronicacid (0.09 g, 0.492 mmol) and K_2CO_3 (0.186 g, 1.34 mmol) in methanol (5 mL). The mixture was degassed with Argon for 20 min then $PdCl_2$(dppf) (0.033 g, 0.045 mmol) was added, and the solution was refluxed at 80 °C for 8 h. After completion of reaction, the reaction mixture was filtered through celite powder and washed with DCM. After evaporation of solvents, the residue was purified by column chromatography over silica gel using 2-4% methanol in dichloromethane as the eluent to give the product as grey solid (0.117 g, 75% yield). ^{1}H NMR (400 MHz, $CDCl_3$) δ ppm: 8.41 (bs, 2H), 7.71 (bs, 2H), 7.44 (s, 2H), 7.37 (d, *J* = 8.41 Hz, 1H), 7.25 (m, 2H), 6.66-6.61 (m, 2H), 3.89 (s, 3H), 3.87 (s, 3H) (**Figure A4.33**). ^{13}C NMR (100 MHz, $CDCl_3$) δ ppm: 162.4, 157.8, 152.8, 148.4, 131.6, 131,3, 131.2, 130.1, 128.3, 128.2, 118.8, 110.3, 105.5, 99.2, 55.7, 55.6 (**Figure A4.34**). ESI-HRMS calcd for $C_{19}H_{18}N_5O_2$ m/z = 348.1455. Found: 348.1482.

2,6-di(1H-imidazol-1-yl)-4-(octyloxy)pyridine (8). A 50 mL two-neck flask was charged with imidazole (0.08 g, 1.18 mmol) and KOH (0.066 g, 1.18 mmol) flakes and heated at 250 °C under high vacuum and cooled to ambient temperature (1 h) gave potassium salt of imidazole. Then compound 6 was added (0.2 g, 0.548 mmol) in dimethylformamide (6 mL) by vigorous stirring under Argon atmosphere at 70 °C for 18 h. The mixture was poured into cold water and extracted into ethyl acetate (3x30 mL) followed by brine solution washing (20 mL). The organic fractions were collected, dried over $MgSO_4$, and then concentrated to dryness. The crude was further purified on silica-gel column chromatography using 2-5% methanol in dichloromethane to afford the desired compound (0.105 g, 56% yield). ^{1}H NMR (400 MHz, $CDCl_3$) δ ppm: 8.35 (s, 2H), 7.61 (s, 2H), 7.20 (s, 2H), 6.75 (s, 2H), 4.14 (t, *J*= 6.47 Hz, 2H), 1.86 (q, 2H), 1.49 (q, 2H), 1.39-1.29 (m, 8H), 0.88 (t, *J*= 6.88 Hz, 3H) (**Figure A4.35**). ^{13}C NMR (100 MHz, $CDCl_3$) δ ppm: 169.66, 149.62, 135.17, 130.80, 116.27, 96.58, 69.40, 31.74, 29.21, 29.15, 28.78, 25.85, 22.62, 14.06 (**Figure A4.36**). ESI-HRMS calcd for $C_{19}H_{26}N_5O$ m/z = 340.2132. Found: 340.2186.

2,6-di(1H-imidazol-1-yl)-N,N-dimethylpyridin-4-amine (9).[259] In a clean and dry 50 mL two-neck flask charged with imidazole (0.325 g, 4.77 mmol) were added KOH (0.268 g, 4.77 mmol) flakes. Heating to 250 °C under high vacuum and cooling to ambient temperature gave the potassium imidazolate. Then 7 (0.250 g, 6.13 mmol) was added in dimethylformamide (8 mL) with vigorous stirring under Argon atmosphere at 70 °C for 18 h. The mixture was poured into cold water and the precipitate that formed was filtered and dried to isolate desired compound (95% yield, 0.382 g) and used for next step without purification. ^{1}H NMR (400 MHz, DMSO-d_6) δ ppm: 8.64 (s, 2H), 8.06 (s, 2H), 7.08 (s, 2H), 6.82 (s, 2H), 3.11 (s, 6H) (**Figure A4.37**).

Ligand L$_1$. Compound **2** (0.09 g, 0.273 mmol) was charged in a 10 mL round bottomed flask and dissolved in 1 mL of DMF. Then added methyl iodide (0.068 mL, 1.09 mmol) and heated the mixture at 130 °C for 1 h. Desired compound was precipitated upon addition of diethyl ether. Solid was

collected by vacuum filtration and washed thrice with diethyl ether and dried under vacuum. Then the solid was dissolved in minimum amount of methanol (ca. 2 mL) and added saturated NH_4PF_6 solution and stirred until the product precipitated. Ligand **L_1** was collected by vacuum filtration and washed 3 times with water and then diethyl ether and dried under vacuum (0.165 g, 93% yield). ^{1}H NMR (400 MHz, CD_3CN) δ ppm: 10.00 (s, 2H), 8.18 (s, 2H), 7.77 (s, 2H), 7.60 (s, 2H), 7.06 (s, 2H), 4.05 (s, 6H), 2.34 (s, 3H), 2.08 (s, 6H) (**Figure A4.38**). ^{13}C NMR (100 MHz, CD_3CN) δ ppm: 159.4, 146.4, 139.7, 136.3, 135.6, 134.3, 12, 125.7, 119.9, 116.3, 37.3, 20.7, 20.2 (**Figure A4.39**). ESI-HRMS calcd for $C_{22}H_{25}N_5$ m/z = 179.6049. Found: 179.6131 [M-2PF_6].

Ligand L_2.It was synthesized according to the procedure as described for above synthesis of **L_1** from compound **3** (0.140 g, 0.371 mmol) with 85% yield (0.220 g). ^{1}H NMR (400 MHz, CD_3CN) δ ppm: 9.49 (s, 2H), 8.24 (s, 2H), 7.94 (s, 2H), 7.84 (d, *J*= 3.75 Hz,1H), 7.62 (s, 2H), 7.05 (d, *J*= 3.71 Hz, 1H), 4.01 (s, 6H), 2.95 (t, *J*= 7.57 Hz, 2H), 1.74 (q, 2H), 1.43-1.32 (m, 6H), 0.90 (t, *J*= 6.82 Hz, 3H) (**Figure A4.40**). ^{13}C NMR (100 MHz, CD_3CN) δ ppm: 153.6, 150.5, 146.8, 136.0, 135.7, 130.5, 127.6, 125.7, 120.1, 110.3, 37.34, 31.8, 31.8, 30.5, 29.0, 22.9, 13.93 (**Figure A4.41**). ESI-HRMS calcd for $C_{23}H_{29}N_5S$ m/z = 203.6066. Found: 203.6138 [M-2PF_6].

Ligand L_3. It was synthesized according to the procedure as described for above synthesis of **L_1** from compound **4** (0.15 g, 0.464 mmol) with 88% yield (0.265 g). ^{1}H NMR (400 MHz, CD_3CN) δ ppm: 9.54 (s, 2H), 8.23 (s, 2H), 8.07 (s, 2H), 7.86-7.80 (m, 1H), 7.63 (s, 2H), 7.29-7.27 (m, 2H) (**Figure A4.42**). ^{13}C NMR (100 MHz, CD_3CN) δ ppm: 166.4, 166.3, 163.9, 163.8, 162.0, 161.9, 159.5, 159.4, 151.8, 146.5, 136.1, 133.1, 133.0, 132.95, 132.9, 125.8, 120.8, 120.7, 120.7, 120.6, 120.1, 115.0, 115.05, 113.6, 113.6, 113.4, 113.3, 106.0, 105.7, 105.5, 37.4 (**Figure A4.43**). ^{19}F NMR (400 MHz, CD_3CN) δ ppm: -71.86 (PF6), -73.73 (PF6), -106.79 (F), -112.65 (F) (**Figure A4.44**). ESI-HRMS calcd for $C_{19}H_{17}F_2N_5$ m/z = 176.5721. Found: 176.5753 [M-2PF_6].

Ligand L_4. It was synthesized according to the procedure as described for above synthesis of **L_1** from compound **5** (0.08 g, 0.230 mmol) with 91% yield (0.140 g). ^{1}H NMR (400 MHz, CD_3CN) δ ppm: 9.70 (bs, 2H), 8.24 (t, *J*= 1.85 Hz, 2H), 8.13 (s, 2H), 7.66-7.63 (m, 3H), 6.80-6.78 (m, 2H), 4.06 (s, 6H), 3.96 (s, 3H), 3.93 (s, 3H) (**Figure A4.45**). ^{13}C NMR (100 MHz, CD_3CN) δ ppm: 163.3, 158.5, 154.5, 145.7, 136.7, 132.3, 125.4, 119.7, 117.4, 114.1, 106.7, 99.4 (**Figure A4.46**). ESI-HRMS calcd for $C_{21}H_{23}N_5O_2$ m/z = 188.5920. Found: 188.5999 (M-2PF_6).

Ligand L_5. It was synthesized according to the procedure as described for above synthesis of **L_1** from compound **8** (0.08 g, 0.235 mmol) with 90% yield (0.140 g). ^{1}H NMR (400 MHz, CD_3CN) δ ppm: 9.40 (s, 2H), 8.16 (t, *J*= 1.90 Hz, 2H), 7.62 (t, *J*= 1.85 Hz, 2H), 7.38 (s, 2H), 4.33 (t, *J*= 6.63 Hz, 2H), 4.01 (s, 6H), 1.90 (q, 2H), 1.52 (q, 2H), 1.44-1.34 (m, 8H), 0.93 (t, *J*= 6.95 Hz, 3H) (**Figure A4.47**). ^{13}C NMR (100 MHz, CD_3CN) δ ppm: 171.7, 147.5, 135.9, 125.7, 120.0, 102.0, 71.5, 37.3, 32.1, 29.5, 29.5, 28.9, 26.0, 23.0, 14.0 (**Figure A4.48**). ESI-HRMS calcd for $C_{21}H_{31}N_5O$ m/z = 184.6259. Found: 184.6259 (M-2PF_6).

Ligand L_6. It was synthesized according to the procedure as described for above synthesis of **L_1** from compound **9** (0.08 g, 0.314 mmol) with 97% yield (0.175 g). ^{1}H NMR (400 MHz, CD_3CN) δ ppm: 9.46 (s, 2H), 8.17 (t, *J*= 1.92 Hz, 2H), 7.58 (t, *J*= 1.88 Hz, 2H), 6.92 (s, 2H), 4.00 (s, 6H), 3.23 (s,

6H) (**Figure A4.49**). ^{13}C NMR (100 MHz, CD_3CN) δ ppm: 159.56, 146.88, 135.75, 125.26, 119.85, 96.40, 40.29, 37.11 (**Figure A4.50**). ESI-HRMS calcd for $C_{15}H_{19}N_6$ m/z = 283.1666. Found: 283.1664 [M-2PF6].

ARM14. To a solution of $\mathbf{L_1}$ (0.102 g, 0.157 mmol) and $\mathbf{L_7}$ (0.09 g, 0.157 mmol) in 2 mL of anhydrous DMF was added $FeCl_2$ (0.020 g, 0.157 mmol) and the mixture was degassed with Argon for 10 min. Then added *t*-BuOK (0.088 g, 0.789 mmol) to the above mixture and stirred at room temperature for 20 min. A saturated solution of NH_4PF_6 was added (10 ml), followed by 2 M HNO_3 until the solution becomes acidic (pH ≈ 2) and the precipitate was collected by filtration. Then the crude was further purified on silica gel column chromatography using acetone/H_2O/KNO_3(sat) = 10: 3: 0.5 mixture. The reddish fraction was collected and after the evaporation of acetone, the left solution was treated with a saturated solution of NH_4PF_6 followed by 2 M HNO_3 until the solution becomes acidic (pH ≈ 2). Affording the precipitation of the desired complex, it was then filtered, washed with distilled water, and dried under vacuum. The isolated **ARM14** was obtained as a reddish color (0.021 g, 13% yield). ^{1}H NMR (400 MHz, CD_3CN) δ ppm: 8.31 (s, 2H), 8.18 (d, *J*= 2.17 Hz, 2H), 7.94(d, *J*= 2.17 Hz, 2H), 7.62 (s, 2H), 7.10 (s, 2H), 7.05 (d, *J*= 2.14 Hz, 2H), 6.97 (d, *J*= 2.14 Hz, 2H), 2.65 (s, 6H), 2.49 (s, 6H), 2.36 (s, 3H), 2.12 (s, 6H) (**Figure A4.51**). ^{13}C NMR (100 MHz, CD_3CN) δ ppm: 200.3, 200.2, 165.5, 155.2, 154.2, 153.5, 139.3, 135.8, 135.7, 129.1, 127.3, 127.1, 117.3, 117.2, 107.6, 105.2, 35.2, 35.0, 20.8, 20.1 (**Figure A4.52**). ESI-HRMS calcd for $C_{36}H_{36}FeN_{10}O_2$ m/z = 348.1181. Found: 348.1194 [M-2PF_6].

ARM15. The procedure as described for **ARM14** was repeated from $\mathbf{L_2}$ (0.122 g, 0.175 mmol) and $\mathbf{L_7}$ (0.101 g, 0.175 mmol) leading to **ARM15** in 14 % yield (0.025 g). ^{1}H NMR (400 MHz, CD_3CN) δ ppm: 8.27 (s, 2H), 8.15 (d, *J*= 2.21 Hz, 2H), 8.09 (d, *J*= 2.19 Hz, 2H), 7.95 (s, 2H), 7.83 (d, *J*= 3.73 Hz, 1H), 7.04 (d, *J*= 3.73 Hz, 1H), 7.03 (d, *J*= 2.20 Hz, 2H), 6.99 (d, *J*= 2.18 Hz, 2H), 2.96 (t, *J*= 7.46 Hz, 2H), 2.62 (s, 6H), 2.47 (s, 6H), 1.76 (q, 2H), 146-1.33 (m, 6H), 0.92 (t, *J*= 7.11 Hz, 3H) (**Figure A4.53**). ^{13}C NMR (100 MHz, CD_3CN) δ ppm: 200.1, 200.1, 165.0, 155.3, 154.1, 151.7, 145.4, 139.3, 137.8, 129.0, 127.3, 127.2, 117.2, 117.1, 105.0, 101.9, 35.3, 35.2, 32.0, 31.8, 30.5, 29.0, 22.9, 13.9 (**Figure A4.54**). ESI-HRMS calcd for $C_{37}H_{40}FeN_{10}O_2S$ m/z = 372.1197. Found: 372.1238 [M-2PF_6].

ARM16. The procedure as described for **ARM14** was repeated from $\mathbf{L_3}$ (0.112 g, 0.174 mmol) and $\mathbf{L_7}$ (0.100 g, 0.174 mmol) leading to ARM16 in 14 % yield (0.024 g). ^{1}H NMR (400 MHz, CD_3CN) δ ppm: 8.28 (s, 2H), 8.16 (d, *J*= 2.19 Hz, 2H), 8.06 (d, *J*= 2.16 Hz, 2H), 7.98 (s, 2H), 7.96-7.90 (m, 1H), 7.32-7.25 (m, 2H), 7.03 (d, *J*= 2.15 Hz, 2H), 7.00 (d, *J*= 2.17 Hz, 2H), 2.59 (s, 6H), 2.49 (s, 6H) (**Figure A4.55**). ^{13}C NMR (100 MHz, CD_3CN) δ ppm: 200.0, 199.8, 164.9, 155.2, 154.2, 145.9, 139.6, 133.1, 133.1, 133.0, 132.3, 127.3, 122.3, 122.2, 122.15, 122.1, 117.3, 117.1, 113.4, 113.3, 113.2, 113.1, 106.0, 105.9, 105.9, 105.6, 105.1, 35.2, 35.2 (**Figure A4.56**). ^{19}F NMR (400 MHz, CD_3CN) δ ppm: -71.98 (PF6), -73.85 (PF6), -108.12 (q, 1F), -112.06 (qt, 1F) (**Figure A4.57**). ESI-HRMS calcd for $C_{33}H_{28}F_2FeN_{10}O_2$ m/z = 345.0852. Found: 345.0942 [M-2PF_6].

ARM122. The procedure as described for **ARM14** was repeated from $\mathbf{L_6}$ (0.091 g, 0.157 mmol) and $\mathbf{L_7}$ (0.091 g, 0.157 mmol) leading to **ARM122** in 15 % yield (0.020 g). ^{1}H NMR (400 MHz, CD_3CN) δ ppm: 8.25 (s, 2H), 8.17 (d, *J*= 2.14 Hz, 2H), 7.96 (d, *J*= 2.13 Hz, 2H), 7.07 (d, *J*= 2.14 Hz, 2H), 7.04 (s, 2H), 6.94 (d, *J*= 2.13 Hz, 2H), 3.30 (s, 6H), 2.73 (s, 6H), 2.43 (s, 6H) (**Figure A4.58**). ^{13}C

NMR (100 MHz, CD_3CN) δ ppm: 201.0, 165.3, 158.7, 155.9, 152.9, 137.7, 127.0, 126.6, 117.0, 116.6, 104.4, 90.7, 40.4, 35.2, 35.1 (**Figure A4.59**). ESI-HRMS calcd for $C_{29}H_{31}FeN_{11}O_2$ m/z = 310.6000. Found: 310.6079 [M-2PF_6].

ARM130. The procedure as described for **ARM14** was repeated from **L4** (0.100 g, 0.149 mmol) and **L7** (0.086 g, 0.149 mmol) leading to **ARM130** in 15 % yield (0.022 g). ^{1}H NMR (400 MHz, CD_3CN) δ ppm: 8.30 (s, 2H), 8.19 (d, *J*= 2.14 Hz, 2H), 8.06-8.05 (m, 4H), 7.74 (d, *J*= 9.21 Hz, 1H), 7.06 (d, *J*= 2.08 Hz, 2H), 7.00 (d, *J*= 2.08 Hz, 2H), 6.83-6.81 (m, 2H), 3.99 (s, 3H), 3.94 (s, 3H), 2.64 (s, 6H), 2.49 (s, 6H) (**Figure A4.60**). ^{13}C NMR (100 MHz, CD_3CN) δ ppm: 200.3, 199.9, 164.9, 163.6, 159.1, 155.4, 153.6, 150.5, 139.0, 132.5, 127.2, 127.0, 118.9, 117.2, 117.0, 106.7, 106.3, 104.9, 99.7, 56.4, 56.0, 35.2, 35.1 (**Figure A4.61**). ESI-HRMS calcd for $C_{35}H_{34}FeN_{10}O_4$ m/z = 357.1051. Found: 357.1076 (M-2PF_6).

ARM132. The procedure as described for **ARM14** was repeated from **L5** (0.084 g, 0.127 mmol) and **L7** (0.073 g, 0.127 mmol) leading to **ARM132** in 16 % yield (0.020 g). ^{1}H NMR (400 MHz, CD_3CN) δ ppm: 8.26 (s, 2H), 8.17 (d, *J*= 2.11 Hz, 2H), 7.96 (d, *J*= 2.11 Hz, 2H), 7.39 (s, 2H), 7.06 (d, *J*= 2.10 Hz, 2H), 6.98 (d, *J*= 2.08 Hz, 2H), 4.36 (t, *J*= 6.57 Hz, 2H), 2.66 (s, 6H), 2.46 (s, 6H), 1.94-1.91 (m, 2H), 1.57 (q, 2H), 1.46-1.36 (m, 8H), 0.94 (t, *J*= 6.85 Hz, 3H) (**Figure A4.62**). ^{13}C NMR (100 MHz, CD_3CN, δ ppm): 201.11, 200.26, 170.04, 164.94, 155.65, 154.12, 138.37, 127.13, 117.15, 116.91, 104.72, 94.70, 71.17, 35.19, 32.15, 29.54, 29.07, 26.14, 22.96, 13.97 (**Figure A4.63**). ESI-HRMS calcd for $C_{35}H_{42}FeN_{10}O_3$ m/z = 353.1390. Found: 353.1438 [M-2PF_6].

4.2.4c DSSC fabrication

The photoanode were prepared according to the indications described in the previous Chapters. The procedure was repeated up to three times to obtain a thicker film. As a final treatment the titania scattering layer could be obtained by blade casting the reflective paste on the top of the transparent film, followed by heating according to the same temperature program described for sintering the transparent layers. The catalytic counter electrodes were obtained by electrodepositing PEDOT on FTO according to the procedure reported in the previous chapters.
Cells were assembled in an open configuration by confining the electrolyte with the aid of a thermoplastic Surlyn 25 spacer, the FTO slides were kept together with a couple of clamps. The redox electrolyte (*el3*) was composed as follows: 0.1 M LiI, 0.6 M PMII, 0.1 M I_2, 0.1 MgI_2, 0.1 M GuNCS, 0.1 M TBAI in acetonitrile (see **Chapter 4b**).

4.2.5c Computational details

The computational analysis was realized by Dr. Mariachiara Pastore's group of the University of Lorraine, in the following way:
The opto-electronic properties of the dyes by means of Time-Dependent DFT calculations have been investigated employing the same procedure as established in the previous chapter. More in detail, the modified B3LYP* functional (with a 15% of Hartree-Fock exchange-correlation fraction) and 6-311G(d) basis set due to its well-known success in reproducing the opto-electronic properties of Fe(II) complexes were used.[88, 243-245] The solvent environment (methanol in our case) was taking into account implicitly by employing the Conductive Polarizable Continuum Model[246] The ground state

geometries of the dyes were fully optimized, prior to the study of the 50 lowest energy vertical transitions, which was been done by TD-DFT. A half-width at full-length of 0.17 eV was employed to build the static simulated TD-DFT spectra. All set of calculations were performed within the Gaussian16 suite of programs.[212]

Regarding the electronic properties of **ARM130**/TiO_2 system, the methodology employed in the previous study (see **Chapter 4b**) was used. The relaxed GS structure of the dye was anchored to a $(TiO_2)_{82}$ cluster in a bidentate fashion by transferring the carboxylic proton to one oxygen of the surface. This cluster model was built by exposure of the bulk anatase to the (101) surface, yielding to a 2x2 nm surface model which has been demonstrated especially suitable to reproduce the electronic structure of Fe complex dye/TiO_2 system. Afterwards, the optimization of the **ARM130**/TiO_2 geometries by means of DFT calculations was performed by employing the Perdew–Burke-Ernzerhof (PBE) functional,[260] COnductor-like Screening MOde model for solvents,[250] and D3 Grimme's dispersion correction;[251] as they have been developed in the ADF package.[252] DZP/TZP basis sets were employed here for C, N, H, S, O/ Fe, Ti atoms, respectively. Finally, the electronic structure of the **ARM130**/TiO_2 system was estimated by using the same functional, basis set solvent model as the one described above for the isolated dyes. The diabatic analysis which gave the access to the electron injection properties was carried out by following the method developed by Thoss and co-workers.[253] In this scheme, the charge injection rates k_{inj} are directly proportional to the sum over the diabatic couplings, estimated here by resorting to a Fermi golden rule framework, and they have been calculated by applying the following formula:

$$k_{inj} = \frac{2\pi}{\hbar}\sum_k |V_{dk}|^2 \rho(\varepsilon_k) \qquad \textbf{eq.4.8}$$

Where $|V_{dk}|^2$ is the square of the coupling elements between the k TiO_2 acceptor states of interest, and d states of the dye donor, $\rho(\varepsilon_k)$ is the semiconductor partial density of states, and their product $|V_{dk}|^2\rho(\varepsilon_k)$ corresponds to the so-called probability distribution $\Gamma(\varepsilon_k)$. The diabatic states for Donor (dye) and Acceptor (TiO_2) manifolds were calculated by localizing the MOs of the entire complex into the Donor and Acceptor moieties. By doing so, one ends up in a Fock matrix where the diagonal elements represent the energies for the localized states, whereas the off-diagonal terms contain the coupling values V_{kd}. Finally, the electron injection time constants were extracted by following this formula:

$$\tau(\text{fs}) = \frac{658}{\Gamma(\text{meV})} \qquad \textbf{eq. 4.9}$$

4.3c Results and Discussions

4.3.1c Synthesis of ligand precursors and iron(II) complexes

As discussed above and in the first sections, the preparation of the Iron complexes for photovoltaic applications, were synthesized by Dr. Gros of the University of Lorraine.

The pyridyl-NHC ligands to be coordinated to iron required the prior preparation of the corresponding imidazolium salts precursors **L1**–**L6** (scheme in **Figure 4.26**). **L1**, **L2**, **L3** and **L4** were obtained in good yields respectively by quaternization of pyridylimidazoles **2**, **3**, **4** and **5** resulting from a Suzuki coupling of the bromo derivative **1** (**see Chapter 4b**) with the appropriate aryl boronic acids. **L5** and **L6** were obtained from amination of respectively dibromo and difluoropyridines **6**[261] and **7**[262] using potassium imidazolate at 70°C in DMF and final quaternization with methyl iodide. The target heteroleptic complexes were obtained using a one-pot synthesis by reacting $FeCl_2$ with an equimolar

mixture of the appropriate ligand **L1**–**L6** with **L7**,[6] bearing the carboxylic function, in the presence of t-BuOK as the base.

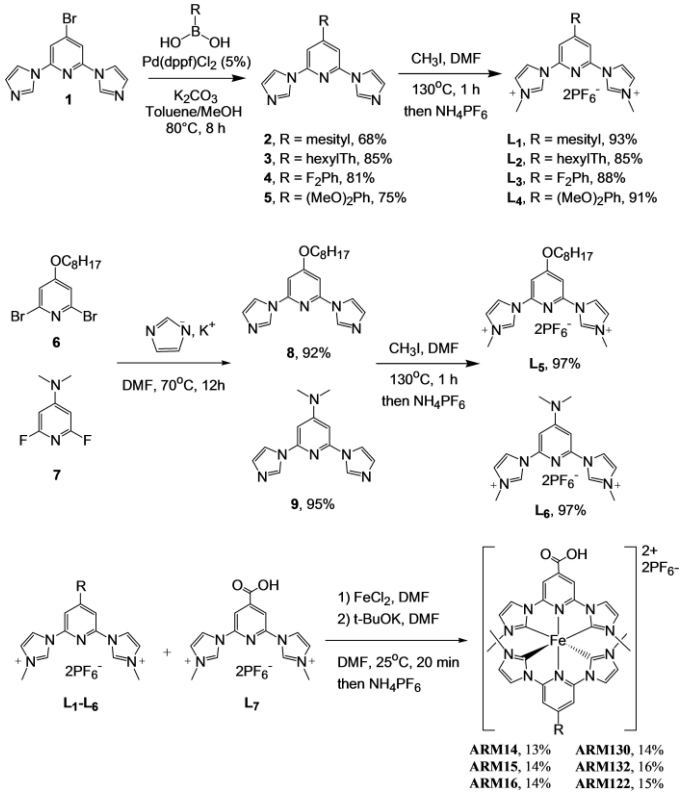

Figure 4.26: Steps involved in synthesis of the ligand precursors and complexes. From ref 257

4.3.2c Spectroscopic characterization

Figure 4.27 reports the absorption spectra of the Fe(II)NHC complexes in methanol and the calculated one (the data are summarized in **Table 4.6**). All the complexes exhibited three well defined bands, the transition at higher energy (250-350 nm) is assigned to π-π^* transition, while the two a lower energy, are relative to the Fe-carbene MLCT (340 - 440 nm) and Fe-Pyridine MLCT transitions (410 - 600 nm). The lowest energy region of the four aryl tethered complexes **ARM14**, **ARM15**, **ARM16** and **ARM130**, are characterized by a broad absorption ranging from 410 to 600 nm while in the case of **ARM122** and **ARM132** (N,N-dimethylamino donor and O-Octyl on the pyridine respectively) the absorption is narrower ranging between 450 to 600 nm. Among the series, **ARM15**, which is characterized by the thiophene moieties, exhibited the most red shifted and intense molar extinction coefficients (501 nm, 25228 $M^{-1}cm^{-1}$) due to the π-conjugation. The strong donating capability of the N,N-dimethylamino and O-Octyl groups in **ARM122** and **ARM132**, led to two MLCT bands of similar intensity, with a lower ε of 12447 $M^{-1}cm^{-1}$ and 11459 $M^{-1}cm^{-1}$ respectively.

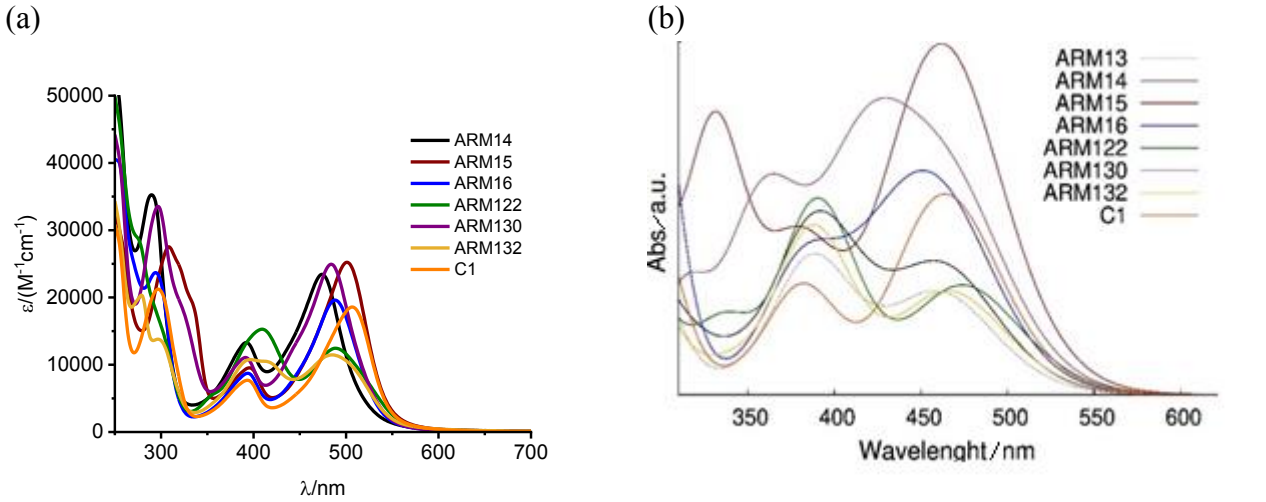

Figure 4.27: Absorption spectra for the Fe(II)NHC series in (a) methanolic solutions and (b) the computed ones. From ref 257

In this context, TD-DFT calculations were performed to shed light on the main characteristics of the lowest energy MLCT absorption bands which have been discussed above. Although a systematic slight blue-shift of ca. 0.2 eV is obtained, as reported in the previous section, the main trends in the absorption features are consistently reproduced by the calculations (**Figure 4.27b** and **Table A4.4**). In particular, **ARM14**, **ARM15**, **ARM16** and **ARM130** displayed larger MCLT absorption band intensities (oscillator strengths larger than 0.2) with respect to **ARM122** and **ARM-132**, with **ARM15** being the one showing the most intense absorption. To analyze the nature of the HOMO-2→LUMO transition, composing the lowest energy MLCT band, a Natural Transition Orbital (NTO) analysis has carried out,[263] which provides insights on the topology of the excited state (see **Figure A4.64**). Notably, all the dyes showed an identical delocalization, for both holes and electrons, to the one displayed by the unsubstituted **ARM13** reference dye, thus evidencing the negligible role played by the chemical substitution in the nature of the MLCT band. For a more quantitative estimation of the hole/electron localization on the different molecule moieties, the transition density matrix by using the TheoDORE package was analysed.[247] The results are collected in **Table A4.5**, where the values calculated for the reference homoleptic (**C1**) and unsubstituted heteroleptic (**ARM13**) are also shown. As already evidenced by the NTOs, globally the presence of the substituent (SG) on the non-anchored ligand (NHC_{top}) does not significantly modify the charge transfer properties. Overall, upon excitation, about 72–75% of the hole is localized on the Iron center and 12–18% on the ligand bearing the carboxylic group (NHC_{bot}), while less than 1% is on the NHC_{top}. Concerning the electron, the largest fraction is still localized on the NHC_{bot} (60–70 %), with a small fraction (14-16%) reaching the anchoring group. The substituent group is generally not involved in the transition. Within the Fe(II)NHC series, **ARM15** presents the less efficient and unidirectional CT: a small fraction of the electron (ca. 13%) is indeed localized on the non-anchored NHC_{bot} ligand, and a reduced amount of charge reaches the anchoring group, thus the TiO_2 substrate. Based on these results, it may therefore expect a less efficient TiO_2 sensitization by **ARM15** despite its intense and red-shifted absorption (**Figure 4.27a**).

Table 4.6: Experimental absorption maxima in MeOH and on TiO_2, calculated vertical excitation energies with relative oscillator strengths and nature of the main single particle excitations contributing to these excited states (percentage for each transition)

	Experimental		Calculated	
Dye	**λ_{max}/nm $\varepsilon*10^4$ $M^{-1}cm^{-1}$**	**λ_{max} /nm (TiO_2)**	**E_{exc} /nm (oscillator strength)**	**Transition %**
ARM13	507 (1.85)	478	461 (0.15)	H-2→L (63.4%)
ARM14	474 (2.35)	500	464 (0.20)	H-2→L (63.8%)
ARM15	501 (2.52)	500	470 (0.43)	H-2→L (60.6%)
ARM16	488 (1.96)	482	464 (0.27)	H-2→L (63.4%)
ARM122	489 (1.24)	490	475 (0.18)	H-2→L (63.5%)
ARM130	484 (2.49)	486	469 (0.30)	H-2→L (63.4%)
ARM132	485 (1.14)	498	467 (0.16)	H-2→L (63.5%)

4.3.3c Spectroscopic and electrochemical properties on thin films

We have selected a first set of dye, consisting of **ARM16**, **ARM122**, **ARM130** and the standard **C1**, in order to optimize the photon to electron conversion by preparing ca. 16μm transparent TiO_2 films. **Figure 4.28** displays the absorption spectra of the dyed TiO_2 that are characterized by an intense MLCT band centered around 500 nm that harvests ≥ 99% of the incident light in correspondence of the λ_{max}. According to the following **eq. 4.10** it is possible to extrapolate the average surface loading Γ where, as already reported in the previous chapter, A and ε represent the absorbance and the molar extinction coefficient of each dye respectively.

$$\Gamma = \frac{A(\lambda)}{1000\varepsilon(\lambda)} \qquad \textbf{eq. 4.10}$$

In particular, a Γ of 0.114, 0.120, 0.102 and 0.114 μmol cm^{-2} for **ARM16**, **ARM122**, **ARM130** and **C1** was obtained. Despite the good absorbance at the MLCT maximum, the spectra of the dyed TiO_2 are relatively narrow, causing the harvesting fall off for $\lambda > 550$nm. To better harvest the visible light, we have prepared thicker films (three transparent layers for a total thickness around 20 μm and a scattering overlayer) that generally show a broadened main visible band, which extends the spectral sensitization to longer wavelengths. **ARM15** exhibits the broader absorption extended up to 650 nm (**Figure 4.28b**).

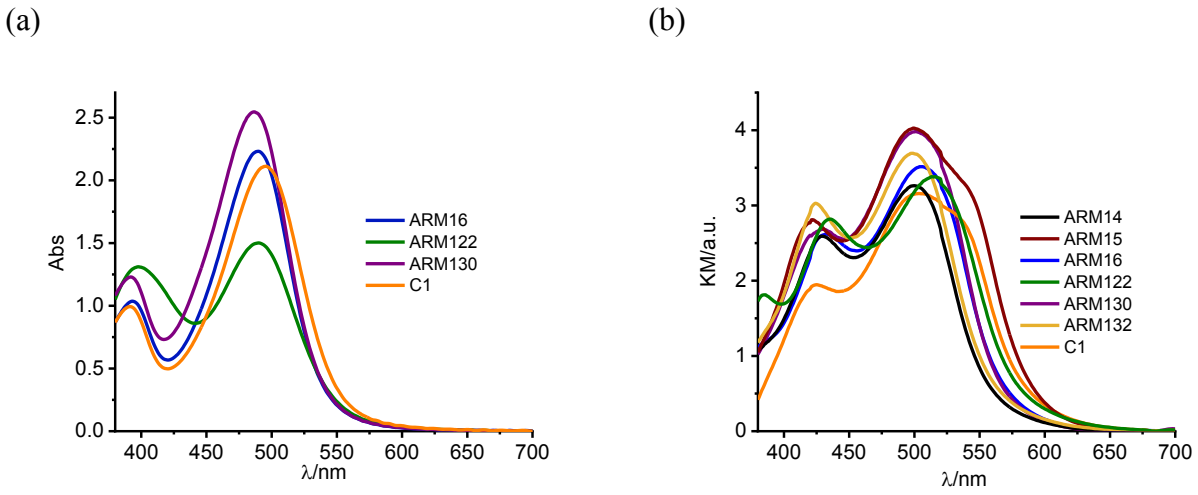

Figure 4.28: (a) Absorption spectra recorded for some selected Fe(II)NHC complexes loaded on 16 µm TiO_2 recorded against an identical undyed electrode as a reference. (b) Absorption spectra for the Fe(II)NHC sensitized TiO_2 recorded in diffuse reflectance mode (illumination was through the FTO back contact) and reported in KM units (16 µm transparent TiO_2 + scattering layer). From ref 257

The thermodynamic properties relevant for the Fe(II)NHC-based Dye Sensitized Solar Cells functioning were carried out by cyclic voltammetry of TiO_2 or ZrO_2 thin films in contact with 0.1 M $LiClO_4$/ACN (**Figure 4.29**) and are listened in **Table 4.7**. Zirconia substrate was employed as inert substrate[154, 225, 264] to extrapolate the reduction potentials of the dyes that are precluded on titania semiconductor for the conduction band reduction which occurs at lower potentials. All the species exhibited a quasi-reversible Fe(II)/(III) oxidation potential ($\Delta E \approx$ 80-100 mV), whose E_{ox} ranges from 0.5 V Vs SCE (**ARM122**) to ca. 0.7 V (**ARM14**). The extrapolated parameters are fully consistent with those observed on ZrO_2, with in some cases, a cathodic shift of ca. 50 mV. We observed a quite important role on the Fe(II)NHC energy of the substituent group in 4 position of the pyridine. We obtained the most positive potentials (from 0.70 to 0.69 V Vs SCE) in the case of the functionalized benzene or thiophene rings (**ARM14** > **ARM16** > **ARM15**), particularly when modified with electron accepting moieties. The introduction of donor groups such as -OR either as substituents of the benzene ring (**ARM130**, 0.64 V) or directly attached to the pyridine (**ARM132**, 0.65 V) led to a cathodic shift around 50 mV. The less positive E_{ox} was recorded in the case of **ARM122**, the Fe(II)NHC complex characterized by a stronger electron donor group (dimethylamine) directly bonded to the NHC ligand (0.40 V).

(a) (b)

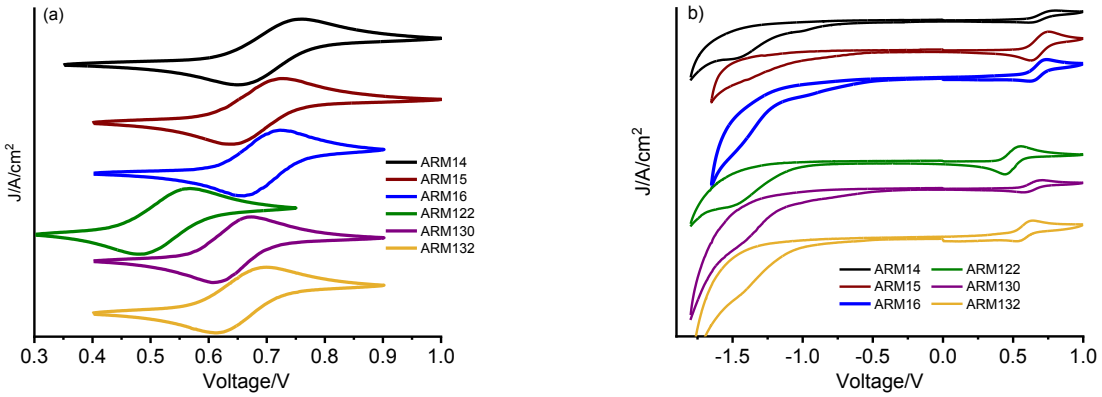

Figure 4.29: Cyclic voltammetries recorded for the Fe(II)NHC complexes on (a) TiO_2 (anodic scan) and on (b) ZrO_2 (full scan) in 0.1 M $LiClO_4$/ACN solution. From ref 257

From these results, it is possible to affirm a driving force for the regeneration process by the iodide/iodine redox couple, on the order of 150 - 300 meV. The Fe(II)NHC series exhibited an irreversible reduction wave centered around -1.5 V. The energy difference between the anodic and cathodic waves on ZrO_2, well agree with the onset of the absorption spectrum of the dye anchored on thin film (E^{00}) and indicates that the spectroscopic states are energetically related with the electrochemical levels, supporting the metal to ligand charge transfer nature of the main visible band of all the iron family. From the estimated excited state oxidation potential we evaluated the driving force for the charge injection ($\Delta G_{inj} = -e(|E_{ox}^*|-E_{FB})$, that in all the case is of at least 800 meV, using the commonly accepted TiO_2 flat band potential of -0.7 V in the presence lithium containing organic solvent.

Table 4.7: Electrochemical parameters for the Fe(II)NHC sensitized TiO_2 or ZrO_2

Dye	E_{Ox} (TiO_2)/V	E_{Ox} (ZrO_2)/V	E_{peak}Red (ZrO_2)/V	E_{ox}-E_{red} CV(ZrO_2)/V	E^{00} abs (TiO_2)/eV
ARM14	0.705	0.706	-1.55	2.25	2.09
ARM15	0.682	0.691	-1.45	2.14	2.09
ARM16	0.691	0.678	-1.49	2.17	2.11
ARM122	0.524	0.494	-1.55	2.04	2.05
ARM130	0.641	0.638	-1.51	2.15	2.10
ARM132	0.654	0.585	-1.48	2.06	2.04

4.3.4c Transient absorption spectroscopy

As already discussed in the previous chapters, when the sensitized films are in contact with small high-density cations such as Li^+ and Mg^{2+}, a bathochromic shift for the Stark Effect occurs for the absorption of these cations on the TiO_2 (**Figure 4.30a**). We employed transient absorption spectroscopy to investigate the regeneration and recombination dynamics. **Figure 4.30b** reports the transient difference spectra for all the Fe(II)NHC series which are characterized by similar features: a strong bleach around 500 nm mirrors the MLCT absorption in contact with the small high-density cations and it is consistent with the photoinduced formation of the charge separation state (Fe(III)/e^- (TiO_2)). The ground state bleaching is followed by a weak and featureless absorption band extending

in the 600 - 740 nm region, arising by a combination of cation absorption (LMCT) and from electrons photoinjected and trapped in the TiO_2, these features remain practically constant for hundreds of ms.

(a) (b)

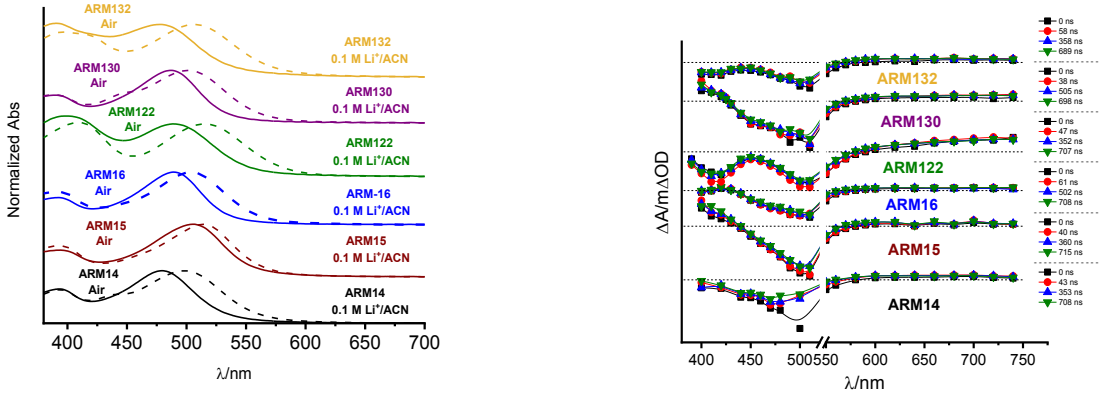

Figure 4.30: (a) Absorption spectra for the different Fe(II)NHC complexes recorded in air and in contact with 0.1 M Li^+/ACN. (b) Transient absorption spectra for the different complexes in contact with 0.1 M Li^+/ACN. Input impedance: 350 Ω. Laser power: 8 mJ/cm^2/pulse. From ref 257

To investigate the recombination dynamics and extrapolate a time constant (**Figure 4.31a**), we analyzed the 500 nm kinetics decreasing the laser power to 400 µJ/cm^2/pulse. The decays were obtained by joining traces recorded with 10 kΩ and 1 MΩ input impedance. For the inhomogeneity of the surface sites, the recombination showed a complex behavior that required to fit the faster part (ca. 50% of the total amplitude) with a power low function,[265] owing to bimolecular electron/hole recombination events occurring at the earliest times (see **eq. 4.11**)). The second part of the decay, was fitted with a stretched exponential function (see **eq. 4.12**))[191, 240] for the energy distribution of semiconductor/electrolyte states that lead to different recombination rate constants, generated by detrapping of electrons from localized surface states close to the conduction band edge:

$$\Delta A_{t<2ms} = A + bt^{-c} \qquad \textbf{eq. 4.11}$$

$$\Delta A_{t>2ms} = A' + b'e^{\left(-\frac{t}{\tau}\right)^d} \qquad \textbf{eq. 4.12}$$

where the d parameters in the **eq. 4.12** is close to 0.5 in all the cases, as reported in literature and in the previous section.[240] The new Fe(II)NHC family exhibits a longer lifetime than the standard **C1**, in the 100 – 200 ms range (**Table 4.8**). These differences are not significant considering the faster regeneration in the presence of the reduced form of the redox mediator (I^-) (electrolyte composition: 0.1 M LiI, 0.6 M PMII, 0.1MgI_2, 0.1 M GuNCS, 0.1 TBAI) that occurs within the time resolution of our spectrophotometer when amplified with a 10 kΩ impedance (base width 4 µs, FWHM 1.5 µs) (**Figure 4.31b**). Among the series, **ARM122** exhibited the slowest regeneration being complete on the 0.1 ms time scale, consistent with its lower driving force for iodide oxidation. In this latter case it was possible to extrapolate a regeneration time constant of the order of 30 µs. The recovery of the bleach is followed, in all the cases, by a long-lived Stark absorption,[191] arising from the electron accumulation in the semiconductor, no longer compensated by holes localized on the dye sensitizers. The time evolution of this spectroscopic feature is convolved with the instrumental response of our apparatus and sets an upper limit for the regeneration time constant (< 4 µs). This leads to regeneration efficiency η_{reg} close to the unit and can be written as follow in the **eq. 4.13**:

$$\eta_{reg} = \frac{k_{reg}}{k_{rec}+k_{reg}} \qquad \textbf{eq. 4.13}$$

where k_{reg} represents the pseudo first order rate constant for the regeneration of the oxidized dye in contact with the reduced form of the redox mediator and it is in the order of 10^6 s^{-1} for all the Fe(II)NHC complexes and K_{rec} represents the rate constant of the recombination process that is in the $10^2 – 10^3$ s^{-1} range so, it is possible to affirm to have $K_{reg} >> K_{rec}$ and η_{reg} close to 1.

(a) (b)

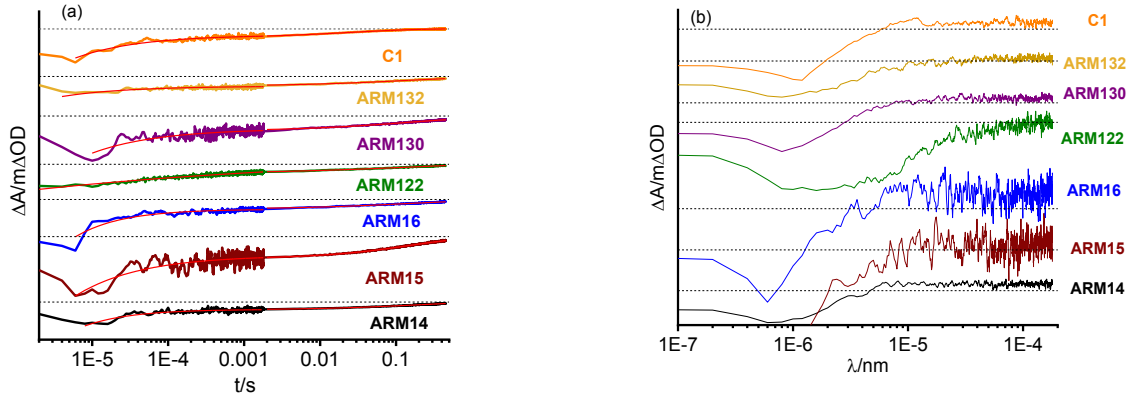

Figure 4.31: (a) Recombination kinetics recorded at 500 nm for the different complexes obtained by joining traces recorded with 10 KΩ and 1 MΩ input impedances. Laser power: 400 μJ/cm^2/pulse. Thin films were in contact with 0.1 M Li^+/ACN. (b) Regeneration kinetics recorded at 500 nm for the Fe(II)NHC complexes in contact with the reduced form of electrolyte (0.1 M LiI, 0.6 M PMII, 0.1MI_2, 0.1 M GuNCS, 0.1M TBAI). Input impedance: 10 KΩ. From ref 257

Table 4.8: Charge separated state lifetime on TiO_2

Dye	τ/ms (Stretched exponential)
ARM14	209
ARM15	191
ARM16	129
ARM122	129
ARM130	133
ARM132	129
C1	27

4.3.5c Photoelectrochemical characterization

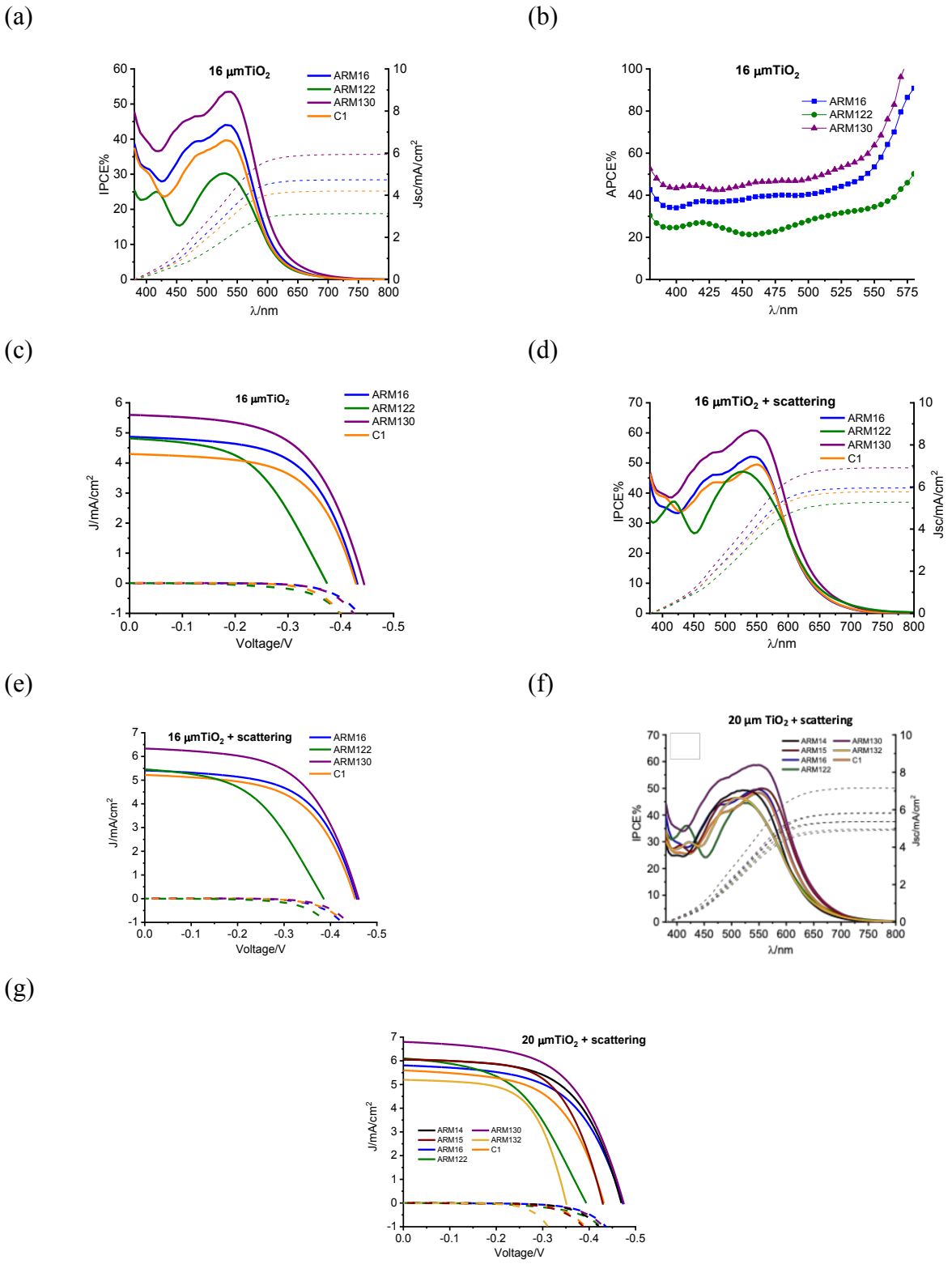

Figure 4.32: (a) IPCE, (b) APCE (by taking into account the red shift which occurs upon exposing the dyed films to a Li^+ containing electrolyte) and (c) J-V curves for the Fe(II)NHC complexes for the 16 µm transparent TiO_2 cells. (d) IPCE and (e) J-Vs for cells equipped with the 16 µm TiO_2 + top scattering overlayer and (f) IPCE, and (g) J-Vs for cells assembled in combination with ca. 20 µm TiO_2 + scattering layer. From ref 257

The photoelectrochemical performances of the new family in DSSCs were evaluated by employed the MgI_2/TBAI based electrolyte formulated in our previous work (0.1M Li, 0.6 PMII, 0.1M I_2, 0.1M

MgI_2, 0.1 M GuNCS, 0.1 M TBAI in acetonitrile) (**Chapter 4b**). The role of the small high-density cations was ascribed to increase the directionality of the MLCT states and increase the coupling between the dye and the semiconductor's conduction band, with consequent better electron injection. The role of the TBAI instead was attributable to decrease the cell resistance by increasing further iodide concentration without further lowering the TiO_2 flat band potential. As above discussed, we have initially selected three dye of our series (**ARM16**, **ARM122** and **ARM130**) and tested in combination with a 16 μm thick TiO_2, showing an Incident Photon to Current Conversion Efficiency (IPCE) ranging from 45% (**ARM122**) to 60% (**ARM130**) (**Figure 4.32a**). This latter complex displays the best combination of high IPCE and light harvesting leading to an integrated (J_{sc}) around 6 mA/cm^2 in good agreement with the short circuit photocurrent density recorded under AM1.5G conditions (**Figure 4.32c**). The higher photocurrent density recorded under monochromatic light could be due to some diffusional limitations when cells are exposed to the entire AM1.5G spectrum. Normalizing the IPCE for the Light Harvesting Efficiency terms, the resulting Absorbed Photon to Current conversion Efficiency is around 55 – 60% (**Figure 4.32b**). η_c represents the efficiency of electron collection at the counter electrode and it is related to the regeneration of the oxidized dye by the iodide that, as above described, it was demonstrated to be practically unitary so it is possible to conclude an injection quantum yield of ca. 50%. Until now, this latter parameter results to be the main limiting factor of Fe(II)-based solar cells. Under AM1.5G conditions, we recorded a Power Conversion Efficiencies of 1.43%, 1.24%, 1.10% and 0.91% for **ARM130**, **ARM16**, **C1** and **ARM122** respectively. A further improvement was obtained by adding a scattering top layer having the function to increase the optical path of photons in the nanostructured semiconductor, leading to a better harvesting at those longer wavelengths, which are poorly absorbed by the sensitizers. In these conditions the IPCE resulted broader with a higher integrated J_{sc} of 7 mA/cm^2 (**Figure 4.32d**). Under white light (**Figure 4.32e**), **ARM130** exhibited the best J_{sc} among the series of 6.33 mA/cm^2, a V_{oc} of 0.46 V and an overall efficiency of 1.65%. Owing to the good regeneration efficiency, which should result in negligible recombination and long diffusion length for the photoinjected electrons, the thickness of the transparent active TiO_2 layer was further increased to ca. 20 μm, while a light scattering overlayer was added to increase the optical path of the photons striking the sensitized film. These photoanode configuration was extended to the complete Fe(II)NHC series. In **Figure 4.32f** the IPCE spectra together with the integrated photocurrent are reported. Comparing these data with those one reported in **Figure 4.32a**, the photoaction spectra resulted broader (extended slightly beyond 700 nm), due to the thicker film together with the scattering top layer, with the large photoconversion in the 450-650 nm region coherently with the spectra reported in K.M. units in **Figure 4.28b**. The IPCE range between 40 - 60%, with top level for **ARM15** and **ARM130**. Our best sensitizer (**ARM130**) reached a peak around 60% at 570 nm leading to a 7 mA/cm^2 due to the best combination of light harvesting and injection quantum yield. The recorded trend was coherent with the J-V curves recorded under AM1.5G illumination where **ARM130** exhibited the best performances due to the best combination of photocurrent density (7 mA/cm^2) and open circuit photovoltage (0.47 V) leading to the best power conversion efficiency of 1.83% that to now, results in the best value ever recorded for an iron-based solar cell (**Figure 4.32g** and **Table 4.9**).

Table 4.9: Efficiency parameters recorded for Fe(II)NHC with 16 μm transparent TiO_2, with 16 μm transparent TiO_2 + scattering overlayer and with 20 μm transparent TiO_2 + scattering overlayer

Dye	TiO_2 thickness	J_{sc}/mA/cm^2	V_{oc}/V	FF%	PCE%
ARM16	16 μm	4.87±0.31	0.43±0.01	59±2	1.24±0.10
ARM122	16 μm	4.82±0.31	0.37±0.02	51±2	0.91±0.12
ARM130	16 μm	5.59±0.18	0.44±0.01	58±1	1.43±0.10
C1	16 μm	4.30±0.30	0.43±0.01	59±3	1.10±0.09
ARM16	16 μm + scattering	5.41±0.30	0.46±0.01	58±1	1.44±0.10
ARM122	16 μm + scattering	5.45±0.10	0.39±0.01	47±4	1.00±0.15
ARM130	16 μm + scattering	6.33±0.30	0.46±0.01	57±1	1.65±0.12
C1	16 μm + scattering	5.22±0.18	0.45±0.01	57±2	1.35±0.07
ARM14	20 μm + scattering	6.03±0.34	0.47±0.01	59±1	1.68±0.14
ARM15	20 μm + scattering	6.07±0.45	0.43±0.01	61±3	1.58±0.13
ARM16	20 μm + scattering	5.81±0.41	0.47±0.01	57±3	1.56±0.18
ARM122	20 μm + scattering	6.11±0.46	0.39±0.01	49±2	1.17±0.15
ARM130	20 μm + scattering	6.80±0.17	0.47±0.02	57±1	1.83±0.10
ARM132	20 μm + scattering	5.20±0.33	0.35±0.01	61±2	1.11±0.12
C1	20 μm + scattering	5.60±0.29	0.44±0.01	56±1	1.39±0.13

4.3.6c Electrochemical impedance spectroscopy

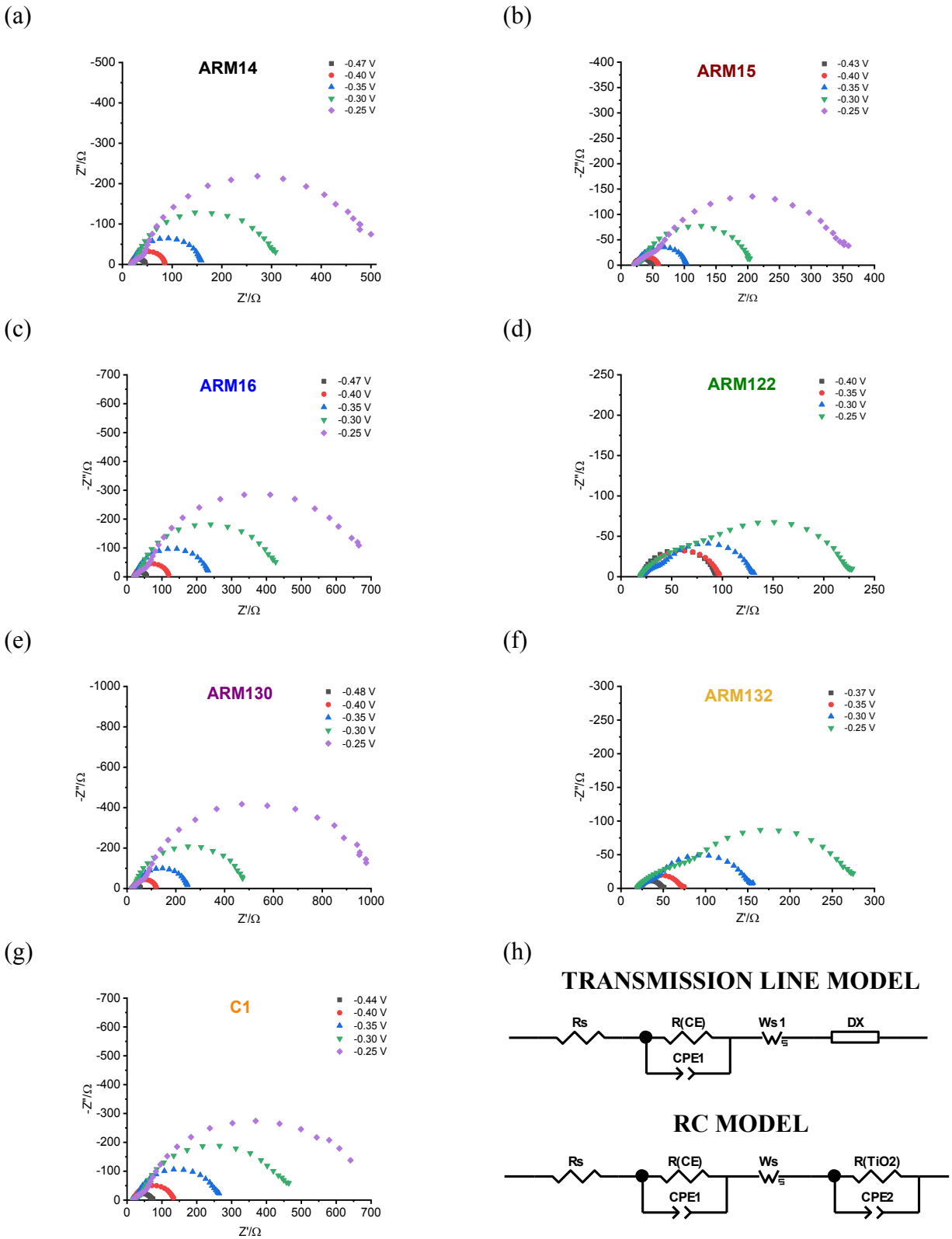

Figure 4.33: (a)-(g) Nyquist plots recorded for the different Fe(II)NHC based cells. Each plot has been recorded with the cell biased along the descending branch of the characteristic J/V curve from the proper V_{oc} to -0.25 V for (a) **ARM14**, (b) **ARM15**, (c) **ARM16**, (d) **ARM122**, (e) **ARM130**, (f) **ARM132** and (g) **C1.** Perturbation frequency decreases from 10^5 to 10^{-1} Hz when moving from left to right. h) Transmission line and RC Equivalent circuits used for fitting the EIS data. From ref 257

To better understand the photoelectrochemical behavior we performed electrochemical impedance experiments under AM1.5G illumination. The J-V curves have been sampled at forward bias along the discerning branch between the open circuit photovoltage to -0.25 V (onset of the plateau region of the J-Vs). This potential region should be dominated by the chemical capacitance of the semiconductor film and by its interfacial recombination resistance $RTiO_2$ that leads to a one dominant depressed semicircle in the Nyquist plots (**Figure 4.33**). The EIS data have been fitted both with the transmission line model elaborated by Bisquert et al.[192] and with the simplified model composed by two RC meshes accounting for the electrochemical interfaces of the photoanode and the counter electrode respectively (**Figure 4.33h**). We introduced a short Warburg in both the models for the electrolyte diffusion in the thin layer cell, which generates low frequency features in the complex plane plot. The transmission line model well fitted the intermediate forward applied bias (-0.25/-0.3 V) where the transport resistance is not completely negligible compared to $RTiO_2$. In any case, the recombination resistance range between 10^3 to 10^1 and it is higher than the transport resistance at least by a 10-factor, confirming the good agreement of the two models.

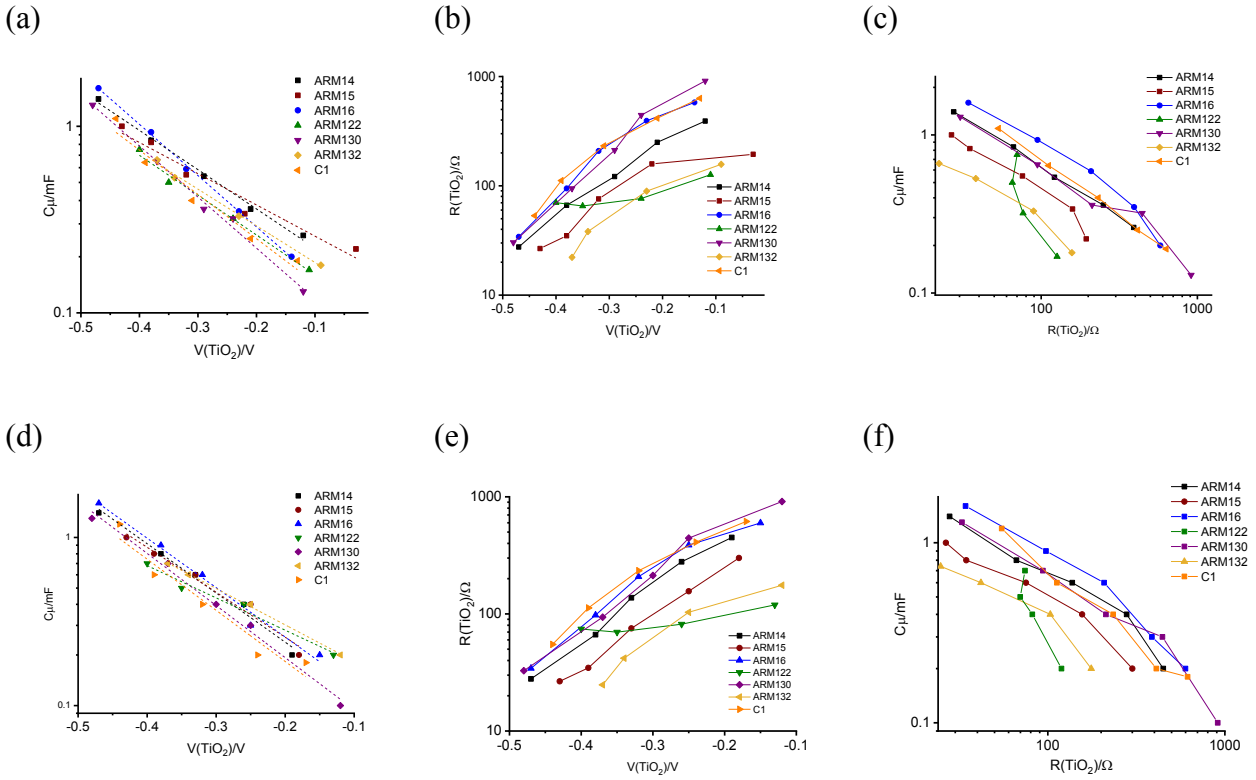

Figure 4.34: TiO_2 (b) and (d) capacitance and (b) and (e) recombination resistance of Fe(II)NHC plotted vs $VTiO_2$, (c) and (f) Chemical Capacitance vs recombination Resistance of the TiO_2 for both the transmission line and RC model employed. From ref 257

Both the models have been validated by the good agreement between the sum of all the resistance extracted by the fits and the reciprocal derivative $\partial V/\partial I$ of the I-V curves (**Figure A4.65**). We have reported the chemical capacitance in log scale[197] of the sensitized titania film (Cμ), as a function of $VTiO_2$ ($VTiO_2$ = Vcell -I∑R where I is the photocurrent and ∑R the resistances due to the other cell components) (**Figures 4.34a** and **d**), Cμ decrease exponentially by decreasing the applied forward voltage to the electron extraction from the semiconductor. All the complexes exhibited a similar range of photoanodic capacitance at a comparable $VTiO_2$, which is originated by the steady state electronic population of the semiconductor at each given voltage, determined by the competition between charge

injection and recombination. The recombination resistance R(TiO_2) decrease with increasing the chemical capacitance of the TiO_2 which reflects in an improved electronic conductivity of the latter (**Figures 4.34b** and **e**). To conclude we plotted the Cμ vs. RTiO_2 to compare the recombination resistance of the Fe(II)NHC complexes at a comparable value of electronic population of the semiconductor. The best sensitizer should have the best chemical capacitance and the highest recombination resistance, which means having the most favorable competition of charge separation and election recombination. Analyzing the plot of **Figure 4.3c**, **ARM16**, **ARM 14** and **ARM130** show the best behavior while **ARM122** and **ARM132** exhibit the lowest recombination resistance coherently with the lower V_{oc} recorded under AM1.5G illumination. We can conclude that the best performances recorded for **ARM130** seems to result from an ideal combination of best injection efficiency and light harvesting while the recombination processes are not dramatically different from those of the other dyes bearing aromatic substituents.

4.3.7c Charge transfer at the ARM130/TiO_2 interface

To get deeper insights on the effect of the chemical substitution in the best **ARM130** sensitizer on the interfacial charge injection and recombination properties, here the **ARM130**/TiO_2 interface (**Figure 4.35a**) has been modelled and calculated its energetics (**Figure 4.35b**), injection and recombination kinetics (**Table 4.10** and **Table A4.6**, respectively). Here the data with those obtained for the unsubstituted **ARM13** compound (see **Chapter 4b**) have been compared to check if the presence of a substituent on the ancillary NHC ligand effectively induces an improvement in the interfacial electron/transfer kinetics. It is important to stress that here the presence of the Mg^{2+} cation at the interface wasn't considered, that, as we have already discussed in the previous section, is going to systematically increase the interfacial electronic coupling, without acting in a differential way on the two dyes, thus allowing us to still draw reliable conclusions. The relaxed structure of **ARM130** anchored on the TiO_2 slab (**Figure 4.35a**) shows a rather pronounced bending of the dye toward the metal oxide surface (displaying tilted angles θ about 47°), as already found for other NHC-Fe(II) complexes.[241] The O - Ti covalent bonds are in the range 2.10–2.20 Å, typical values for carboxylic acid groups anchoring to TiO_2 surfaces (see **Table A4.7**). The interfacial electronic structure, evidenced by the Projected Density of States (PDOS) in **Figure 4.35b**, shows a favorable energy level alignment and a notable broadening of the dye's LUMO over the TiO_2 conduction band (CB) states, which, indeed, qualitatively account for the good injection performances measured for this complex. By looking at data in **Table 4.10**, the differences in the electron injection kinetics of **ARM130**/TiO_2 and **ARM13**/TiO_2 can be quantitatively assessed. The diabatic LUMO of **ARM130** is up shifted of about 0.1 eV with respect to the LUMO of **ARM13**, thus lying more deeply in the TiO_2 CB, as indicated by the larger number of semiconductor states (ca. 14000 vs. 12600). This LUMO up shift in **ARM130** basically compensates the slightly lower electronic coupling with the TiO_2 states around the LUMO energy level (**Figure A4.66**), finally yielding injection properties (Γ_{inj} and τ_{inj}) similar to those calculated for the unsubstituted **ARM13** complex. Analogously, comparable back electron recombination kinetics are also predicted (**Table A4.6**). Therefore, this chemical substitution on the ancillary ligand does not seem to significantly affect the interfacial charge generation properties. Based on this analysis, therefore, the record photovoltaic performances, i. e., the record photocurrent, of **ARM130** can be attributable to the effect of electron donating OMe groups attached to the benzene ring, which improve the light harvesting capability without deteriorating the excited directionality, as it was the case, instead, of **ARM15**.

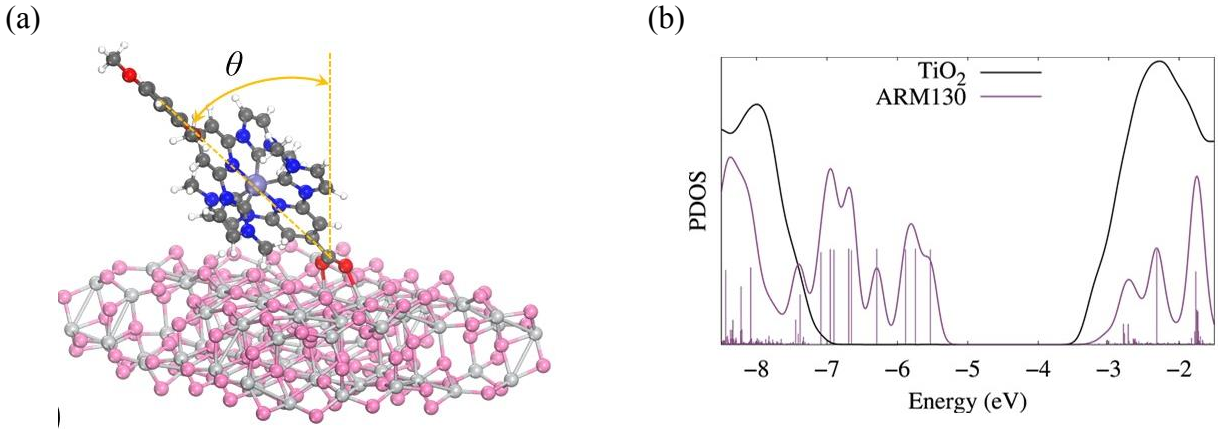

Figure 4.35: a) Perspective view of the optimized **ARM130**/TiO_2 structure; and b) Projected Density of States (PDOS) of **ARM130**/TiO_2 over the atoms belonging to the dye (purple) and TiO_2 surface (black), as calculated by Mulliken population analysis. For visualization purposes, only the vertical bars of the dye's PDOS are represented here and the TiO_2 DOS intensity has been divided by a factor of 10. From ref 257

Table 4.10: Probability Distributions, $\Gamma_{inj}(\varepsilon)$/eV and DOS (number of states/eV) calculated at the diabatic LUMO energies and associated Injection times, τ_{inj} (s^{-1}). The diabatic TiO_2 conduction band maximum (CBM) is also reported

System	Dye LUMO/ eV	CBM/ eV	TiO_2 DOS (states/eV)	Γinj/ eV	τ_{inj}/ fs
ARM130/TiO_2	-2.51	-3.32	13962	0.150	4.39
ARM13/TiO_2[a]	-2.60	-3.34	12651	0.152	4.33

[a] Data taken from **Chapter 4b**

4.4c Conclusions

In this last chapter of my thesis about iron-based solar cells, we reported a further improvement by employing a new family of heteroleptic complexes designed with different electronic properties to try to improve the charge separation as well as the light harvesting. In particular, among the series, **ARM130** bearing a dimethoxyphenyl group, exhibited the best performances. By employing computational analysis and electrochemical impedance spectroscopy we can conclude that this dye is characterized by an improved light harvesting capability introduced by the electron-donating -OMe moieties and by a favorable excited directionality and recombination kinetics. Combining our Mg^{2+} and TBAI based electrolyte, optimized in our previous work, with a relative thick TiO_2, we obtained for **ARM130**, a Power Conversion Efficiency of 1.83%, that at the best of our knowledge, results the higher ever reported in literature for an iron sensitizer.

CHAPTER 5: Electrodeposited PEDOT/Nafion as Catalytic Counter Electrodes for Cobalt and Copper Bipyridyl Redox Mediators in Dye-Sensitized Solar Cells

5.1 Introduction

This last chapter of my thesis is still about the optimization of the components for Dye Sensitized Solar Cells, in particular, it is about the counter electrode compartment. At the beginning of DSSC developments, the most typical catalytic CEs were based on noble metals, such as Pt, which offers both high electron transfer rates and high stability in the presence of the iodide/iodine redox mediator. However, platinum was not the optimal electrocatalyst in conjunction with monoelectronic redox couples based on coordination compounds, among which Co(II) and Cu(I) polypyridine complexes are the most successful examples.[266] When used in some Co(II) and Cu(I) mediated DSSC, counter electrodes based on the conductive polymer poly(3,4-ethylenedioxythiophene) often outperformed platinum, contributing to the achievement of record power conversion efficiencies. The most efficient PEDOT based counter electrodes were electrodeposited in the presence of sodium dodecyl sulfate (SDS) or $LiClO_4$, the former in water solution whereas the latter in organic media.[107, 267] Surprisingly, counter electrodes based on the well-known electrodeposited PEDOT/polystyrene sulfonate (PEDOT/PSS), which can be prepared from a water solution of EDOT and sodium polystyrene sulfonate, exhibited a bad kinetic response towards iodide/iodine and alternative redox mediators. Trying to work in an eco-friendly environment, we selected another water-soluble polymeric ionomers, where Nafion is one of the most used ion exchange membranes, thanks to a high proton conductivity as well as a large ionic capacitance.[268, 269] For the first time, we have prepared electrodeposited PEDOT/Nafion-based counter electrode for DSSCs in combination with $[Cu(tmbpy)_2]^{2+/+}$ (tmbpy = 4,4′-6,6′-dimethyl-2,2′- bipyridine) and $Co(bpy)_3^{3+/2+}$ (bpy = 2,2'-bipyridine) redox mediators. This study was based on a comparison with the best performer PEDOT/ClO_4 (prepared in acetonitrile medium) and with the PEDOT/**PSS** (electrodeposited in water). PEDOT/Nafion exhibited a quite comparable PCE% to those one recorded for PEDOT/ClO_4 and significantly higher compared to those one obtained for PEDOT/**PSS**.

5.2 Experimental

5.2.1 Materials

97% EDOT, Alconox, Titanium(IV) isopropoxide, Magnesium trifluoromethanesulfonate (MgOTf, where OTf = trifluoromethanesulfonate), Poly(sodium 4-styrene-sulfonate) (NaPSS), 5 wt.% Nafion perfluorinated ion-exchange resin solution in a mixture of lower aliphatic alcohols and water, 98% Benzimidazole (BzIm), 96% TBPy, and solvents (99.8% anhydrous Acetonitrile (ACN), ACS grade 2-propanol ≥ 99.8%, ACS grade absolute EtOH, 99.9% 1-butanol) were purchased from Sigma-Aldrich and used without further purification. LiTFSI (TFSI = bis(trifluoromethanesulfonyl)imide) and 98% Nitrosonium tetrafluoroborate ($NOBF_4$) were bought from Alfa Aesar. $LiClO_4$ ≥ 99% was purchased from Acros organics. FTO TEC-7 was bought from NSG, 18NR-T TiO_2 paste was purchased from Greatcell Solar. Surlyn 25 was supplied by Dyepower Consortium. **D35** dye was obtained from Dyenamo. $[Co(bpy)_3](OTf)_2$) and $[Co(II)(bpy)_3](PF_6)_3$ were prepared according to a previous work.[270] $[Cu(tmbpy)_2]$TFSI was synthesized according to literature procedures.[126, 271]

5.2.2 Methods

Absorption spectra of the various PEDOT coated FTO electrodes (**PER**, **NAF**, **PSS**, geometric area = 2.7 cm^2) were registered in the 900 – 380 nm by evaluating the transmitted (T%) and reflected (R%) light by each substrate type with a Jasco V570 spectrophotometer equipped with an integrating sphere. The spectra are reported as Absorptance (A%) vs λ(nm) were A% = 100% - T% - R%.

SEM was used to analyze the morphology and the thickness of the PEDOT films. Measurements were performed using a JEOL JSM-7001F FEG-SEM at 20.0 keV electron beam energy. The SEM apparatus is equipped with an Energy Dispersive X-ray Spectroscopy detector (EDXS, Oxford INCA PentaFETx3). The working distance was maintained between 3 to 8 mm. Surface morphology images were acquired in top-down and tilted mode whereas cross section analysis was performed putting the films on a 90° stub. To avoid deformations of the polymer layers, all sample sections were prepared by cutting the glass substrate with a Struers Minitom precision cutting machine, followed by fracturing in liquid nitrogen. A layer of about 20 nm of carbon was then deposited on all samples.

AFM images of the different PEDOT substrates were collected by the aid of a Digital Instruments Nanoscope III scanning probe microscope (Digital Instruments, CA). The instrument was equipped with a silicon tip (RTESP-300 Bruker) and operated in tapping mode. Surface morphology analysis of raw images was carried out with NanoScope analysis 1.5 and the postproduction of the images were carried out with Gwyddion program.

All electrochemical experiments were performed either with EcoChemie PGSTAT 302N or PGSTAT30 potenstiostats. Cyclic voltammetry to explore the PEDOT electroactivity on FTO electrodes was performed in a three-electrode setup with a Platinum sheet (4 cm^2) counter electrode and a double jacket SCE as reference. The faradaic charge (Q) of PEDOT films was calculated by integration of the cyclic voltammograms in the potential range of 0.2 V to -1 V (Vs SCE). The capacitances (C) were obtained according to the formula $C = I/\nu$, where I = current (average of the anodic and cathodic currents at E_{dc}=0.4 V) and ν = potential scan rate.[272] The voltage was scanned at 20 mVs^{-1} in a 0.1 M LiTFSI/ACN. Polarization curves of the symmetric thin layer cells (STLC) were obtained at 10 mVs^{-1} in the -0.8 V - + 0.8 V range with a two-electrode arrangement. The current/voltage characteristic of each STLC was recorded after achieving of a stable voltammetric response (equilibration) of the cell, testified by the appearance of more than two subsequent super-imposable voltammetric curves, established during 20 conditioning cyclic scans between -0.8 V and +0.8 V. Electrochemical impedance spectroscopy (EIS) of equilibrated PEDOT based STLC was carried out with a PGSTAT 302N equipped with a FRA module by applying a 10 mV sinusoidal perturbation in the 10^5-10^{-1} Hz range at 0 V.

The photocurrent density – voltage curves of 0.25 cm^2 active area DSSCs were carried out with a PGSTAT 302N equipped with an ABET AM 1.5G sun simulator by scanning from short circuit (0 V) to the open circuit voltage (V_{oc}) in linear sweep mode at a scan rate of 20 mVs^{-1}. The irradiance was set to 0.1 Wcm^{-2} each cell was placed on a black opaque platform to avoid back scattered radiation.

Incident Photon-to-Electron Conversion Efficiency spectra were collected with a home-made apparatus based on a Xe lamp (Ceralux CL300BF) optically coupled with a motorized Newport Cornerstone monochromator. The selected wavelength is focussed on the solar cell with an optical fibre. A National Instruments PXI 1033 system was used to acquire the incident irradiance measured by a calibrated photodiode and the photocurrent generated by the solar cells under short circuit

condition. A black mask bordered the active layer to reduce the contribution of the scattered light from the FTO electrodes and other reflective cell components surrounding the sensitized TiO_2 layer.

5.2.3 FTO Cleaning for electrodes fabrication

Careful cleaning of the FTO was carried out by subsequent ultra-sonication in 2% w/w aqueous Alconox solution and 2-propanol for 10' each. After drying at RT, the slides were heated at 450 °C in air in order to burn residual organic contaminants and naturally cooled at room temperature (RT). The resulting FTO slides were usually employed immediately after completing the cleaning process for electrode fabrication.

5.2.4 PEDOT Counter Electrodes fabrication

0.25 cm^2 PEDOT coated counter electrode substrates were prepared by potentiostatic electropolymerization of EDOT on top of well cleaned FTO. The same amount of anodic charge (58 $mCcm^{-2}$) was passed during the electrolysis. A mask either made of Kapton 70 µm or surlyn 25 µm was used to delimit the exposed FTO geometric area to the value reported above. The electropolymerization was achieved in a three-electrode cell where the FTO working electrode and a 4 cm^2 titanium sheet counter was kept face-to-face at a ca. 2 mm distance from each other, while a double jacket Standard Calomel Electrode (SCE) served as the reference electrode. The EDOT solutions and the proper electrodeposition conditions used to prepare the three different PEDOT types were defined as follows (all potentials are referred to SCE):
1) PEDOT/ClO_4 (**PER**): electrodeposited at 1.6 V from a solution of 10^{-2} M EDOT in 0.1 M $LiClO_4$/ACN.
2) PEDOT/Nafion (**NAF**): the commercial solution of Nafion (5 % wt) was diluted with water (1:5 v/v, 0.8 % wt) and the pH was adjusted to 6.5 - 7 with a small amount of diluted $NaOH_{aq}$. The electrodeposition solution was prepared by dissolving EDOT (10^{-2} M) in the neutralized solution of Nafion, and a potential of 1.1 V was used.
3) PEDOT/PSS (**PSS**): electrodeposition was performed in an aqueous solution of 10^{-2} M EDOT in 0.8% wt. NaPSS at 1 V.
The electrodes for the Uv-Vis spectroscopy were prepared in a similar fashion by scaling the charge according to the surface area.

5.2.5 Symmetric Thin Layer Cell (STLC) fabrication

These cells were fabricated by clamping two PEDOT electrodes with a 70 µm CAPTON spacer The redox electrolytes were: a) 0.18 M $[Co(bpy)_3](OTf)_2$, 0.028 M $[Co(bpy)_3](PF_6)_3$, 0.1 M MgOTf, 0.2 M TBPy, 0.2 M BzIm and b) 0.208 M $[Cu(tmbpy)_2]$TFSI, 0.028 M $NOBF_4$, 0.1 M LiTFSI, 0.2 M TBPy, 0.2 M BzIm.

5.2.6 Solar Cell fabrication

Photoanodes for solar cells were fabricated as follows: first, a TiO_2 blocking underlayer was fabricated by spin coating (10"/1000 rpm followed by 20"/2000 rpm) a 0.3 M titanium

isopropoxide/butanol solution and sintering in a 500°C preheated oven for 15'. The porous TiO_2 semiconductor was obtained by spreading the 18NR-T paste on top of the blocking layer. This was achieved by manually sliding a glass blade on top of a couple of 3M stripes, acting as spacers, placed at distance of 5 mm from each other. Sintering of porous TiO_2 was obtained according to the following temperature program: RT-120°C in 10', 120 – 450 °C in 30', 20' at 450 °C, 450 – 500 °C in 10', 500 °C for 10 minutes. After cooling at RT, the resulting electrodes were stained in a 0.2 mM ethanolic solution of **D35** overnight, rinsed with fresh ethanol and dried at RT. Cells were assembled in an open configuration with the aid of two clamps using surlyn 25 μm as spacer. Cells were filled with the same electrolytes reported for the STLC.

5.3 Results and Discussion

5.3.1 General considerations of PEDOT-based CEs

The electrochemical oxidation of EDOT at a FTO working electrode, investigated by cyclic voltammetry either in the presence of $LiClO_4$/ACN or in aqueous Nafion and polystyrene sulfonate sodium salts, is reported in **Figure 5.1a**. The onset of irreversible oxidation of EDOT is observed at 0.8 V with **PSS**, at 0.9 V in the presence of Nafion (**NAF**) and at 1.1 V in ACN/$LiClO_4$ (**PER**). The presence of two crossing points during the reverse sweep, readily appreciated in the **PER** electrolyte, is consistent with the nucleation of the polymer on the electrode.[273] The strong dependence of the EDOT oxidation threshold on the supporting electrolyte agrees with the known fact that the oxidation potential of EDOT is cathodically shifted in an aqueous electrolyte, if compared to organic media.[274] In addition, this phenomenon is more pronounced in micellar solutions, thereby suggesting that the oxidation of EDOT is thermodynamically facilitated in the presence of counter ions and/or solvents that provide a better stabilization of EDOT(+) cations.[274] This explains the anticipated oxidation onset of EDOT in **NAF** and **PSS** with respect to the **PER** based monomer solution (**Figure 5.1**).

(a) (b)

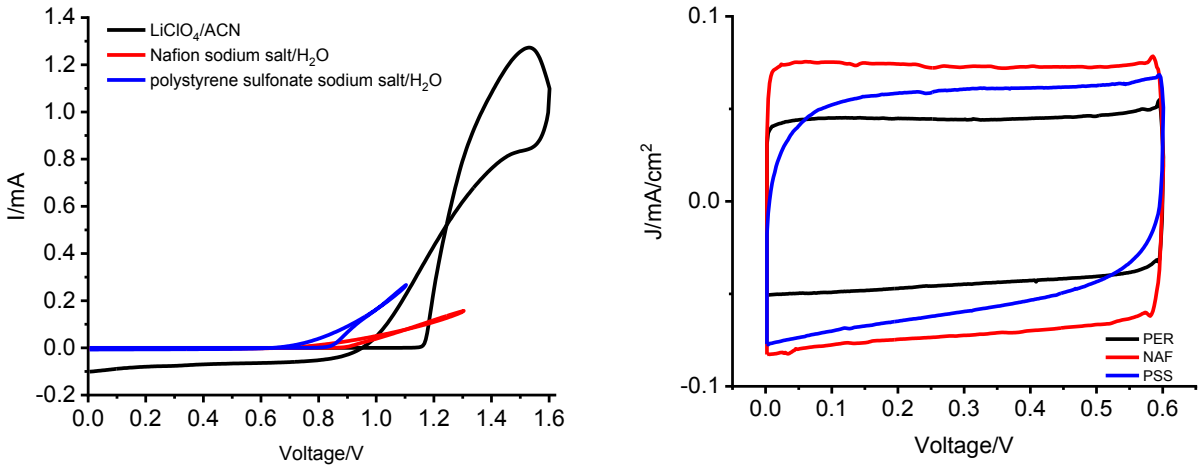

Figure 5.1: (a) CV of 0.01 M EDOT in 0.1 M $LiClO_4$/ACN (black line) or Nafion sodium salt/H_2O (red line) or polystyrene sulfonate sodium salt/H_2O (blue line) at FTO working electrode. (b) CV analysis of **PER**, **NAF** and **PSS** based counter electrodes in 0.1 M LiTFSI/ACN electrolyte, in the potential rage of 0 V to 0.6 V, showing the typical capacitive behavior of PEDOT

Within the explored conditions, a well-defined diffusional peak associated to the steepest current/voltage of ~7 mAV^{-1}characteristic and the highest faradaic current is observed with the **PER** electrolyte, while in aqueous electrolytes, the slope of the voltammograms was significantly lower, on the order of 1 mAV^{-1} and 0.4 mAV^{-1} for **PSS** and **NAF**, respectively, and so the current density observed at equivalent overvoltages with respect to the EDOT oxidation threshold (see **Figure 5.1a**). This behavior might be due to a combination of kinetic and mass transport limitations due to the increased viscosity, hence resistivity, of the aqueous medium containing bulky poly-anions with respect to the small ions contained in the organic **PER** electrolyte. In addition, a higher resistivity of EDOT/Nafion with respect to EDOT/**PSS** has been reported.[275] Owing to the electrolyte dependent electrochemical response of EDOT, the potentiostatic electrodeposition conditions were adjusted in each electrolyte in order to properly trigger EDOT oxidation, without intercepting its undesired and detrimental over-oxidation, which, particularly in water, it is known to occur. To ensure a comparable thickness of the electrodeposited **PER**, **NAF** and **PSS** PEDOT films, we ensured that, in all cases, the same amount of charge (58 $mCcm^{-2}$) was passed during the electrodeposition. Indeed, it was demonstrated that the thickness of the film, which is linked to the deposited total mass of the polymer coating, is proportional to the amount of the faradaic charge flowing during the electrodeposition and that the thickness of the film can affect the electrocatalytic properties of the counter electrode and of the resulting solar cell.[267, 276, 277] Indeed, the obtained PEDOT coatings range within 220-340 nm average thickness, as estimated by cross-sectional SEM imaging in **Figures 2a-c**. **PER** is the thickest and most irregular layer (340 ± 80nm) and with its very porous and rapidly varying rough morphology yields a varying profile, making it difficult to provide a very reliable thickness estimate. On the other hand, **NAF** and **PSS** films display a very similar thickness (211 ± 52 nm and 223 ± 77 nm respectively) and also a much smoother and more compact appearance with respect to **PER**. Absorption spectra of **PER**, **NAF** and **PSS** counter electrodes can be observed in **Figure 5.2d**. In

particular, the progressive increase of the absorptance from 400 to 900 nm and the absence of any relevant features are consistent with the formation of highly doped PEDOT.[104, 269, 278] The similar absorptance of the polymer films means that the same amount of absorbing chromophore is present on the FTO surface, consistent with the equal amount of anodic charge passed during electrodeposition. This also confirms that the thicker appearance of the **PER** film is probably due to the formation of a highly porous sponge-like PEDOT structure observed in previous study.[107] The CV response of **PER**, **PSS** and **NAF** films, conducted in an inert electrolyte made of 0.1 M LiTFSI in ACN, outlined the presence of a cathodic process centered at about -0.65 V, reported in **Figure 5.2e**. This process is referred to the reduction of the conductive film, which reflects the transition from the fully doped and conductive state to the neutral and insulating form of PEDOT.[278] The large separation peak of about 500 mV is consistent with kinetic limitations for the re-oxidation process probably due to a slow diffusion of ions from the bulk electrolyte to the inner sites of the neutral polymeric film.[279]

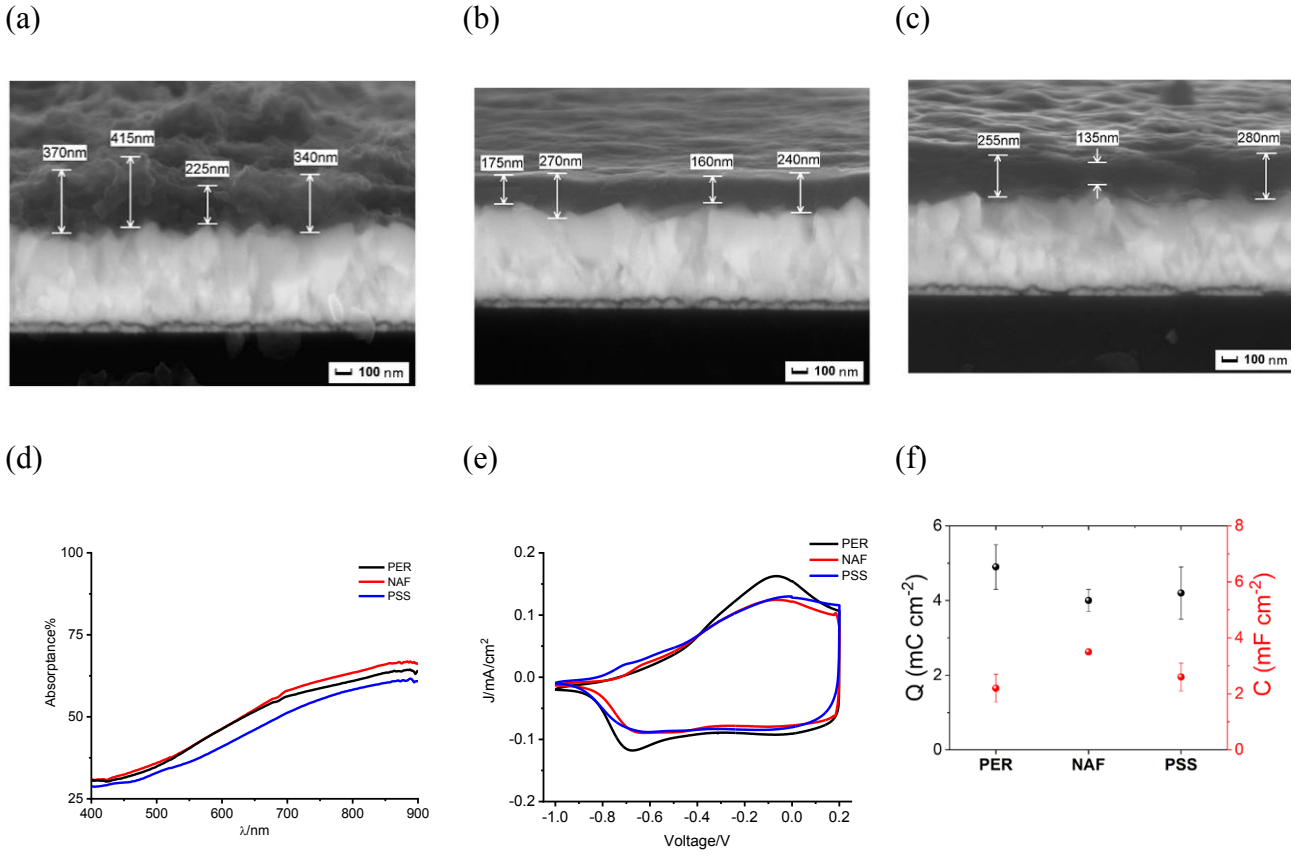

Figure 5.2: Preliminary characterization of PEDOT based CEs. a), b), c) cross-section SEM of **PER**, **NAF** and **PSS**, respectively. d) absorptance and e) CV analysis for **PER**, **NAF** and **PSS**. f) charge values (black dots) extracted from CV analysis in e) and capacitances (red dots) obtained from CV curves reported in **Figure 5.1b** (data are reported as mean values ± std, n = 3)

Cathodic charge extracted by CV traces can be used to provide an estimation of the amount of charge carriers in **PER**, **PSS** and **NAF** counter electrodes, assuming that one electron interacts with each active site of the conductive polymer.[274, 276] As depicted in **Figure 5.2f** (see also **Table 5.1**), quite comparable charges between 4 and 5 mCcm^{-2} are stored in **PER**, **NAF** and **PSS** counter electrodes, which confirms that the adopted fabrication protocol ensures the injection of a similar amount of charge carriers (holes) for all PEDOT based CEs. The double layer capacitance, extracted from the

capacitive response of the polymer films recorded between 0 and 0.6 v vs SCE (see **Figure 5.1b**), is slightly larger (≈ 3.5 $mFcm^{-2}$) for **NAF**, whereas **PER** and **PSS** exhibited a lower value of about 3 $mFcm^{-2}$ (**Table 5.1**). It was reported that **NAF** films electrodeposited on gold microelectrodes exhibit higher capacitance values if compared to **PSS** coating prepared in the same conditions. This was mainly ascribed to a faster and more efficient ion diffusion inside the pores of **NAF** with respect to **PSS**.[275] Thus it is likely that the good ion transport properties of the ionomer Nafion plays a crucial role to determine the improved capacitance of **NAF** compared to **PER** and **PSS** CEs. In addition, it is known that the nature of both the anionic dopant and the solvent used during the electrodeposition strongly affect the surface morphology of the resulting PEDOT films.[107, 274, 280]

Table 5.1: Relevant parameters extracted from CV analysis in 0.1 M LiTFSI/ACN (data are reported as mean values ± std, n = 3)

CE	Q[a)]/ mC cm^{-2}	C[b)]/ mF cm^{-2}
PER	4.9 ± 0.6	2.2 ± 0.5
NAF	4.0 ± 0.3	3.5 ± 0.1
PSS	4.2 ± 0.7	2.6 ± 0.5

a) obtained by integration of the cyclic voltammograms (see **Figure 5.2e**) in the potential range of 0.2 V to -1 V vs SCE; b) extracted from CV analysis reported in **Figure 5.1b**

As depicted in **Figures 5.3**, SEM top-down imaging reveals a very porous morphology with sub-micron pore-size for **PER**, while **NAF** and **PSS** exhibit more compact surfaces where spherical features with diameter below 100 nm are visible on top of the underlying FTO features. This was also corroborated by AFM analysis which outlined a porous structure for **PER** (see **Figures 5.3d**), with large pores approximately 300 - 400 nm wide. This is in line with the sponge-like morphology described in the literature for PEDOT films electrodeposited in organic media and in the presence of small counter ions, like ClO_4^-.[107, 280] Instead, **NAF** and **PSS** films are composed by tiny globular substructures, where the nanoglobules's diameter is about 10-20 nm, as shown in **Figure 5.3e** and **Figure 5.3f**. This is the typical morphology which is observed when the electrodeposition of PEDOT is carried out in aqueous micellar solutions.[107, 275] The highest surface roughness (R_q) of 167 nm was observed for **PER**, whereas **NAF** and **PSS** exhibited a smoother morphology in agreement with SEM imaging (R_q = 38 and 23 nm, respectively), as detailed in **Table 5.2**.

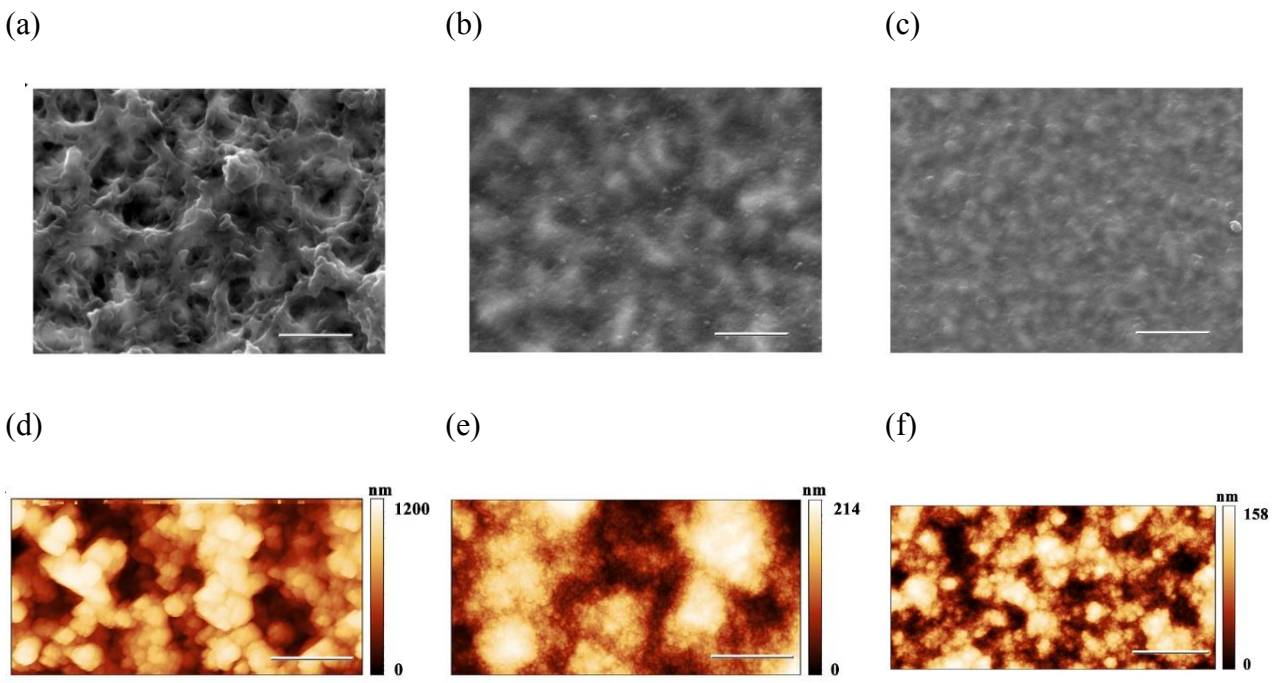

Figure 5.3: SEM images for a) **PER**, b) **NAF** and c) **PSS** (scale bar 500 nm). AFM analysis of d) **PER**, e) **NAF** and f) **PSS** (scale bar 1 μm)

Table 5.2: AFM analysis of PEDOT based counter electrodes

CE	R_q/ nm	R_a/ nm	R_{max}/ nm
PER	167	128	1408
NAF	38.3	29.5	262
PSS	23.5	18.8	156

5.3.2 Electrocatalytic characterization of the PEDOT substrates

The electrocatalytic behavior of **PER**, **PSS** and **NAF** has been investigated in symmetric TLC by means of LSV and EIS, in the presence of either Cobalt or Copper based electrolyte. In this study the redox mediators were based on the well-known complexes $[Co(bpy)_3]^{2+/3+}$ (**Figure 5.4a**) and $[Cu(tmbpy)_3]^{1+/2+}$ (**Figure 5.4b**). These redox shuttles, in conjunction with PEDOT based counter electrodes, enable the fabrication of highly efficient DSSCs.[105]

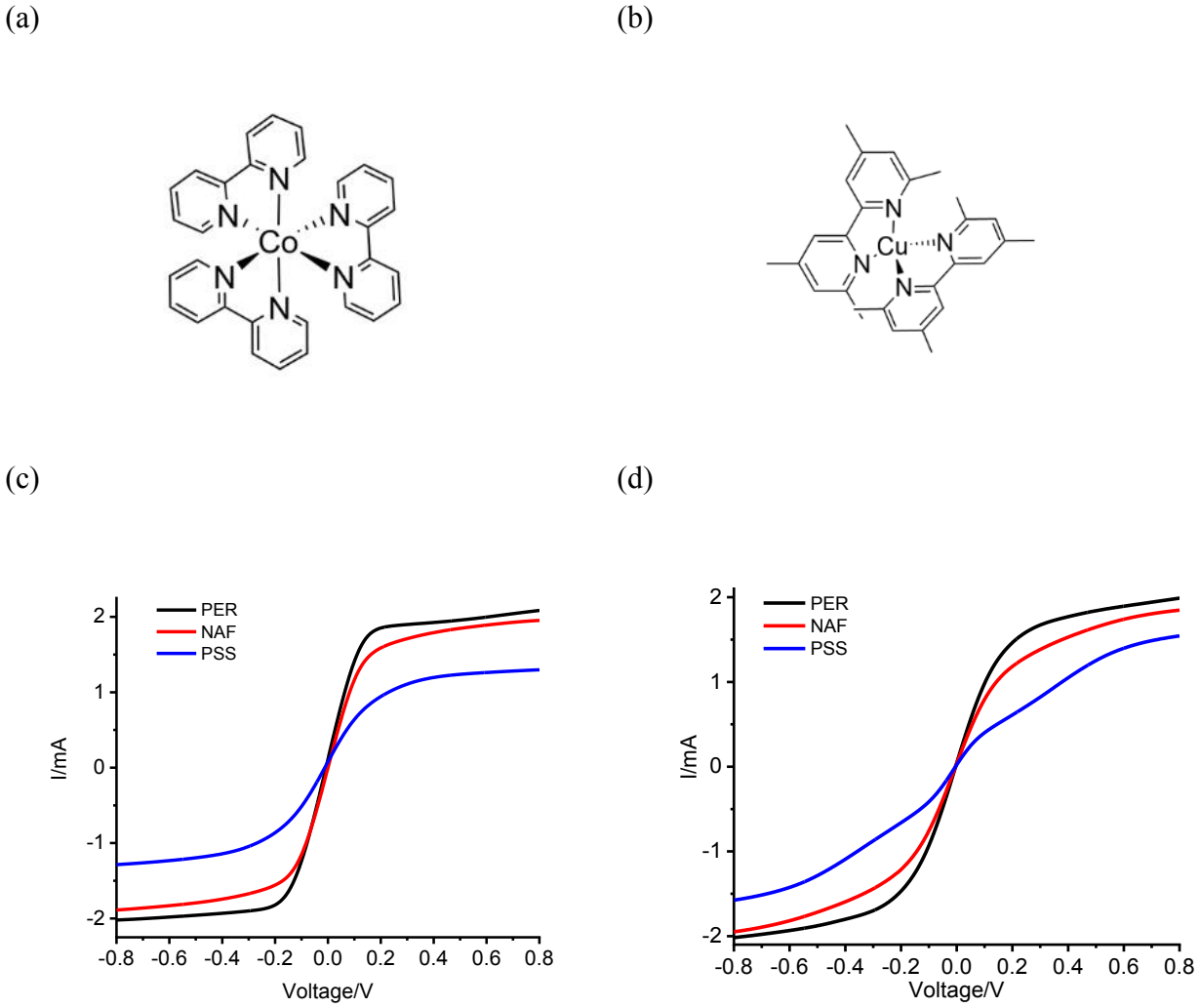

Figure 5.4: Chemical structure of a) $[Co(bpy)_3]^{2+/3+}$ and b) $[Cu(tmbpy)_3]^{1+/2+}$. LSV characterization of dummy cells assembled with c) $[Co(bpy)_3]^{2+/3+}$ or d) $[Cu(tmbpy)_3]^{1+/2+}$ based redox mediators, respectively

The LSV of symmetric cells assembled with PEDOT counter electrodes in conjunction with the $[Co(bpy)_3]^{2+/3+}$ redox mediator exhibits a linear response at low overpotentials, as shown in **Figure 5.4c**. The total resistance R_{IV} of the cell can be calculated around the equilibrium potential, according to the Ohm's law $I = (1/R_{IV})\eta$, where I is the current, η is the overpotential and $(1/R_{IV})$ is the slope of the curve. It should be noted that large values of R_{IV} are originated either by a slow kinetic response at the electrode||electrolyte interface, or by mass transport limitation or both.[185] Relatively fast but bulky monoelectronic redox couples like these polypyridine complexes were predominantly characterized by mass transport limitations even at very low overvoltages (ca. 10 mV). For higher

overpotentials, the fully diffusion controlled maximum current I_{lim} (A) can be extracted according to **eq. 5.1**:

$$I_{lim} = \frac{2FCDA}{L} \qquad \textbf{eq. 5.1}$$

where F is the Faraday's constant (96485 C mol^{-1}), C is the concentration of the redox couple ($molcm^{-3}$), D is the diffusion coefficient of the redox specie in the electrolyte (cm^2s^{-1}), L is the thickness of the spacer (cm) and A is the electroactive surface area (cm^{-2}).[107, 267] **PER** and **NAF** exhibited comparable R values on the order of 80 Ω in the presence of $[Co(bpy)_3]^{2+/3+}$ redox mediator, whereas **PSS**, in the same conditions, yielded the highest total resistance of 170 Ω, as summarized in **Table 5.3**. This might account for a faster charge transfer and better mass transport at the interface between the cobalt based redox shuttle and **PER**, and **NAF**, if compared to **PSS** counter electrodes. The poor response of **PSS** based counter electrodes in the presence of polypyridine cobalt complexes was already highlighted in a previous study.[107] The highest diffusion limited current of ≈ 2 mA (8 $mAcm^{-2}$) was obtained with **PER** and **NAF** dummy cells, suggesting that these two materials outline a comparable electrocatalytic activity when used in conjunction with $[Co(bpy)_3]^{2+/3+}$ redox mediator. In addition, considering that all the parameters in **eq. 5.1** are constant, except the term A, the variations of the limiting current can be linked only to the electroactive surface area (ESA) of PEDOT based counter electrodes. Thus, results are consistent with an improved ESA for **PER** and **NAF** with respect to the **PSS** electrodes. This trend is in accordance with the results obtained by AFM analysis which highlighted a higher roughness for both **PER** and **NAF** which may better expose polymer redox active sites to the electrolyte and also facilitate the diffusion of the redox couple through the porous structure of these materials. Similar results were obtained for thin cells assembled with the redox shuttle $[Cu(tmbpy)_3]^{+/2+}$, as reported in **Figure 5.4d**. Nevertheless, with the $Cu^{+/2+}$ couple, **PER** exhibited a slightly improved I/V response if compared to **NAF**, as it can be confirmed by the steeper slope of the voltammogram of the former compared to the latter, which translates into R_{IV} values of 109 Ω and 128 Ω for **PER** and **NAF**, respectively. Also in this case, **PSS** outlined the slowest faradaic response, with a total resistance on the order of 215 Ω. Comparable limiting currents of approximately 2 mA were displayed by **PER** and **NAF** in the presence of Cu based redox shuttle, unlike PSS based dummy cells which yielded a lower current of about 1.6 mA. It is interesting to note that larger diffusion coefficients of 11 - 22 $\times 10^{-6}$ $cm^2s^{-1}$was reported for $[Cu(tmbpy)_3]^{+/2+}$ if compared to $[Co(bpy)_3]^{2+/3+}$($6 - 7 \times 10^{-6}$ cm^2s^{-1}) and this is not surprisingly since that the rate of diffusion scales with the hydrodynamical radius of the complex.[126] Thanks to their improved diffusion rate, copper based redox mediators have been introduced in DSSCs to mitigate the mass-transport limitation of cobalt-complex redox electrolytes.[124, 281] Now, according to **eq. 5.1** one would expect higher diffusional current values for dummy cells assembled with $[Cu(tmbpy)_3]^{+/2+}$ with respect to $[Co(bpy)_3]^{2+/3+}$. Thus, the fact that **PER** and **NAF** exhibited a comparable I_{LIM} values of approximately 2 mA in the presence of both cobalt and copper based redox shuttles is somehow counterintuitive. Apparently, this may be linked to a less efficient diffusion of $[Cu(tmbpy)_3]^{+/2+}$ in **PER** and **NAF** porous structure if compared to $[Co(bpy)_3]^{2+/3+}$. Indeed, it should be reminded that, unlike with conventional metal counter electrodes, where electron transfer occurs entirely at the electrodic surface, PEDOT is, as a matter of fact, a three-dimensional electrode, being constituted by a relatively porous film, whose pores are permeated by the electrolyte. Thus, the redox couple will need to diffuse through the pores of the PEDOT layer before reaching active polymer sites and undergo electron transfer. Besides geometric constraints, specific interactions between the redox

couple, the conductive polymer and anionic dopants may further affect the local diffusion coefficient of these cationic electronic shuttles.

Table 5.3: Electrochemical parameters extracted from thin layer cell characterization: LSV analysis (cell area = 0.25 cm^2)

CE	Redox mediator	R_{IV}/ Ω	I_{lim}/ mA
PER	$[Co(bpy)_3]^{2+/3+}$	77 ± 7	2.0 ± 0.2
NAF		84 ± 9	1.9 ± 0.1
PSS		170 ± 14	1.3 ± 0.1
PER	$[Cu(tmbpy)_3]^{1+/2+}$	109 ± 12	2.0 ± 0.2
NAF		128 ± 8	1.9 ± 0.1
PSS		216 ± 16	1.6 ± 0.1

In order to gain more precise information on the electrochemical properties of these PEDOT based CEs, EIS of the TLC were collected and fitted to an equivalent circuit model. In **Figures 5.5a** and **5.5b** the Nyquist and the Bode plots, respectively, for PEDOT symmetric cells assembled with $[Co(bpy)_3]^{2+/3+}$ are reported. It can be seen that the Nyquist plots are dominated by a large loop over the low frequency range from ~ 1 Hz to 0.01 Hz, which is linked to the strong peak at ≈ 0.1 Hz in the Bode plots. In the high frequency domain, an additional depressed semicircle can be observed (see the inset in **Figure 5.5a**), with a time constant in the $10^4/10^5$ Hz range for **NAF** and **PER** counter electrodes, and one order of magnitude lower ($10^3/10^4$ Hz) for **PSS** (**Figure 5.5b**).

(a)

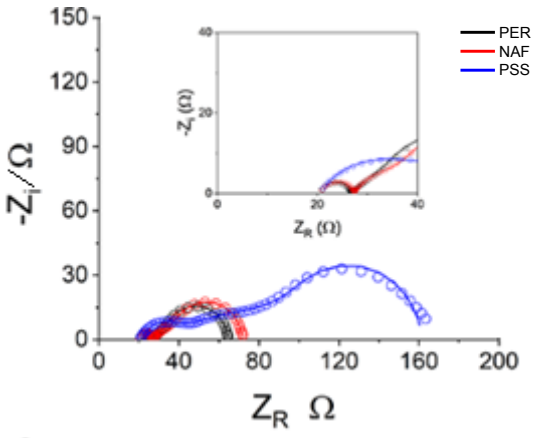

(b)

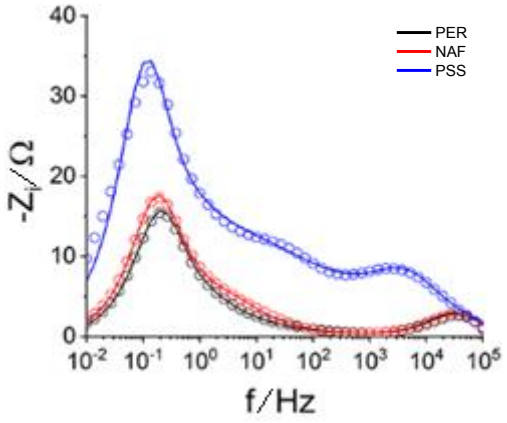

(c) (d)

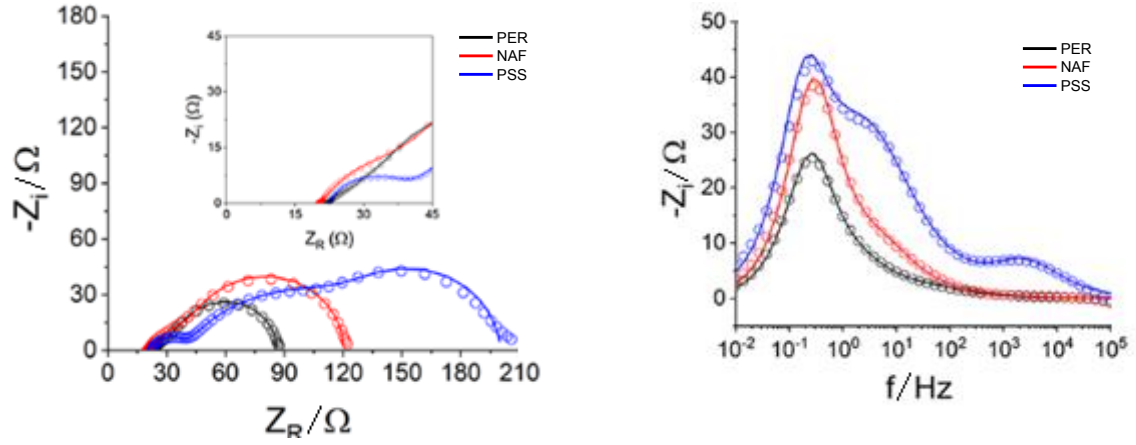

Figure 5.5: Experimental (circles) and fitted (lines) Nyquist and Bode plots for dummy cells assembled with a,b) $Co(bpy)_3]^{2+/3+}$ and c,d) $[Cu(tmbpy)_3]^{+/2+}$ based redox mediators

Table 5.4: Relevant parameters extracted from EIS fittings, according to the equivalent circuit reported in **Figure 5.6**

CE	Redox mediator	R_S/ Ω	$2R_{IT}$/ Ω	$2R_{CT}$/ Ω	$\Re_{CT}$/ Ω cm²	R_D/ Ω	τ_D/ s	D/ 10^{-6} / cm^2s^{-1}	R_{EIS}/ Ω
PER		20	8.2	0.6	1.1	35	2.1	5.8	64
NAF	$[Co(bpy)_3]^{2+/3+}$	21	3.7	2.8	0.8	42	2.2	5.5	71
PSS		20	18.8	48.4	8.4	73	2.7	4.5	165
PER		20	//	2.0	0.25	70	1.5	8.2	92
NAF	$[Cu(tmbpy)_3]^{1+/2+}$	23	//	19.1	2.4	68	1.7	7.0	110
PSS		21	17.3	78.5	12	94	1.9	6.4	211

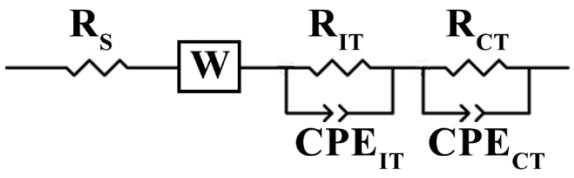

Figure 5.6: Electrical Equivalent of the symmetric thin layer cell. Kirchoff's laws afford equivalent R_{IT} = $2R'_{IT}$, R_{CT} = $2R'_{CT}$, CPE_{IT} = $\frac{1}{2}$ CPE'_{IT} and CPE_{CT} = $\frac{1}{2}$ CPE'_{CT}, R' and CPE' are the parameters of each single counter electrode

The presence of a further semicircle in the frequency domain of ≈100 - 10 Hz can be clearly outlined only in the case of **PSS**, whereas for **NAF** and **PER** this feature is much less evident, although it still produces a shoulder at ca. 10 Hz in the Bode plot of **Figure 5.5b**. The shape of the large signal, which dominates the impedance from middle to low frequencies, is indicative of finite transmissive boundary conditions and it is consistent with finite-length diffusion behavior.[282] Thus, the equivalent circuit model adopted in this study consists of the serial resistance R_s in series with two parallel (RC) elements describing the relevant charge transfer processes occurring through the polymer and at the polymer/electrolyte interface. A further finite-length diffusion impedance Z_D (**Figure 5.6**) models the mass transport of the redox couple.[107, 267] The diffusional impedance Z_D can be expressed by the **eq. 5.2**:

$$Z_D = R_D tanh(j\omega\tau_D)^{1/2}/(j\omega\tau_D)^{1/2} \quad \textbf{eq. 5.2}$$

where R_D is the diffusional resistance and τ_D is the diffusional lifetime. To improve the quality of the fitting, two constant phase elements were used to model the capacitances. The CPE impedance is given by the **eq. 5.3:**

$$Z_{CPE} = 1/[Y_0(j\omega)^n] \quad \textbf{eq. 5.3}$$

where Y_0 is the admittance of the CPE, j is the imaginary unit, ω represents the angular frequency and n denotes the exponent of the CPE. Referring to the experimental EIS spectra, the highest frequency region contains the contribution of the ohmic resistance R_s, which is mostly linked to the solution resistance, FTO and PEDOT conductivities and by electric contacts. Comparable R_s values of ≈ 20 Ω were observed for all CEs materials, confirming that this parameter is not affected by the intrinsic conductivity of PEDOT based coatings but rather by the conductivity of FTO. The highest frequency process was referred to the ion compensated charge transport inside porous PEDOT structure, in accordance with the literature, and the circuit element that models its impedance consists of an ion transport resistance (R_{IT}) in parallel with a constant phase element (CPE_{IT}) (**Figure 5.6**).[283, 284] Interestingly, it was found that this process can be observed for all PEDOT based CEs assembled with the cobalt mediator but, in the case of copper redox shuttle, it was very noticeable only with **PSS**, as can be seen in **Figure 5.5c**. In contrast, at frequencies higher than 1 kHz, the impedance was frequency independent in the case of **PER** and **NAF** dummy cells assembled with $[Cu(tmbpy)_3]^{+/2+}$ based redox mediator, thereby suggesting that the charge transport resistance across these PEDOT films, can be considered negligible for these materials or that the time constant of this process falls at frequencies higher than 10^5 Hz. The fact that this signal is strongly affected by the nature of the electrolyte, rather than by the type of PEDOT, further corroborates the hypothesis that the high frequency process is not linked to the charge transfer at the interface FTO||PEDOT, as previously suggested in the literature.[285] In the case of $[Co(bpy)_3]^{2+/3+}$ redox mediator, a lower value of ion transport resistance was observed for **NAF** (R_{IT} ≈ 1 Ω) suggesting that this process is facilitated with this material, if compared to **PER** (R_{IT} ≈ 4 Ω, see **Table 5.4**). The largest values of R_{IT} ≈ 9 Ω was yielded by PSS to indicate that ion transport is less efficient in **PSS** if compared to **PER** and **NAF**. The charge transfer at the interface PEDOT||$[Co(bpy)_3]^{2+/3+}$ can be observed in the frequency range of ~100-1 Hz.[286] A lower charge transfer resistances R_{CT} of 0.3 Ω and 1.4 Ω were found for **PER** and **NAF**, respectively, whereas **PSS** exhibited the significantly larger R_{CT} value of ≈ 24 Ω. It is important to note that the charge transfer resistance is directly linked to the heterogeneous electron transfer rate constant k_0.[287] Thus, low values of R_{CT} are desired to yield fast regeneration of the redox mediator at the counter electrode side in the solar cell device. In this study, an effective charge transfer resistance ($\Re_{CT}$) has been considered, in accordance with the literature.[286] This formalism implies that the overall charge transfer resistance must be calculated by considering both the contributions provided by the ion transport resistance (high frequency peak) and the charge transfer resistance (middle-frequency semicircle), according to the formula $\Re_{CT} = R_{IT} + R_{CT}$. Currently, optimal photoanodes can yield photocurrent values J_{SC} of up to 20 $mAcm^{-2}$ at AM 1.5G illumination.[288] This means that a good counter electrode should ensure the generation of comparable exchange currents J_0 at the counter electrode side, in order to avoid losses. Assuming a J_{SC} current of 20 $mAcm^{-2}$, an ideal value of $\Re_{CT}$ = 1.3 Ω cm^2 can be calculated, according to the relationship $J_0 = RT/nF\Re_{CT}$ where R, T, n and F are the gas constant, the temperature, the number of electrons and the Faraday

constant, respectively. As summarized in **Table 5.4**, **NAF** and **PER** yielded the lower $\Re_{CT}$ values of 0.8 Ωcm^2 and 1.1 Ωcm^2, respectively, thereby confirming that these two materials can be efficiently used as counter electrodes in a solar cell assembled with $[Co(bpy)_3]^{2+/3+}$ redox mediator. By contrast, a $\Re_{CT} > 8\ \Omega\ cm^2$ was obtained for **PSS**, which would correspond ideally to an exchange current J_0 of $\approx 3\ mAcm^{-2}$, making this catalytic material likely unsuitable to be used in conjunction with $[Co(bpy)_3]^{2+/3+}$ redox shuttle in DSSCs. As far as the mass transport is concerned, it should be noted that Z_D accounts not only for diffusion processes that occur in the bulk electrolyte, but it also describes mass transport inside the porous structure of the conductive PEDOT film. This can be clearly understood by considering that PEDOT films is expected to behave like a mixed ionic and electronic electrode. Thus, the highest value of $R_D = 73\ \Omega$ observed for **PSS** suggest that ionic diffusion is somehow impeded inside this material. On the other hand, diffusion of $[Co(bpy)_3]^{2+/3+}$ is more efficient through the 3D structure of **PER** and **NAF**, as confirmed by their lower R_D values of 35 Ω and 42 Ω, respectively. As reported in **Table 5.4**, it can be seen that also the parameter τ_D depends on the catalytic material. The diffusional lifetime can be related to the diffusion coefficient (D) of the redox species by the following **eq. 5.4**:

$$\tau_D = L^2/D \qquad \textbf{eq. 5.4}$$

where L represents the diffusional length which, in the case of symmetric thin layer cells, was reported to be set as the half of the cell spacer (L = 35 μm in this study).[107] The thickness of the PEDOT film (~300 nm as above discussed) is negligible with respect to the spacing between the counter electrodes, and we reasonably assume that the whole polymer film is permeated by the electrolyte. L is expected to be constant during dummy cell characterization (35 μm in this study) thus, diffusion coefficients can be extracted from the $\tau_D$values of **eq. 5.4** obtained by EIS fittings (**Table 5.4**). Increasing diffusion lifetime values of 2.1, 2.2 and 2.7 s were calculated for dummy cells assembled with **PER**, **NAF** and **PSS**, respectively, in the presence of $[Co(bpy)_3]^{2+/3+}$ redox mediator. This further confirms that the diffusion of $[Co(bpy)_3]^{2+/3+}$ species is slower inside the porous structure of **PSS**, if compared to **PER** and **NAF**. Indeed, the corresponding diffusion coefficients of 5.8, 5.5 and 4.5 $\times 10^{-6}\ cm^2s^{-1}$ were calculated for **PER**, **NAF** and **PSS**, respectively. These values are in line with the diffusion coefficients of $\approx 4.5 - 6 \times 10^{-6}\ cm^2s^{-1}$ reported for $Co(bpy)^{2+/3+}$ for similar electrolyte compositions.[107] The trend here observed can be related to the morphological properties of PEDOT counter electrodes. Indeed, according to AFM analysis (see **Table 5.2**), the diffusion of $[Co(bpy)_3]^{2+/3+}$ is expected to be facilitated within the highly open 3D structure of **PER** (R_q = 167 nm). On the other hand, the more compact surface morphology of **PSS** (R_q = 23.5 nm) is likely to hinder the diffusion of $[Co(bpy)_3]^{2+/3+}$ complexes. In addition, it is also expected that the bulkier molecular structure of polystyrene sulfonate and Nafion in **PSS** and **NAF**, respectively, would translate into a less favored diffusion of $[Co(bpy)_3]^{2+/3+}$ due to a higher steric hindrance and electrostatic interaction between sulfonate groups and hard Co(III) ions if compared to what it is experienced in the presence of the smaller molecular anion ClO_4^- present inside **PER**. From this perspective, the most significant difference between polystyrene sulfonate and Nafion can be linked to the presence of the bulkier phenyl rings in the former. This is consistent with previous reports, where the combination of sterically hindered Co(II)/(III) with other, but related, types of PEDOT/**PSS** electrodes produced very large diffusional resistances hence a poor electrochemical response.[107] TLCs assembled with the $[Cu(tmbpy)_3]^{+/2+}$ redox shuttle produced the EIS response reported in **Figure 5.5c** and **Figure 5.5d,** with overall features analogous to those just discussed in the case of Co(II)/(III). In the high frequency domain,

the semicircle related to the ion transport can be clearly distinguished only in the case of **PSS**, with a time constant of ≈ 3 kHz. A larger charge transfer resistance $\Re_{CT}$ = 2.4 Ω cm^2 was observed for **NAF**, if compared to **PER** ($\Re_{CT}$ = 0.4 Ω cm^2), thereby suggesting that the regeneration of $[Cu(tmbpy)]^+$ is slightly less effective for **NAF**. Nevertheless, comparable diffusional resistances R_D of 70 and 68 Ω were observed for **NAF** and **PER**, respectively, to indicate that the diffusion of $[Cu(tmbpy)_3]^{+/2+}$ species in **NAF** is not impaired by the presence of the polymeric ionomer Nafion, with respect to the smaller ClO_4^-. The highest $\Re_{CT}$ of 12 Ωcm^2 and R_D of 94 Ω were found with **PSS**, which confirmed that this material is not the best catalytic counter electrode also for the copper based redox mediator. It was reported that the electrocatalytic properties of Cu-based redox mediators are strongly influenced by the presence of 4-TBPy in the electrolyte. In particular, this additive tends to increase both the charge transfer resistance $\Re_{CT}$ and the diffusional resistance R_D, if compared to a 4-TBPy-free redox electrolyte composition.[289] Diffusion lifetime of 1.5, 1.7, 1.9 s were extracted from EIS fitting for **PER**, **NAF** and **PSS**, which translates into diffusion coefficients of 8.2, 7 and 6.4 ×10^{-6} cm^{2}s^{-1}, respectively (**Table 5.4**). This trend is similar to what observed for **PER**, **NAF** and **PSS** in conjunction with $[Co(bpy)_3]^{2+/3+}$ based redox mediators and it is consistent with the AFM analysis, which outlined R_q(**PER**) > R_q(**NAF**) > R_q(**PSS**). It is relevant to observe that the larger values of R_D obtained for $[Cu(tmbpy)_3]^{+/2+}$, if compared to $[Co(bpy)_3]^{2+/3+}$ (see **Table 5.4**) are indicative of an impaired diffusion of the diffusion-controlling $[Cu(tmbpy)_3]^{2+}$ species, with respect to $[Co(bpy)_3]^{3+}$. It is known that upon oxidation to the Cu(II) state, the coordination sphere of $[Cu(tmbpy)_3]^{2+}$ will change from tetrahedral to distorted tetragonal, by coordinating TBPy, thereby yielding larger radius of the complex.[289]

5.3.3 Photoelectrochemical characterization of DSSC

The electrocatalytic properties of **PER**, **NAF** and **PSS** counter electrodes were tested in DSSC devices assembled with the organic dye **D35**. As discussed in **Chapter 1**, the molecular structure of **D35** is based on the Donor-π-Acceptor architecture and the bulky alkyl chains were introduced on the triphenylamine donor unit to efficiently suppress the photoanode recombination.[59]

(a) (b)

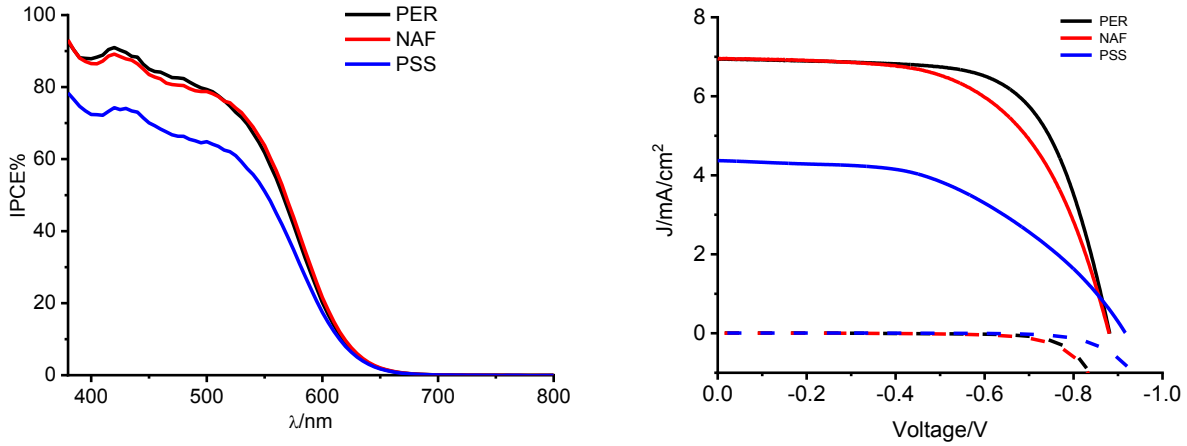

(c) (d)

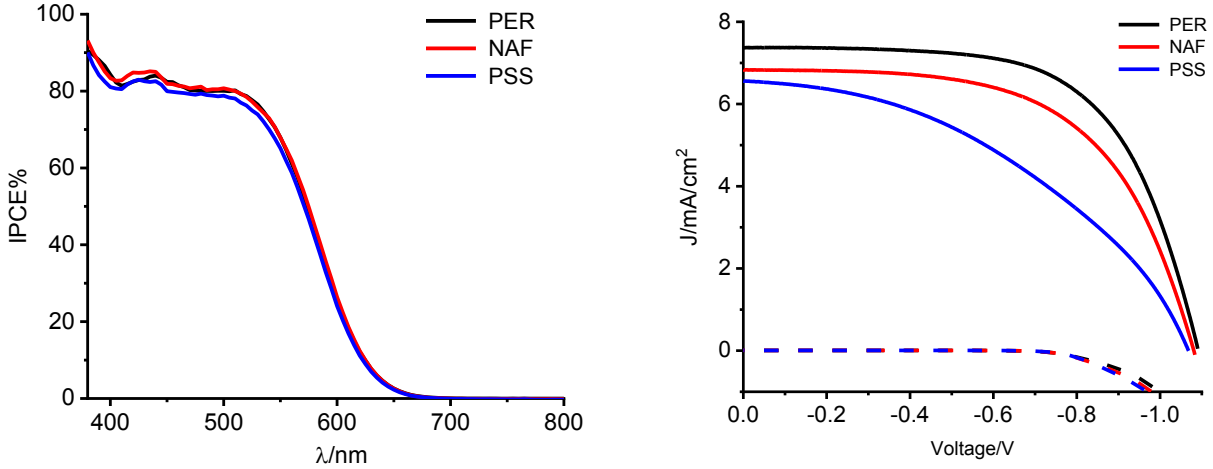

Figure 5.7: (a,c) Representative IPCE and J-V (b,d) characteristics of **D35** sensitized solar cells assembled with **PER**, **NAF** and **PSS** CEs and (a,b) $[Co(bpy)_3]^{2+/3+}$ or (c,d) $[Cu(tmbpy)_3]^{+/2+}$ redox mediators

The IPCE% and the J-V characteristics spectra of DSSCs assembled with $[Co(bpy)_3]^{2+/3+}$ redox mediator are reported in **Figure 5.7a** and **Figure 5.7b**, respectively. Relevant efficiency DSSCs parameters are summarized in **Table 5.5**. As shown in **Figure 5.7a**, devices fabricated with **PER** and

NAF based counter electrodes exhibited comparable photoaction spectra. This translates into similar short-circuit currents (J_{sc}) of ~ 7 $mAcm^{-2}$ under J-V measurements, as depicted in **Figure 5.7b**. This is not surprisingly since J_{sc} scales with IPCE%, and it also relates to the $\Re_{CT}$ values extracted from dummy cell characterization, as above discussed, which were comparable for counter electrodes based on **NAF** and **PER** in conjunction with Cobalt redox mediator.[10] The highest efficiency of ~ 4% was obtained for DSSC fabricated with **PER** counter electrodes, although solar devices assembled with **NAF** resulted only slightly inferior, exhibiting an efficiency mean value of 3.6%. This was mainly due to a lower fill factor of 59 for DSSC based on **NAF** if compared to **PER** (FF% = 66). As expected from dummy cell characterization results, solar cells assembled with **PSS** based counter electrodes yielded the lowest efficiency η% = 2, which is linked to the smallest values of J_{sc} (4.4 $mAcm^{-2}$) and FF% = 50. It is interesting to note that the slow kinetic response of **PSS** counter electrodes, which was also observed during dummy cells analysis, (see **Table 5.4**), represents a limitation to the photocurrent not only during J-V characterization, but also during IPCE collections, which are typically recorded under reduced light intensity. In the case of solar cells fabricated with $[Cu(tmbpy)_3]^{+/2+}$ redox mediator, **NAF** counter electrodes yielded a lower J_{SC} value of ~ 6.8 $mAcm^{-2}$, if compared to **PER** (~ 7.4 $mAcm^{-2}$), and this may result from the larger $\Re_{CT}$ exhibited by the former (**Table 5.4**) which is consistent with a slower regeneration of the redox mediator and, in turn, of the dye at the photoanode (see **Figure 5.7c** and **Figure 5.7d** , and **Table 5.5**). Nevertheless, the lower photocurrent represents only a small limitation of **NAF**, with respect to **PER**, when used as counter electrodes in solar cells with the $[Cu(tmbpy)_3]^{+/2+}$ redox shuttle, as confirmed by the slightly lower efficiency η% = 4.3 exhibited by DSSCs assembled with **NAF**, if compared with **PER** (η% = 5). As deduced from dummy cell characterization, the kinetic response of **PSS** versus the $[Cu(tmbpy)_3]^{+/2+}$ redox couple is less problematic, if compared to $[Co(bpy)_3]^{2+/3+}$, at least at low light intensity, as can be clearly confirmed by photoaction spectra reported in **Figure 5.7c**. Nevertheless, at full sunlight irradiation, DSSC fabricated with **PSS** yielded to lowest solar conversion efficiency η% = 3.

Table 5.5: Efficiency parameters obtained from the J-V characterization at 1 SUN light intensity (1 SUN = 100 $mWcm^{-2}$) for **D35** assembled in combination with the different PEDOT-based substrates

CE	Redox mediator	J_{SC}/ $mAcm^{-2}$	V_{oc}/ V	FF%	η%
PER		6.9 ± 0.3	0.88 ± 0.01	66 ± 3	4.1 ± 0.3
NAF	$[Co(bpy)_3]^{2+/3+}$	6.9 ± 0.4	0.88 ± 0.01	59 ± 3	3.6 ± 0.3
PSS		4.4 ± 0.1	0.91 ± 0.01	50 ± 4	2.0 ± 0.2
PER		7.4 ± 0.3	1.09 ± 0.01	63 ± 2	5.0 ± 0.4
NAF	$[Cu(tmbpy)_3]^{+/2+}$	6.8 ± 0.3	1.08 ± 0.02	59 ± 3	4.3 ± 0.5
PSS		6.6 ± 0.5	1.07 ± 0.02	42 ± 5	3.0 ± 0.5

5.3.4 Adhesion test

For a possible industrialization, the ideal DSSC device is expected to provide a stable efficient photoconversion over prolonged time of sunlight irradiation. Several aspects contribute to lowering the DSSC stability, including the dye and TiO_2 degradation, the redox electrolyte chemical changes, evaporation of the solvent and, of course, chemical instability and mechanical detachment of catalytic material at the counter electrode site. From this point of view, it is known that a possible drawback of PEDOT based counter electrodes is represented by their tendency to delaminate under mechanical and/or thermal stress. It was reported, for instance, a protocol to covalently bond PEDOT to the FTO surface, and the resulting films resulted highly stable to the delamination if compared to conventional **PER** coatings. Thus, mechanical stability of **PER**, **NAF** and **PSS** based counter electrodes was monitored by means of a modified scotch test type. In **Figure 5.8** the images of the counter electrodes before and after the peel off test are reported. As already reported, the as-prepared **PER** film (**Figure 5.8a**), tends to delaminate under these conditions, as confirmed by the presence of several detached areas (**Figure 5.8b**). Interestingly, both **NAF** and **PSS** displayed an encouraging mechanical stability when subjected to the same experimental conditions, as confirmed by the absence of any relevant detached area after the treatment. The nature of this improved adhesion is not clear but, in the case of **NAF** for instance, it was reported that the counter ion Nafion interacts strongly with the hydrophilic surface of FTO, thereby contributing to increase the mechanical adhesion of the conductive film.

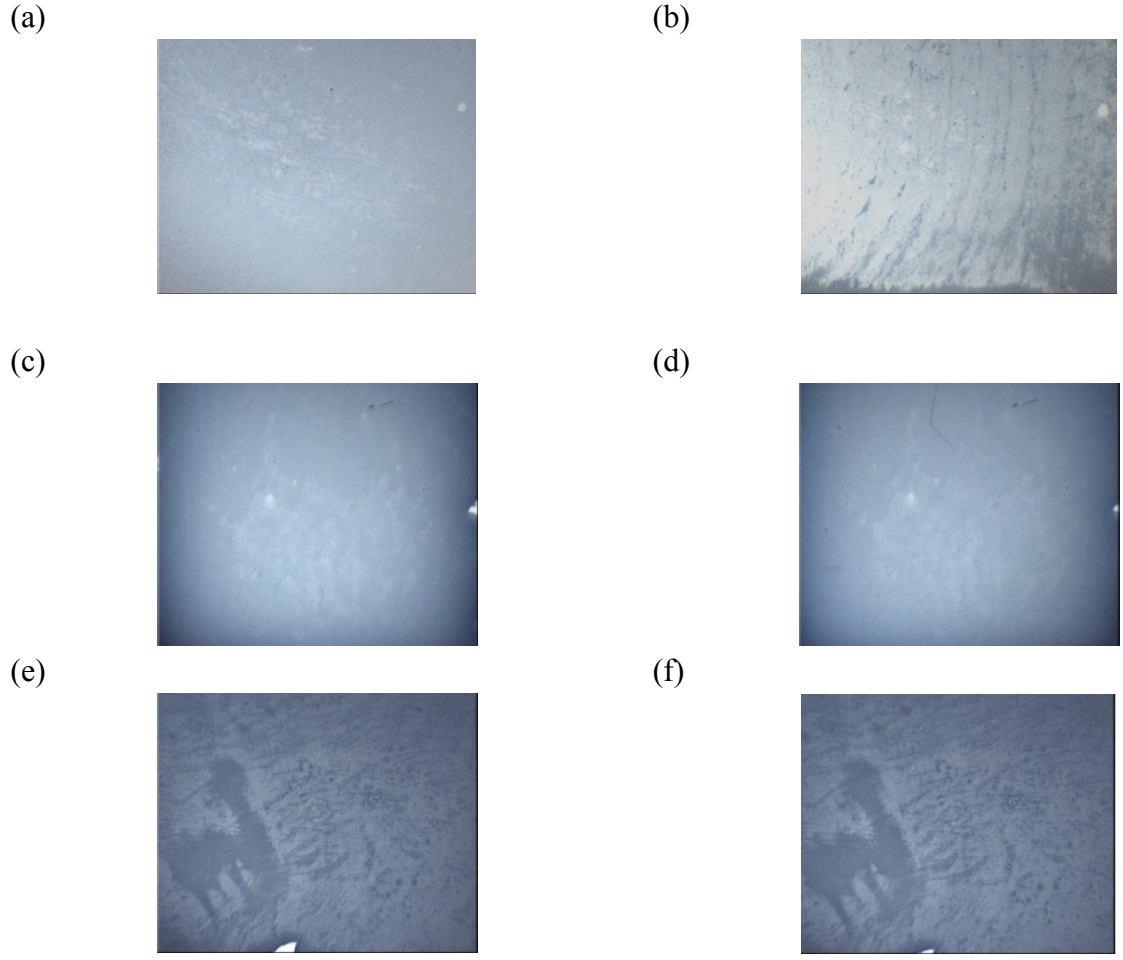

Figure 5.8: Adhesion test performed on a,b) **PER**, c,d) **NAF** and e,f) **PSS** counter electrodes: a,c,d) before, and b,d,f) after the peel-off stress

5.4 Conclusions

In this last chapter of my thesis, our contribution about the preparation of a new water electrodeposited PEDOT/Nafion counter electrode is reported. This study was conducted comparing the electrocatalytic behavior of **NAF** with those one of the well know **PER** and **PSS**, prepared in acetonitrile and in aqueous medium respectively. To ensure the same thickness of the substrate and so to equally compare the performances, we set the amount of charge, exchange during the electrodeposition, to the same value of 58 $mCcm^{-2}$, confirmed by the absorption spectra and the cathodic charge extrapolated by CV analysis. SEM and AFM characterization have shown a very porous morphology for **PER** and a more compact surface for **NAF** and **PSS**. The LSV analysis of the STLC exhibited a comparable cell resistance for **NAF** and **PSS** both in conjunction with Co and with Cu based electrolyte while, **PSS** has shown the higher resistance attributable to the faster charge transfer and better mass transport at the interface between the redox couple and the first substrates. The EIS analysis revealed a quite comparable $\Re_{CT}$ for **NAF** and **PER** and also in this case lower than that one extrapolated for **PSS** arguing therefore the better catalytic behavior for DSSC applications of the first two substrates. Under AM1.5G illumination, **D35** in conjunction with the PEDOT substrate were tested with both the redox couples employed in this study, **PER** overcome the PCE% obtained for **NAF** and **PSS** in both the case but the cell efficiency for **NAF** resulted closer to the efficiency recorded for the best substrate, just slightly lower mainly for the lower Fill Factor attributable at the higher charge transfer resistance. PEDOT/Nafion resulted so a good and more sustainable CE for DSSC application.

APPENDIX

CHAPTER 3: New examples of Ru(II)-tetrazolato complexes as thiocyanate-free sensitizers for dye sensitized solar cells

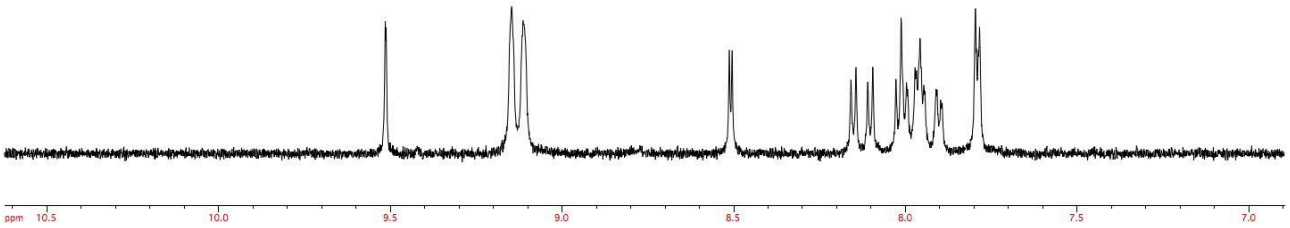

Figure A3.1: ^{1}H-NMR of **D1**, CD_3OD. From ref 210

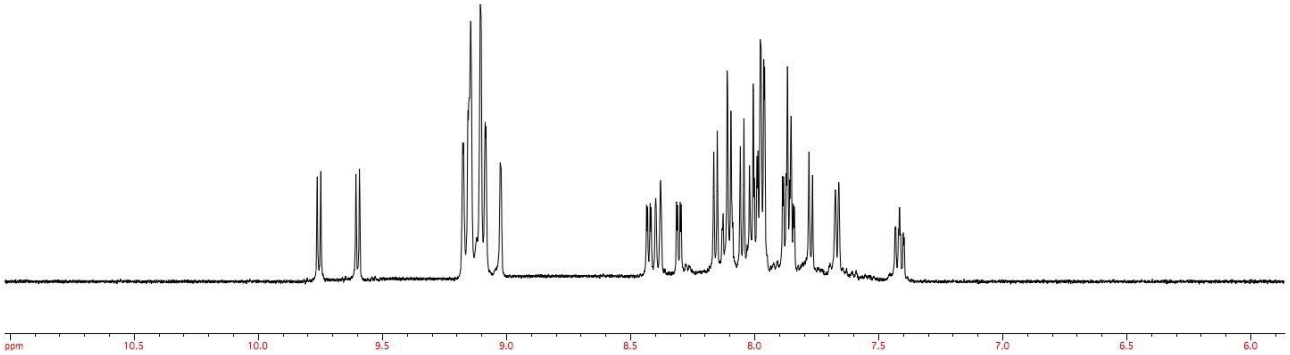

Figure A3.2: ^{1}H-NMR of **D2**, CD_3OD. From ref 210

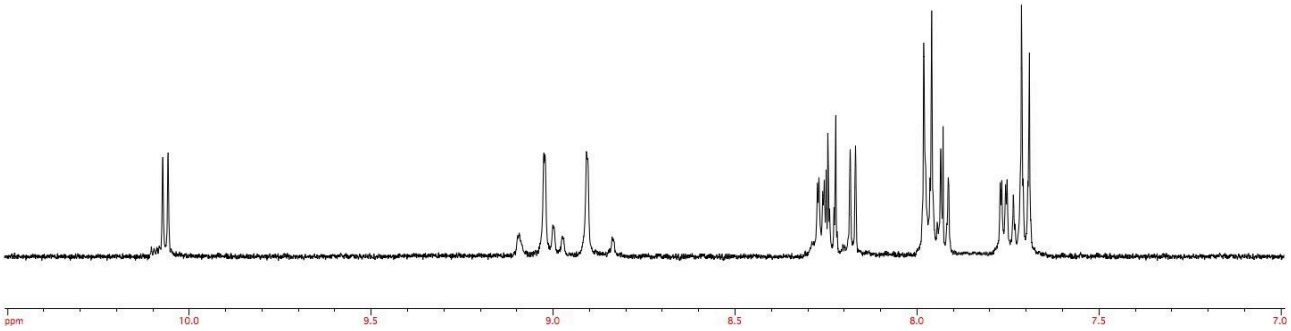

Figure A3.3: ^{1}H-NMR of **D3**, CD_3OD. From ref 210

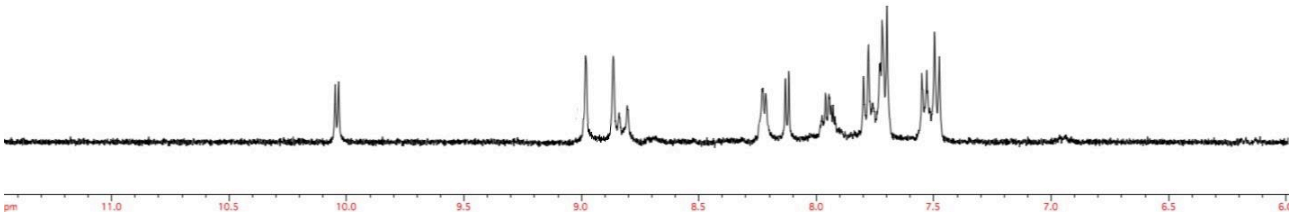

Figure A3.4: ^{1}H-NMR of **D4**, CD_3OD. From ref 210

Table A3.1: Major atom contribution (%) to HSOMO in the oxidized moieties

D1	**%**	**D3**	**%**	**D4**	**%**	**N719**	**%**
Ru (63)	11,17	**C (72)**	9,65	**C (59)**	7,55	**S (52)**	45,25
C (6)	7,12	**C (74)**	9,54	**C (74)**	7,44	**S (53)**	36,72
C (4)	6,30	**C (57)**	8,84	**C (57)**	7,41	**C (48)**	7,66
C (57)	6,02	**C (59)**	8,55	**C (72)**	7,27	**C (49)**	6,65
C (12)	5,70	**N (85)**	5,89	**Br (84)**	6,66	**N (50)**	1,42
C (55)	5,47	**N (87)**	5,28	**Br (85)**	6,56	**N (51)**	1,08

C (11)	5,39	**Ru (83)**	1,92	**Ru (83)**	1,06	**Ru**	<1

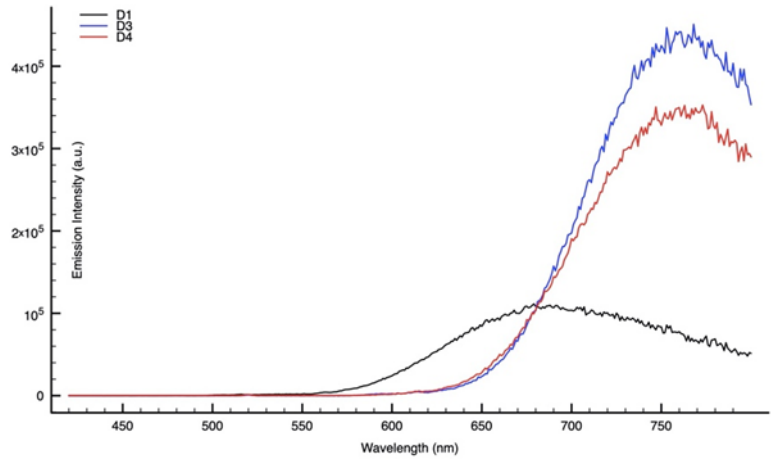

Figure A3.5: Emission spectra of the **D**-series recorded in methanol (**D3** and **D4**) and ethanol/TBAOH (**D1**), 298K. From ref 210

Dye	**λ_{emi}**	**E^{00}**	**λ_{emi} 10% emi max**	**E^{00} (10% rule)**
D1*	686	1.81	583	2.13
D3	760	1.63	662	1.87
D4	760	1.63	654	1.90

*= measured in EtOH/TBAOH

$E^{00} = 1240,8/\lambda_{emi}$

E^{00} (10% rule) = energy estimated at the 10% of the emission intensity observed at λ_{max}

CHAPTER 4a: Recombination and regeneration dynamics in Fe(II)NHC-sensitized solar cells

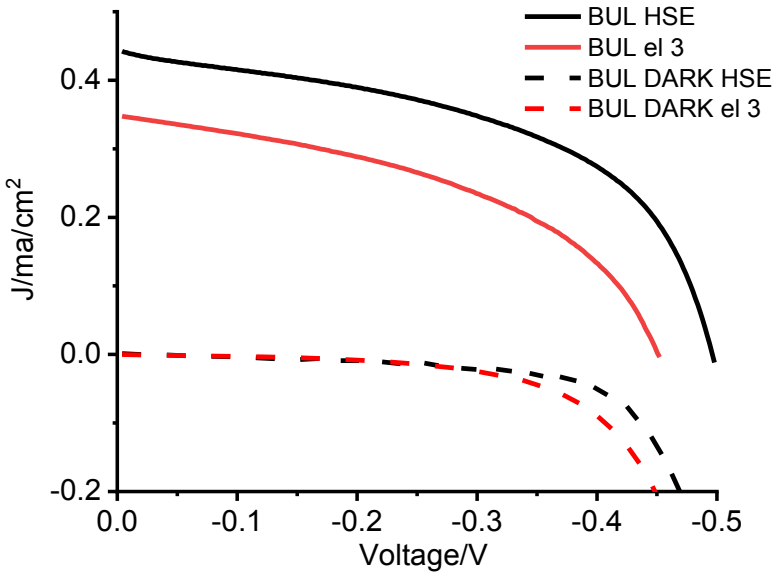

Figure A4.1: J-V curves of **C1**/TiO_2 sensitized solar cells under AM 1.5G illumination in the presence of HSE and 4-TBPy. From ref 237

(a) (b)

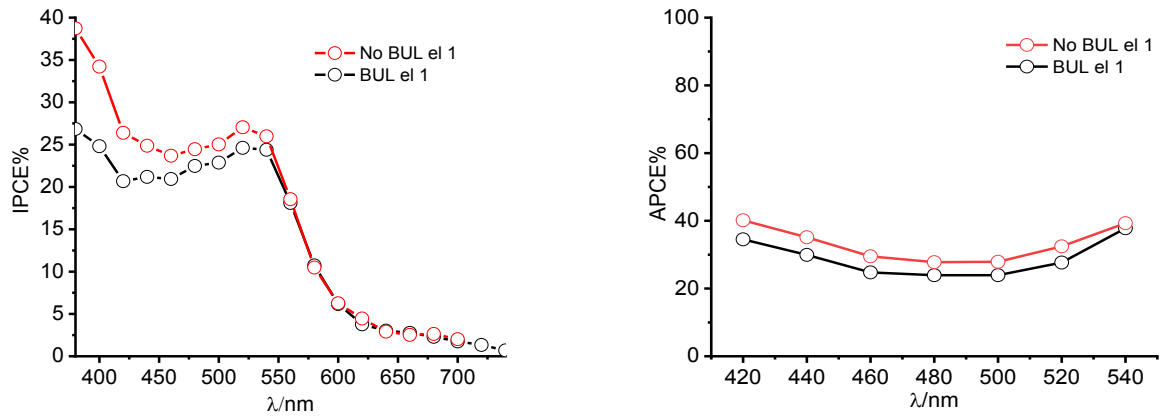

Figure A4.2: (la) IPCE curves recorded with transparent **C1** /SnO_2 with (black) and without (red) blocking underlayer. (b) APCE spectra. Spectra recorded under + 0.2 V bias corresponding to the plateau of the J-V characteristics in **Figure A4.3**. From ref 237

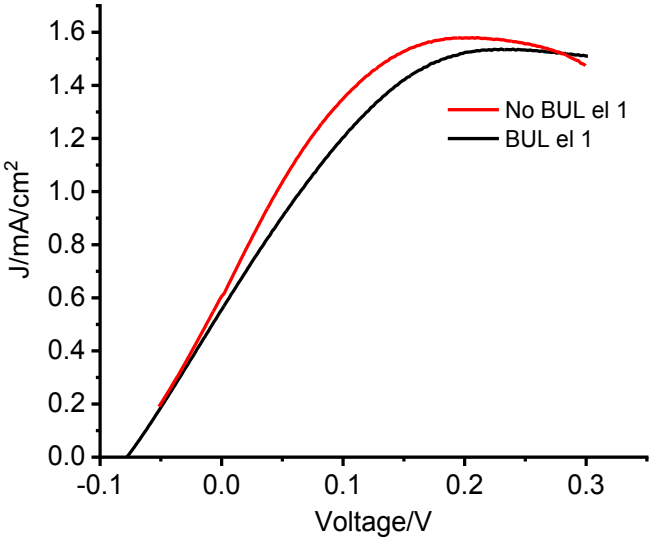

Figure A4.3: J-V curves of **C1** /SnO_2 sensitized solar cells under AM 1.5G illumination in the presence of *el1*. From ref 237

CHAPTER 4b: Record power conversion efficiencies for iron(II)-NHC-sensitized DSSCs from rational molecular engineering and electrolyte optimization

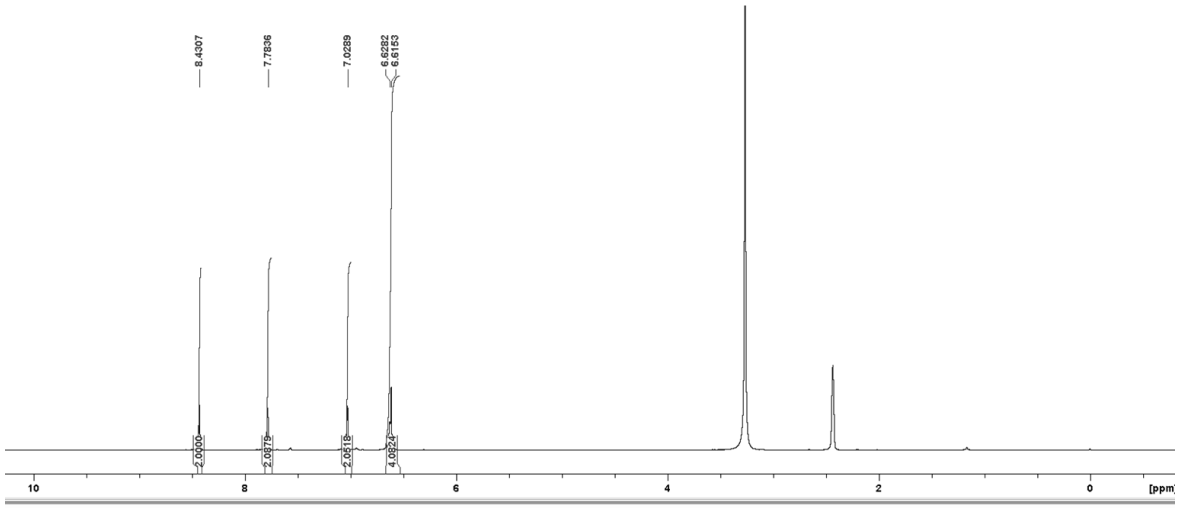

Figure A4.4: ^{1}H NMR spectrum of compound **1**, DMSO-d_6. From ref 254

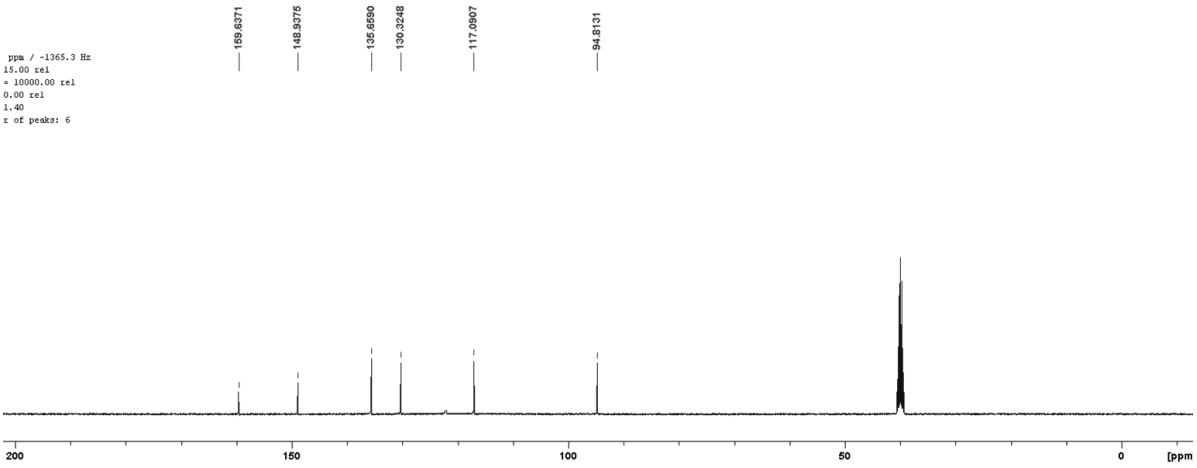

Figure A4.5: ^{13}C NMR spectrum of compound **1**, DMSO-d_6. From ref 254

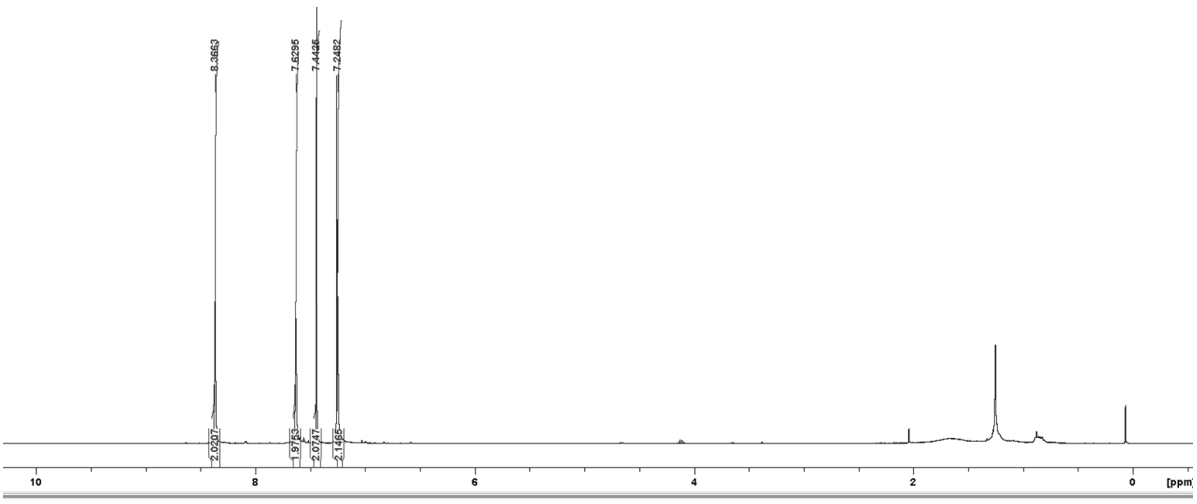

Figure A4.6: ^{1}H NMR spectrum of compound **2**, $CDCl_3$. From ref 254

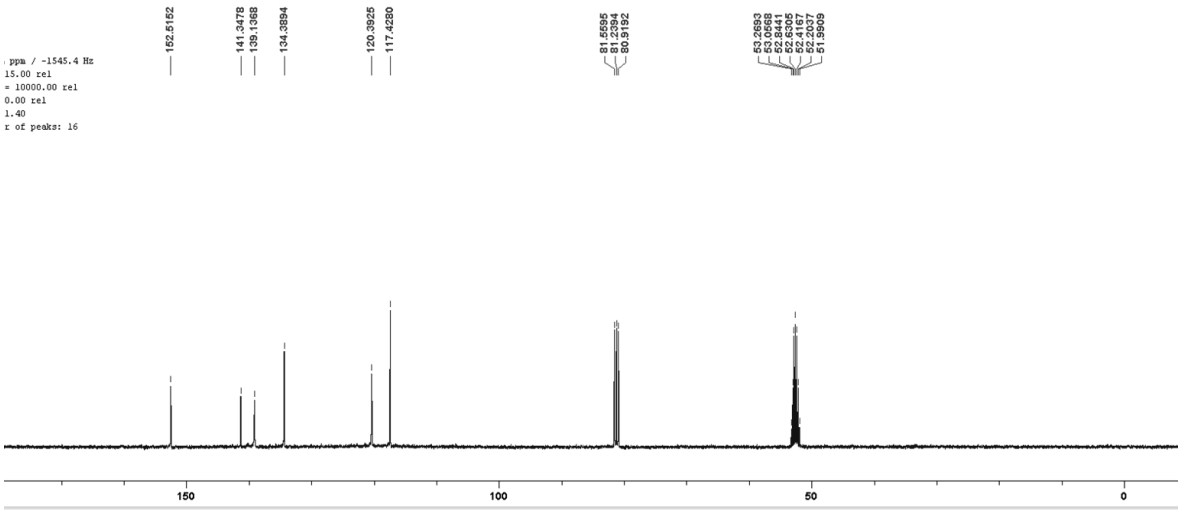

Figure A4.7: ^{13}C NMR spectrum of compound **2**, $CDCl_3$+CD_3OD. From ref254

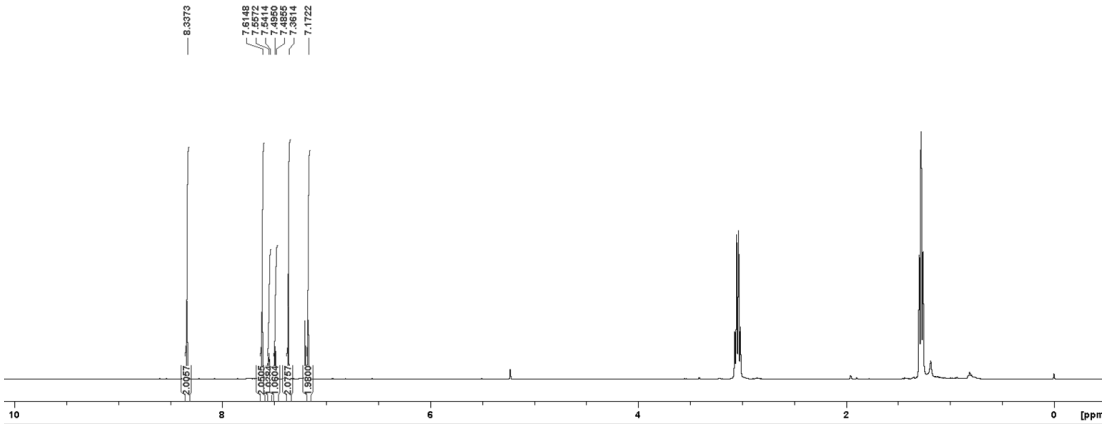

Figure A4.8: ^{1}H NMR spectrum of compound 3, $CDCl_3$ + TEA. From ref 254

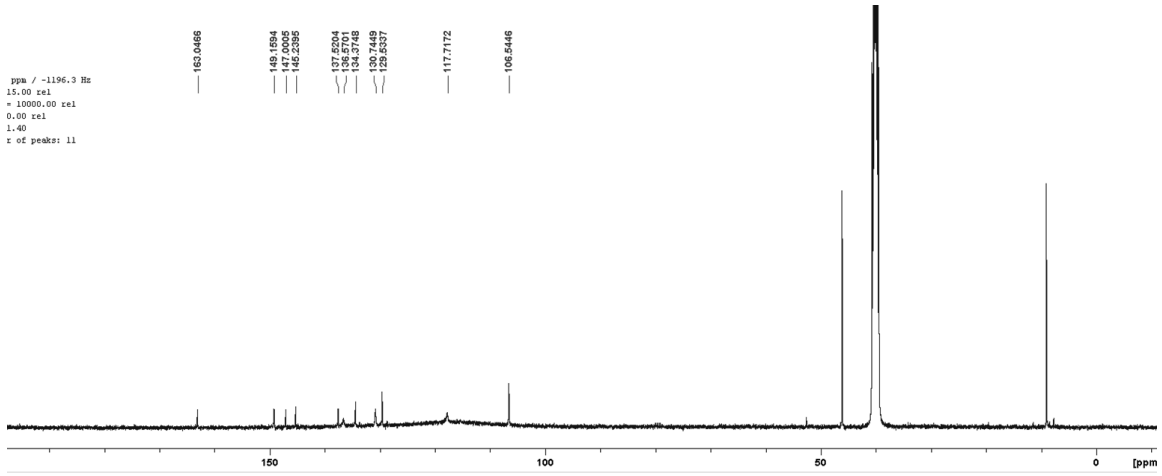

Figure A4.9: 13C NMR spectrum of compound **3**, DMSO-d6 + TEA. From ref 254

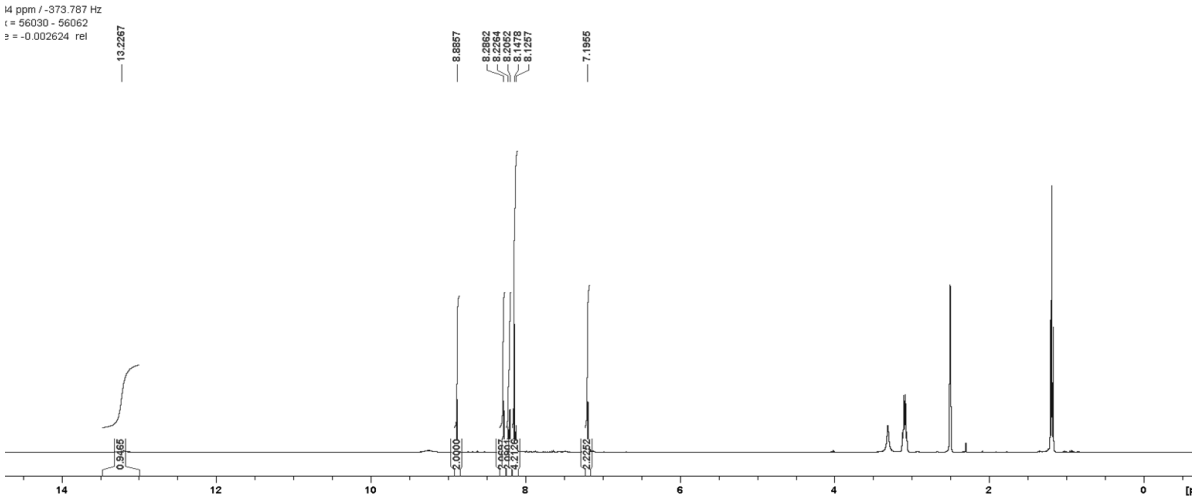

Figure A4.10: ^{1}H NMR spectrum of compound **4**, DMSO-d_6 + TEA. From ref 254

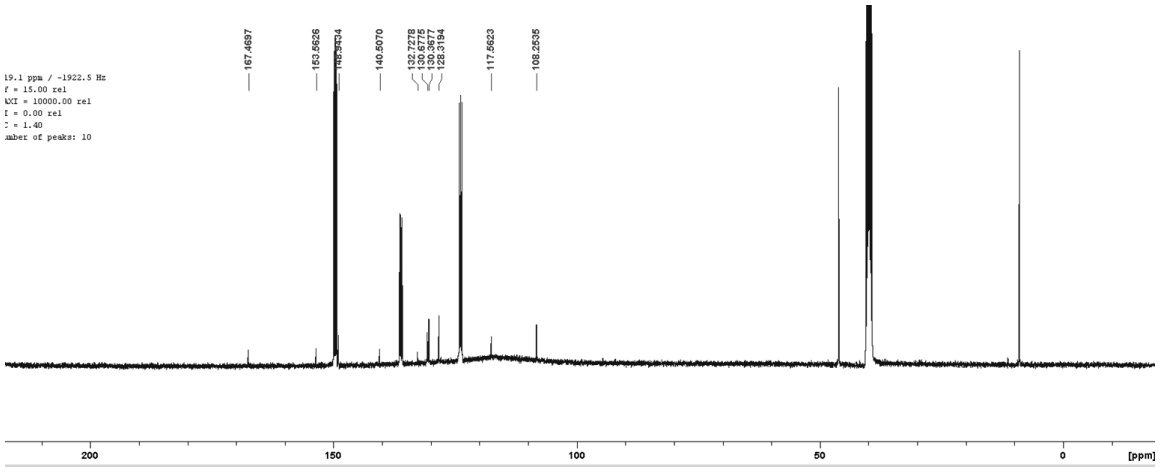

Figure 4.11: ^{13}C NMR spectrum of compound **4**, DMSO-d_6 + pyridine-d_5 + TEA. From ref 254

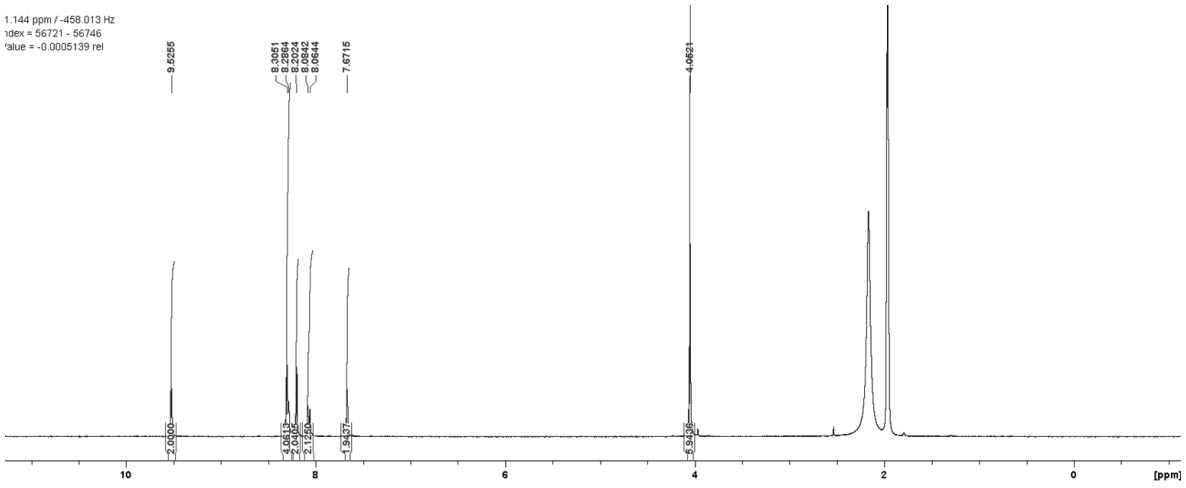

Figure A4.12: ^{1}H NMR spectrum of **L1**, CD_3CN. From ref 254

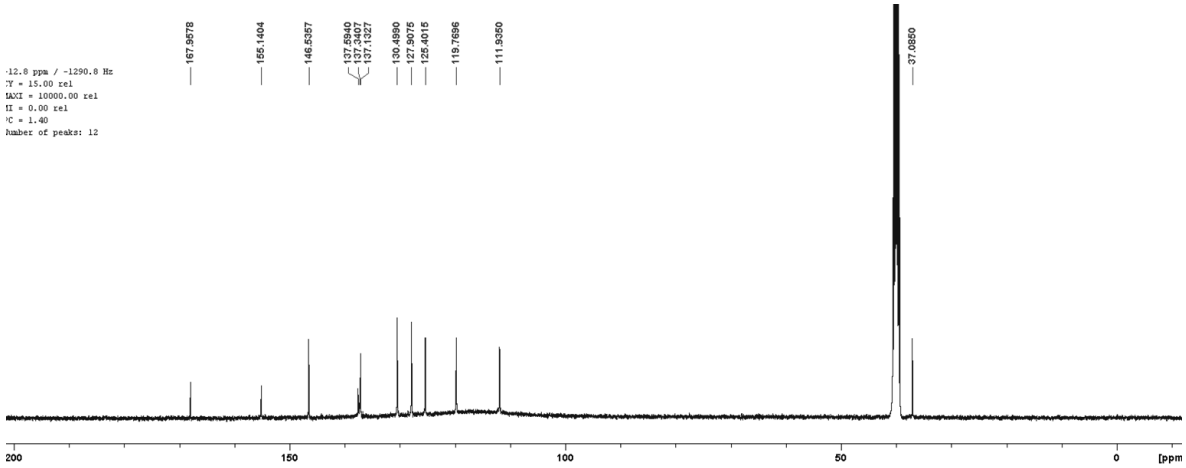

Figure A4.13: ^{13}C NMR spectrum of **L1**, DMSO-d_6. From ref 254

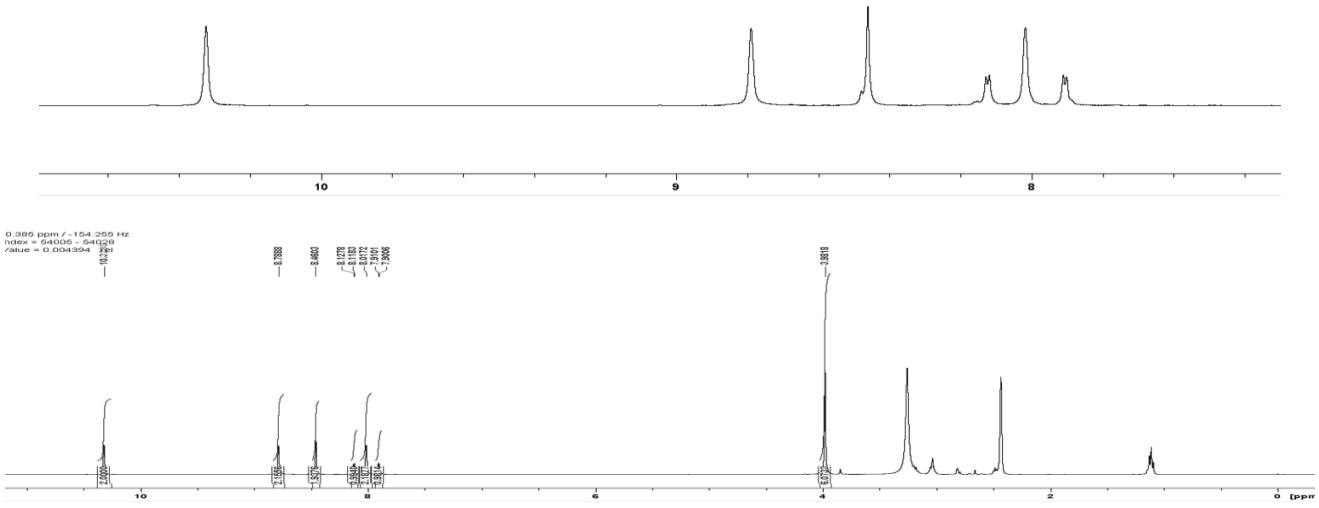

Figure A4.14: ^{1}H NMR spectrum of **L2**, DMSO-d_6. From ref 254

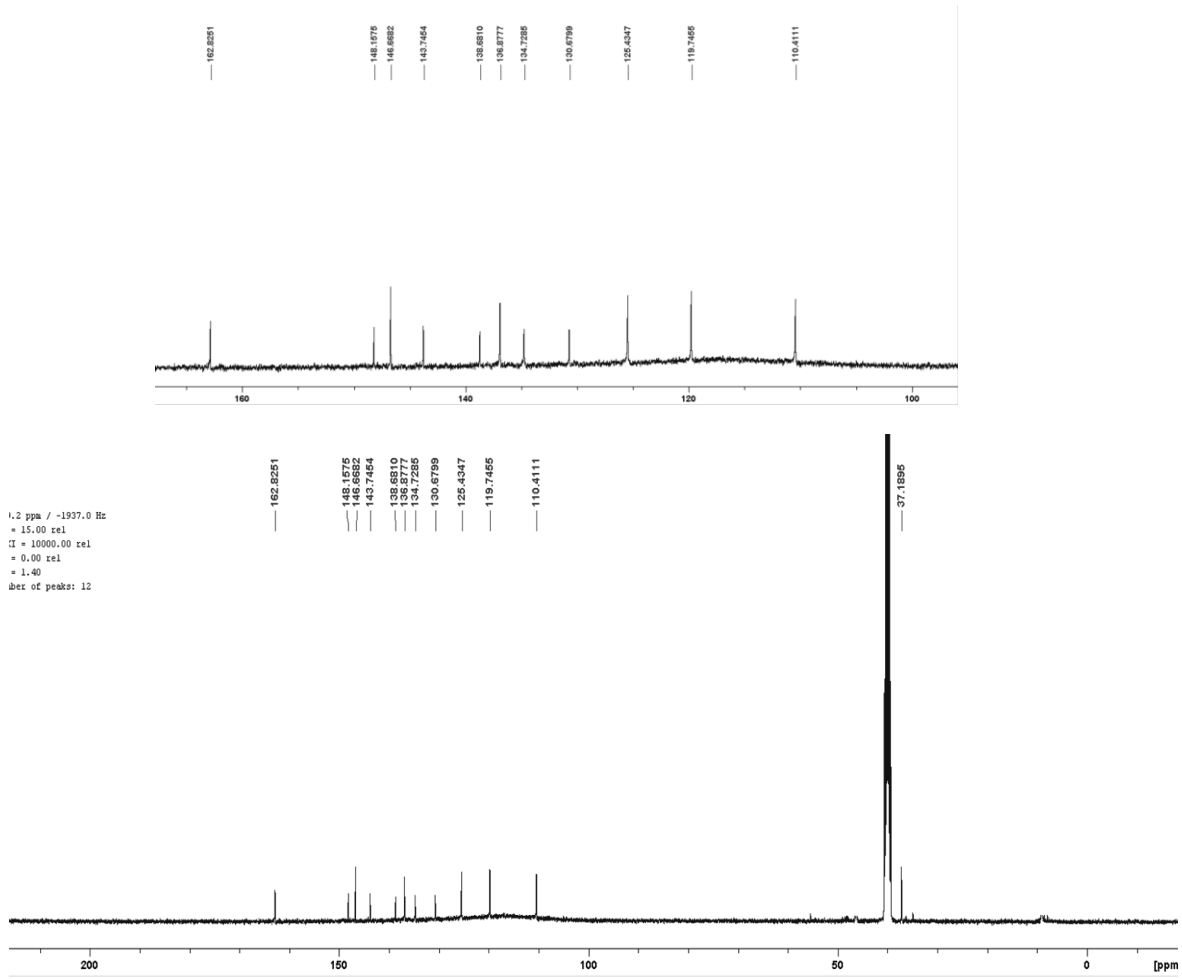

Figure A4.15: ^{13}C NMR spectrum of **L2**, DMSO-d_6. From ref 254

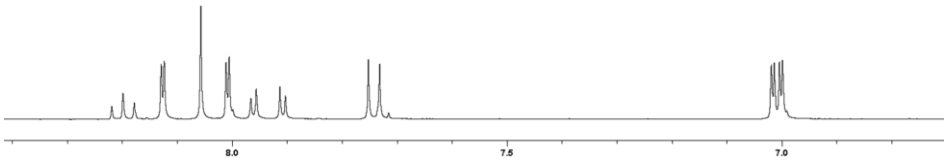

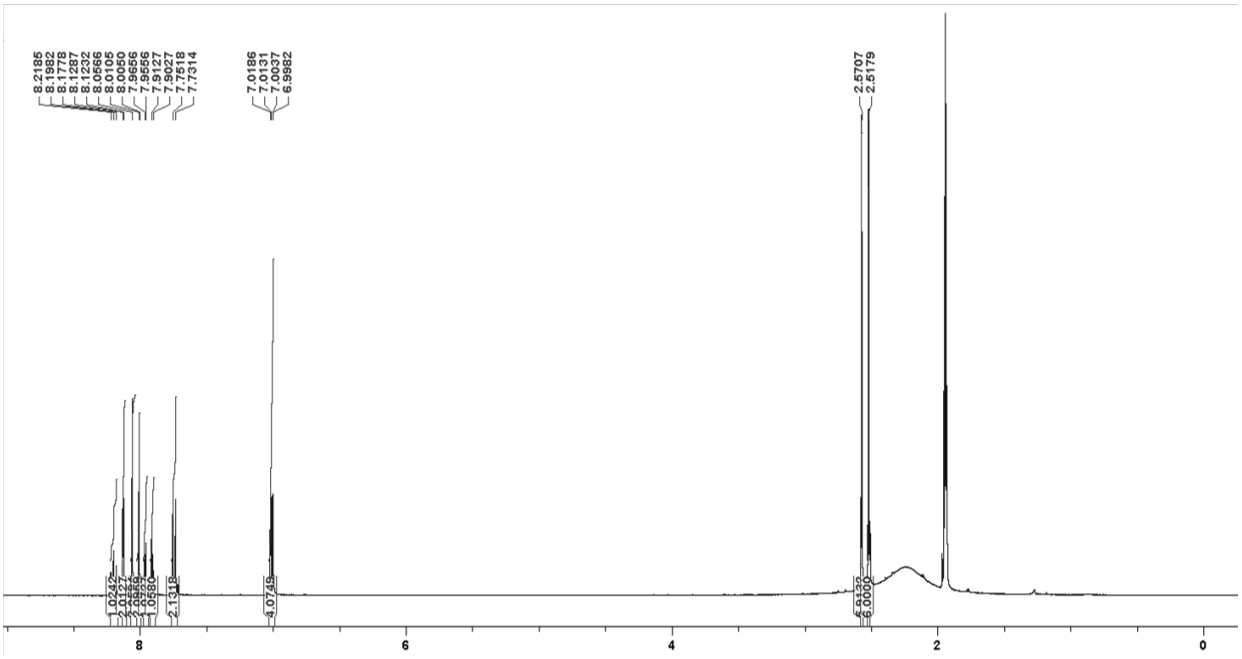

Figure A4.16: ^{1}H NMR spectrum of **ARM7**, CD_3CN. From ref 254

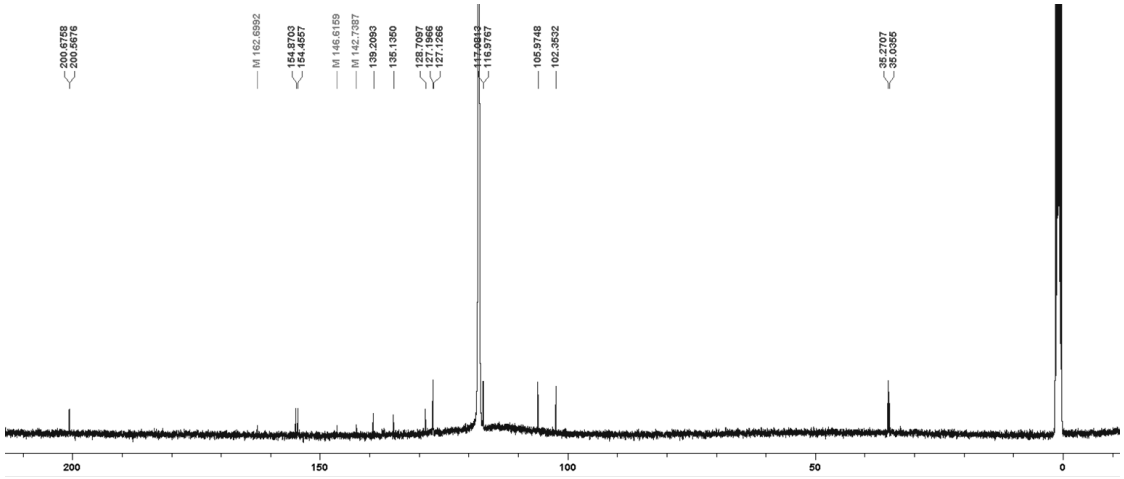

Figure A4.17: ^{13}C NMR spectrum of **ARM7**, CD_3CN. From ref 254

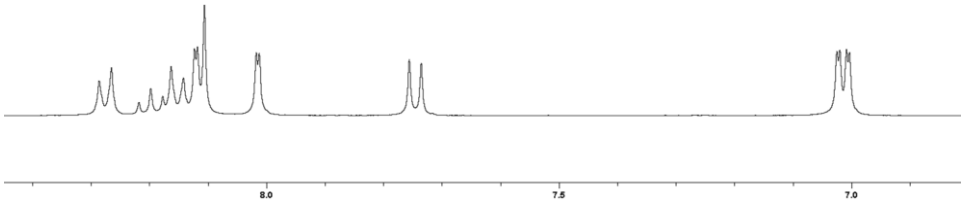

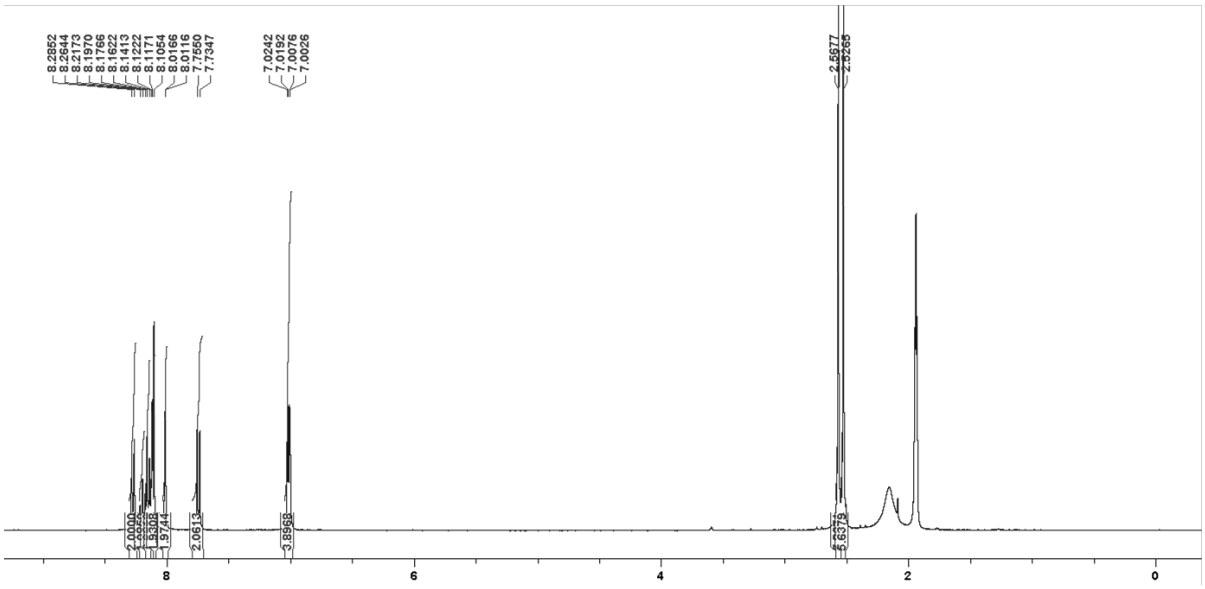

Figure A4.18: ^{1}H NMR spectrum of **ARM-11**, CD_3CN. From ref 254

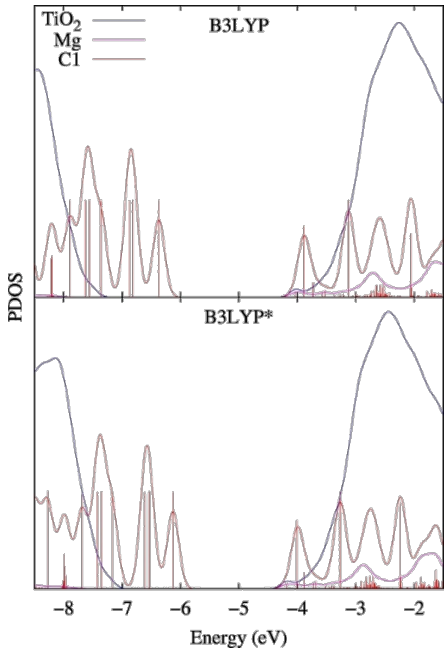

Figure A19: Projected Density of States (PDOS) of the **C1**/Mg-TiO_2 systems over the atoms belonging to the **C1** dye (red), TiO_2 surface (blue) and Mg^{2+} cation (magenta) moieties as calculated by Mulliken population analysis and employing B3LYP (top) and B3LYP*(HF xc=15%, bottom panel) functionals. Note that for the sake of a better visualization, only the vertical bars conforming the **C1** DOS are represented here and the TiO_2 DOS intensity has been divided by a factor of 10. From ref 254

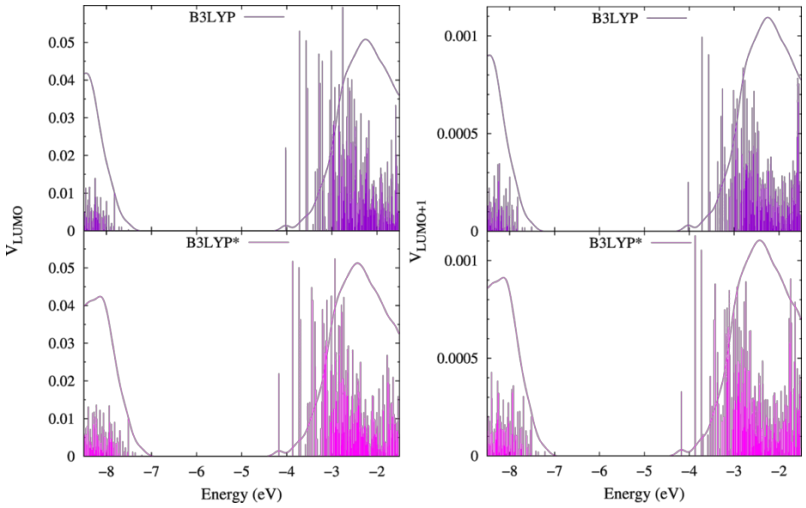

Figure A4.20: Electronic coupling *V* between the frontier unoccupied MOs of **C1** and the states of the TiO_2-Mg surface (vertical bars); and diabatic TiO_2-Mg DOS (continuous lines), as calculated by using B3LYP (purple) and B3LYP* (magenta color) functionals. From ref 254

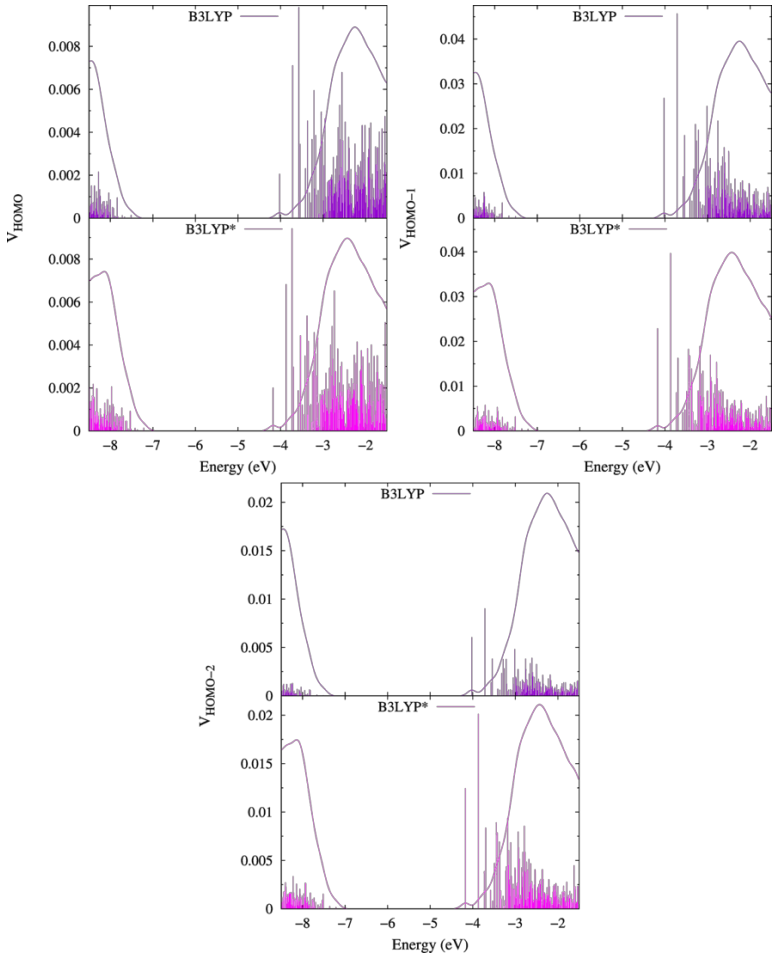

Figure A4.21: Electronic coupling *V* between the frontier occupied MOs of **C1** and the states of the TiO_2-Mg surface (vertical bars); and diabatic TiO_2-Mg DOS (continuous lines), as calculated by using B3LYP (purple) and B3LYP* (magenta color) functionals. From ref 254

Table A4.1: Probability distributions (Γ) and related recombination/injection lifetimes (τ) calculated at the diabatic H-2, H-1, HOMO, LUMO and L+1 energies, as estimated by employing B3LYP and B3LYP* functionals. The relevant diabatic injection properties are marked with orange color

Functional	Γ_{H-2} (eV)	Γ_{H-1} (eV)	Γ_{HOMO} (eV)	Γ_{LUMO} (eV)	Γ_{L+1} (eV)
B3LYP	3.32E-08	4.71E-07	1.56E-10	0.1640	5.36E-05
B3LYP*	1.83E-07	5.87E-07	3.40E-10	0.1673	7.54E-05
	τ_{H-2} (fs)	τ_{H-1} (fs)	τ_{HOMO} (fs)	τ_{LUMO} (fs)	τ_{L+1} (fs)
B3LYP	1.98E+07	1.40E+06	4.21E+09	4.01	12273
B3LYP*	3.61E+06	1.12E+06	1.93E+09	3.93	8723

Table A4.2: Diabatic energy levels for the dye (H-2, H-1, HOMO, LUMO and L+1 energies) and TiO_2 surface (Conductance Band Minimum (CBM) and Valence Band Minimum (VBM)) with their corresponding energy gaps (E_g), for **C1**/TiO_2, **C1**/Mg-TiO_2, **ARM13**/TiO_2 and **ARM13**/Mg-TiO_2 systems. All values are given in eV

Dye/TiO_2	H-2	H-1	HOMO	LUMO	L+1	E_g/Dye	VBM	CBM	E_g/TiO_2
C1	-6.11	-6.08	-5.72	-3.04	-2.66	2.66	-7.07	-3.34	3.72
C1-Mg	-6.54	-6.52	-6.11	-3.38	-3.26	2.74	-7.21	-4.17	3.04
ARM13	-5.98	-5.96	-5.61	-2.6	-2.29	3.01	-7.05	-3.34	3.71
ARM13-Mg	-6.43	-6.41	-6.02	-3.34	-2.55	2.69	-7.21	-4.17	3.05

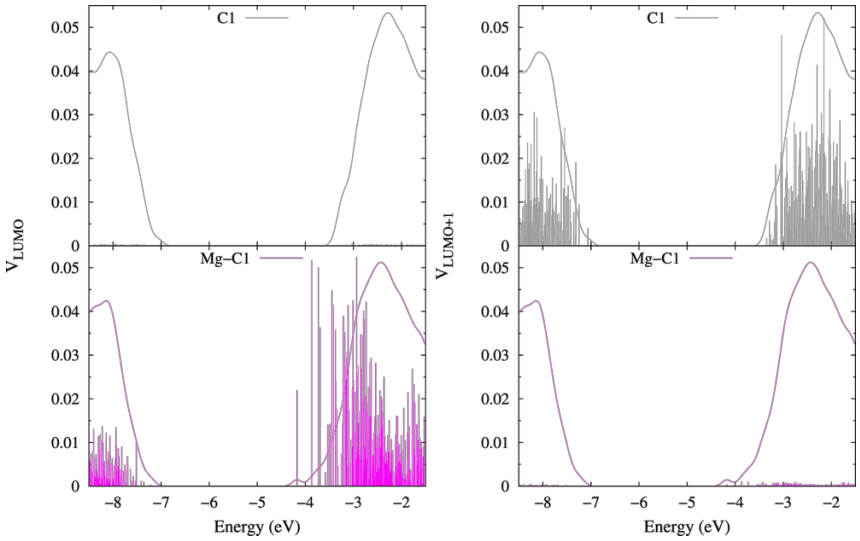

Figure A4.22: Calculated electronic coupling V between the frontier unoccupied MOs of **C1** and the states of the TiO_2 (grey) and TiO_2-Mg (magenta color) surfaces (vertical bars); the corresponding diabatic TiO_2 and TiO_2-Mg DOS (dashed lines) are also reported. From ref 254

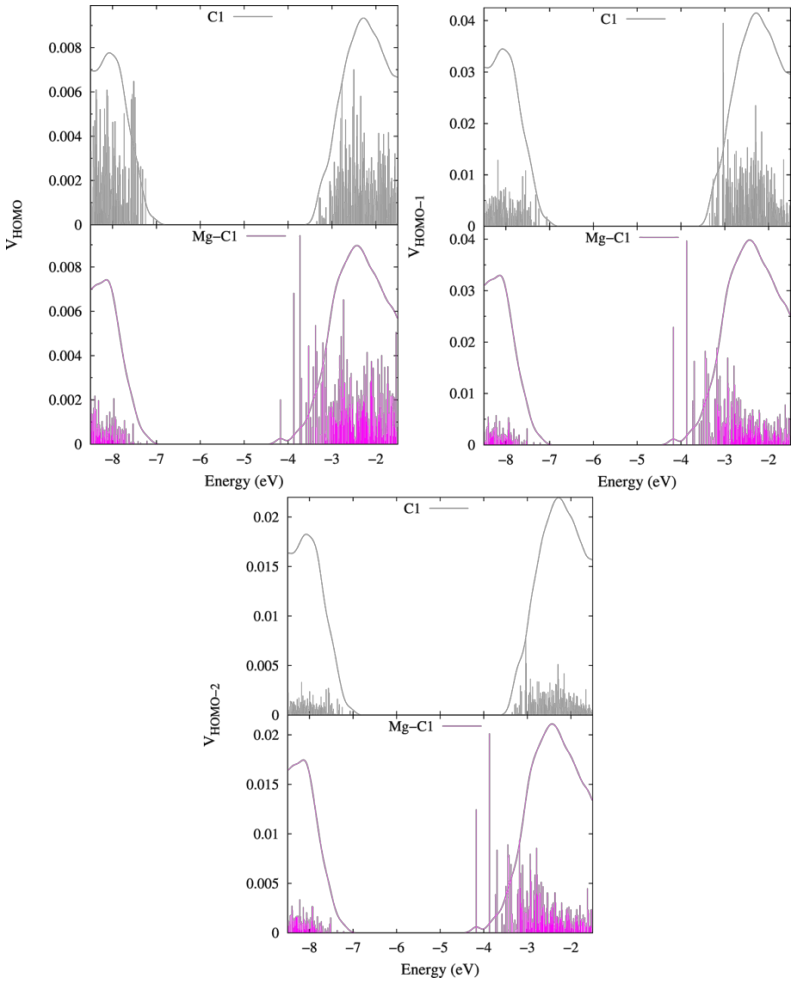

Figure A4.23: Calculated electronic coupling *V* between the frontier occupied MOs of **C1** and the states of the TiO_2 (grey) and TiO_2-Mg (magenta color) surfaces (vertical bars); the corresponding diabatic TiO_2 and TiO_2-Mg DOS (dashed lines) are also reported. From ref 254

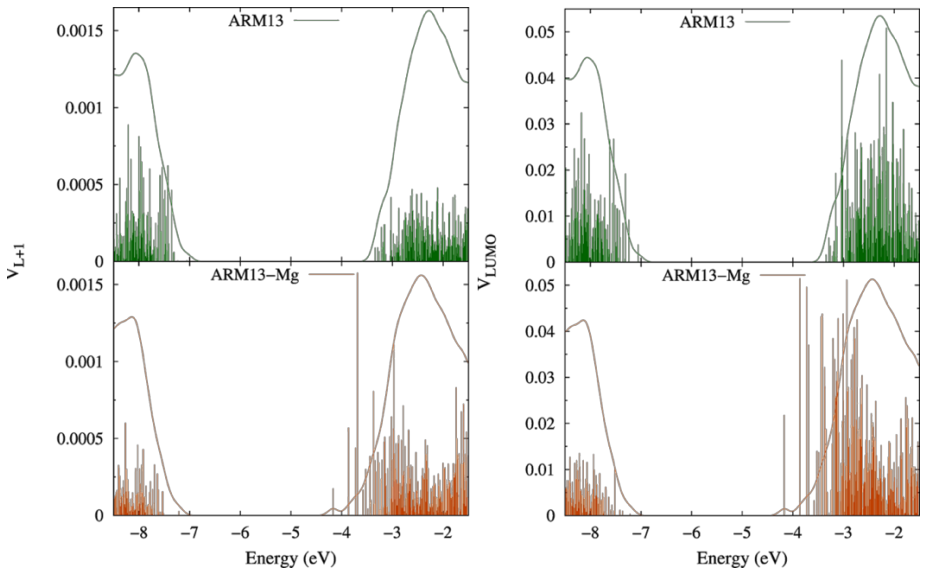

Figure A4.24: Calculated electronic coupling *V* between the frontier unoccupied MOs of **ARM13** and the states of the TiO_2 (grey) and TiO_2-Mg (magenta color) surfaces (vertical bars); the corresponding diabatic TiO_2 and TiO_2-Mg DOS (dashed lines) are also reported. From ref 254

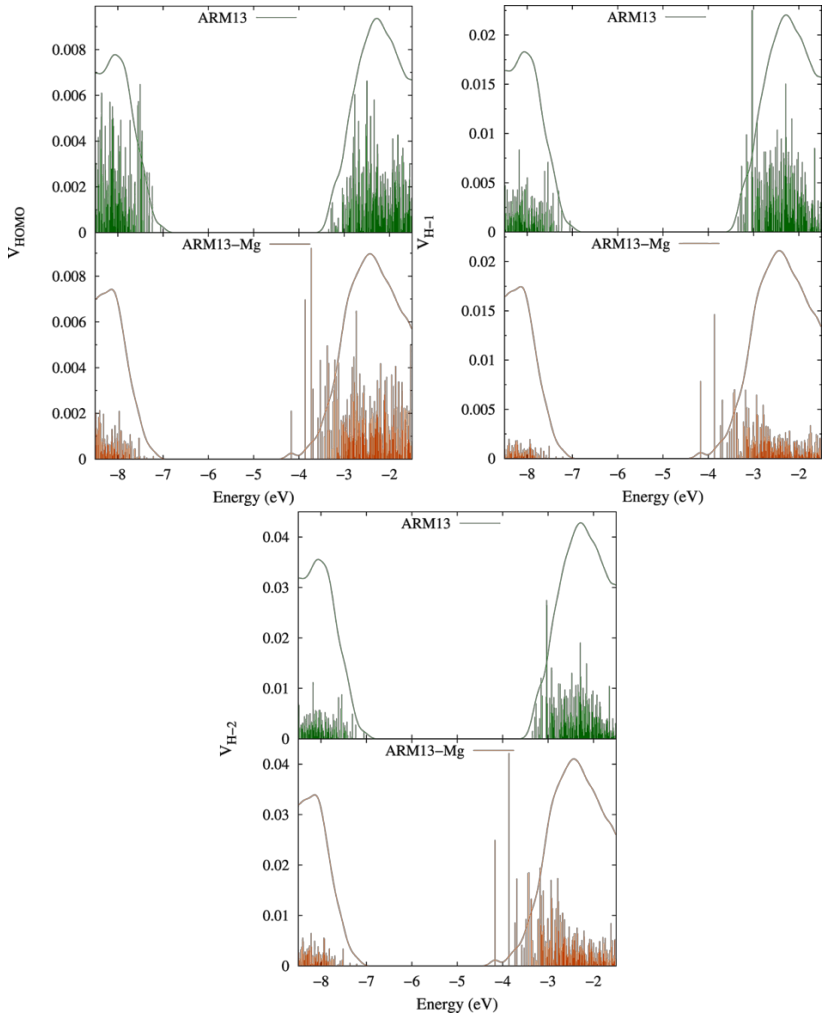

Figure A4.25: Calculated electronic coupling V between the frontier occupied MOs of **ARM13** and the states of the TiO_2 (grey) and TiO_2-Mg (magenta color) surfaces (vertical bars); the corresponding diabatic TiO_2 and TiO_2-Mg DOS (dashed lines) are also reported. From ref 254

Table A4.3: Probability distributions (Γ) and related recombination/injection lifetimes (τ) calculated at the diabatic H-2, H-1, HOMO, LUMO and L+1 energies for **C1**/TiO_2, **C1**/Mg-TiO_2, **ARM13**/TiO_2 and **ARM13**/Mg-TiO_2. The relevant diabatic injection properties are marked with orange color

Dye/TiO_2	Γ_{H-2} **(eV)**	Γ_{H-1} **(eV)**	Γ_{HOMO} **(eV)**	Γ_{LUMO} **(eV)**	Γ_{L+1} **(eV)**
C1	2.28E-08	2.83E-07	2.18E-10	1.12E-05	0.142
C1-Mg	1.83E-07	5.87E-07	3.40E-10	0.167	7.54E-05
ARM13	4.93E-08	2.62E-08	4.13E-11	0.152	3.07E-05
ARM13-Mg	2.49E-07	2.72E-08	9.13E-11	0.179	4.43E-05
	τ_{H-2} **(fs)**	τ_{H-1} **(fs)**	τ_{HOMO} **(fs)**	τ_{LUMO} **(fs)**	τ_{L+1} **(fs)**
C1	2.89E+07	2.32E+06	3.01E+09	58530	4.63
C1-Mg	3.61E+06	1.12E+06	1.93E+09	3.93	8723
ARM13	1.33E+07	2.51E+07	1.59E+10	4.33	21428
ARM13-Mg	2.64E+06	2.42E+07	7.20E+09	3.67	14840

CHAPTER 4c: A Series of Iron(II)-NHC Sensitizers with Remarkable Power Conversion Efficiency in Photoelectrochemical Cells

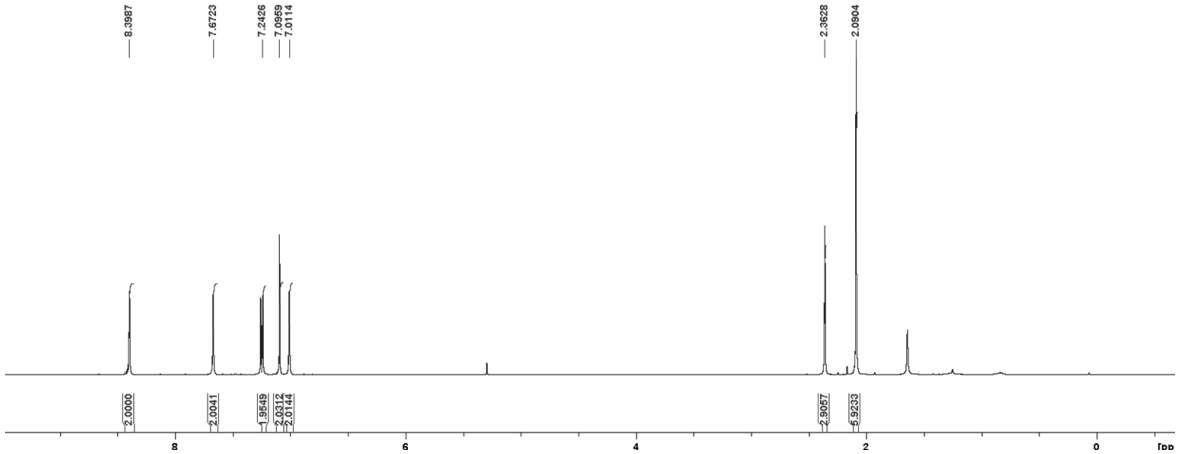

Figure A4.26: ^{1}H NMR spectrum of compound **2**, $CDCl_3$. From ref 257

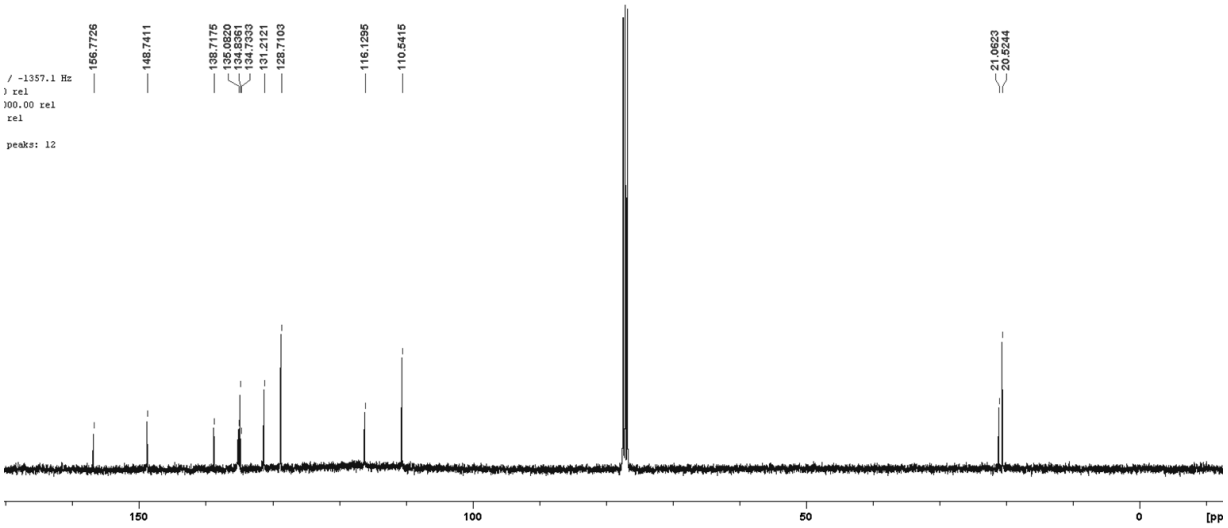

Figure A4.27: ^{13}C NMR spectrum of compound **2**, $CDCl_3$. From ref 257

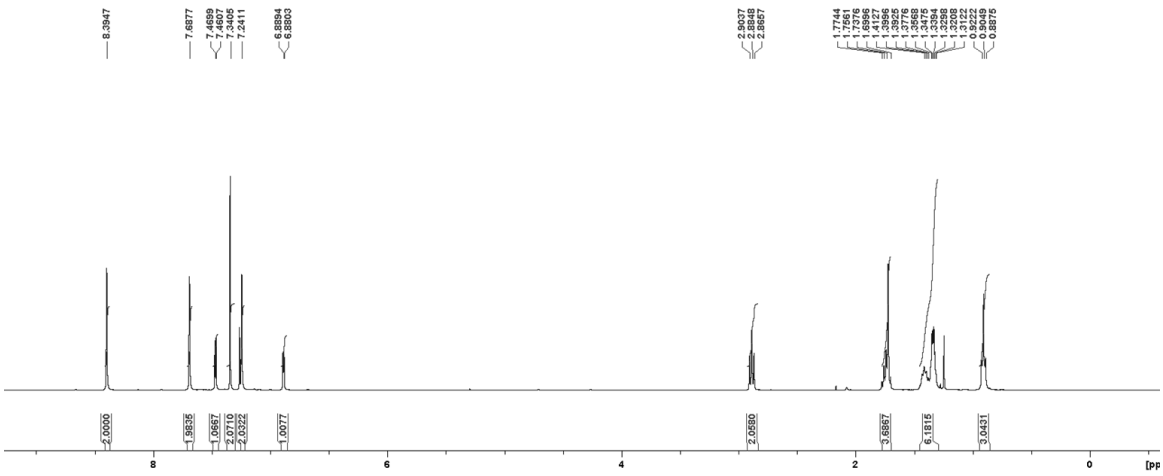

Figure A4.28: ^{1}H NMR spectrum of compound **3**, $CDCl_3$. From ref 257

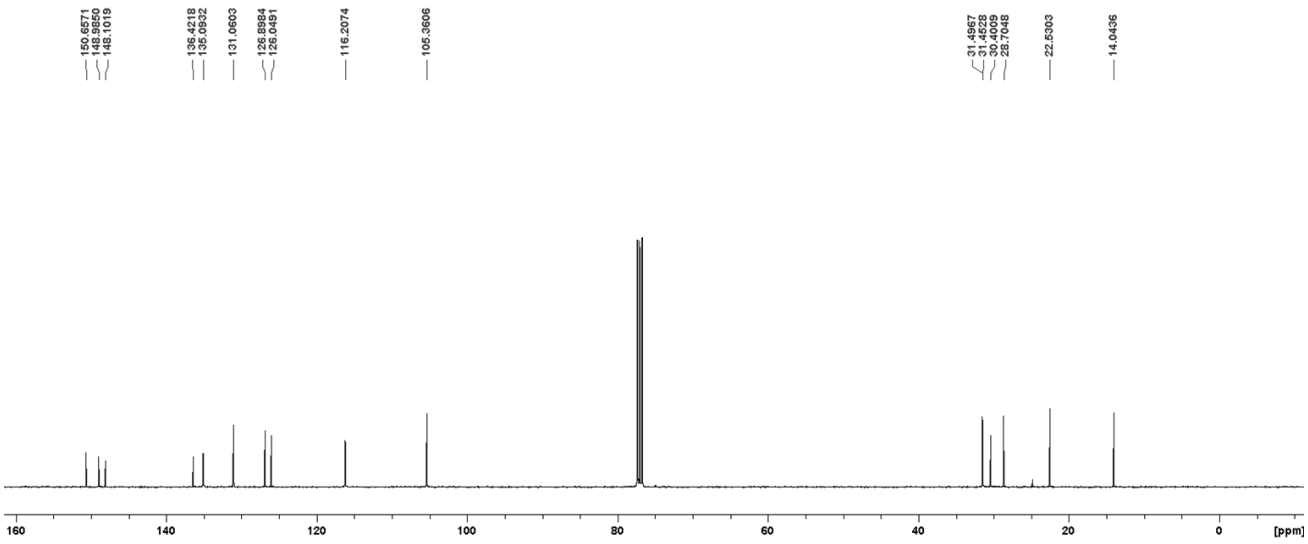

Figure A4.29.: ^{13}C NMR spectrum of compound **3**, $CDCl_3$. From ref 257

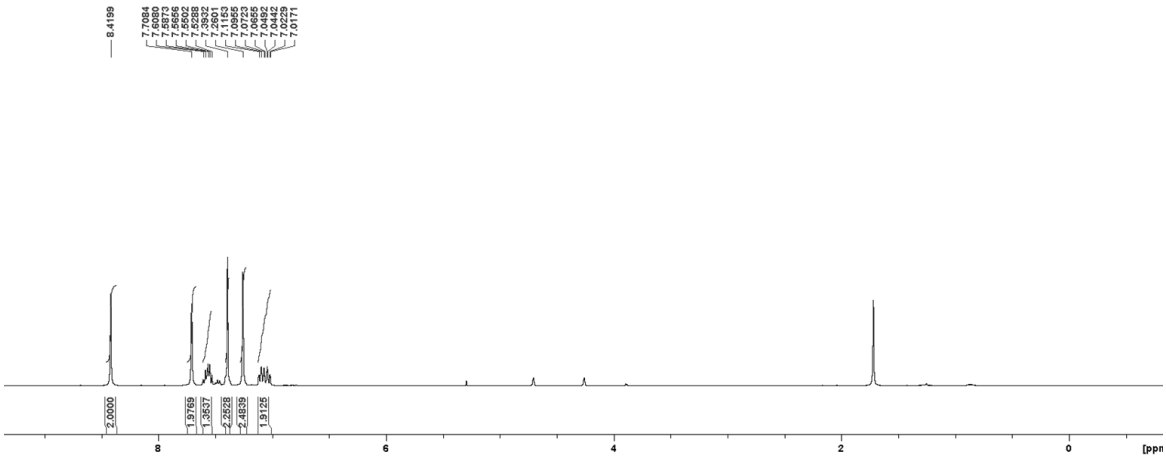

Figure A4.30: ^{1}H NMR of compound **4**, $CDCl_3$. From ref 257

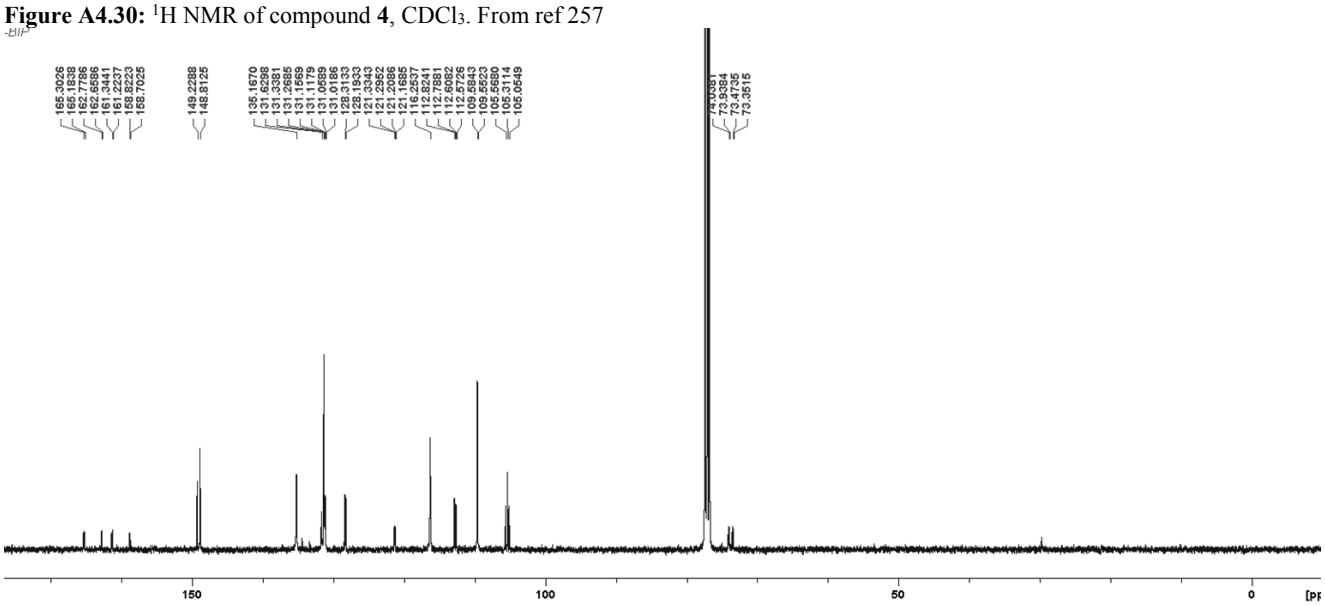

Figure A4.31: ^{13}C NMR of compound **4**, $CDCl_3$. From ref 257

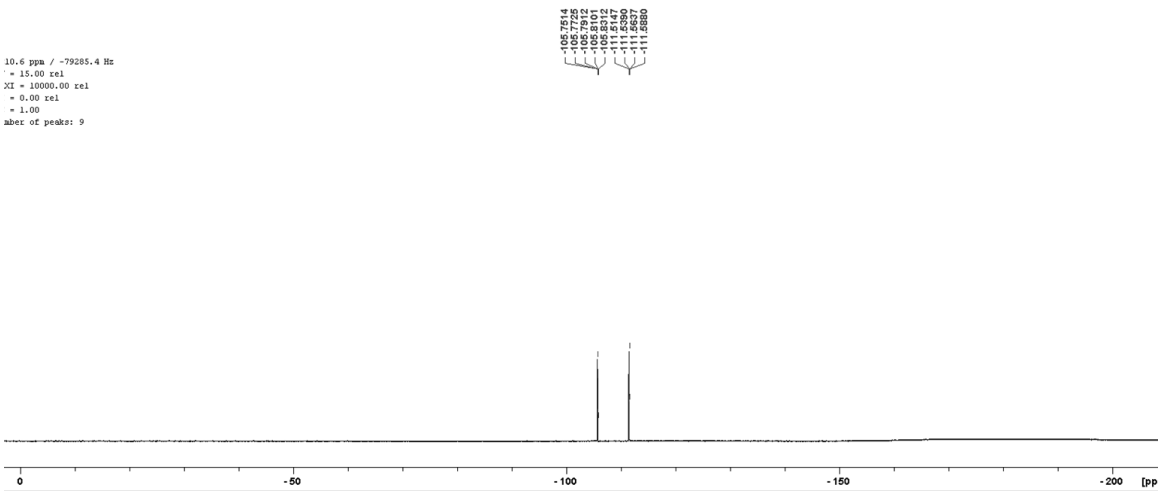

Figure A4.32: ^{19}F NMR of compound **4**, $CDCl_3$. From ref 257

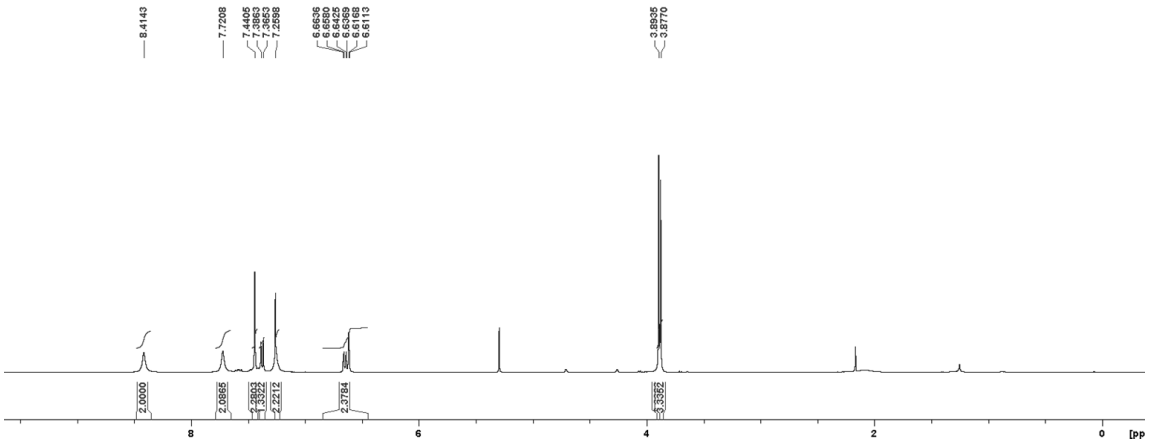

Figure A4.33: ^{1}H NMR spectra of compound **5**, $CDCl_3$. From ref 257

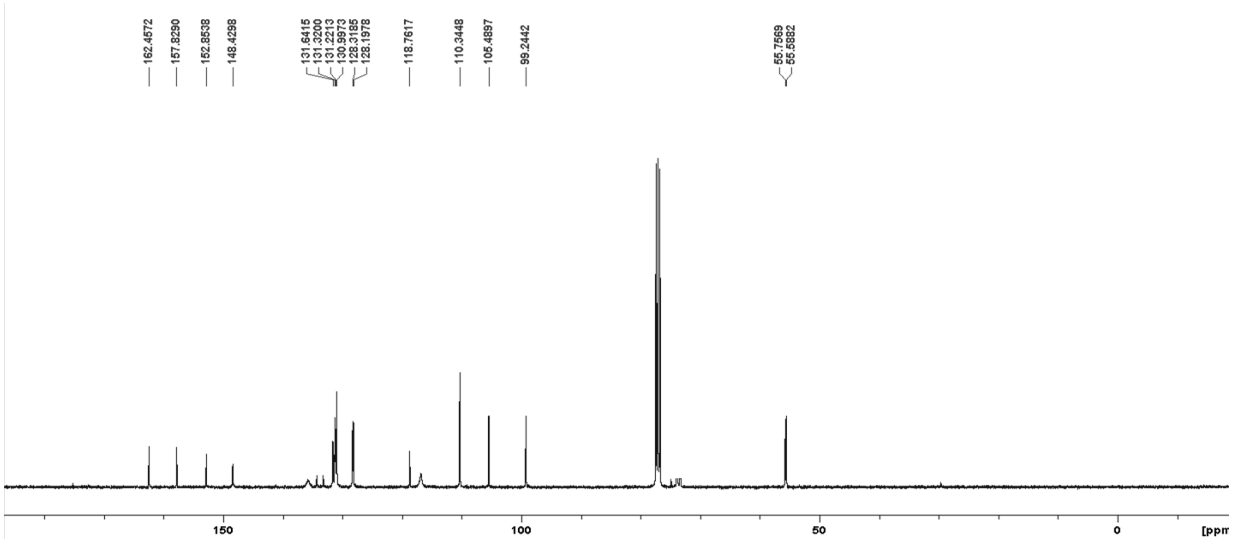

Figure A4.34: ^{13}C NMR spectra of compound **5**, $CDCl_3$. From ref 257

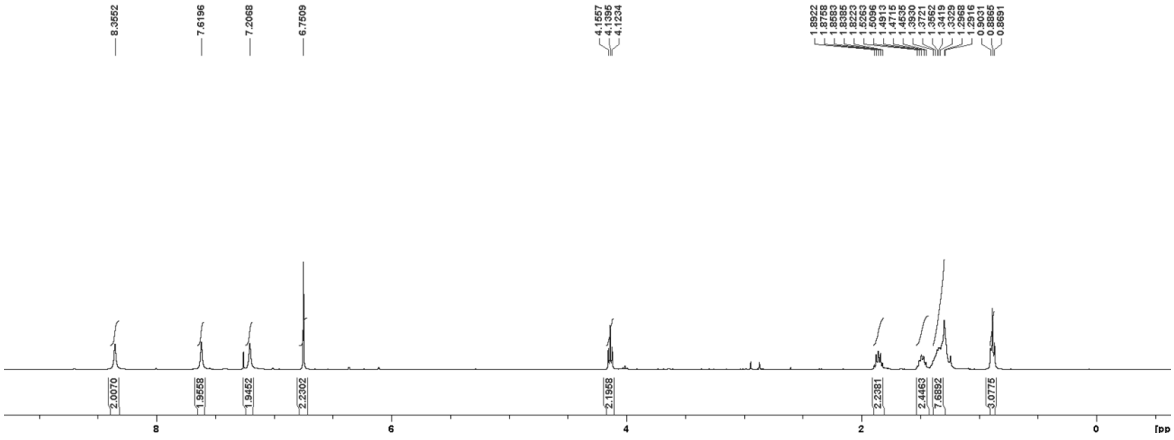

Figure A4.35: [1]H NMR spectrum of compound **8**, $CDCl_3$. From ref 257

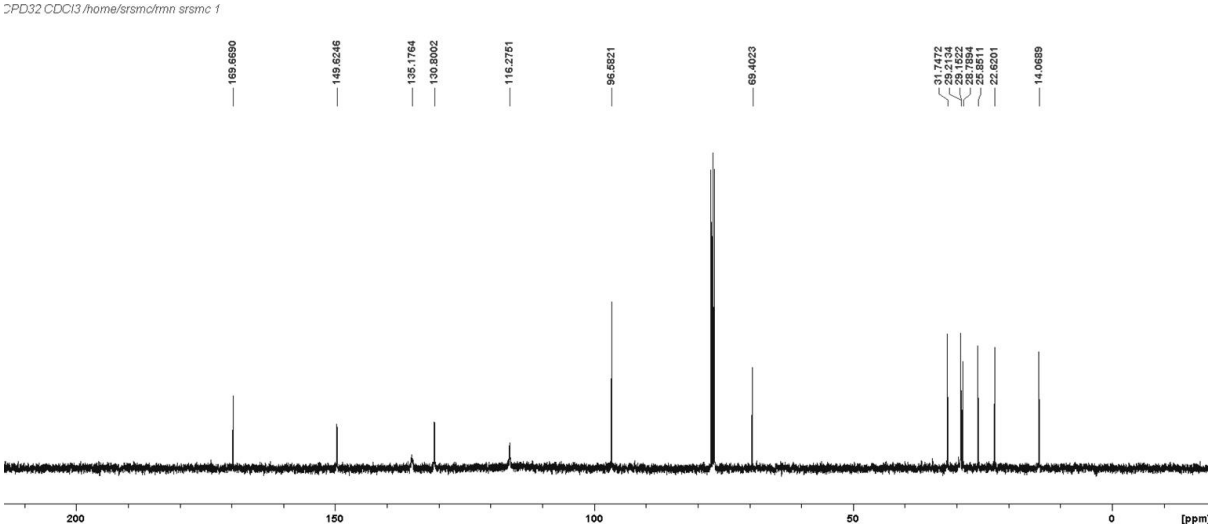

Figure A4.36: [13]C NMR spectrum of compound **8**, $CDCl_3$. From ref 257

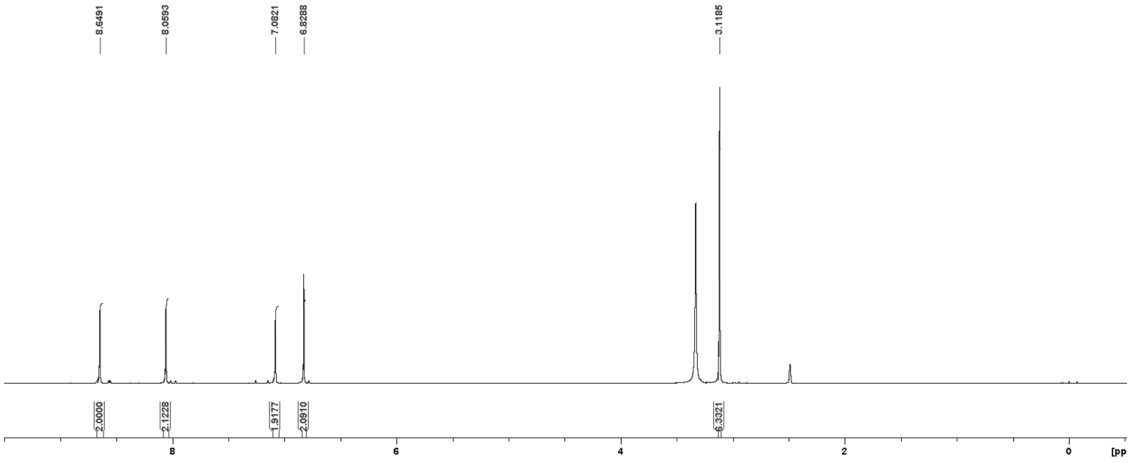

Figure A4.37: [1]H NMR spectra of compound **9**, DMSO-d_6. From ref 257

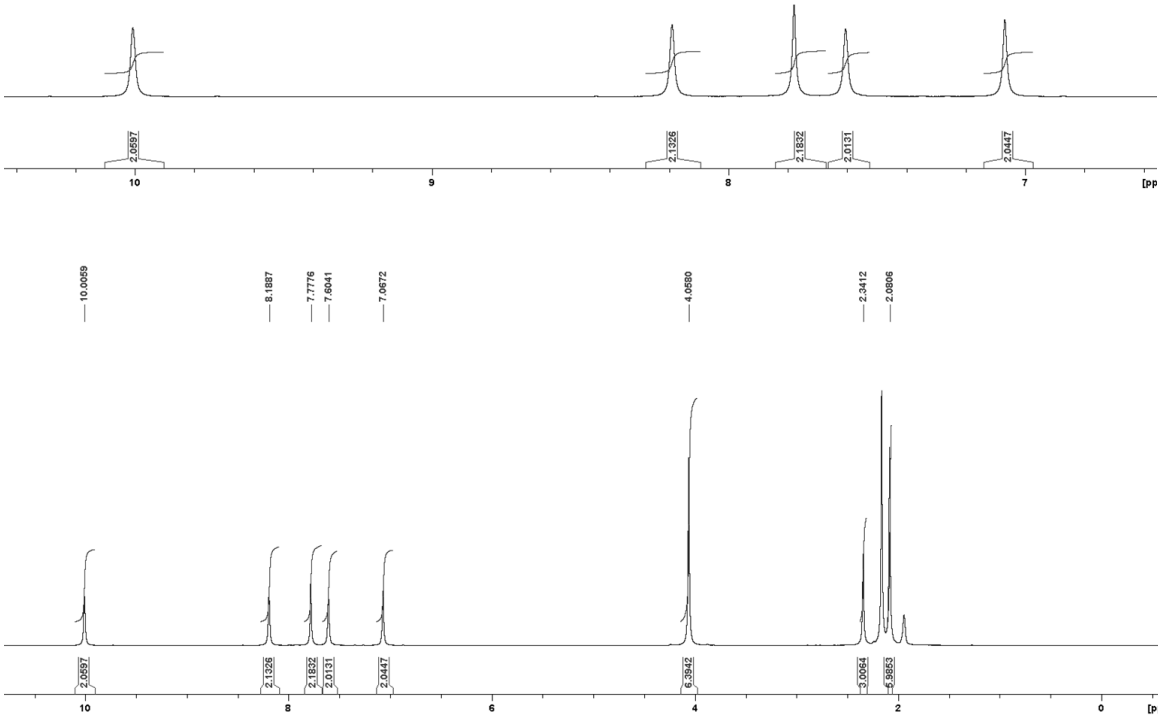

Figure A4.38: ^{1}H NMR spectrum of **L1**, CD_3CN. From ref 257

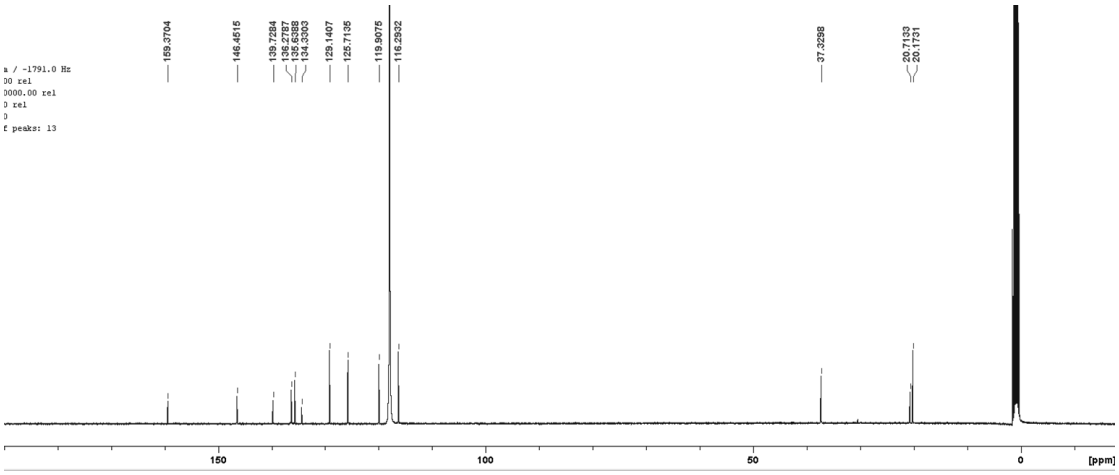

Figure A4.39: ^{13}C NMR spectrum of **L1**, CD_3CN. From ref 257

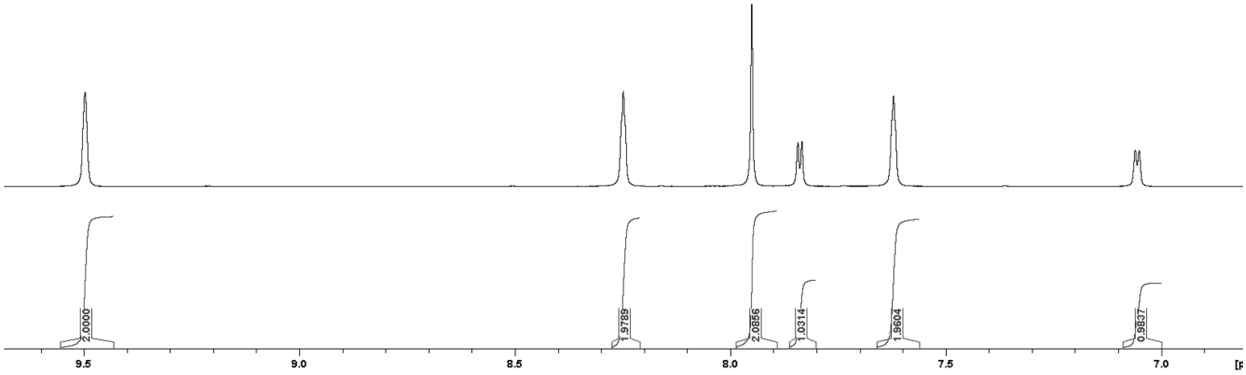

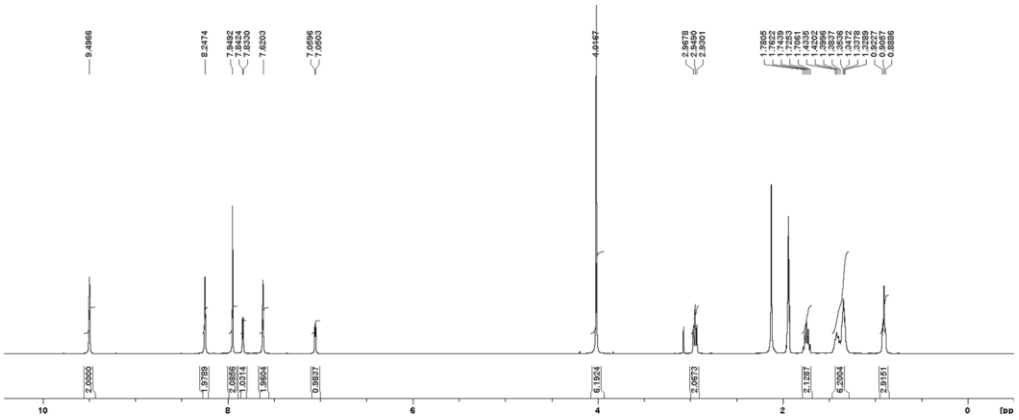

Figure A4.40: ^{1}H NMR spectrum of **L2**, CD_3CN. From ref 257

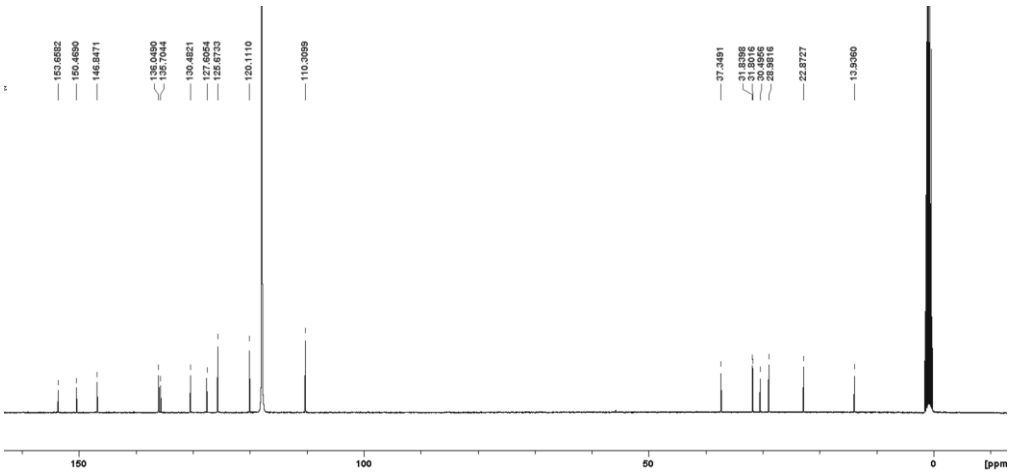

Figure A4.41: ^{13}C NMR spectrum of **L2**, CD_3CN. From ref 257

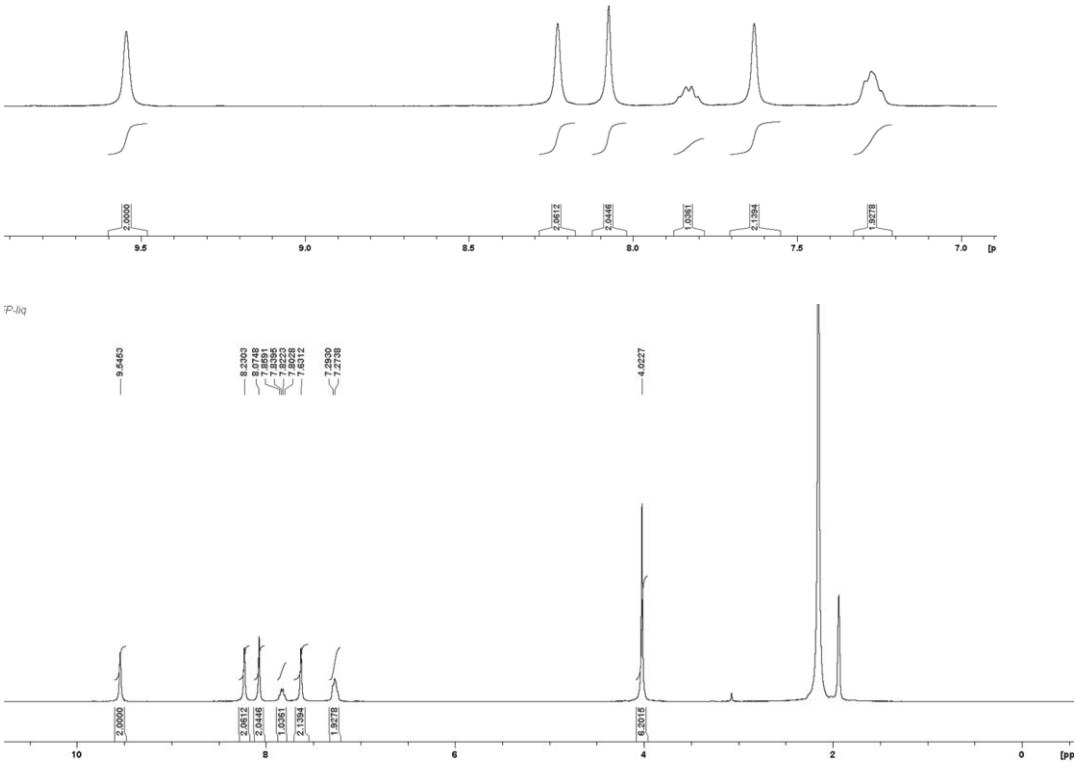

Figure A4.42: ^{1}H NMR of ligand **L3**, CD_3CN. From ref 257

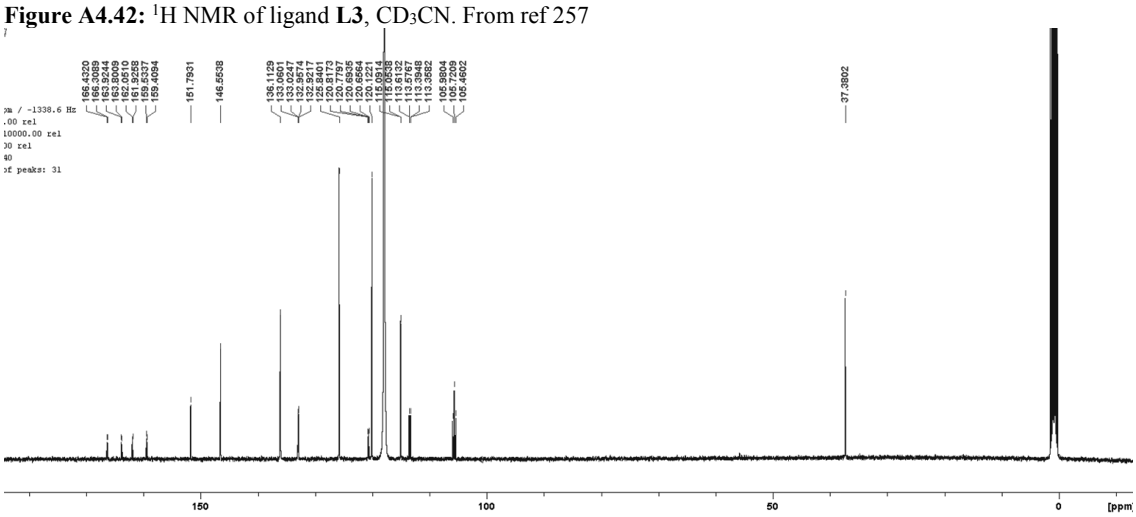

Figure A4.43: ^{13}C NMR of ligand **L3**, CD_3CN. From ref 257

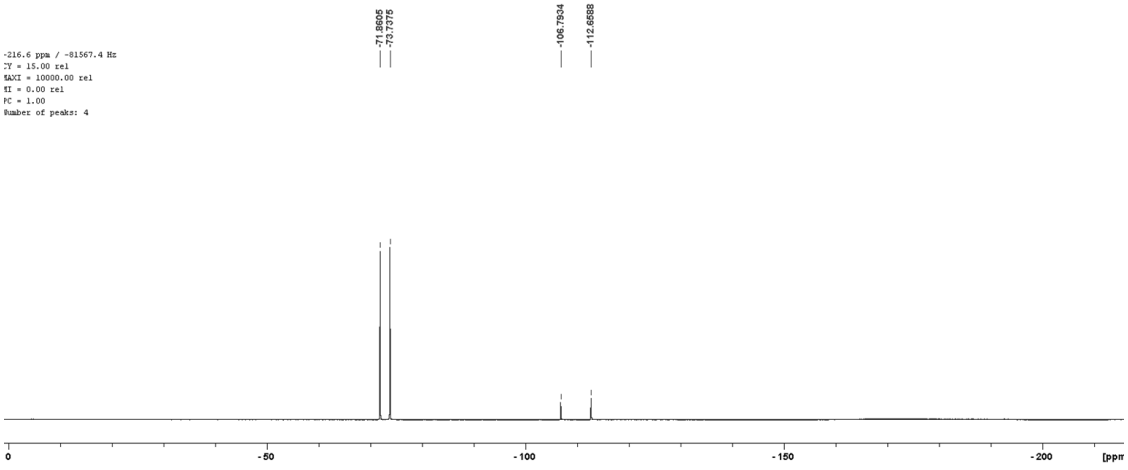

Figure A4.44: ^{19}F NMR of ligand **L3**, CD_3CN. From ref 257

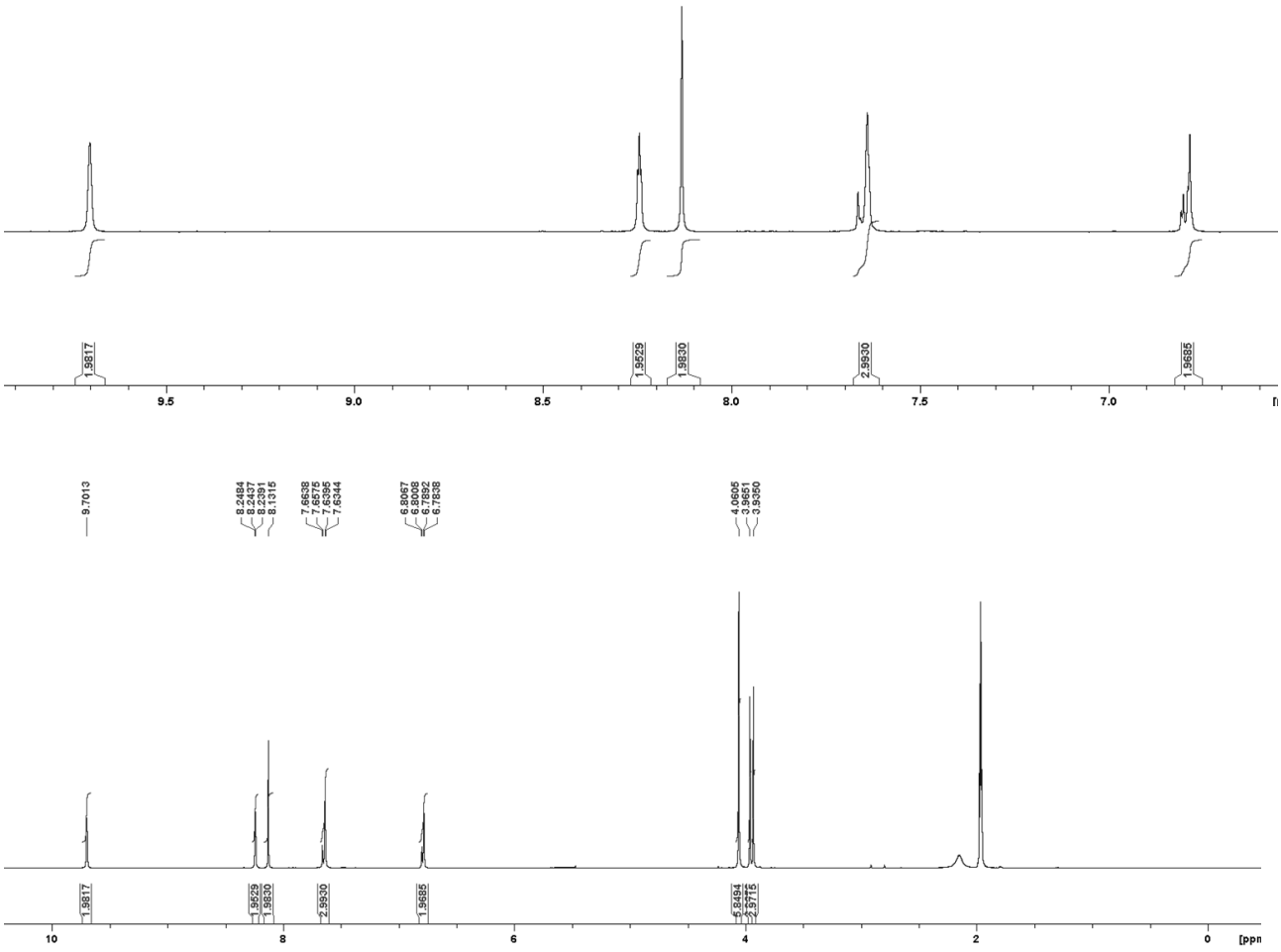

Figure A4.45: ^{1}H NMR spectra of ligand **L4**, CD_3CN. From ref 257

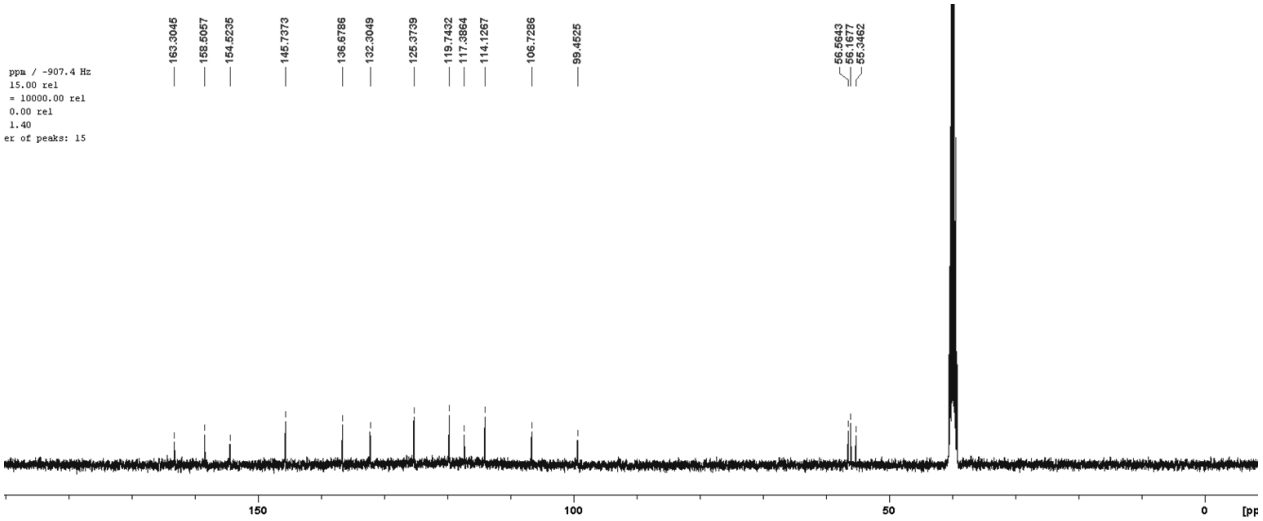

Figure A4.46: ^{13}C NMR spectra of ligand **L4**, CD_3CN. From ref 257

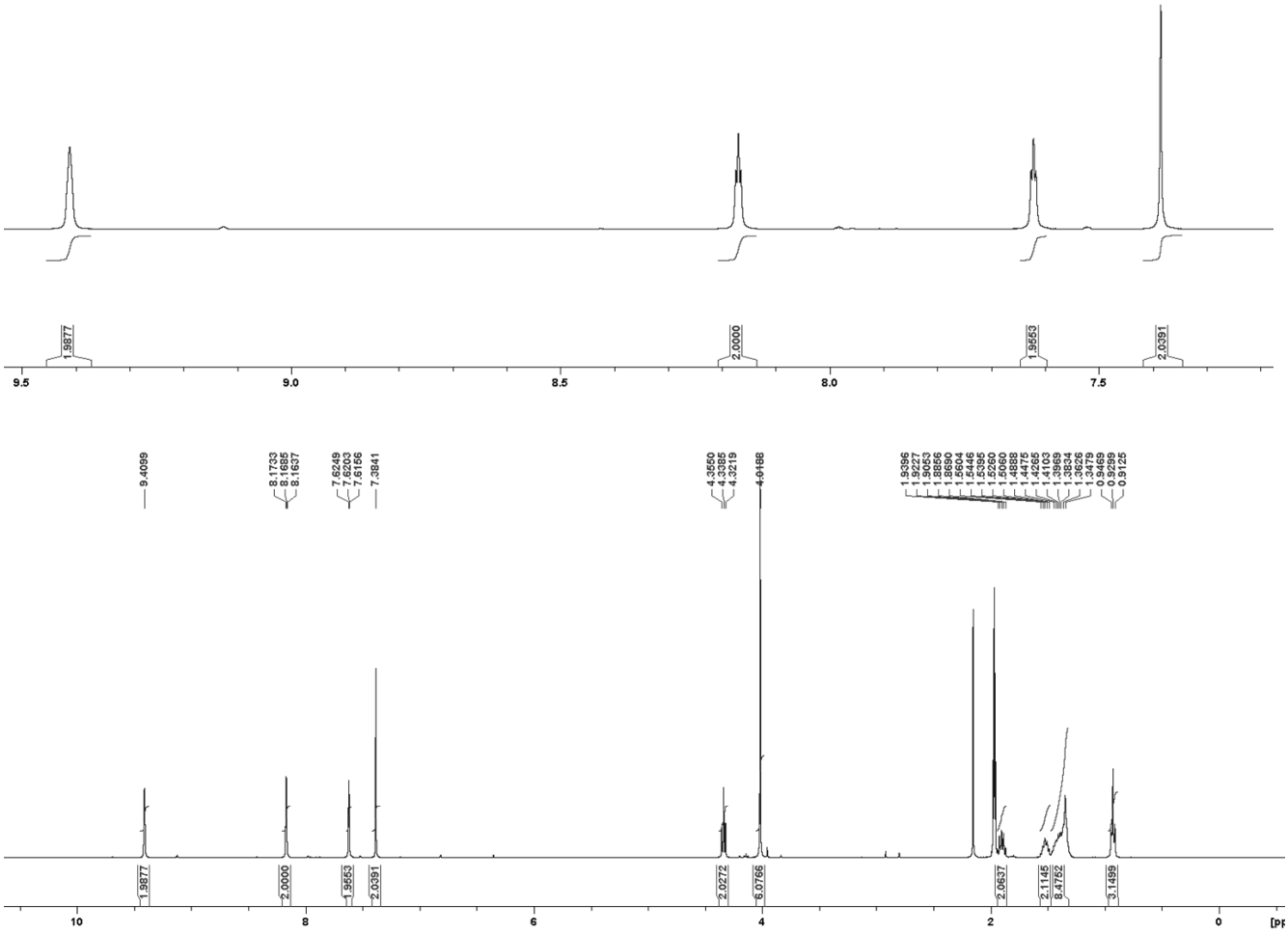

Figure A4.47: ^{1}H NMR spectrum of **L5**, CD_3CN. From ref 257

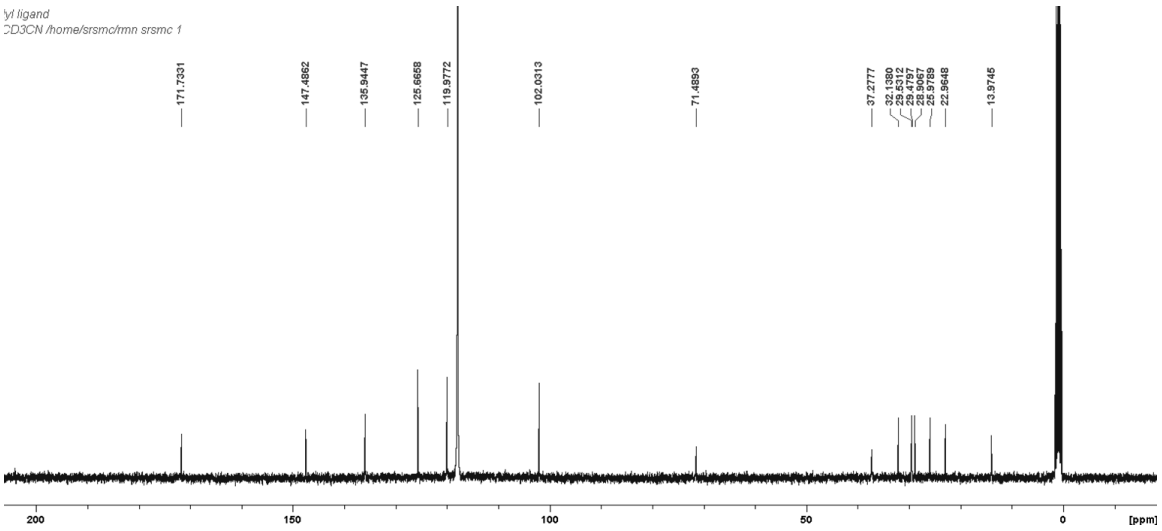

Figure A4.48: ^{13}C NMR spectrum of **L5**, CD_3CN. From ref 257

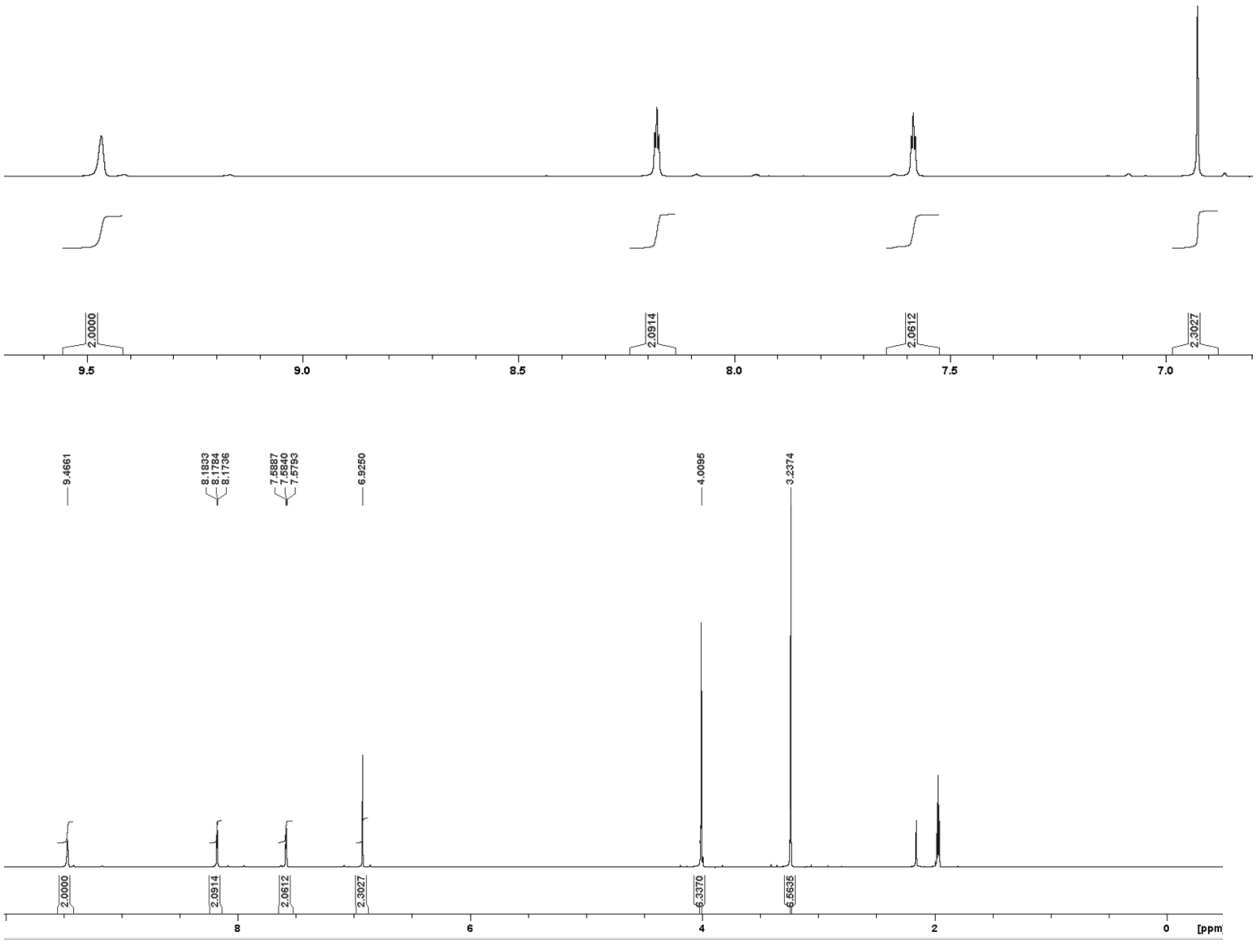

Figure A4.49: ^{1}H NMR of compound **L6**, CD_3CN. From ref 257

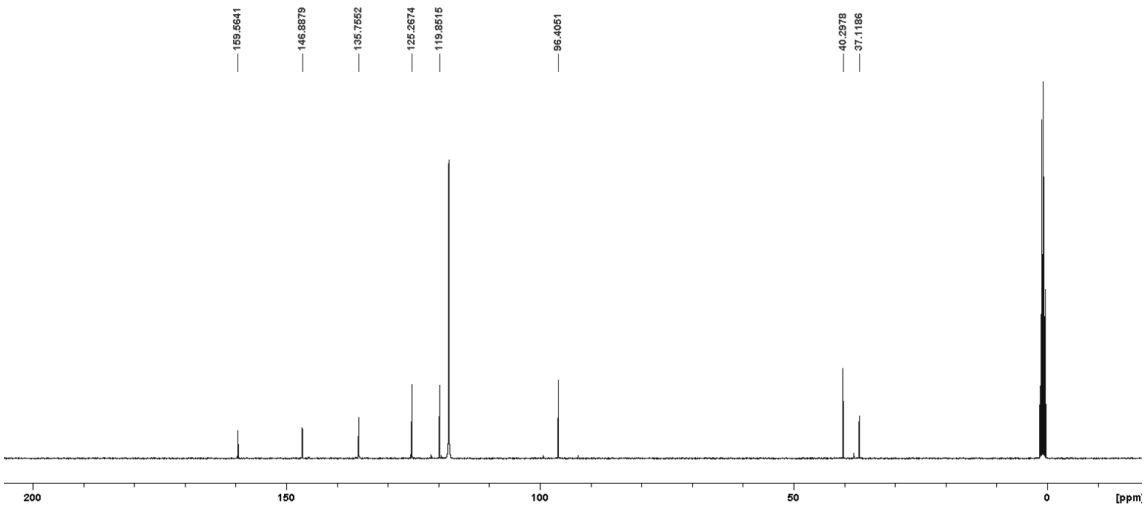

Figure A 4.50: ^{13}C NMR of compound **L6**, CD_3CN. From ref 257

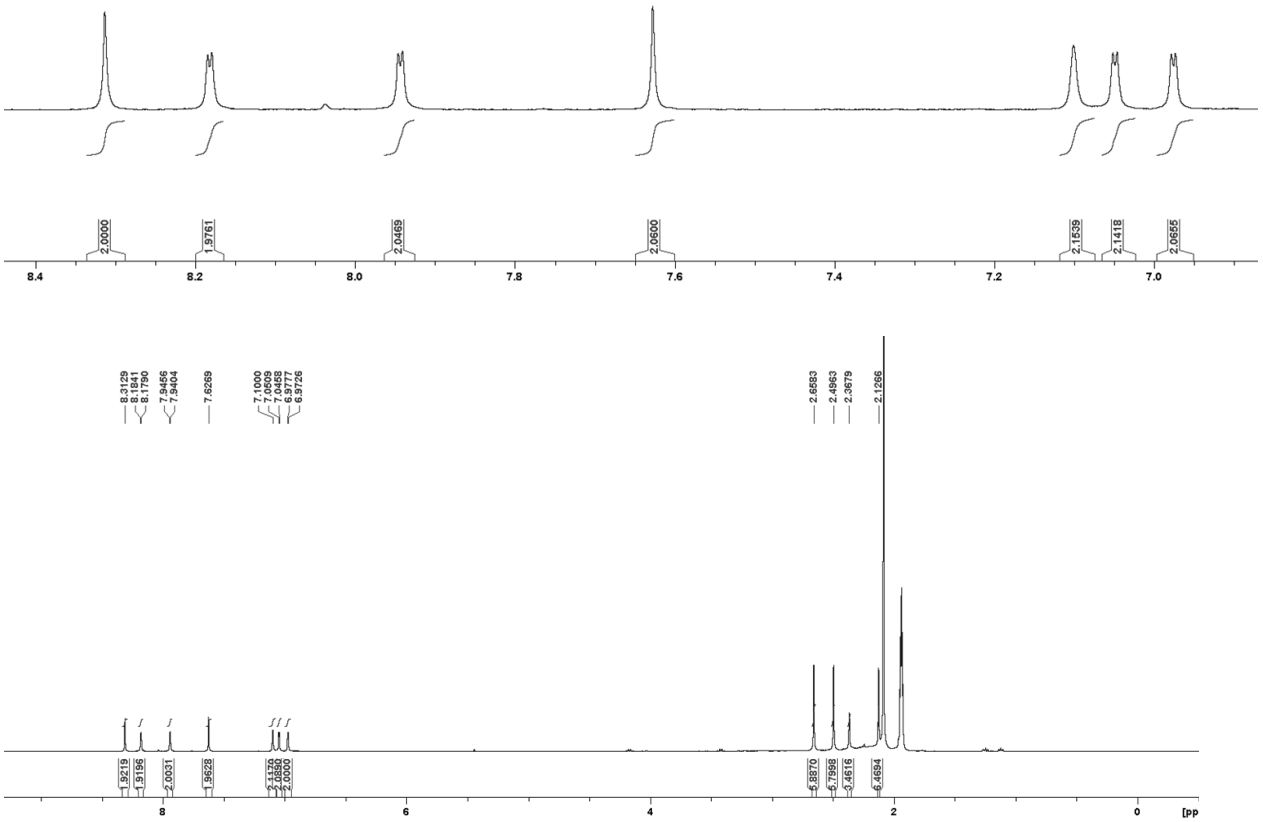

Figure A4.51: ^{1}H NMR spectrum of **ARM14**, CD_3CN. From ref 257

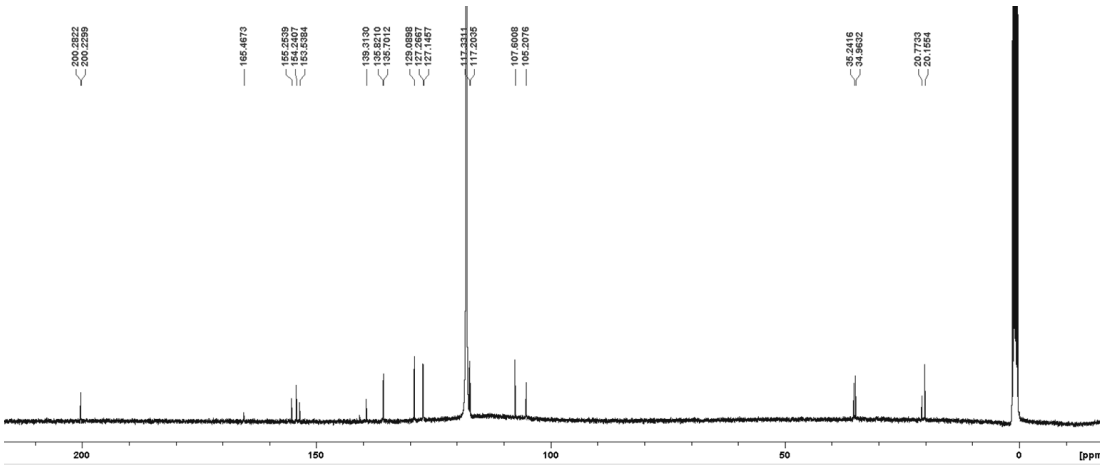

Figure A4.52: ^{13}C NMR spectrum of **ARM14**, CD_3CN. From ref 257

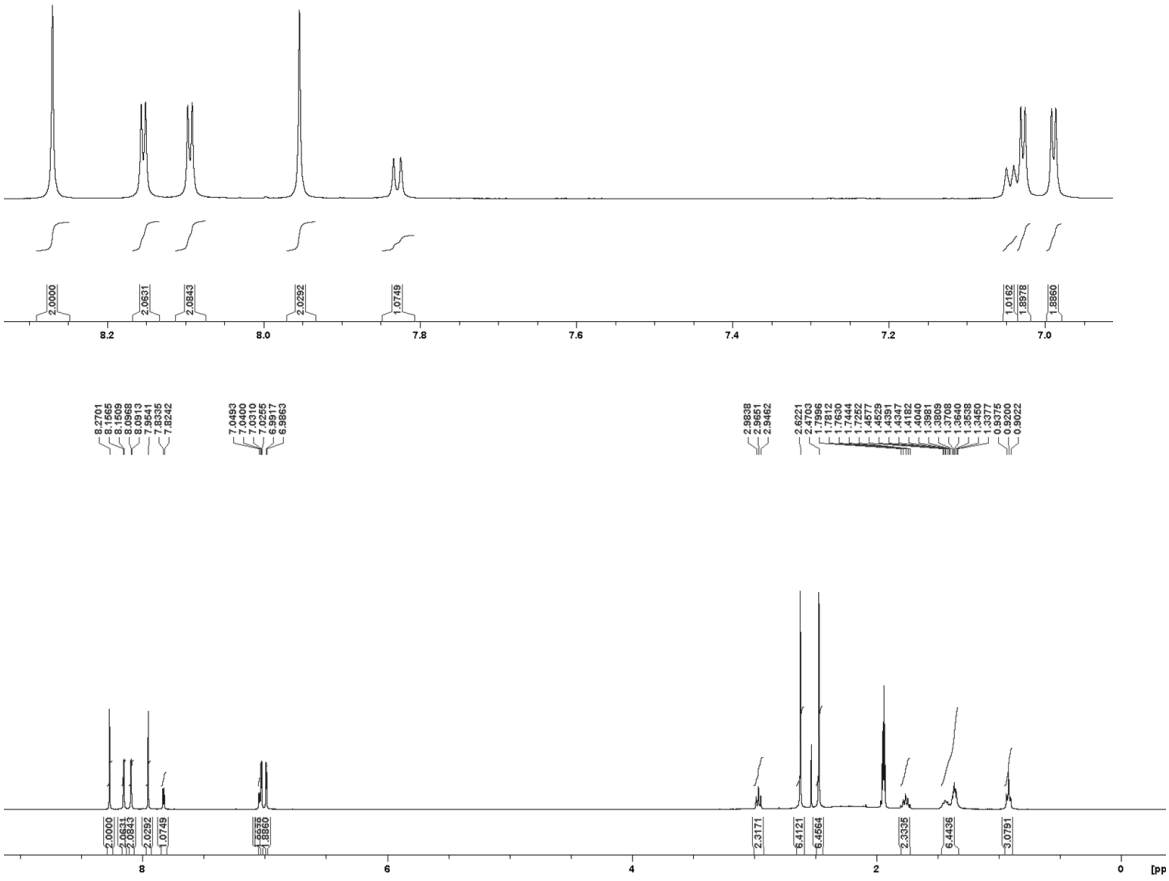

Figure A4.53: ^{1}H NMR spectrum of **ARM15**, CD_3CN. From ref 257

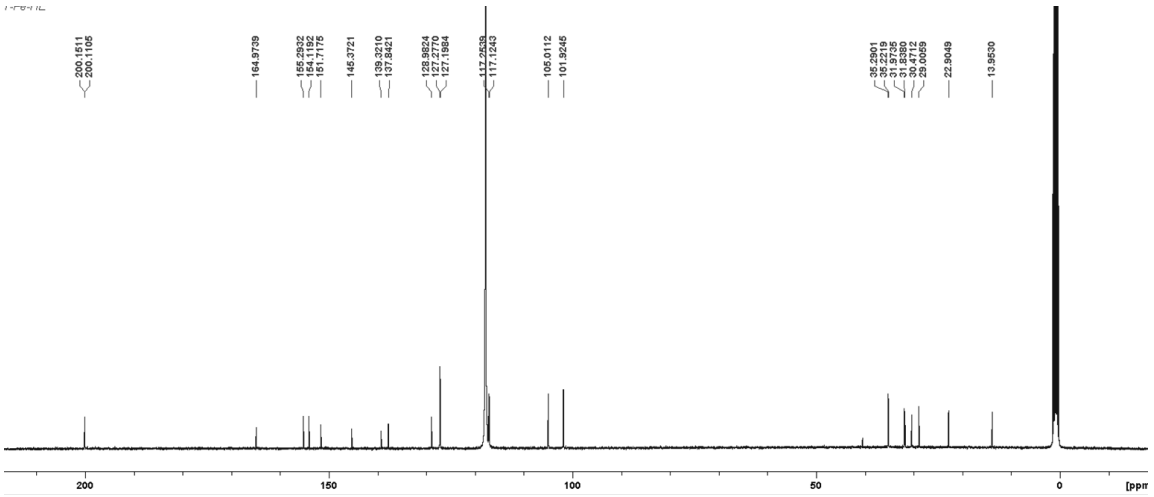

Figure A4.54: ^{13}C NMR spectrum of **ARM15**, CD_3CN. From ref 257

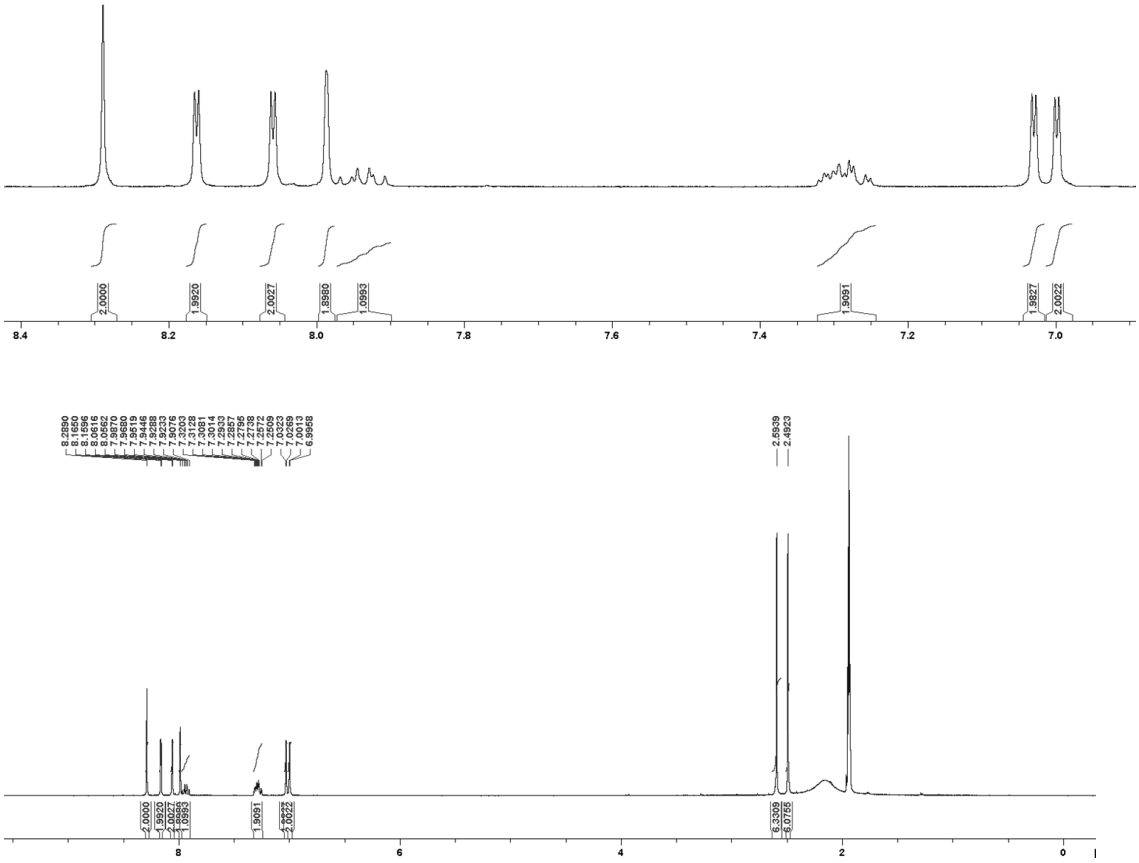

Figure A4.55: ^{1}H NMR of **ARM16**, CD_3CN. From ref 257

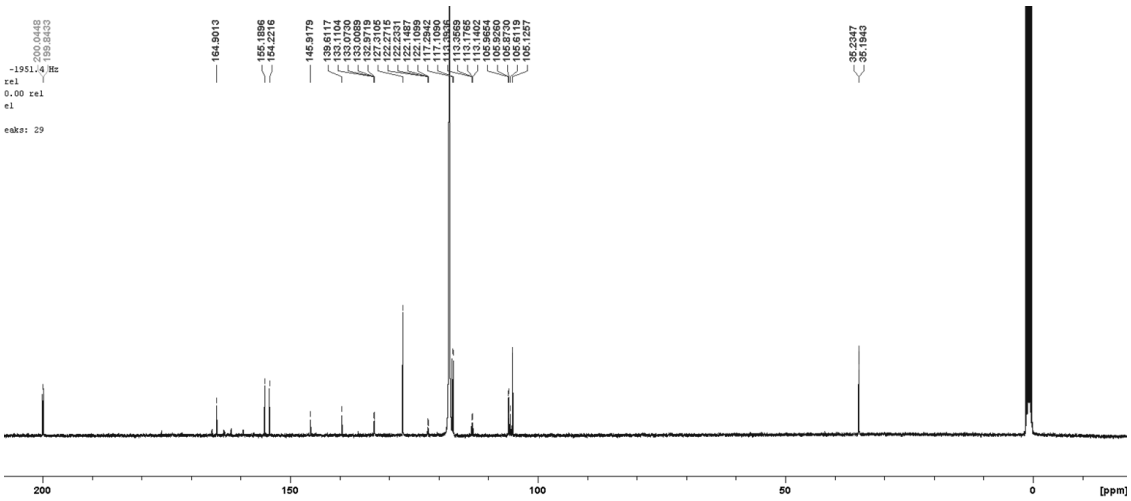

Figure A4.56: ^{13}C NMR of **ARM16**, CD_3CN. From ref 257

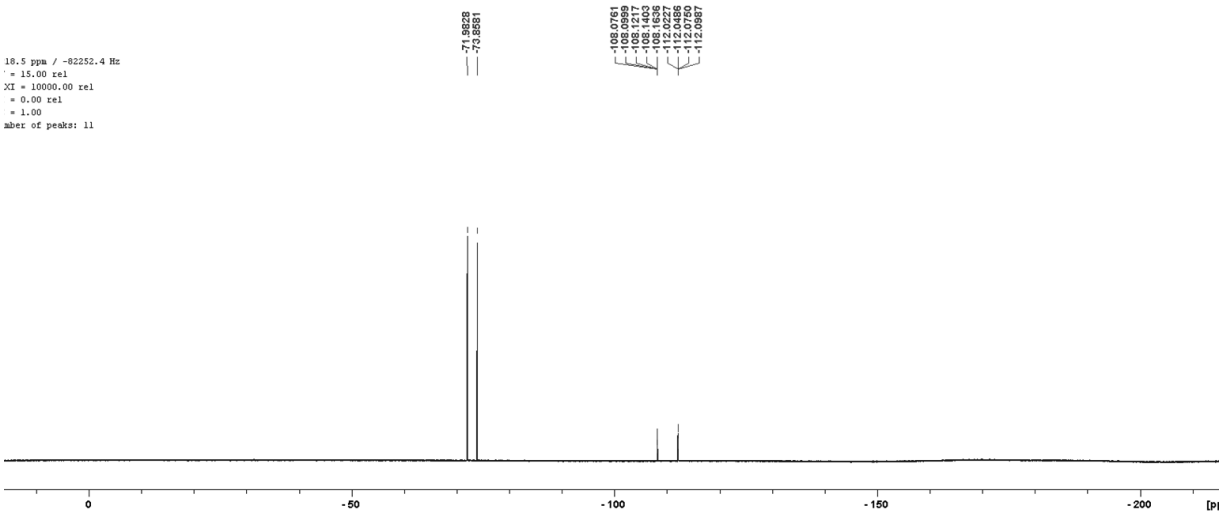

Figure A4.57: ^{19}F NMR of **ARM16**, CD_3CN. From ref 257

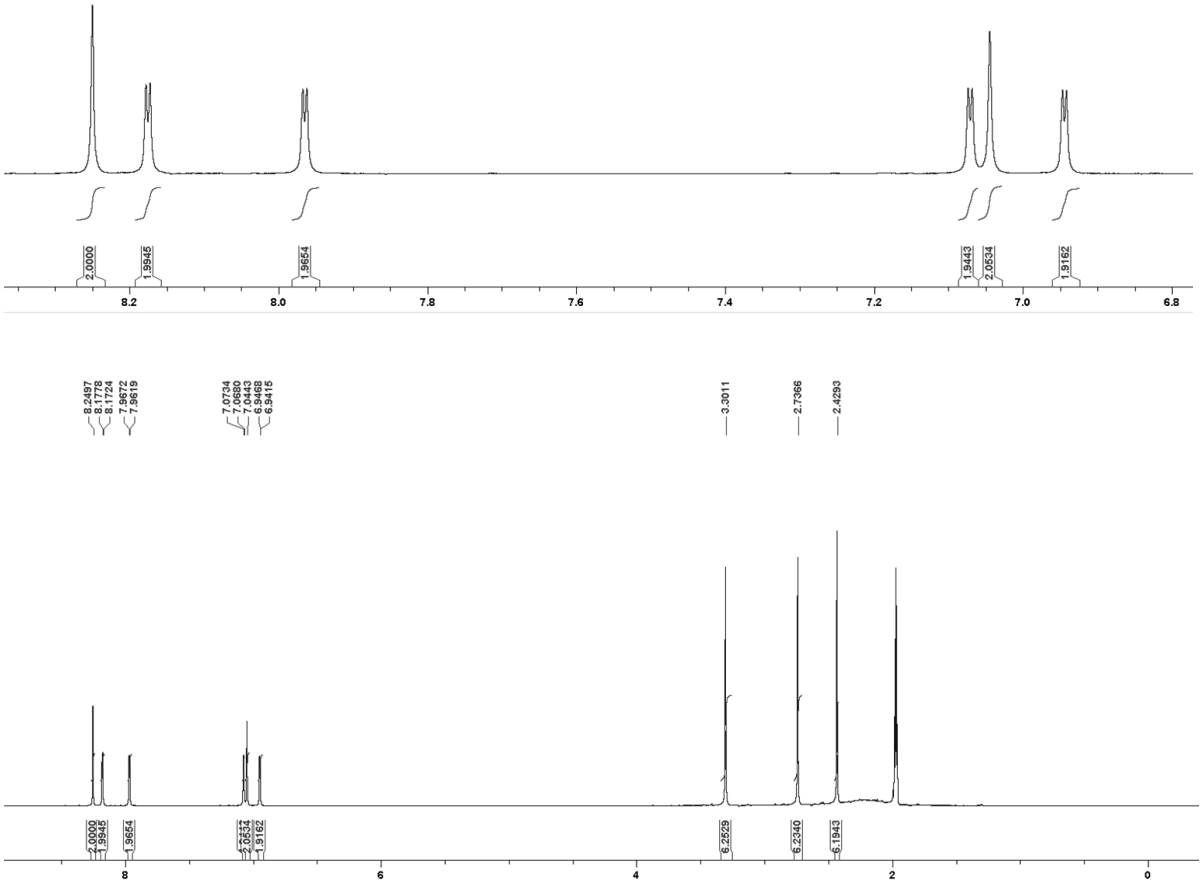

Figure A4.58: ^{1}H NMR spectra of **ARM122**, CD_3CN. From ref 257

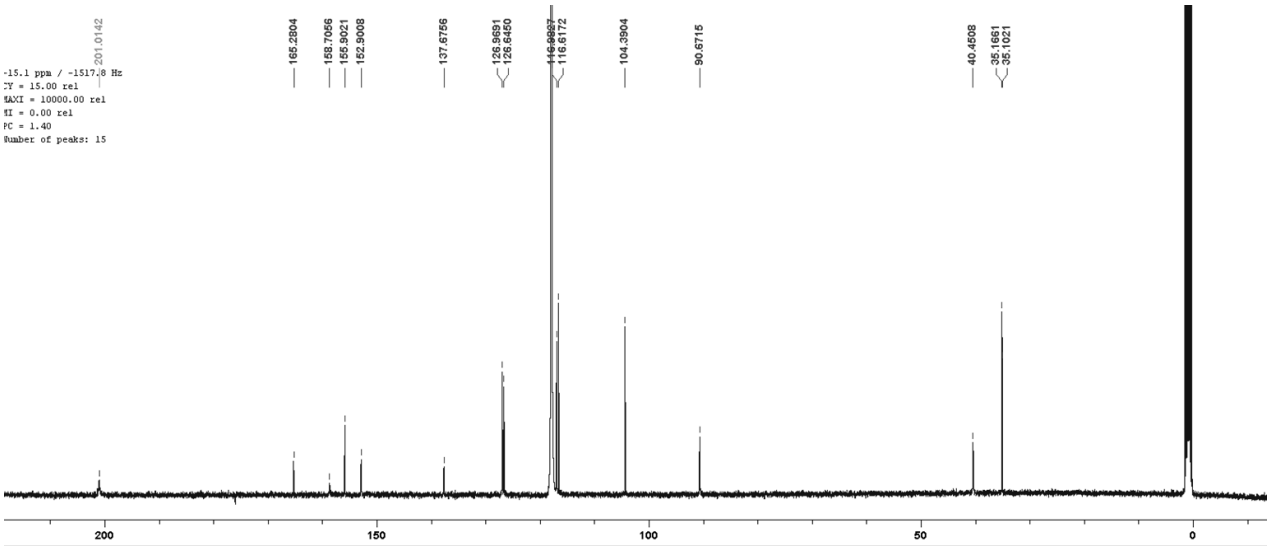

Figure A4.59: ^{13}C NMR spectra of **ARM122**, CD_3CN. From ref 257

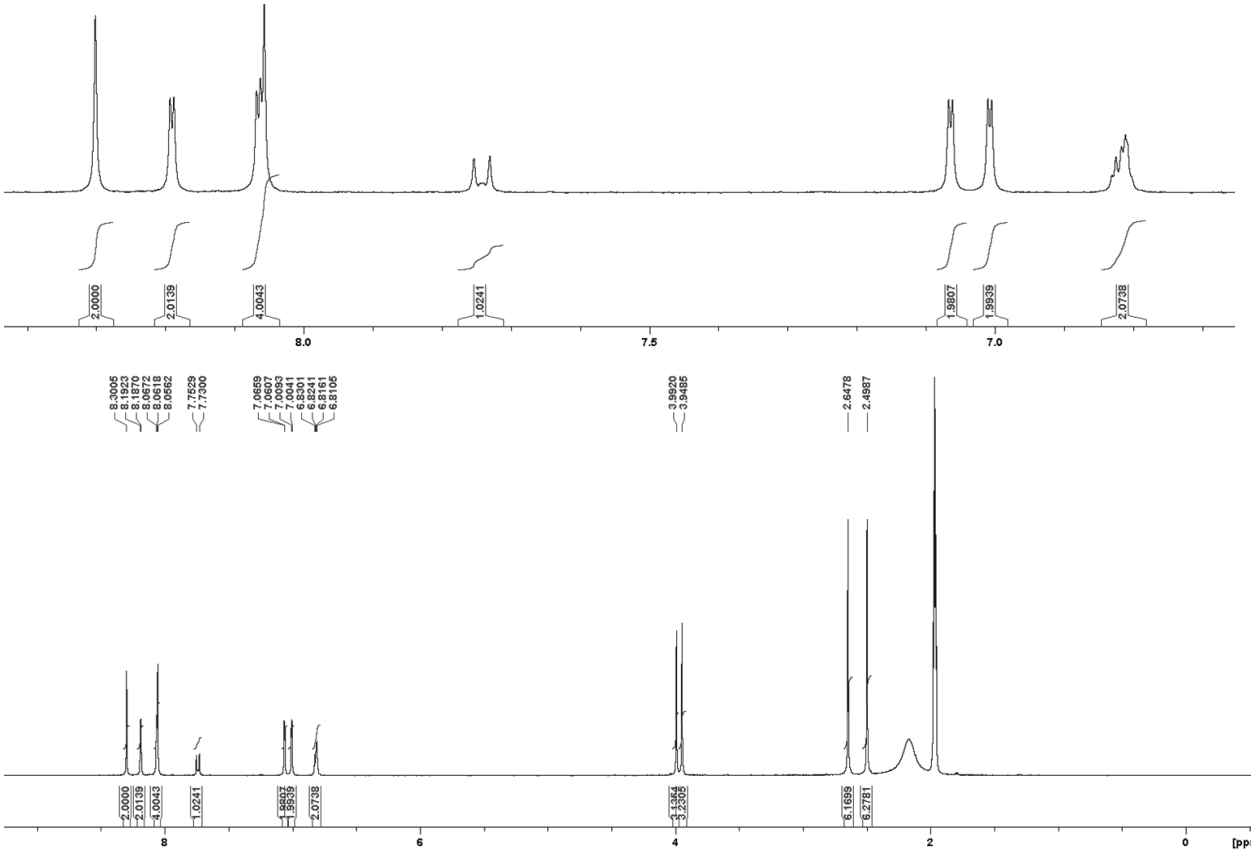

Figure A4.60: ^{1}H NMR spectra of **ARM130**, CD_3CN. From ref 257

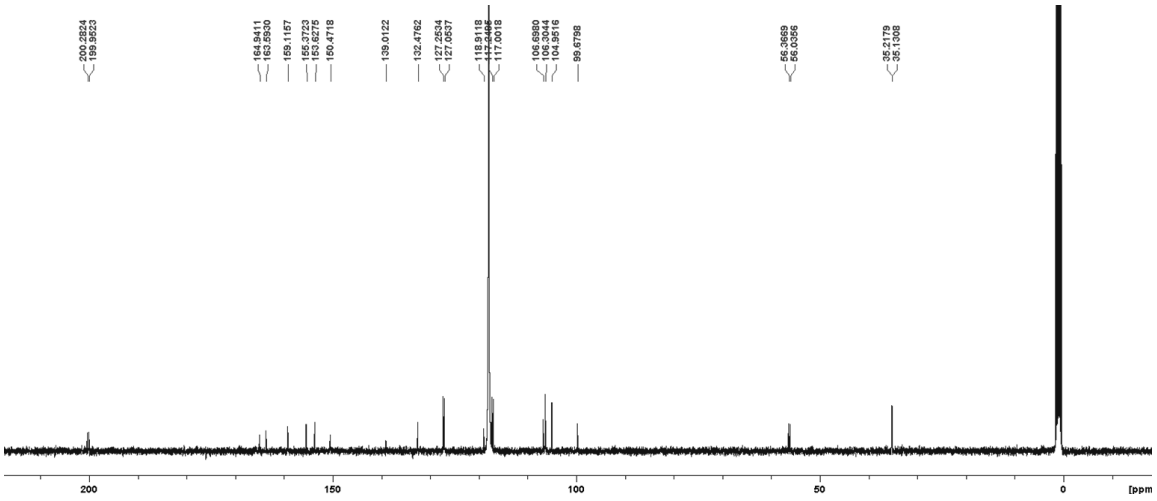

Figure A4.61: ^{13}C NMR spectra of **ARM130**, CD_3CN. From ref 257

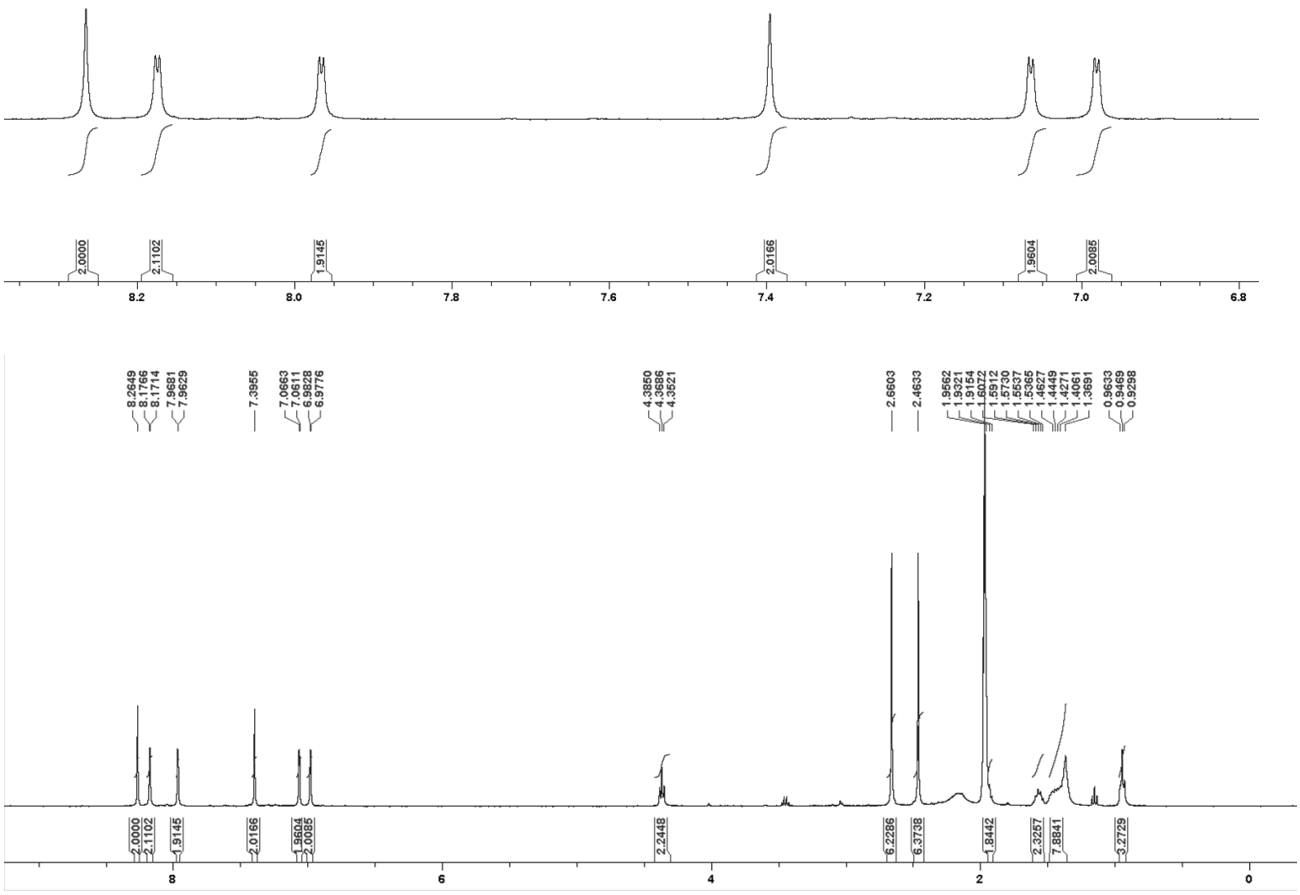

Figure A4.62: ^{1}H NMR spectrum of **ARM132**, CD_3CN. From ref 257

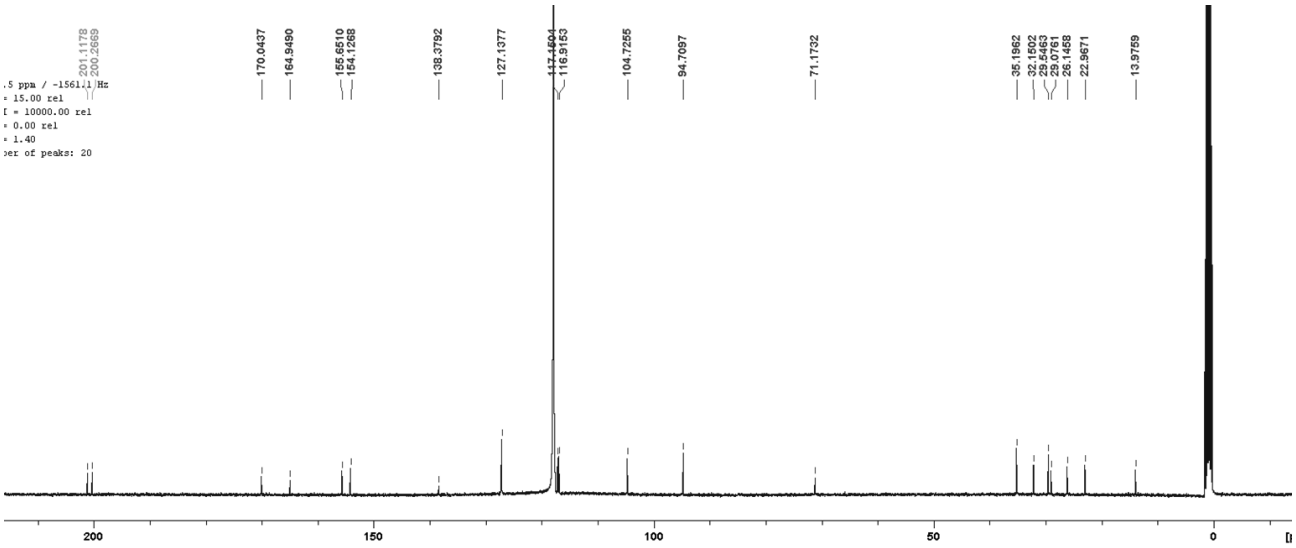

Figure A4.63: ^{13}C NMR spectrum of **ARM132**, CD_3CN. From ref 257

Table A4.4: State Number (*n*), excitation energies (E_x), wavelengths (λ), oscillator strengths (f), major contributions and related percentage (%) of the main transitions in the visible region for the considered dyes. Transitions related with MLCT excitations are marked with orange color

	n	E_x (eV)	λ (nm)	f (a.u.)	Transition	%
C1	5	2.68	463	0.308	H-2→ L+1	45.4
	9	3.23	384	0.155	H→ L+3	69.4
ARM13	4	2.69	461	0.148	H-2→ L	63.4
	9	3.22	385	0.150	H→ L+3	55.0
ARM14	4	2.67	464	0.199	H-2→ L	63.8
	8	3.04	408	0.122	H-1→ L+1	52.9
	9	3.22	386	0.189	H→ L+3	57.9
ARM15	4	2.64	470	0.434	H-2→ L	60.6
	6	2.81	441	0.196	H-1→ L+1	56.6
	10	3.22	385	0.196	H→ L+3	56.8
ARM16	4	2.67	464	0.273	H-2→ L	63.4
	6	2.90	427	0.166	H-1→ L+1	58.2
	9	3.22	385	0.186	H→ L+3	59.7
ARM122	3	2.61	475	0.176	H-2→ L	63.5
	8	3.16	392	0.271	H→ L+1	60.4
ARM130	4	2.64	469	0.301	H-2→ L	63.4
	7	2.94	421	0.319	H-1→ L+1	53.9
	11	3.24	383	0.127	H→ L+3	49.0
ARM132	3	2.65	467	0.164	H-2→ L	63.5
	10	3.20	387	0.180	H→ L+3	44.4

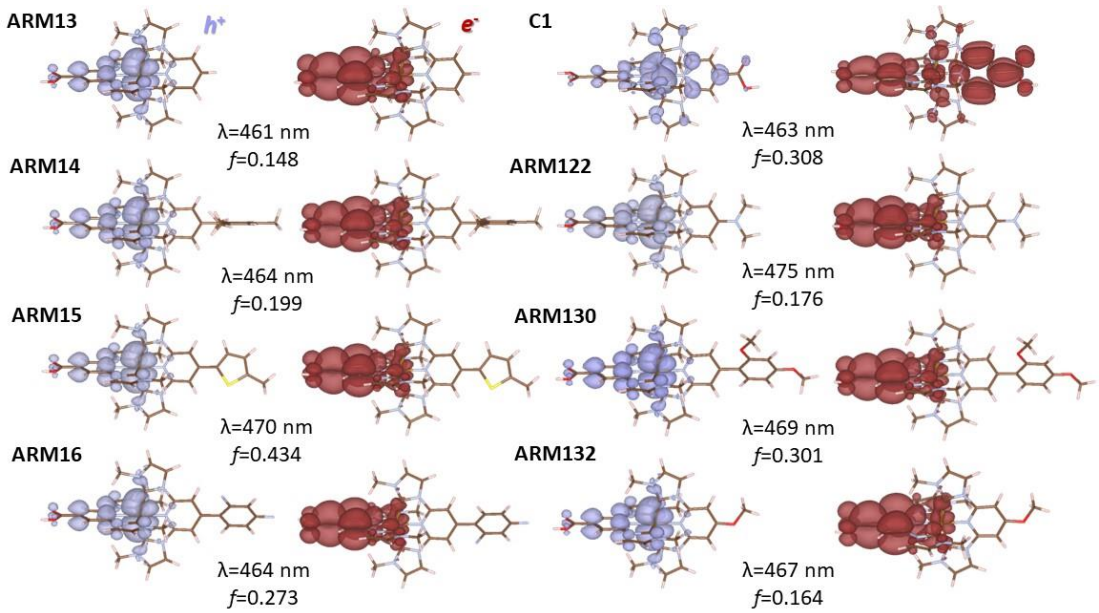

Figure A4.64: NTOs for the main transition forming the MLCT excitations of the Fe complex dyes studied in this work. Purple/red colors are employed to display hole/electron isodensity plots. The isovalues used for this plot was 0.02 a.u. From ref 257

Table A4.5: Calculated fraction of holes (h^+) and electrons (e^-) localized along the different fragments conforming the studied dyes: carboxylic anchoring group (COOH), bounded ligand (NHC_{bot}), metal cation (Fe), unbounded ligand (NHC_{top}) and substituent group (SG)

Dye	Fragment	h^+	e^-	Dye	Fragment	h^+	e^-
	$COOH_{bot}$	0.009	0.160		$COOH_{bot}$	0.005	0.092
	NHC_{bot}	0.173	0.709		NHC_{bot}	0.121	0.373
ARM13	Fe	0.730	0.078	**C1**	Fe	0.749	0.071
	NHC_{top}	0.091	0.057		NHC_{top}	0.121	0.374
	-	-	-		$COOH_{top}$	0.005	0.092
	COOH	0.009	0.161		COOH	0.010	0.163
	NHC_{bot}	0.175	0.702		NHC_{bot}	0.183	0.705
ARM14	Fe	0.726	0.080	**ARM122**	Fe	0.718	0.086
	NHC_{top}	0.092	0.059		NHC_{top}	0.093	0.050
	SG	0.001	0.001		SG	0.001	0.001
	COOH	0.009	0.145		COOH	0.010	0.160
	NHC_{bot}	0.158	0.593		NHC_{bottom}	0.174	0.678
ARM15	Fe	0.719	0.075	**ARM130**	Fe	0.718	0.080
	NHC_{top}	0.094	0.138		NHC_{top}	0.091	0.075
	SG	0.024	0.051		SG	0.011	0.010
	COOH	0.009	0.158		COOH	0.010	0.161
	NHC_{bot}	0.169	0.672		NHC_{bot}	0.179	0.704
ARM16	Fe	0.729	0.077	**ARM132**	Fe	0.722	0.083
	NHC_{top}	0.092	0.083		NHC_{top}	0.093	0.056
	SG	0.004	0.012		SG	0.000	0.001

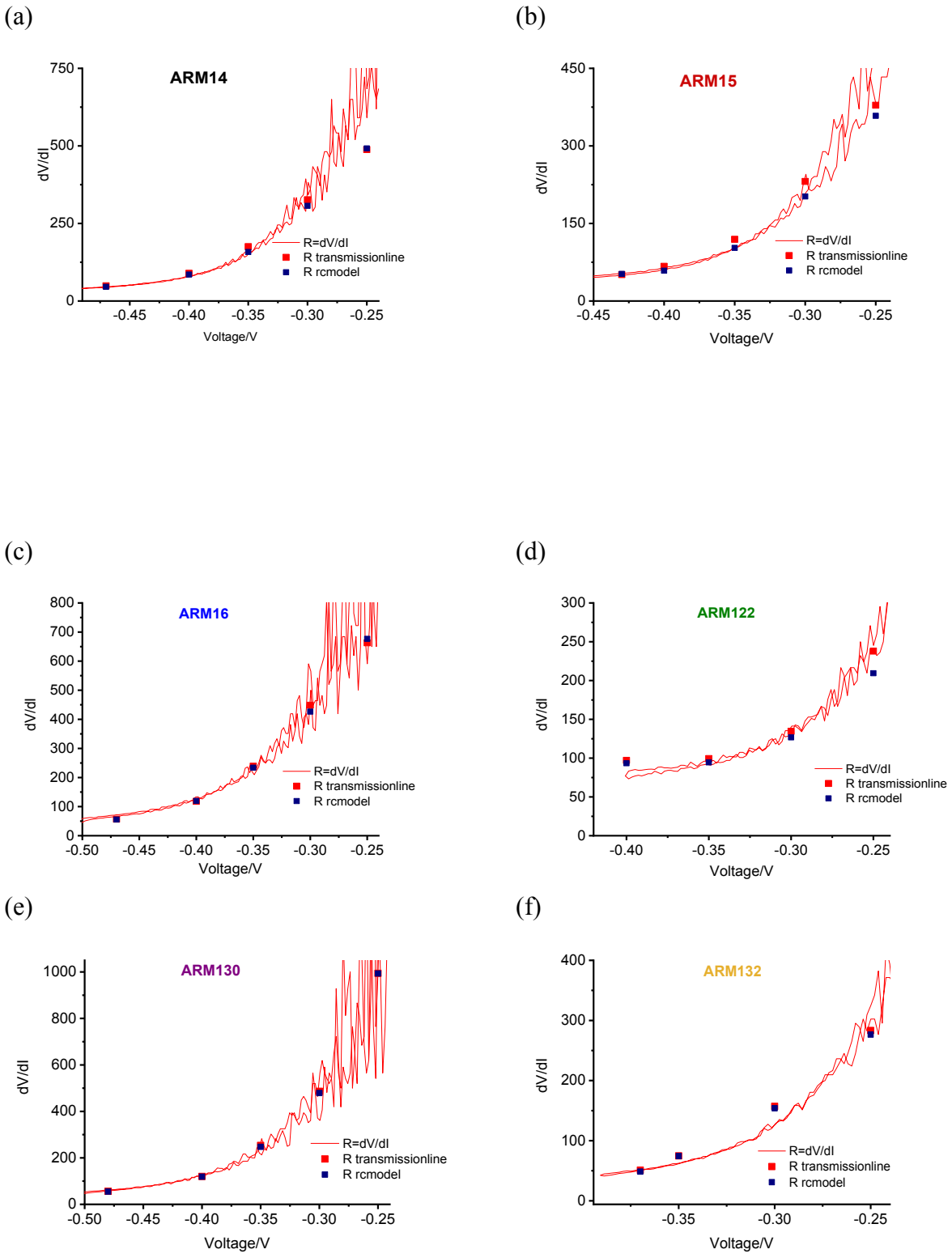

Figure A4.65: Reciprocal of the derivative of the I/V curves (red line) (R=∂V/∂I) and total resistance extrapolated by fitting the EIS data. Resistances extracted with the transmission line model (blue squares) and with the simpler RC model (red dots); (a) **ARM14**, (b) **ARM15**, (c) **ARM16**, (d) **ARM122**, (e) **ARM130** and (f) **ARM132.** From ref 257

Table A4.6: Probability Distributions, Γ(ε) (eV) and DOS (number of states/eV) calculated at the diabatic HOMO, HOMO-1 and HOMO-2 energies and associated recombination times, τ_{rec} (s^{-1}). The diabatic TiO_2 valence band maximum (VBM) energy is also reported

System	H-2 (eV)	H-1 (eV)	HOMO (eV)	VBM (eV)	Γ_{HOMO} (eV)	Γ_{H-1} (eV)	Γ_{H-2} (eV)	τ_{HOMO} (fs)	τ_{H-1} (fs)	τ_{H-2} (fs)
ARM13	-5.98	-5.96	-5.61	-7.05	4.93E-08	2.62E-08	4.13E-11	1.33E+07	2.51E+07	1.59E+10
ARM130	-5.87	-5.74	-5.53	-7.12	2.72E-08	1.90E-10	1.77E-11	2.42E+07	3.46E+09	3.71E+10

Table A4.7: Geometrical properties **ARM13**/TiO_2 and **ARM130**/TiO_2 systems: anchoring bonding length and tilted angles (θ) defined as the angle formed by the normal surface vector and the dye, as represented in **Figure 4.35a**

System	$(Ti\text{-}O)_{anch1}$ (Å)	$(Ti\text{-}O)_{anch2}$ (Å)	θ (º)
ARM13	2.210	2.116	37.69
ARM130	2.215	2.089	47.17

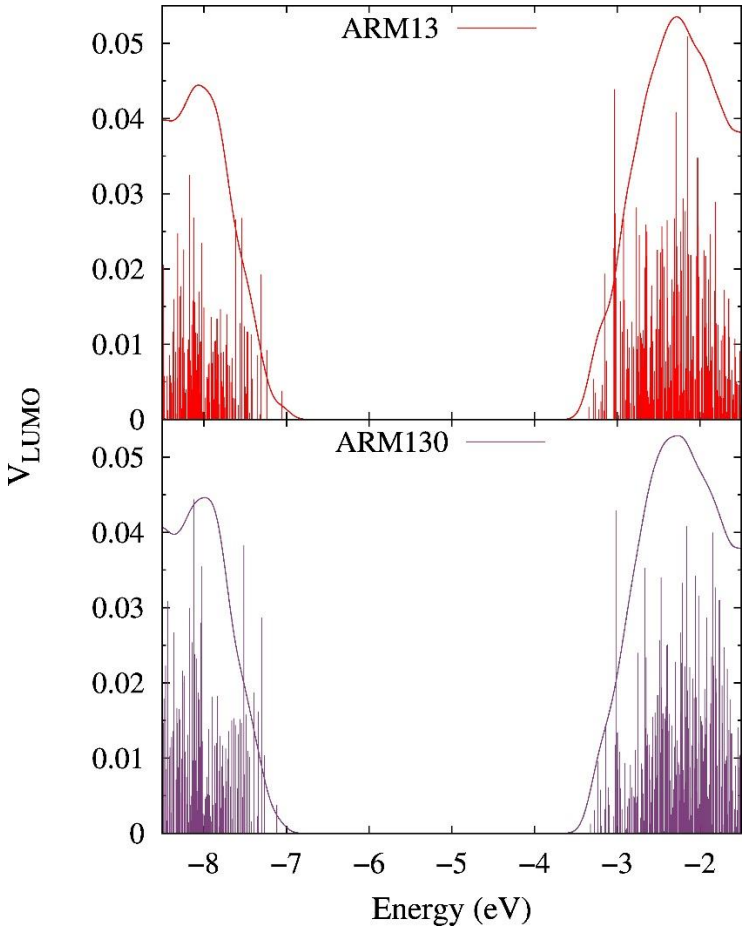

Figure A4.66: Electronic coupling *V* between the LUMOs of **ARM13** (top) and **ARM130** (bottom) and the states of the TiO_2- surface (vertical bars) together with the diabatic TiO_2 DOS (continuous lines). From ref 257

LIST OF PUBBLICATIONS

1) Recombination and regeneration dynamics in FeNHC(II)-sensitized solar cells, Edoardo Marchini, Mohamed Darari, Luca Lazzarin, Rita Boaretto, Roberto Argazzi, Carlo Alberto Bignozzi, Philippe C. Gros and Stefano Caramori, Chem. Commun., 2020,56, 543-546.
DOI: 10.1039/C9CC07794D

2) New examples of Ru(II)-tetrazolato complexes as thiocyanate-free sensitizers for Dye-Sensitized Solar Cells, Valentina Fiorini, Edoardo Marchini, Mattia Averardi, Loris Giorgini, Sara Muzzioli, Angela Dellai, Roberto Argazzi, Alessandra Sanson, Nicola Sangiorgi, Stefano Caramori and Stefano Stagni, Dalton Trans., 2020,49, 14543-14555.
DOI: 0.1039/d0dt02621b

3) Record power conversion efficiencies for iron(II)-NHC-sensitized DSSCs from rational molecular engineering and electrolyte optimization, Anil Reddy Marri, Edoardo Marchini, Valentin Diez Cabanes, Roberto Argazzi, Mariachiara Pastore, Stefano Caramori and Philippe C. Gros, J. Mater. Chem. A, 2021, 9, 3540-3554.
DOI: 10.1039/D0TA10841C

4) Self-Assembled Multinuclear Complexes for Cobalt(II/III) Mediated Sensitized Solar Cells, Edoardo Marchini, Stefano Caramori, Rita Boaretto, Vito Cristino, Roberto Argazzi, Alessandro Niorettini and Carlo Alberto Bignozzi, Appl. Sci. 2021, 11(6), 2769.
DOI: 10.3390/app11062769

5) On the use of PEDOT as a Catalytic Counter Electrode Material in Dye Sensitized Solar Cells., Edoardo Marchini, Stefano Caramori, Carlo Alberto Bignozzi, and Stefano Carli, Appl. Sci. 2021, 11(9), 3795.
DOI: 10.3390/app11093795

6) A series of Iron(II)-NHC Sensitizers with remarkable power conversion efficiency in photoelectrochemical cells, Anil Reddy Marri, Edoardo Marchini, Valentin Diez Cabanes, Roberto Argazzi, Mariachiara Pastore, Stefano Caramori, Carlo Alberto Bignozzi and Philippe C. Gros, Chem. Eur. J., Chem. Eur. J. 2021, 27, 1 –11.
DOI: 10.1002/chem.202103178

7) Transparent Polymeric Formulations Effective Against SARS-CoV-2 infection, Valentina Gentili, Daniele Pazzi, Sabrina Rizzo, Giovanna Schiuma, Edoardo Marchini, Stefania Papadia, Andrea Sartorel, Dario Di Luca, Francesca Caccuri, Carlo Alberto Bignozzi, Roberta Rizzo, ACS Appl. Mater. Interfaces 2021, 13, 46, 54648–546551.
DOI: 10.1021/acsami.1c10404

8) Electrodeposited PEDOT/Nafion as Catalytic Counter Electrodes for Cobalt and Copper Bipyridyl Redox Mediators in Dye-Sensitized Solar Cells, Edoardo Marchini, Michele Orlandi, Nicola Bazzanella, Rita Boaretto, Stefano Caramori and Stefano Carli (manuscript under preparation)

REFERENCES

1. U S Energy Information Administration, International Energy Outlook, https://www.eia.gov/outlooks/ieo/. **2017**.
2. International Energy Agency, Energy and Climate Change, OECD/IEA, www.iea.org/publications/freepublications/publication/weo-2015-special-report-2015-energy-and-climate-change.html. **2015**.
3. IPCC, Climate Change 2014, Intergovernmental Panel on Climate Change, Geneva. http://www.ipcc.ch/report/ar5/wg3/. **2015**.
4. Sessolo, M.; Bolink, H. J., Solar cells. Perovskite solar cells join the major league. *Science* **2015,** *350* (6263), 917.
5. Haillant, O., Accelerated weathering testing principles to estimate the service life of organic PV modules. *Solar Energy Materials and Solar Cells* **2011,** *95* (5), 1284-1292.
6. Duchanois, T.; Etienne, T.; Cebrián, C.; Liu, L.; Monari, A.; Beley, M.; Assfeld, X.; Haacke, S.; Gros, P. C., An Iron-Based Photosensitizer with Extended Excited-State Lifetime: Photophysical and Photovoltaic Properties. *European Journal of Inorganic Chemistry* **2015,** *2015* (14), 2469-2477.
7. Becquerel, A.-E. J. C. A. S., Recherches sur les effets de la radiation chimique de la lumiere solaire au moyen des courants electriques. **1839,** *9* (145), 1.
8. Shockley, W.; Queisser, H. J. J. J. o. a. p., Detailed balance limit of efficiency of p-n junction solar cells. **1961,** *32* (3), 510-519.
9. O'Regan, B.; Grätzel, M., A low-cost, high-efficiency solar cell based on dye-sensitized colloidal TiO2 films. *Nature* **1991,** *353* (6346), 737-740.
10. Hagfeldt, A.; Boschloo, G.; Sun, L.; Kloo, L.; Pettersson, H., Dye-sensitized solar cells. *Chem Rev* **2010,** *110* (11), 6595-663.
11. Cornaro, C.; Renzi, L.; Pierro, M.; Di Carlo, A.; Guglielmotti, A., Thermal and Electrical Characterization of a Semi-Transparent Dye-Sensitized Photovoltaic Module under Real Operating Conditions. *Energies* **2018,** *11* (1).
12. Tanaka, E.; Michaels, H.; Freitag, M.; Robertson, N., Synergy of co-sensitizers in a copper bipyridyl redox system for efficient and cost-effective dye-sensitized solar cells in solar and ambient light. *Journal of Materials Chemistry A* **2020,** *8* (3), 1279-1287.
13. Gratzel, M., Photoelectrochemical cells. *Nature* **2001,** *414* (6861), 338-44.
14. Hagfeldt, A.; Gratzel, M., Molecular photovoltaics. *Acc Chem Res* **2000,** *33* (5), 269-77.
15. Nazeeruddin, M. K.; Baranoff, E.; Grätzel, M., Dye-sensitized solar cells: A brief overview. *Solar Energy* **2011,** *85* (6), 1172-1178.
16. Bisquert, J.; Cahen, D.; Hodes, G.; Rühle, S.; Zaban, A., Physical Chemical Principles of Photovoltaic Conversion with Nanoparticulate, Mesoporous Dye-Sensitized Solar Cells. *The Journal of Physical Chemistry B* **2004,** *108* (24), 8106-8118.
17. Gerischer, H. J. P.; Chemistry, A., Heterogeneous electrochemical systems for solar energy conversion. **1980,** *52* (12), 2649-2667.
18. Hannay, N. B.; Sundheim, B. R., Semiconductors. *Journal of The Electrochemical Society* **1959,** *106* (8), 226C.
19. Memming, R. In *Photoinduced charge transfer processes at semiconductor electrodes and particles*, Berlin, Heidelberg, Springer Berlin Heidelberg: Berlin, Heidelberg, 1994; pp 105-181.
20. Bard, A. J.; Stratmann, M.; Licht, S., Encyclopedia of Electrochemistry, Semiconductor Electrodes and Photoelectrochemistry. *WILEY* **2002**.
21. Saito, M.; Fujihara, S., Large photocurrent generation in dye-sensitized ZnO solar cells. *Energy & Environmental Science* **2008,** *1* (2).

22. Memarian, N.; Concina, I.; Braga, A.; Rozati, S. M.; Vomiero, A.; Sberveglieri, G., Hierarchically assembled ZnO nanocrystallites for high-efficiency dye-sensitized solar cells. *Angew Chem Int Ed Engl* **2011,** *50* (51), 12321-5.
23. He, Y.; Hu, J.; Xie, Y., High-efficiency dye-sensitized solar cells of up to 8.03% by air plasma treatment of ZnO nanostructures. *Chem Commun (Camb)* **2015,** *51* (90), 16229-32.
24. Zhang, Q.; Dandeneau, C. S.; Zhou, X.; Cao, G., ZnO Nanostructures for Dye-Sensitized Solar Cells. *Advanced Materials* **2009,** *21* (41), 4087-4108.
25. Onwona-Agyeman, B.; Kaneko, S.; Kumara, A.; Okuya, M.; Murakami, K.; Konno, A.; Tennakone, K., Sensitization of Nanocrystalline SnO2Films with Indoline Dyes. *Japanese Journal of Applied Physics* **2005,** *44* (No. 23), L731-L733.
26. Birkel, A.; Lee, Y.-G.; Koll, D.; Meerbeek, X. V.; Frank, S.; Choi, M. J.; Kang, Y. S.; Char, K.; Tremel, W., Highly efficient and stable dye-sensitized solar cells based on SnO2nanocrystals prepared by microwave-assisted synthesis. *Energy Environ. Sci.* **2012,** *5* (1), 5392-5400.
27. Zaban, A.; Chen, S. G.; Chappel, S.; Gregg, B. A., Bilayer nanoporous electrodes for dye sensitized solar cells. *Chemical Communications* **2000,** (22), 2231-2232.
28. Chen, S. G.; Chappel, S.; Diamant, Y.; Zaban, A., Preparation of Nb2O5Coated TiO2Nanoporous Electrodes and Their Application in Dye-Sensitized Solar Cells. *Chemistry of Materials* **2001,** *13* (12), 4629-4634.
29. Burnside, S.; Moser, J.-E.; Brooks, K.; Grätzel, M.; Cahen, D., Nanocrystalline Mesoporous Strontium Titanate as Photoelectrode Material for Photosensitized Solar Devices: Increasing Photovoltage through Flatband Potential Engineering. *The Journal of Physical Chemistry B* **1999,** *103* (43), 9328-9332.
30. Yang, S.; Kou, H.; Wang, J.; Xue, H.; Han, H., Tunability of the Band Energetics of Nanostructured SrTiO3 Electrodes for Dye-Sensitized Solar Cells. *The Journal of Physical Chemistry C* **2010,** *114* (9), 4245-4249.
31. Tan, B.; Toman, E.; Li, Y.; Wu, Y., Zinc stannate (Zn2SnO4) dye-sensitized solar cells. *J Am Chem Soc* **2007,** *129* (14), 4162-3.
32. Lana-Villarreal, T.; Boschloo, G.; Hagfeldt, A., Nanostructured Zinc Stannate as Semiconductor Working Electrodes for Dye-Sensitized Solar Cells. *The Journal of Physical Chemistry C* **2007,** *111* (14), 5549-5556.
33. Chen, J.; Lu, L.; Wang, W., Zn2SnO4 Nanowires as Photoanode for Dye-Sensitized Solar Cells and the Improvement on Open-Circuit Voltage. *The Journal of Physical Chemistry C* **2012,** *116* (20), 10841-10847.
34. Chen, J.; Wang, W., Carrier transport processes in dye sensitized solar cells based on Zn2SnO4 nanostructures studied by intensity modulated photocurrent/photovoltage spectroscopy. *Applied Physics Letters* **2013,** *102* (21).
35. Sayama, K.; Sugihara, H.; Arakawa, H., Photoelectrochemical Properties of a Porous Nb2O5Electrode Sensitized by a Ruthenium Dye. *Chemistry of Materials* **1998,** *10* (12), 3825-3832.
36. Hamann, T. W.; Jensen, R. A.; Martinson, A. B. F.; Van Ryswyk, H.; Hupp, J. T., Advancing beyond current generation dye-sensitized solar cells. *Energy & Environmental Science* **2008,** *1* (1).
37. Takahashi, J., Dye adsorption behavior of anatase-and rutile-type TiO 2 nanoparticles modified by various heat-treatments. *Journal of Materials Science* **2003,** *38* (8), 1695-1702.
38. Park, N. G.; van de Lagemaat, J.; Frank, A. J., Comparison of Dye-Sensitized Rutile- and Anatase-Based TiO2 Solar Cells. *The Journal of Physical Chemistry B* **2000,** *104* (38), 8989-8994.
39. Chen, X.; Mao, S. S., Titanium dioxide nanomaterials: synthesis, properties, modifications, and applications. *Chem Rev* **2007,** *107* (7), 2891-959.
40. Grätzel, M., Sol-Gel Processed TiO2 Films for Photovoltaic Applications. *Journal of Sol-Gel Science and Technology* **2001,** *22* (1/2), 7-13.
41. Galoppini, E., Linkers for anchoring sensitizers to semiconductor nanoparticles. *Coordin Chem Rev* **2004,** *248* (13-14), 1283-1297.

42. Kalyanasundaram, K.; Gratzel, M., Applications of functionalized transition metal complexes in photonic and optoelectronic devices. *Coordin Chem Rev* **1998,** *177* (1), 347-414.
43. Nazeeruddin, M. K.; Kay, A.; Rodicio, I.; Humphry-Baker, R.; Mueller, E.; Liska, P.; Vlachopoulos, N.; Graetzel, M., Conversion of light to electricity by cis-X2bis(2,2'-bipyridyl-4,4'-dicarboxylate)ruthenium(II) charge-transfer sensitizers (X = Cl-, Br-, I-, CN-, and SCN-) on nanocrystalline titanium dioxide electrodes. *Journal of the American Chemical Society* **1993,** *115* (14), 6382-6390.
44. Nazeeruddin, M. K.; Zakeeruddin, S. M.; Humphry-Baker, R.; Jirousek, M.; Liska, P.; Vlachopoulos, N.; Shklover, V.; Fischer, C. H.; Gratzel, M., Acid-Base Equilibria of (2,2'-Bipyridyl-4,4'-dicarboxylic acid)ruthenium(II) Complexes and the Effect of Protonation on Charge-Transfer Sensitization of Nanocrystalline Titania. *Inorg Chem* **1999,** *38* (26), 6298-6305.
45. Wang, P.; Zakeeruddin, S. M.; Moser, J. E.; Humphry-Baker, R.; Comte, P.; Aranyos, V.; Hagfeldt, A.; Nazeeruddin, M. K.; Grätzel, M., Stable New Sensitizer with Improved Light Harvesting for Nanocrystalline Dye-Sensitized Solar Cells. *Advanced Materials* **2004,** *16* (20), 1806-1811.
46. Zukalova, M.; Zukal, A.; Kavan, L.; Nazeeruddin, M. K.; Liska, P.; Gratzel, M., Organized mesoporous TiO2 films exhibiting greatly enhanced performance in dye-sensitized solar cells. *Nano Lett* **2005,** *5* (9), 1789-92.
47. Wang, P.; Zakeeruddin, S. M.; Moser, J. E.; Nazeeruddin, M. K.; Sekiguchi, T.; Gratzel, M., A stable quasi-solid-state dye-sensitized solar cell with an amphiphilic ruthenium sensitizer and polymer gel electrolyte. *Nat Mater* **2003,** *2* (6), 402-7.
48. Nazeeruddin, M. K.; Pechy, P.; Renouard, T.; Zakeeruddin, S. M.; Humphry-Baker, R.; Comte, P.; Liska, P.; Cevey, L.; Costa, E.; Shklover, V.; Spiccia, L.; Deacon, G. B.; Bignozzi, C. A.; Gratzel, M., Engineering of efficient panchromatic sensitizers for nanocrystalline TiO(2)-based solar cells. *J Am Chem Soc* **2001,** *123* (8), 1613-24.
49. Aghazada, S.; Nazeeruddin, M., Ruthenium Complexes as Sensitizers in Dye-Sensitized Solar Cells. *Inorganics* **2018,** *6* (2).
50. Onicha, A. C.; Castellano, F. N., Electrolyte-Dependent Photovoltaic Responses in Dye-Sensitized Solar Cells Based on an Osmium(II) Dye of Mixed Denticity. *The Journal of Physical Chemistry C* **2010,** *114* (14), 6831-6840.
51. Redmond, G.; Fitzmaurice, D.; Graetzel, M., Effect of surface chelation on the energy of an intraband surface state of a nanocrystalline titania film. *The Journal of Physical Chemistry* **2002,** *97* (27), 6951-6954.
52. Paoprasert, P.; Laaser, J. E.; Xiong, W.; Franking, R. A.; Hamers, R. J.; Zanni, M. T.; Schmidt, J. R.; Gopalan, P., Bridge-Dependent Interfacial Electron Transfer from Rhenium−Bipyridine Complexes to TiO2 Nanocrystalline Thin Films. *The Journal of Physical Chemistry C* **2010,** *114* (21), 9898-9907.
53. Wu, W.; Xu, X.; Yang, H.; Hua, J.; Zhang, X.; Zhang, L.; Long, Y.; Tian, H., D–π–M–π–A structured platinum acetylide sensitizer for dye-sensitized solar cells. *Journal of Materials Chemistry* **2011,** *21* (29).
54. Bessho, T.; Constable, E. C.; Graetzel, M.; Hernandez Redondo, A.; Housecroft, C. E.; Kylberg, W.; Nazeeruddin, M. K.; Neuburger, M.; Schaffner, S., An element of surprise--efficient copper-functionalized dye-sensitized solar cells. *Chem Commun (Camb)* **2008,** (32), 3717-9.
55. Kuang, D.; Uchida, S.; Humphry-Baker, R.; Zakeeruddin, S. M.; Grätzel, M., Organic Dye-Sensitized Ionic Liquid Based Solar Cells: Remarkable Enhancement in Performance through Molecular Design of Indoline Sensitizers. *Angewandte Chemie* **2008,** *120* (10), 1949-1953.
56. Howie, W. H.; Claeyssens, F.; Miura, H.; Peter, L. M., Characterization of solid-state dye-sensitized solar cells utilizing high absorption coefficient metal-free organic dyes. *J Am Chem Soc* **2008,** *130* (4), 1367-75.

57. Tanaka, H.; Takeichi, A.; Higuchi, K.; Motohiro, T.; Takata, M.; Hirota, N.; Nakajima, J.; Toyoda, T., Long-term durability and degradation mechanism of dye-sensitized solar cells sensitized with indoline dyes. **2009,** *93* (6-7), 1143-1148.
58. Hagberg, D. P.; Jiang, X.; Gabrielsson, E.; Linder, M.; Marinado, T.; Brinck, T.; Hagfeldt, A.; Sun, L., Symmetric and unsymmetric donor functionalization. comparing structural and spectral benefits of chromophores for dye-sensitized solar cells. *Journal of Materials Chemistry* **2009,** *19* (39).
59. Feldt, S. M.; Gibson, E. A.; Gabrielsson, E.; Sun, L.; Boschloo, G.; Hagfeldt, A., Design of organic dyes and cobalt polypyridine redox mediators for high-efficiency dye-sensitized solar cells. *J Am Chem Soc* **2010,** *132* (46), 16714-24.
60. Tsao, H. N.; Yi, C.; Moehl, T.; Yum, J. H.; Zakeeruddin, S. M.; Nazeeruddin, M. K.; Gratzel, M., Cyclopentadithiophene bridged donor-acceptor dyes achieve high power conversion efficiencies in dye-sensitized solar cells based on the tris-cobalt bipyridine redox couple. *ChemSusChem* **2011,** *4* (5), 591-4.
61. Hara, K.; Wang, Z. S.; Sato, T.; Furube, A.; Katoh, R.; Sugihara, H.; Dan-Oh, Y.; Kasada, C.; Shinpo, A.; Suga, S., Oligothiophene-containing coumarin dyes for efficient dye-sensitized solar cells. *J Phys Chem B* **2005,** *109* (32), 15476-82.
62. Hara, K.; Sato, T.; Katoh, R.; Furube, A.; Ohga, Y.; Shinpo, A.; Suga, S.; Sayama, K.; Sugihara, H.; Arakawa, H., Molecular Design of Coumarin Dyes for Efficient Dye-Sensitized Solar Cells. *The Journal of Physical Chemistry B* **2003,** *107* (2), 597-606.
63. Hara, K.; Sayama, K.; Arakawa, H.; Ohga, Y.; Shinpo, A.; Suga, S., A coumarin-derivative dye sensitized nanocrystalline TiO2 solar cell having a high solar-energy conversion efficiency up to 5.6%. *Chemical Communications* **2001,** (6), 569-570.
64. Ning, Z.; Zhang, Q.; Wu, W.; Pei, H.; Liu, B.; Tian, H., Starburst triarylamine based dyes for efficient dye-sensitized solar cells. *J Org Chem* **2008,** *73* (10), 3791-7.
65. Li, Q.; Lu, L.; Zhong, C.; Shi, J.; Huang, Q.; Jin, X.; Peng, T.; Qin, J.; Li, Z., New indole-based metal-free organic dyes for dye-sensitized solar cells. *J Phys Chem B* **2009,** *113* (44), 14588-95.
66. Choi, H.; Baik, C.; Kang, S. O.; Ko, J.; Kang, M.-S.; Nazeeruddin, M. K.; Grätzel, M., Highly Efficient and Thermally Stable Organic Sensitizers for Solvent-Free Dye-Sensitized Solar Cells. *Angewandte Chemie* **2008,** *120* (2), 333-336.
67. Kim, S.; Lee, J. K.; Kang, S. O.; Ko, J.; Yum, J. H.; Fantacci, S.; De Angelis, F.; Di Censo, D.; Nazeeruddin, M. K.; Grätzel, M., Molecular Engineering of Organic Sensitizers for Solar Cell Applications. *Journal of the American Chemical Society* **2006,** *128* (51), 16701-16707.
68. Liang, M.; Lu, M.; Wang, Q.-L.; Chen, W.-Y.; Han, H.-Y.; Sun, Z.; Xue, S., Efficient dye-sensitized solar cells with triarylamine organic dyes featuring functionalized-truxene unit. *Journal of Power Sources* **2011,** *196* (3), 1657-1664.
69. Hagberg, D. P.; Marinado, T.; Karlsson, K. M.; Nonomura, K.; Qin, P.; Boschloo, G.; Brinck, T.; Hagfeldt, A.; Sun, L., Tuning the HOMO and LUMO Energy Levels of Organic Chromophores for Dye Sensitized Solar Cells. *The Journal of Organic Chemistry* **2007,** *72* (25), 9550-9556.
70. Xu, M.; Li, R.; Pootrakulchote, N.; Shi, D.; Guo, J.; Yi, Z.; Zakeeruddin, S. M.; Grätzel, M.; Wang, P., Energy-Level and Molecular Engineering of Organic D-π-A Sensitizers in Dye-Sensitized Solar Cells. *The Journal of Physical Chemistry C* **2008,** *112* (49), 19770-19776.
71. Liu, W. H.; Wu, I. C.; Lai, C. H.; Lai, C. H.; Chou, P. T.; Li, Y. T.; Chen, C. L.; Hsu, Y. Y.; Chi, Y., Simple organic molecules bearing a 3,4-ethylenedioxythiophene linker for efficient dye-sensitized solar cells. *Chem Commun (Camb)* **2008,** (41), 5152-4.
72. Li, R.; Liu, J.; Cai, N.; Zhang, M.; Wang, P., Synchronously reduced surface states, charge recombination, and light absorption length for high-performance organic dye-sensitized solar cells. *J Phys Chem B* **2010,** *114* (13), 4461-4.

73. Zhang, X.; Xu, Y.; Giordano, F.; Schreier, M.; Pellet, N.; Hu, Y.; Yi, C.; Robertson, N.; Hua, J.; Zakeeruddin, S. M.; Tian, H.; Gratzel, M., Molecular Engineering of Potent Sensitizers for Very Efficient Light Harvesting in Thin-Film Solid-State Dye-Sensitized Solar Cells. *J Am Chem Soc* **2016,** *138* (34), 10742-5.
74. Kakiage, K.; Aoyama, Y.; Yano, T.; Oya, K.; Fujisawa, J.; Hanaya, M., Highly-efficient dye-sensitized solar cells with collaborative sensitization by silyl-anchor and carboxy-anchor dyes. *Chem Commun (Camb)* **2015,** *51* (88), 15894-7.
75. Emsley, J., The Elements 3rd ed.: Clarendon. Oxford: 1998.
76. Ferrere, S.; Gregg, B. A., Photosensitization of TiO2by [FeII(2,2'-bipyridine-4,4'-dicarboxylic acid)2(CN)2]: Band Selective Electron Injection from Ultra-Short-Lived Excited States. *Journal of the American Chemical Society* **1998,** *120* (4), 843-844.
77. Sun, Q.; Mosquera-Vazquez, S.; Suffren, Y.; Hankache, J.; Amstutz, N.; Lawson Daku, L. M.; Vauthey, E.; Hauser, A., On the role of ligand-field states for the photophysical properties of ruthenium(II) polypyridyl complexes. *Coordin Chem Rev* **2015,** *282-283*, 87-99.
78. Sun, Q.; Dereka, B.; Vauthey, E.; Lawson Daku, L. M.; Hauser, A., Ultrafast transient IR spectroscopy and DFT calculations of ruthenium(ii) polypyridyl complexes. *Chem Sci* **2017,** *8* (1), 223-230.
79. Juban, E. A.; Smeigh, A. L.; Monat, J. E.; McCusker, J. K., Ultrafast dynamics of ligand-field excited states. *Coordin Chem Rev* **2006,** *250* (13-14), 1783-1791.
80. Cannizzo, A.; Milne, C. J.; Consani, C.; Gawelda, W.; Bressler, C.; van Mourik, F.; Chergui, M., Light-induced spin crossover in Fe(II)-based complexes: The full photocycle unraveled by ultrafast optical and X-ray spectroscopies. *Coordin Chem Rev* **2010,** *254* (21-22), 2677-2686.
81. Wenger, O. S., Is Iron the New Ruthenium? *Chemistry* **2019,** *25* (24), 6043-6052.
82. Caspar, J. V.; Meyer, T. J., Application of the energy gap law to nonradiative, excited-state decay. *The Journal of Physical Chemistry* **2002,** *87* (6), 952-957.
83. Jamula, L. L.; Brown, A. M.; Guo, D.; McCusker, J. K., Synthesis and characterization of a high-symmetry ferrous polypyridyl complex: approaching the 5T2/3T1 crossing point for Fe(II.). *Inorg Chem* **2014,** *53* (1), 15-7.
84. Mengel, A. K.; Forster, C.; Breivogel, A.; Mack, K.; Ochsmann, J. R.; Laquai, F.; Ksenofontov, V.; Heinze, K., A heteroleptic push-pull substituted iron(II) bis(tridentate) complex with low-energy charge-transfer states. *Chemistry* **2015,** *21* (2), 704-14.
85. Fatur, S. M.; Shepard, S. G.; Higgins, R. F.; Shores, M. P.; Damrauer, N. H., A Synthetically Tunable System To Control MLCT Excited-State Lifetimes and Spin States in Iron(II) Polypyridines. *J Am Chem Soc* **2017,** *139* (12), 4493-4505.
86. Shepard, S. G.; Fatur, S. M.; Rappe, A. K.; Damrauer, N. H., Highly Strained Iron(II) Polypyridines: Exploiting the Quintet Manifold To Extend the Lifetime of MLCT Excited States. *J Am Chem Soc* **2016,** *138* (9), 2949-52.
87. Mukherjee, S.; Bowman, D. N.; Jakubikova, E., Cyclometalated Fe(II) complexes as sensitizers in dye-sensitized solar cells. *Inorg Chem* **2015,** *54* (2), 560-9.
88. Dixon, I. M.; Alary, F.; Boggio-Pasqua, M.; Heully, J. L., Reversing the relative 3MLCT-3MC order in Fe(ii) complexes using cyclometallating ligands: a computational study aiming at luminescent Fe(ii) complexes. *Dalton Trans* **2015,** *44* (30), 13498-503.
89. Dixon, I. M.; Khan, S.; Alary, F.; Boggio-Pasqua, M.; Heully, J. L., Probing the photophysical capability of mono and bis(cyclometallated) Fe(ii) polypyridine complexes using inexpensive ground state DFT. *Dalton Trans* **2014,** *43* (42), 15898-905.
90. Liu, Y.; Kjaer, K. S.; Fredin, L. A.; Chabera, P.; Harlang, T.; Canton, S. E.; Lidin, S.; Zhang, J.; Lomoth, R.; Bergquist, K. E.; Persson, P.; Warnmark, K.; Sundstrom, V., A heteroleptic ferrous complex with mesoionic bis(1,2,3-triazol-5-ylidene) ligands: taming the MLCT excited state of iron(II). *Chemistry* **2015,** *21* (9), 3628-39.
91. Liu, Y.; Harlang, T.; Canton, S. E.; Chabera, P.; Suarez-Alcantara, K.; Fleckhaus, A.; Vithanage, D. A.; Goransson, E.; Corani, A.; Lomoth, R.; Sundstrom, V.; Warnmark, K., Towards

longer-lived metal-to-ligand charge transfer states of iron(II) complexes: an N-heterocyclic carbene approach. *Chem Commun (Camb)* **2013,** *49* (57), 6412-4.
92. Liu, Y.; Persson, P.; Sundstrom, V.; Warnmark, K., Fe N-Heterocyclic Carbene Complexes as Promising Photosensitizers. *Acc Chem Res* **2016,** *49* (8), 1477-85.
93. Duchanois, T.; Liu, L.; Pastore, M.; Monari, A.; Cebrián, C.; Trolez, Y.; Darari, M.; Magra, K.; Francés-Monerris, A.; Domenichini, E.; Beley, M.; Assfeld, X.; Haacke, S.; Gros, P., NHC-Based Iron Sensitizers for DSSCs. *Inorganics* **2018,** *6* (2).
94. Liu, L.; Duchanois, T.; Etienne, T.; Monari, A.; Beley, M.; Assfeld, X.; Haacke, S.; Gros, P. C., A new record excited state (3)MLCT lifetime for metalorganic iron(ii) complexes. *Phys Chem Chem Phys* **2016,** *18* (18), 12550-6.
95. Chen, C.-M.; Chen, C.-H.; Wei, T.-C., Chemical deposition of platinum on metallic sheets as counterelectrodes for dye-sensitized solar cells. *Electrochimica Acta* **2010,** *55* (5), 1687-1695.
96. Tsao, H. N.; Burschka, J.; Yi, C.; Kessler, F.; Nazeeruddin, M. K.; Grätzel, M., Influence of the interfacial charge-transfer resistance at the counter electrode in dye-sensitized solar cells employing cobalt redox shuttles. *Energy & Environmental Science* **2011,** *4* (12).
97. Hauch, A.; Georg, A., Diffusion in the electrolyte and charge-transfer reaction at the platinum electrode in dye-sensitized solar cells. *Electrochimica Acta* **2001,** *46* (22), 3457-3466.
98. Papageorgiou, N.; Maier, W. F.; Grätzel, M., An Iodine/Triiodide Reduction Electrocatalyst for Aqueous and Organic Media. *Journal of The Electrochemical Society* **2019,** *144* (3), 876-884.
99. Olsen, E.; Hagen, G.; Eric Lindquist, S., Dissolution of platinum in methoxy propionitrile containing LiI/I2. *Solar Energy Materials and Solar Cells* **2000,** *63* (3), 267-273.
100. Yun, S.; Hagfeldt, A.; Ma, T., Pt-free counter electrode for dye-sensitized solar cells with high efficiency. *Adv Mater* **2014,** *26* (36), 6210-37.
101. Kay, A.; Grätzel, M., Low cost photovoltaic modules based on dye sensitized nanocrystalline titanium dioxide and carbon powder. *Solar Energy Materials and Solar Cells* **1996,** *44* (1), 99-117.
102. Pettersson, H.; Gruszecki, T.; Bernhard, R.; Häggman, L.; Gorlov, M.; Boschloo, G.; Edvinsson, T.; Kloo, L.; Hagfeldt, A., The monolithic multicell: a tool for testing material components in dye-sensitized solar cells. *Progress in Photovoltaics: Research and Applications* **2007,** *15* (2), 113-121.
103. Friedrich, J. K., S.; Gerhard, H.; Werner, S.; Jurgen, H.; Michael, D, Polythiophenes, Process for Their Preparation and Their Use. *Patent US4987042A* **22 April 1988**.
104. Zozoulenko, I.; Singh, A.; Singh, S. K.; Gueskine, V.; Crispin, X.; Berggren, M., Polarons, Bipolarons, And Absorption Spectroscopy of PEDOT. *ACS Applied Polymer Materials* **2018,** *1* (1), 83-94.
105. Marchini, E.; Caramori, S.; Bignozzi, C. A.; Carli, S., On the Use of PEDOT as a Catalytic Counter Electrode Material in Dye-Sensitized Solar Cells. *Applied Sciences* **2021,** *11* (9).
106. Saito, Y.; Kitamura, T.; Wada, Y.; Yanagida, S., Application of Poly(3,4-ethylenedioxythiophene) to Counter Electrode in Dye-Sensitized Solar Cells. *Chemistry Letters* **2002,** *31* (10), 1060-1061.
107. Carli, S.; Busatto, E.; Caramori, S.; Boaretto, R.; Argazzi, R.; Timpson, C. J.; Bignozzi, C. A., Comparative Evaluation of Catalytic Counter Electrodes for Co(III)/(II) Electron Shuttles in Regenerative Photoelectrochemical Cells. *The Journal of Physical Chemistry C* **2013,** *117* (10), 5142-5153.
108. Cao, Y.; Liu, Y.; Zakeeruddin, S. M.; Hagfeldt, A.; Grätzel, M., Direct Contact of Selective Charge Extraction Layers Enables High-Efficiency Molecular Photovoltaics. *Joule* **2018,** *2* (6), 1108-1117.
109. Boschloo, G.; Hagfeldt, A., Characteristics of the iodide/triiodide redox mediator in dye-sensitized solar cells. *Acc Chem Res* **2009,** *42* (11), 1819-26.
110. Wang, P.; Wenger, B.; Humphry-Baker, R.; Moser, J. E.; Teuscher, J.; Kantlehner, W.; Mezger, J.; Stoyanov, E. V.; Zakeeruddin, S. M.; Gratzel, M., Charge separation and efficient light

energy conversion in sensitized mesoscopic solar cells based on binary ionic liquids. *J Am Chem Soc* **2005,** *127* (18), 6850-6.
111. Papageorgiou, N.; Grätzel, M.; Infelta, P. P., On the relevance of mass transport in thin layer nanocrystalline photoelectrochemical solar cells. *Solar Energy Materials and Solar Cells* **1996,** *44* (4), 405-438.
112. Kubo, W.; Kambe, S.; Nakade, S.; Kitamura, T.; Hanabusa, K.; Wada, Y.; Yanagida, S., Photocurrent-Determining Processes in Quasi-Solid-State Dye-Sensitized Solar Cells Using Ionic Gel Electrolytes. *The Journal of Physical Chemistry B* **2003,** *107* (18), 4374-4381.
113. Nusbaumer, H.; Moser, J.-E.; Zakeeruddin, S. M.; Nazeeruddin, M. K.; Grätzel, M., CoII(dbbip)22+ Complex Rivals Tri-iodide/Iodide Redox Mediator in Dye-Sensitized Photovoltaic Cells. *The Journal of Physical Chemistry B* **2001,** *105* (43), 10461-10464.
114. Meyer TJ; H, T., In: Wilkinson G (ed) Comprehensive coordination chemistry: the synthesis, reactions, properties and applications of coordination compounds,. *Pergamon Press, Oxford, vol 1.*, p 331.
115. Mosconi, E.; Yum, J. H.; Kessler, F.; Gomez Garcia, C. J.; Zuccaccia, C.; Cinti, A.; Nazeeruddin, M. K.; Gratzel, M.; De Angelis, F., Cobalt electrolyte/dye interactions in dye-sensitized solar cells: a combined computational and experimental study. *J Am Chem Soc* **2012,** *134* (47), 19438-53.
116. Yum, J. H.; Baranoff, E.; Kessler, F.; Moehl, T.; Ahmad, S.; Bessho, T.; Marchioro, A.; Ghadiri, E.; Moser, J. E.; Yi, C.; Nazeeruddin, M. K.; Gratzel, M., A cobalt complex redox shuttle for dye-sensitized solar cells with high open-circuit potentials. *Nat Commun* **2012,** *3*, 631.
117. Feldt, S. M.; Wang, G.; Boschloo, G.; Hagfeldt, A., Effects of Driving Forces for Recombination and Regeneration on the Photovoltaic Performance of Dye-Sensitized Solar Cells using Cobalt Polypyridine Redox Couples. *The Journal of Physical Chemistry C* **2011,** *115* (43), 21500-21507.
118. Feldt, S. M.; Lohse, P. W.; Kessler, F.; Nazeeruddin, M. K.; Gratzel, M.; Boschloo, G.; Hagfeldt, A., Regeneration and recombination kinetics in cobalt polypyridine based dye-sensitized solar cells, explained using Marcus theory. *Phys Chem Chem Phys* **2013,** *15* (19), 7087-97.
119. Nelson, J. J.; Amick, T. J.; Elliott, C. M., Mass Transport of Polypyridyl Cobalt Complexes in Dye-Sensitized Solar Cells with Mesoporous TiO2 Photoanodes. *The Journal of Physical Chemistry C* **2008,** *112* (46), 18255-18263.
120. Klahr, B. M.; Hamann, T. W., Performance Enhancement and Limitations of Cobalt Bipyridyl Redox Shuttles in Dye-Sensitized Solar Cells. *The Journal of Physical Chemistry C* **2009,** *113* (31), 14040-14045.
121. Sapp, S. A.; Elliott, C. M.; Contado, C.; Caramori, S.; Bignozzi, C. A., Substituted polypyridine complexes of cobalt(II/III) as efficient electron-transfer mediators in dye-sensitized solar cells. *J Am Chem Soc* **2002,** *124* (37), 11215-22.
122. Kashif, M. K.; Nippe, M.; Duffy, N. W.; Forsyth, C. M.; Chang, C. J.; Long, J. R.; Spiccia, L.; Bach, U., Stable dye-sensitized solar cell electrolytes based on cobalt(II)/(III) complexes of a hexadentate pyridyl ligand. *Angew Chem Int Ed Engl* **2013,** *52* (21), 5527-31.
123. Bai, Y.; Yu, Q.; Cai, N.; Wang, Y.; Zhang, M.; Wang, P., High-efficiency organic dye-sensitized mesoscopic solar cells with a copper redox shuttle. *Chem Commun (Camb)* **2011,** *47* (15), 4376-8.
124. Freitag, M.; Giordano, F.; Yang, W.; Pazoki, M.; Hao, Y.; Zietz, B.; Grätzel, M.; Hagfeldt, A.; Boschloo, G., Copper Phenanthroline as a Fast and High-Performance Redox Mediator for Dye-Sensitized Solar Cells. *The Journal of Physical Chemistry C* **2016,** *120* (18), 9595-9603.
125. Hattori, S.; Wada, Y.; Yanagida, S.; Fukuzumi, S., Blue copper model complexes with distorted tetragonal geometry acting as effective electron-transfer mediators in dye-sensitized solar cells. *J Am Chem Soc* **2005,** *127* (26), 9648-54.
126. Saygili, Y.; Soderberg, M.; Pellet, N.; Giordano, F.; Cao, Y.; Munoz-Garcia, A. B.; Zakeeruddin, S. M.; Vlachopoulos, N.; Pavone, M.; Boschloo, G.; Kavan, L.; Moser, J. E.; Gratzel,

M.; Hagfeldt, A.; Freitag, M., Copper Bipyridyl Redox Mediators for Dye-Sensitized Solar Cells with High Photovoltage. *J Am Chem Soc* **2016,** *138* (45), 15087-15096.
127. Nazeeruddin, M. K.; Kay, A.; Rodicio, I.; Humphry-Baker, R.; Mueller, E.; Liska, P.; Vlachopoulos, N.; Graetzel, M., Conversion of light to electricity by cis-X2bis(2,2'-bipyridyl-4,4'-dicarboxylate)ruthenium(II) charge-transfer sensitizers (X = Cl-, Br-, I-, CN-, and SCN-) on nanocrystalline titanium dioxide electrodes. *Journal of the American Chemical Society* **2002,** *115* (14), 6382-6390.
128. Schlichthörl, G.; Huang, S. Y.; Sprague, J.; Frank, A. J., Band Edge Movement and Recombination Kinetics in Dye-Sensitized Nanocrystalline TiO2 Solar Cells: A Study by Intensity Modulated Photovoltage Spectroscopy. *The Journal of Physical Chemistry B* **1997,** *101* (41), 8141-8155.
129. Haque, S. A.; Tachibana, Y.; Willis, R. L.; Moser, J. E.; Grätzel, M.; Klug, D. R.; Durrant, J. R., Parameters Influencing Charge Recombination Kinetics in Dye-Sensitized Nanocrystalline Titanium Dioxide Films. *The Journal of Physical Chemistry B* **1999,** *104* (3), 538-547.
130. Zhang, C.; Huang, Y.; Huo, Z.; Chen, S.; Dai, S., Photoelectrochemical Effects of Guanidinium Thiocyanate on Dye-Sensitized Solar Cell Performance and Stability. *The Journal of Physical Chemistry C* **2009,** *113* (52), 21779-21783.
131. Nusbaumer, H.; Zakeeruddin, S. M.; Moser, J. E.; Gratzel, M., An alternative efficient redox couple for the dye-sensitized solar cell system. *Chemistry* **2003,** *9* (16), 3756-63.
132. Kavan, L.; Grätzel, M., Highly efficient semiconducting TiO2 photoelectrodes prepared by aerosol pyrolysis. *Electrochimica Acta* **1995,** *40* (5), 643-652.
133. Cameron, P. J.; Peter, L. M., Characterization of titanium dioxide blocking layers in dye-sensitized nanocrystalline solar cells. *J The Journal of Physical Chemistry B* **2003,** *107* (51), 14394-14400.
134. Gregg, B. A.; Pichot, F.; Ferrere, S.; Fields, C. L., Interfacial Recombination Processes in Dye-Sensitized Solar Cells and Methods To Passivate the Interfaces. *The Journal of Physical Chemistry B* **2001,** *105* (7), 1422-1429.
135. Carli, S.; Casarin, L.; Caramori, S.; Boaretto, R.; Busatto, E.; Argazzi, R.; Bignozzi, C. A., A viable surface passivation approach to improve efficiency in cobalt based dye sensitized solar cells. *Polyhedron* **2014,** *82*, 173-180.
136. Balzani, V.; Ceroni, P.; Juris, A., Photochemistry and Photophysics. Concepts, Research, Applications. *Angewandte Chemie International Edition* **2014,** *53* (34), 8817-8817.
137. Nasr, C.; Hotchandani, S.; Kamat, P. V., Role of Iodide in Photoelectrochemical Solar Cells. Electron Transfer between Iodide Ions and Ruthenium Polypyridyl Complex Anchored on Nanocrystalline SiO2 and SnO2 Films. *The Journal of Physical Chemistry B* **1998,** *102* (25), 4944-4951.
138. Gardner, J. M.; Giaimuccio, J. M.; Meyer, G. J., Evidence for iodine atoms as intermediates in the dye sensitized formation of I-I bonds. *J Am Chem Soc* **2008,** *130* (51), 17252-3.
139. Marcus, R. A., Chemical and Electrochemical Electron-Transfer Theory. *Annual Review of Physical Chemistry* **1964,** *15* (1), 155-196.
140. Marcus, R. A.; Sutin, N., Electron transfers in chemistry and biology. *Biochimica et Biophysica Acta (BBA) - Reviews on Bioenergetics* **1985,** *811* (3), 265-322.
141. Ardo, S.; Meyer, G. J., Photodriven heterogeneous charge transfer with transition-metal compounds anchored to TiO2 semiconductor surfaces. *Chem Soc Rev* **2009,** *38* (1), 115-64.
142. Gerischer, H., Electrochemical Techniques for the Study of Photosensitization*. *Photochemistry and Photobiology* **2008,** *16* (4), 243-260.
143. Marcus, R. A., On the Theory of Electron-Transfer Reactions. VI. Unified Treatment for Homogeneous and Electrode Reactions. *The Journal of Chemical Physics* **1965,** *43* (2), 679-701.
144. Prezhdo, O. V.; Duncan, W. R.; Prezhdo, V. V., Dynamics of the photoexcited electron at the chromophore-semiconductor interface. *Acc Chem Res* **2008,** *41* (2), 339-48.

145. Listorti, A.; O'Regan, B.; Durrant, J. R., Electron Transfer Dynamics in Dye-Sensitized Solar Cells. *Chemistry of Materials* **2011,** *23* (15), 3381-3399.
146. Cardon, F.; Gomes, W. P., On the determination of the flat-band potential of a semiconductor in contact with a metal or an electrolyte from the Mott-Schottky plot. *Journal of Physics D: Applied Physics* **1978,** *11* (4), L63-L67.
147. Westermark, K.; Henningsson, A.; Rensmo, H.; Södergren, S.; Siegbahn, H.; Hagfeldt, A., Determination of the electronic density of states at a nanostructured TiO2/Ru-dye/electrolyte interface by means of photoelectron spectroscopy. *Chemical Physics* **2002,** *285* (1), 157-165.
148. Morris, A. J.; Meyer, G. J., TiO2 Surface Functionalization to Control the Density of States. *The Journal of Physical Chemistry C* **2008,** *112* (46), 18224-18231.
149. O'Regan, B. C.; Durrant, J. R.; Sommeling, P. M.; Bakker, N. J., Influence of the TiCl4 Treatment on Nanocrystalline TiO2 Films in Dye-Sensitized Solar Cells. 2. Charge Density, Band Edge Shifts, and Quantification of Recombination Losses at Short Circuit. *The Journal of Physical Chemistry C* **2007,** *111* (37), 14001-14010.
150. Quintana, M.; Edvinsson, T.; Hagfeldt, A.; Boschloo, G., Comparison of Dye-Sensitized ZnO and TiO2 Solar Cells: Studies of Charge Transport and Carrier Lifetime. *The Journal of Physical Chemistry C* **2006,** *111* (2), 1035-1041.
151. Bailes, M.; Cameron, P. J.; Lobato, K.; Peter, L. M., Determination of the density and energetic distribution of electron traps in dye-sensitized nanocrystalline solar cells. *J Phys Chem B* **2005,** *109* (32), 15429-35.
152. Duffy, N. W.; Peter, L. M.; Rajapakse, R. M. G.; Wijayantha, K. G. U., A novel charge extraction method for the study of electron transport and interfacial transfer in dye sensitised nanocrystalline solar cells. *Electrochemistry Communications* **2000,** *2* (9), 658-662.
153. Tachibana, Y.; Haque, S. A.; Mercer, I. P.; Moser, J. E.; Klug, D. R.; Durrant, J. R., Modulation of the Rate of Electron Injection in Dye-Sensitized Nanocrystalline TiO2 Films by Externally Applied Bias. *The Journal of Physical Chemistry B* **2001,** *105* (31), 7424-7431.
154. Tachibana, Y.; Moser, J. E.; Grätzel, M.; Klug, D. R.; Durrant, J. R., Subpicosecond Interfacial Charge Separation in Dye-Sensitized Nanocrystalline Titanium Dioxide Films. *The Journal of Physical Chemistry* **1996,** *100* (51), 20056-20062.
155. Montanari, I.; Nelson, J.; Durrant, J. R., Iodide Electron Transfer Kinetics in Dye-Sensitized Nanocrystalline TiO2 Films. *The Journal of Physical Chemistry B* **2002,** *106* (47), 12203-12210.
156. Pelet, S.; Moser, J.-E.; Grätzel, M., Cooperative Effect of Adsorbed Cations and Iodide on the Interception of Back Electron Transfer in the Dye Sensitization of Nanocrystalline TiO2. *The Journal of Physical Chemistry B* **2000,** *104* (8), 1791-1795.
157. Clifford, J. N.; Palomares, E.; Nazeeruddin, M. K.; Grätzel, M.; Durrant, J. R., Dye Dependent Regeneration Dynamics in Dye Sensitized Nanocrystalline Solar Cells: Evidence for the Formation of a Ruthenium Bipyridyl Cation/Iodide Intermediate. *The Journal of Physical Chemistry C* **2007,** *111* (17), 6561-6567.
158. Upadhyaya, H. M.; Hirata, N.; Haque, S. A.; de Paoli, M. A.; Durrant, J. R., Kinetic competition in flexible dye sensitised solar cells employing a series of polymer electrolytes. *Chem Commun (Camb)* **2006,** (8), 877-9.
159. Nei de Freitas, J.; Nogueira, A. F.; De Paoli, M.-A., New insights into dye-sensitized solar cells with polymer electrolytes. *Journal of Materials Chemistry* **2009,** *19* (30).
160. Kroeze, J. E.; Hirata, N.; Koops, S.; Nazeeruddin, M. K.; Schmidt-Mende, L.; Gratzel, M.; Durrant, J. R., Alkyl chain barriers for kinetic optimization in dye-sensitized solar cells. *J Am Chem Soc* **2006,** *128* (50), 16376-83.
161. O'Regan, B.; Moser, J.; Anderson, M.; Graetzel, M., Vectorial electron injection into transparent semiconductor membranes and electric field effects on the dynamics of light-induced charge separation. *The Journal of Physical Chemistry* **2002,** *94* (24), 8720-8726.

162. Soedergren, S.; Hagfeldt, A.; Olsson, J.; Lindquist, S.-E., Theoretical Models for the Action Spectrum and the Current-Voltage Characteristics of Microporous Semiconductor Films in Photoelectrochemical Cells. *The Journal of Physical Chemistry* **2002,** *98* (21), 5552-5556.
163. Solbrand, A.; Lindström, H.; Rensmo, H.; Hagfeldt, A.; Lindquist, S.-E.; Södergren, S., Electron Transport in the Nanostructured TiO2−Electrolyte System Studied with Time-Resolved Photocurrents. *The Journal of Physical Chemistry B* **1997,** *101* (14), 2514-2518.
164. Kopidakis, N.; Schiff, E. A.; Park, N. G.; van de Lagemaat, J.; Frank, A. J., Ambipolar Diffusion of Photocarriers in Electrolyte-Filled, Nanoporous TiO2. *The Journal of Physical Chemistry B* **2000,** *104* (16), 3930-3936.
165. Nistér, D.; Keis, K.; Lindquist, S.-E.; Hagfeldt, A., A detailed analysis of ambipolar diffusion in nanostructured metal oxide films. *Solar Energy Materials and Solar Cells* **2002,** *73* (4), 411-423.
166. Kambe, S.; Nakade, S.; Kitamura, T.; Wada, Y.; Yanagida, S., Influence of the Electrolytes on Electron Transport in Mesoporous TiO2−Electrolyte Systems. *The Journal of Physical Chemistry B* **2002,** *106* (11), 2967-2972.
167. Nakade, S.; Kambe, S.; Kitamura, T.; Wada, Y.; Yanagida, S., Effects of Lithium Ion Density on Electron Transport in Nanoporous TiO2 Electrodes. *The Journal of Physical Chemistry B* **2001,** *105* (38), 9150-9152.
168. Nakade, S.; Kanzaki, T.; Kubo, W.; Kitamura, T.; Wada, Y.; Yanagida, S., Role of electrolytes on charge recombination in dye-sensitized TiO(2) solar cell (1): the case of solar cells using the I(-)/I(3)(-) redox couple. *J Phys Chem B* **2005,** *109* (8), 3480-7.
169. Fredin, K.; Gorlov, M.; Pettersson, H.; Hagfeldt, A.; Kloo, L.; Boschloo, G., On the Influence of Anions in Binary Ionic Liquid Electrolytes for Monolithic Dye-Sensitized Solar Cells. *The Journal of Physical Chemistry C* **2007,** *111* (35), 13261-13266.
170. Boschloo, G.; Haggman, L.; Hagfeldt, A., Quantification of the effect of 4-tert-butylpyridine addition to I-/I3- redox electrolytes in dye-sensitized nanostructured TiO2 solar cells. *J Phys Chem B* **2006,** *110* (26), 13144-50.
171. Forro, L.; Chauvet, O.; Emin, D.; Zuppiroli, L.; Berger, H.; Lévy, F., High mobilityn-type charge carriers in large single crystals of anatase (TiO2). *Journal of Applied Physics* **1994,** *75* (1), 633-635.
172. Dloczik, L.; Ileperuma, O.; Lauermann, I.; Peter, L. M.; Ponomarev, E. A.; Redmond, G.; Shaw, N. J.; Uhlendorf, I., Dynamic Response of Dye-Sensitized Nanocrystalline Solar Cells: Characterization by Intensity-Modulated Photocurrent Spectroscopy. *The Journal of Physical Chemistry B* **1997,** *101* (49), 10281-10289.
173. van de Lagemaat, J.; Frank, A. J., Effect of the Surface-State Distribution on Electron Transport in Dye-Sensitized TiO2 Solar Cells: Nonlinear Electron-Transport Kinetics. *The Journal of Physical Chemistry B* **2000,** *104* (18), 4292-4294.
174. Bisquert, J.; Vikhrenko, V. S., Interpretation of the Time Constants Measured by Kinetic Techniques in Nanostructured Semiconductor Electrodes and Dye-Sensitized Solar Cells. *The Journal of Physical Chemistry B* **2004,** *108* (7), 2313-2322.
175. Fisher, A. C.; Peter, L. M.; Ponomarev, E. A.; Walker, A. B.; Wijayantha, K. G. U., Intensity Dependence of the Back Reaction and Transport of Electrons in Dye-Sensitized Nanocrystalline TiO2 Solar Cells. *The Journal of Physical Chemistry B* **2000,** *104* (5), 949-958.
176. Bisquert, J., Chemical Diffusion Coefficient of Electrons in Nanostructured Semiconductor Electrodes and Dye-Sensitized Solar Cells. *The Journal of Physical Chemistry B* **2004,** *108* (7), 2323-2332.
177. Kelly, C. A.; Farzad, F.; Thompson, D. W.; Stipkala, J. M.; Meyer, G. J., Cation-Controlled Interfacial Charge Injection in Sensitized Nanocrystalline TiO2. *Langmuir* **1999,** *15* (20), 7047-7054.
178. Haque, S. A.; Tachibana, Y.; Klug, D. R.; Durrant, J. R., Charge Recombination Kinetics in Dye-Sensitized Nanocrystalline Titanium Dioxide Films under Externally Applied Bias. *The Journal of Physical Chemistry B* **1998,** *102* (10), 1745-1749.

179. Kuciauskas, D.; Freund, M. S.; Gray, H. B.; Winkler, J. R.; Lewis, N. S., Electron Transfer Dynamics in Nanocrystalline Titanium Dioxide Solar Cells Sensitized with Ruthenium or Osmium Polypyridyl Complexes. *The Journal of Physical Chemistry B* **2000,** *105* (2), 392-403.
180. Nelson, J.; Haque, S. A.; Klug, D. R.; Durrant, J. R., Trap-limited recombination in dye-sensitized nanocrystalline metal oxide electrodes. *Physical Review B* **2001,** *63* (20).
181. Clifford, J. N.; Palomares, E.; Nazeeruddin, M. K.; Gratzel, M.; Nelson, J.; Li, X.; Long, N. J.; Durrant, J. R., Molecular control of recombination dynamics in dye-sensitized nanocrystalline TiO2 films: free energy vs distance dependence. *J Am Chem Soc* **2004,** *126* (16), 5225-33.
182. Bisquert, J.; Zaban, A.; Greenshtein, M.; Mora-Sero, I., Determination of rate constants for charge transfer and the distribution of semiconductor and electrolyte electronic energy levels in dye-sensitized solar cells by open-circuit photovoltage decay method. *J Am Chem Soc* **2004,** *126* (41), 13550-9.
183. Cameron, P. J.; Peter, L. M., How does back-reaction at the conducting glass substrate influence the dynamic photovoltage response of nanocrystalline dye-sensitized solar cells? *J Phys Chem B* **2005,** *109* (15), 7392-8.
184. Papageorgiou, N.; Athanassov, Y.; Armand, M.; Bonho⁄te, P.; Pettersson, H.; Azam, A.; Grätzel, M., The Performance and Stability of Ambient Temperature Molten Salts for Solar Cell Applications. *Journal of The Electrochemical Society* **2019,** *143* (10), 3099-3108.
185. Bard, A. J.; Faulkner, L. R., Electrochemical methods Fundamentals and applications. **2001,** *2* (482), 580-632.
186. Randles, J. E. B., Kinetics of rapid electrode reactions. *Discussions of the Faraday Society* **1947,** *1*.
187. Sacco, A., Electrochemical impedance spectroscopy: Fundamentals and application in dye-sensitized solar cells. *Renewable and Sustainable Energy Reviews* **2017,** *79*, 814-829.
188. Orazem, M. E.; Tribollet, B., Electrochemical impedance spectroscopy. **2008**.
189. Balzani, V.; Ceroni, P.; Juris, A., Photochemistry and Photophysics: Concepts, Research, Applications. **April 2014**.
190. Scaiano, J. C., Nanosecond Laser Flash Photolysis: A Tool for Physical Organic Chemistry. **2003**.
191. Ardo, S.; Sun, Y.; Staniszewski, A.; Castellano, F. N.; Meyer, G. J., Stark effects after excited-state interfacial electron transfer at sensitized TiO(2) nanocrystallites. *J Am Chem Soc* **2010,** *132* (19), 6696-709.
192. Fabregat-Santiago, F.; Bisquert, J.; Garcia-Belmonte, G.; Boschloo, G.; Hagfeldt, A., Influence of electrolyte in transport and recombination in dye-sensitized solar cells studied by impedance spectroscopy. *Solar Energy Materials and Solar Cells* **2005,** *87* (1-4), 117-131.
193. Han, L.; Koide, N.; Chiba, Y.; Mitate, T., Modeling of an equivalent circuit for dye-sensitized solar cells. *Applied Physics Letters* **2004,** *84* (13), 2433-2435.
194. van de Lagemaat, J.; Park, N. G.; Frank, A. J., Influence of Electrical Potential Distribution, Charge Transport, and Recombination on the Photopotential and Photocurrent Conversion Efficiency of Dye-Sensitized Nanocrystalline TiO2 Solar Cells: A Study by Electrical Impedance and Optical Modulation Techniques. *The Journal of Physical Chemistry B* **2000,** *104* (9), 2044-2052.
195. Kern, R.; Sastrawan, R.; Ferber, J.; Stangl, R.; Luther, J., Modeling and interpretation of electrical impedance spectra of dye solar cells operated under open-circuit conditions. *Electrochimica Acta* **2002,** *47* (26), 4213-4225.
196. Fabregat-Santiago, F.; Garcia-Belmonte, G.; Bisquert, J.; Bogdanoff, P.; Zaban, A., Mott-Schottky Analysis of Nanoporous Semiconductor Electrodes in Dielectric State Deposited on SnO[sub 2](F) Conducting Substrates. *Journal of The Electrochemical Society* **2003,** *150* (6).
197. Bisquert, J., Chemical capacitance of nanostructured semiconductors: its origin and significance for nanocomposite solar cells. *Physical Chemistry Chemical Physics* **2003,** *5* (24).
198. Fabregat-Santiago, F.; Garcia-Belmonte, G.; Bisquert, J.; Zaban, A.; Salvador, P., Decoupling of Transport, Charge Storage, and Interfacial Charge Transfer in the Nanocrystalline

TiO2/Electrolyte System by Impedance Methods. *The Journal of Physical Chemistry B* **2001,** *106* (2), 334-339.
199. Bisquert, J., Theory of the Impedance of Electron Diffusion and Recombination in a Thin Layer. *The Journal of Physical Chemistry B* **2001,** *106* (2), 325-333.
200. Pitarch, Á.; Garcia-Belmonte, G.; Mora-Seró, I.; Bisquert, J., Electrochemical impedance spectra for the complete equivalent circuit of diffusion and reaction under steady-state recombination current. *Phys. Chem. Chem. Phys.* **2004,** *6* (11), 2983-2988.
201. Bisquert, J.; Garcia-Belmonte, G.; Fabregat-Santiago, F.; Ferriols, N. S.; Bogdanoff, P.; Pereira, E. C., Doubling Exponent Models for the Analysis of Porous Film Electrodes by Impedance. Relaxation of TiO2 Nanoporous in Aqueous Solution. *The Journal of Physical Chemistry B* **2000,** *104* (10), 2287-2298.
202. Dinca, M.; Dailly, A.; Liu, Y.; Brown, C. M.; Neumann, D. A.; Long, J. R., Hydrogen storage in a microporous metal-organic framework with exposed Mn2+ coordination sites. *J Am Chem Soc* **2006,** *128* (51), 16876-83.
203. Zhao, H.; Qu, Z. R.; Ye, H. Y.; Xiong, R. G., In situ hydrothermal synthesis of tetrazole coordination polymers with interesting physical properties. *Chem Soc Rev* **2008,** *37* (1), 84-100.
204. Steinhauser, G.; Klapotke, T. M., "Green" pyrotechnics: a chemists' challenge. *Angew Chem Int Ed Engl* **2008,** *47* (18), 3330-47.
205. Shavaleev, N. M.; Eliseeva, S. V.; Scopelliti, R.; Bunzli, J. C., Tridentate benzimidazole-pyridine-tetrazolates as sensitizers of europium luminescence. *Inorg Chem* **2014,** *53* (10), 5171-8.
206. D'Alessio, D.; Muzzioli, S.; Skelton, B. W.; Stagni, S.; Massi, M.; Ogden, M. I., Luminescent lanthanoid complexes of a tetrazole-functionalised calix[4]arene. *Dalton Trans* **2012,** *41* (16), 4736-9.
207. Dragonetti, C.; Colombo, A.; Magni, M.; Mussini, P.; Nisic, F.; Roberto, D.; Ugo, R.; Valore, A.; Valsecchi, A.; Salvatori, P.; Lobello, M. G.; De Angelis, F., Thiocyanate-free ruthenium(II) sensitizer with a pyrid-2-yltetrazolate ligand for dye-sensitized solar cells. *Inorg Chem* **2013,** *52* (19), 10723-5.
208. Colombo, A.; Dragonetti, C.; Magni, M.; Meroni, D.; Ugo, R.; Marotta, G.; Grazia Lobello, M.; Salvatori, P.; De Angelis, F., New thiocyanate-free ruthenium(II) sensitizers with different pyrid-2-yl tetrazolate ligands for dye-sensitized solar cells. *Dalton Trans* **2015,** *44* (26), 11788-96.
209. Wu, G.; Kaneko, R.; Zhang, Y.; Shinozaki, Y.; Sugawa, K.; Islam, A.; Han, L.; Bedja, I.; Gupta, R. K.; Shen, Q.; Otsuki, J., Neutral and anionic tetrazole-based ligands in designing novel ruthenium dyes for dye-sensitized solar cells. *Journal of Power Sources* **2016,** *307*, 416-425.
210. Fiorini, V.; Marchini, E.; Averardi, M.; Giorgini, L.; Muzzioli, S.; Dellai, A.; Argazzi, R.; Sanson, A.; Sangiorgi, N.; Caramori, S.; Stagni, S., New examples of Ru(II)-tetrazolato complexes as thiocyanate-free sensitizers for dye-sensitized solar cells. *Dalton Trans* **2020,** *49* (41), 14543-14555.
211. Boaretto, R.; Bignozzi, C. A.; Eva Busatto; Caramori, S.; Carli, S.; Sandro Fracasso; Patent PCT/IT2011/000397, Patent PCT/IT2011/000397, 2011.
212. M. J. Frisch; G. W. Trucks; H. B. Schlegel; G. E. Scuseria; M. A. Robb; J. R. Cheeseman; G. Scalmani; V. Barone; B. Mennucci; G. A. Petersson; H. Nakatsuji; M. Caricato; X. Li, H. P. H.; A. F. Izmaylov; J. Bloino; G. Zheng; J. L. Sonnenberg; M. Hada; M. Ehara; K. Toyota; R. Fukuda; J. Hasegawa; M. Ishida; T. Nakajima; Y. Honda; O. Kitao; H. Nakai; T. Vreven; J. A. Montgomery Jr.; J. E. Peralta; F. Ogliaro; M. J. Bearpark; J. Heyd; E. N. Brothers; K. N. Kudin; V. N. Staroverov; R. Kobayashi; J. Normand; K. Raghavachari; A. P. Rendell; J. C. Burant; S. S. Iyengar; J. Tomasi; M. Cossi; N. Rega; N. J. Millam; M. Klene; J. E. Knox; J. B. Cross; V. Bakken; C. Adamo; J. Jaramillo; R. Gomperts; R. E. Stratmann; O. Yazyev; A. J. Austin; R. Cammi; C. Pomelli; J. W. Ochterski; R. L. Martin; K. Morokuma; V. G. Zakrzewski; G. A. Voth; P. Salvador; J. J. Dannenberg; S. Dapprich; A. D. Daniels; Ö. Farkas; J. B. Foresman; J. V. Ortiz; Cioslowski, J.; D. J. Fox, Gaussian 09 Revison A.02.

213. Lu, T.; Chen, F., Multiwfn: a multifunctional wavefunction analyzer. *J Comput Chem* **2012,** *33* (5), 580-92.
214. Dossing, A.; Ryu, C. K.; Kudo, S.; Ford, P. C., Competitive bimolecular electron- and energy-transfer quenching of the excited state(s) of the tetranuclear copper(I) cluster Cu4I4py4. Evidence for large reorganization energies in an excited-state electron transfer. *Journal of the American Chemical Society* **2002,** *115* (12), 5132-5137.
215. Finnegan, W. G.; Henry, R. A.; Lofquist, R., An Improved Synthesis of 5-Substituted Tetrazoles. *Journal of the American Chemical Society* **2002,** *80* (15), 3908-3911.
216. Koguro, K.; Oga, T.; Mitsui, S.; Orita, R., Novel Synthesis of 5-Substituted Tetrazoles from Nitriles. *Synthesis* **1998,** *1998* (06), 910-914.
217. Trasatti, S., The absolute electrode potential: an explanatory note (Recommendations 1986). *Pure and Applied Chemistry* **1986,** *58* (7), 955-966.
218. Fredin, L. A.; Allison, T. C., Predicting Structures of Ru-Centered Dyes: A Computational Screening Tool. *J Phys Chem A* **2016,** *120* (13), 2135-43.
219. Pastore, M.; Selloni, A.; Fantacci, S.; De Angelis, F., Electronic and optical properties of dye-sensitized TiO(2) interfaces. *Top Curr Chem* **2014,** *347*, 1-45.
220. Prampolini, G.; Ingrosso, F.; Segalina, A.; Caramori, S.; Foggi, P.; Pastore, M., Dynamical and Environmental Effects on the Optical Properties of an Heteroleptic Ru(II)-Polypyridine Complex: A Multilevel Approach Combining Accurate Ground and Excited State QM-Derived Force Fields, MD and TD-DFT. *J Chem Theory Comput* **2019,** *15* (1), 529-545.
221. Cossi, M.; Barone, V.; Cammi, R.; Tomasi, J., Ab initio study of solvated molecules: a new implementation of the polarizable continuum model. *Chemical Physics Letters* **1996,** *255* (4-6), 327-335.
222. Fantacci, S.; De Angelis, F., A computational approach to the electronic and optical properties of Ru(II) and Ir(III) polypyridyl complexes: Applications to DSC, OLED and NLO. *Coordin Chem Rev* **2011,** *255* (21-22), 2704-2726.
223. Englman, R.; Jortner, J., The energy gap law for radiationless transitions in large molecules. *Molecular Physics* **1970,** *18* (2), 145-164.
224. Borgwardt, M.; Wilke, M.; Kampen, T.; Mähl, S.; Xiang, W.; Spiccia, L.; Lange, K. M.; Kiyan, I. Y.; Aziz, E. F., Injection Kinetics and Electronic Structure at the N719/TiO2 Interface Studied by Means of Ultrafast XUV Photoemission Spectroscopy. *The Journal of Physical Chemistry C* **2015,** *119* (17), 9099-9107.
225. Koops, S. E.; O'Regan, B. C.; Barnes, P. R.; Durrant, J. R., Parameters influencing the efficiency of electron injection in dye-sensitized solar cells. *J Am Chem Soc* **2009,** *131* (13), 4808-18.
226. Durrant, J. R.; Haque, S. A.; Palomares, E., Towards optimisation of electron transfer processes in dye sensitised solar cells. *Coordin Chem Rev* **2004,** *248* (13-14), 1247-1257.
227. Boschloo, G.; Gibson, E. A.; Hagfeldt, A., Photomodulated Voltammetry of Iodide/Triiodide Redox Electrolytes and Its Relevance to Dye-Sensitized Solar Cells. *The Journal of Physical Chemistry Letters* **2011,** *2* (24), 3016-3020.
228. Benazzi, E.; Magni, M.; Colombo, A.; Dragonetti, C.; Caramori, S.; Bignozzi, C. A.; Grisorio, R.; Suranna, G. P.; Cipolla, M. P.; Manca, M.; Roberto, D., Bis(1,10-phenanthroline) copper complexes with tailored molecular architecture: from electrochemical features to application as redox mediators in dye-sensitized solar cells. *Electrochimica Acta* **2018,** *271*, 180-189.
229. Dessì, A.; Calamante, M.; Mordini, A.; Peruzzini, M.; Sinicropi, A.; Basosi, R.; Fabrizi de Biani, F.; Taddei, M.; Colonna, D.; di Carlo, A.; Reginato, G.; Zani, L., Thiazolo[5,4-d]thiazole-based organic sensitizers with strong visible light absorption for transparent, efficient and stable dye-sensitized solar cells. *RSC Advances* **2015,** *5* (41), 32657-32668.
230. Sarker, S.; Ahammad, A. J. S.; Seo, H. W.; Kim, D. M., Electrochemical Impedance Spectra of Dye-Sensitized Solar Cells: Fundamentals and Spreadsheet Calculation. *International Journal of Photoenergy* **2014,** *2014*, 1-17.

231. Monat, J. E.; McCusker, J. K., Femtosecond Excited-State Dynamics of an Iron(II) Polypyridyl Solar Cell Sensitizer Model. *Journal of the American Chemical Society* **2000,** *122* (17), 4092-4097.
232. Zhang, W.; Alonso-Mori, R.; Bergmann, U.; Bressler, C.; Chollet, M.; Galler, A.; Gawelda, W.; Hadt, R. G.; Hartsock, R. W.; Kroll, T.; Kjaer, K. S.; Kubicek, K.; Lemke, H. T.; Liang, H. W.; Meyer, D. A.; Nielsen, M. M.; Purser, C.; Robinson, J. S.; Solomon, E. I.; Sun, Z.; Sokaras, D.; van Driel, T. B.; Vanko, G.; Weng, T. C.; Zhu, D.; Gaffney, K. J., Tracking excited-state charge and spin dynamics in iron coordination complexes. *Nature* **2014,** *509* (7500), 345-8.
233. Aubock, G.; Chergui, M., Sub-50-fs photoinduced spin crossover in [Fe(bpy)(3)](2)(+). *Nat Chem* **2015,** *7* (8), 629-33.
234. Magra, K.; Domenichini, E.; Frances-Monerris, A.; Cebrian, C.; Beley, M.; Darari, M.; Pastore, M.; Monari, A.; Assfeld, X.; Haacke, S.; Gros, P. C., Impact of the fac/ mer Isomerism on the Excited-State Dynamics of Pyridyl-carbene Fe(II) Complexes. *Inorg Chem* **2019,** *58* (8), 5069-5081.
235. Darari, M.; Domenichini, E.; Frances-Monerris, A.; Cebrian, C.; Magra, K.; Beley, M.; Pastore, M.; Monari, A.; Assfeld, X.; Haacke, S.; Gros, P. C., Iron(ii) complexes with diazinyl-NHC ligands: impact of pi-deficiency of the azine core on photophysical properties. *Dalton Trans* **2019,** *48* (29), 10915-10926.
236. Ronconi, F.; Syrgiannis, Z.; Bonasera, A.; Prato, M.; Argazzi, R.; Caramori, S.; Cristino, V.; Bignozzi, C. A., Modification of nanocrystalline WO3 with a dicationic perylene bisimide: applications to molecular level solar water splitting. *J Am Chem Soc* **2015,** *137* (14), 4630-3.
237. Marchini, E.; Darari, M.; Lazzarin, L.; Boaretto, R.; Argazzi, R.; Bignozzi, C. A.; Gros, P. C.; Caramori, S., Recombination and regeneration dynamics in FeNHC(ii)-sensitized solar cells. *Chem Commun (Camb)* **2020,** *56* (4), 543-546.
238. Argazzi, R.; Bignozzi, C. A.; Heimer, T. A.; Castellano, F. N.; Meyer, G. J., Enhanced Spectral Sensitivity from Ruthenium(II) Polypyridyl Based Photovoltaic Devices. *Inorganic Chemistry* **2002,** *33* (25), 5741-5749.
239. Karpacheva, M.; Housecroft, C. E.; Constable, E. C., Electrolyte tuning in dye-sensitized solar cells with N-heterocyclic carbene (NHC) iron(II) sensitizers. *Beilstein J Nanotechnol* **2018,** *9*, 3069-3078.
240. Green, A. N.; Palomares, E.; Haque, S. A.; Kroon, J. M.; Durrant, J. R., Charge transport versus recombination in dye-sensitized solar cells employing nanocrystalline TiO2 and SnO2 films. *J Phys Chem B* **2005,** *109* (25), 12525-33.
241. Pastore, M.; Duchanois, T.; Liu, L.; Monari, A.; Assfeld, X.; Haacke, S.; Gros, P. C., Interfacial charge separation and photovoltaic efficiency in Fe(ii)-carbene sensitized solar cells. *Phys Chem Chem Phys* **2016,** *18* (40), 28069-28081.
242. Ferrere, S., New Photosensitizers Based upon [Fe(L)2(CN)2] and [Fe(L)3] (L = Substituted 2,2‘-Bipyridine): Yields for the Photosensitization of TiO2 and Effects on the Band Selectivity. *Chemistry of Materials* **2000,** *12* (4), 1083-1089.
243. Reiher, M.; Salomon, O.; Artur Hess, B., Reparameterization of hybrid functionals based on energy differences of states of different multiplicity. *Theoretical Chemistry Accounts: Theory, Computation, and Modeling (Theoretica Chimica Acta)* **2001,** *107* (1), 48-55.
244. Fredin, L. A.; Papai, M.; Rozsalyi, E.; Vanko, G.; Warnmark, K.; Sundstrom, V.; Persson, P., Exceptional Excited-State Lifetime of an Iron(II)-N-Heterocyclic Carbene Complex Explained. *J Phys Chem Lett* **2014,** *5* (12), 2066-71.
245. Kepp, K. P., Theoretical Study of Spin Crossover in 30 Iron Complexes. *Inorg Chem* **2016,** *55* (6), 2717-27.
246. Tomasi, J.; Mennucci, B.; Cammi, R., Quantum mechanical continuum solvation models. *Chem Rev* **2005,** *105* (8), 2999-3093.
247. Plasser, F., TheoDORE: A toolbox for a detailed and automated analysis of electronic excited state computations. *J Chem Phys* **2020,** *152* (8), 084108.

248. Pastore, M.; Fantacci, S.; De Angelis, F., Modeling Excited States and Alignment of Energy Levels in Dye-Sensitized Solar Cells: Successes, Failures, and Challenges. *The Journal of Physical Chemistry C* **2013,** *117* (8), 3685-3700.
249. Pastore, M.; De Angelis, F., First-Principles Modeling of a Dye-Sensitized TiO2/IrO2 Photoanode for Water Oxidation. *J Am Chem Soc* **2015,** *137* (17), 5798-809.
250. Klamt, A.; Schüürmann, G., COSMO: a new approach to dielectric screening in solvents with explicit expressions for the screening energy and its gradient. *J. Chem. Soc., Perkin Trans. 2* **1993,** (5), 799-805.
251. Grimme, S.; Antony, J.; Ehrlich, S.; Krieg, H., A consistent and accurate ab initio parametrization of density functional dispersion correction (DFT-D) for the 94 elements H-Pu. *J Chem Phys* **2010,** *132* (15), 154104.
252. te Velde, G.; Bickelhaupt, F. M.; Baerends, E. J.; Fonseca Guerra, C.; van Gisbergen, S. J. A.; Snijders, J. G.; Ziegler, T., Chemistry with ADF. *Journal of Computational Chemistry* **2001,** *22* (9), 931-967.
253. Kondov, I.; Čížek, M.; Benesch, C.; Wang, H.; Thoss, M., Quantum Dynamics of Photoinduced Electron-Transfer Reactions in Dye−Semiconductor Systems: First-Principles Description and Application to Coumarin 343−TiO2. *The Journal of Physical Chemistry C* **2007,** *111* (32), 11970-11981.
254. Reddy Marri, A.; Marchini, E.; Cabanes, V. D.; Argazzi, R.; Pastore, M.; Caramori, S.; Gros, P. C., Record power conversion efficiencies for iron(ii)-NHC-sensitized DSSCs from rational molecular engineering and electrolyte optimization. *Journal of Materials Chemistry A* **2021,** *9* (6), 3540-3554.
255. Agrawal, S.; Leijtens, T.; Ronca, E.; Pastore, M.; Snaith, H.; De Angelis, F., Modeling the effect of ionic additives on the optical and electronic properties of a dye-sensitized TiO2 heterointerface: absorption, charge injection and aggregation. *Journal of Materials Chemistry A* **2013,** *1* (46).
256. Ronca, E.; Marotta, G.; Pastore, M.; De Angelis, F., Effect of Sensitizer Structure and TiO2 Protonation on Charge Generation in Dye-Sensitized Solar Cells. *The Journal of Physical Chemistry C* **2014,** *118* (30), 16927-16940.
257. Marri, A. R.; Marchini, E.; Cabanes, V. D.; Argazzi, R.; Pastore, M.; Caramori, S.; Bignozzi, C. A.; Gros, P. C., A Series of Iron(II)-NHC Sensitizers with Remarkable Power Conversion Efficiency in Photoelectrochemical Cells*. *Chemistry* **2021,** *27* (65), 16260-16269.
258. Di Carlo, G.; Caramori, S.; Trifiletti, V.; Giannuzzi, R.; De Marco, L.; Pizzotti, M.; Orbelli Biroli, A.; Tessore, F.; Argazzi, R.; Bignozzi, C. A., Influence of porphyrinic structure on electron transfer processes at the electrolyte/dye/TiO(2) interface in PSSCs: a comparison between meso push-pull and beta-pyrrolic architectures. *ACS Appl Mater Interfaces* **2014,** *6* (18), 15841-52.
259. Yao, W.; Das, S.; DeLucia, N. A.; Qu, F.; Boudreaux, C. M.; Vannucci, A. K.; Papish, E. T., Determining the Catalyst Properties That Lead to High Activity and Selectivity for Catalytic Hydrodeoxygenation with Ruthenium Pincer Complexes. *Organometallics* **2020,** *39* (5), 662-669.
260. Perdew, J. P.; Burke, K.; Ernzerhof, M., Generalized Gradient Approximation Made Simple [Phys. Rev. Lett. 77, 3865 (1996)]. *Physical Review Letters* **1997,** *78* (7), 1396-1396.
261. Abe, H.; Kurokawa, H.; Chida, Y.; Inouye, M., Preparation of ethynylpyridine macrocycles by oxidative coupling of an ethynylpyridine trimer with terminal acetylenes. *J Org Chem* **2011,** *76* (1), 309-11.
262. Schlosser, M.; Bobbio, C.; Rausis, T., Regiochemically flexible substitutions of di-, tri-, and tetrahalopyridines: the trialkylsilyl trick. *J Org Chem* **2005,** *70* (7), 2494-502.
263. Martin, R. L., Natural transition orbitals. *The Journal of Chemical Physics* **2003,** *118* (11), 4775-4777.
264. Santos, T. D.; Morandeira, A.; Koops, S.; Mozer, A. J.; Tsekouras, G.; Dong, Y.; Wagner, P.; Wallace, G.; Earles, J. C.; Gordon, K. C.; Officer, D.; Durrant, J. R., Injection Limitations in a

Series of Porphyrin Dye-Sensitized Solar Cells. *The Journal of Physical Chemistry C* **2010,** *114* (7), 3276-3279.
265. Ma, Y.; Pendlebury, S. R.; Reynal, A.; Le Formal, F.; Durrant, J. R., Dynamics of photogenerated holes in undoped BiVO4 photoanodes for solar water oxidation. *Chem. Sci.* **2014,** *5* (8), 2964-2973.
266. Wu, J.; Lan, Z.; Lin, J.; Huang, M.; Huang, Y.; Fan, L.; Luo, G.; Lin, Y.; Xie, Y.; Wei, Y., Counter electrodes in dye-sensitized solar cells. *Chem Soc Rev* **2017,** *46* (19), 5975-6023.
267. Ellis, H.; Vlachopoulos, N.; Häggman, L.; Perruchot, C.; Jouini, M.; Boschloo, G.; Hagfeldt, A., PEDOT counter electrodes for dye-sensitized solar cells prepared by aqueous micellar electrodeposition. *Electrochimica Acta* **2013,** *107*, 45-51.
268. Mauritz, K. A.; Moore, R. B., State of understanding of nafion. *Chem Rev* **2004,** *104* (10), 4535-85.
269. Carli, S.; Di Lauro, M.; Bianchi, M.; Murgia, M.; De Salvo, A.; Prato, M.; Fadiga, L.; Biscarini, F., Water-Based PEDOT:Nafion Dispersion for Organic Bioelectronics. *ACS Appl Mater Interfaces* **2020,** *12* (26), 29807-29817.
270. Cazzanti, S.; Caramori, S.; Argazzi, R.; Elliott, C. M.; Bignozzi, C. A., Efficient non-corrosive electron-transfer mediator mixtures for dye-sensitized solar cells. *J Am Chem Soc* **2006,** *128* (31), 9996-7.
271. Kelly, N. R.; Goetz, S.; Batten, S. R.; Kruger, P. E., Coordination behaviour and network formation with 4,4′,6,6′-tetracarboxy-2,2′-bipyridine and 4,4′-dicarboxy-2,2′-bipyridineligands with rare and alkaline earth metals. *CrystEngComm* **2008,** *10* (1), 68-78.
272. Tanguy, J.; Mermilliod, N.; Hoclet, M., Capacitive Charge and Noncapacitive Charge in Conducting Polymer Electrodes. *Journal of The Electrochemical Society* **2019,** *134* (4), 795-802.
273. Randriamahazaka, H.; Noël, V.; Chevrot, C., Nucleation and growth of poly(3,4-ethylenedioxythiophene) in acetonitrile on platinum under potentiostatic conditions. *Journal of Electroanalytical Chemistry* **1999,** *472* (2), 103-111.
274. Sakmeche, N.; Aeiyach, S.; Aaron, J.-J.; Jouini, M.; Lacroix, J. C.; Lacaze, P.-C., Improvement of the Electrosynthesis and Physicochemical Properties of Poly(3,4-ethylenedioxythiophene) Using a Sodium Dodecyl Sulfate Micellar Aqueous Medium. *Langmuir* **1999,** *15* (7), 2566-2574.
275. Carli, S.; Bianchi, M.; Zucchini, E.; Di Lauro, M.; Prato, M.; Murgia, M.; Fadiga, L.; Biscarini, F., Electrodeposited PEDOT:Nafion Composite for Neural Recording and Stimulation. *Adv Healthc Mater* **2019,** *8* (19), e1900765.
276. Efimov, I.; Winkels, S.; Schultze, J. W., EQCM study of electropolymerization and redox cycling of 3,4-polyethylenedioxythiophene. *Journal of Electroanalytical Chemistry* **2001,** *499* (1), 169-175.
277. Kayinamura, Y. P.; Ovadia, M.; Zavitz, D.; Rubinson, J. F., Investigation of near ohmic behavior for poly(3,4-ethylenedioxythiophene): a model consistent with systematic variations in polymerization conditions. *ACS Appl Mater Interfaces* **2010,** *2* (9), 2653-62.
278. Kvarnström, C.; Neugebauer, H.; Blomquist, S.; Ahonen, H. J.; Kankare, J.; Ivaska, A., In situ spectroelectrochemical characterization of poly(3,4-ethylenedioxythiophene). *Electrochimica Acta* **1999,** *44* (16), 2739-2750.
279. Ouyang, J.; Xu, Q.; Chu, C.-W.; Yang, Y.; Li, G.; Shinar, J., On the mechanism of conductivity enhancement in poly(3,4-ethylenedioxythiophene):poly(styrene sulfonate) film through solvent treatment. *Polymer* **2004,** *45* (25), 8443-8450.
280. Xia, J.; Masaki, N.; Jiang, K.; Yanagida, S., The influence of doping ions on poly(3,4-ethylenedioxythiophene) as a counter electrode of a dye-sensitized solar cell. *Journal of Materials Chemistry* **2007,** *17* (27).
281. Magni, M.; Giannuzzi, R.; Colombo, A.; Cipolla, M. P.; Dragonetti, C.; Caramori, S.; Carli, S.; Grisorio, R.; Suranna, G. P.; Bignozzi, C. A.; Roberto, D.; Manca, M., Tetracoordinated

Bis-phenanthroline Copper-Complex Couple as Efficient Redox Mediators for Dye Solar Cells. *Inorg Chem* **2016,** *55* (11), 5245-53.
282. Jacobsen, T.; West, K., Diffusion impedance in planar, cylindrical and spherical symmetry. *Electrochimica Acta* **1995,** *40* (2), 255-262.
283. Bianchi, M.; Carli, S.; Di Lauro, M.; Prato, M.; Murgia, M.; Fadiga, L.; Biscarini, F., Scaling of capacitance of PEDOT:PSS: volume vs. area. *Journal of Materials Chemistry C* **2020,** *8* (32), 11252-11262.
284. Roy-Mayhew, J. D.; Bozym, D. J.; Punckt, C.; Aksay, I. A., Functionalized graphene as a catalytic counter electrode in dye-sensitized solar cells. *ACS Nano* **2010,** *4* (10), 6203-11.
285. Tian, H.; Yu, Z.; Hagfeldt, A.; Kloo, L.; Sun, L., Organic redox couples and organic counter electrode for efficient organic dye-sensitized solar cells. *J Am Chem Soc* **2011,** *133* (24), 9413-22.
286. Kavan, L.; Yum, J.-H.; Graetzel, M., Graphene-based cathodes for liquid-junction dye sensitized solar cells: Electrocatalytic and mass transport effects. *Electrochimica Acta* **2014,** *128*, 349-359.
287. Liberatore, M.; Petrocco, A.; Caprioli, F.; La Mesa, C.; Decker, F.; Bignozzi, C. A., Mass transport and charge transfer rates for Co(III)/Co(II) redox couple in a thin-layer cell. *Electrochimica Acta* **2010,** *55* (12), 4025-4029.
288. Stojanović, M.; Flores-Diaz, N.; Ren, Y.; Vlachopoulos, N.; Pfeifer, L.; Shen, Z.; Liu, Y.; Zakeeruddin, S. M.; Milić, J. V.; Hagfeldt, A., The Rise of Dye-Sensitized Solar Cells: From Molecular Photovoltaics to Emerging Solid-State Photovoltaic Technologies. *Helvetica Chimica Acta* **2021,** *104* (4).
289. Kavan, L.; Saygili, Y.; Freitag, M.; Zakeeruddin, S. M.; Hagfeldt, A.; Grätzel, M., Electrochemical Properties of Cu(II/I)-Based Redox Mediators for Dye-Sensitized Solar Cells. *Electrochimica Acta* **2017,** *227*, 194-202.

Università degli Studi di Ferrara

Sezioni

Dottorati di ricerca

Il tuo indirizzo e-mail

mrcdrd@unife.it

Oggetto:

Dichiarazione di conformità della tesi di Dottorato

Io sottoscritto Dott. (Cognome e Nome)

Marchini Edoardo

Nato a:

Ferrara

Provincia:

Ferrara

Il giorno:

18-07-1994

Avendo frequentato il Dottorato di Ricerca in:

Scienze Chimiche

Ciclo di Dottorato

34

Titolo della tesi:

New Components for Dye Sensitized Solar Cells

Titolo della tesi (traduzione):

Nuovi Componenti per Celle Solari Sensibilizzate con Colorante

Tutore: Prof. (Cognome e Nome)

Caramori Stefano - Massi Alessandro

Settore Scientifico Disciplinare (S.S.D.)

CHIM/03

Parole chiave della tesi (max 10):

DSSC, Photovoltaic, Iron Sensitizers, PEDOT, Fotovoltaico, Sensibilizzatori di Ferro

Consapevole, dichiara

CONSAPEVOLE: (1) del fatto che in caso di dichiarazioni mendaci, oltre alle sanzioni previste dal codice penale e dalle Leggi speciali per l'ipotesi di falsità in atti ed uso di atti falsi, decade fin dall'inizio e senza necessità di alcuna formalità dai benefici conseguenti al provvedimento emanato sulla base di tali dichiarazioni; (2) dell'obbligo per l'Università di provvedere al deposito di legge delle tesi di dottorato al fine di assicurarne la conservazione e la consultabilità da parte di terzi; (3) della procedura adottata dall'Università di Ferrara ove si richiede che la tesi sia consegnata dal dottorando in 1 originale cartaceo e 1 in formato PDF/A caricata sulla procedura informatica Esse3 secondo le istruzioni pubblicate sul sito: http://www.unife.it/studenti/dottorato alla voce ESAME FINALE – disposizioni e modulistica; (4) del fatto che l'Università, sulla base dei dati forniti, archivierà e renderà consultabile in rete il testo completo della tesi di dottorato di cui alla presente dichiarazione attraverso la pubblicazione ad accesso aperto nell'Archivio Istituzionale dei Prodotti della Ricerca IRIS-UNIFE (www.iris.unife.it) oltre che attraverso i Cataloghi delle Biblioteche Nazionali Centrali di Roma e Firenze; DICHIARO SOTTO LA MIA RESPONSABILITA': (1) che la copia della tesi depositata presso l'Università di Ferrara in formato cartaceo è del tutto identica a quella caricata in formato PDF/A sulla procedura informatica Esse3, a

quelle da inviare ai Commissari di esame finale e alla copia che produrrò in seduta d'esame finale. Di conseguenza va esclusa qualsiasi responsabilità dell'Ateneo stesso per quanto riguarda eventuali errori, imprecisioni o omissioni nei contenuti della tesi; (2) di prendere atto che la tesi in formato cartaceo è l'unica alla quale farà riferimento l'Università per rilasciare, a mia richiesta, la dichiarazione di conformità di eventuali copie; (3) che il contenuto e l'organizzazione della tesi è opera originale da me realizzata e non compromette in alcun modo i diritti di terzi, ivi compresi quelli relativi alla sicurezza dei dati personali; che pertanto l'Università è in ogni caso esente da responsabilità di qualsivoglia natura civile, amministrativa o penale e sarà da me tenuta indenne da qualsiasi richiesta o rivendicazione da parte di terzi; (4) che la tesi di dottorato non è il risultato di attività rientranti nella normativa sulla proprietà industriale, non è stata prodotta nell'ambito di progetti finanziati da soggetti pubblici o privati con vincoli alla divulgazione dei risultati, non è oggetto di eventuali registrazioni di tipo brevettale o di tutela. PER ACCETTAZIONE DI QUANTO SOPRA RIPORTATO

Dichiarazione per embargo

6 mesi

Richiesta motivata embargo

1. Tesi in corso di pubblicazione

Liberatoria consultazione dati Eprints

Consapevole del fatto che attraverso l'Archivio Istituzionale ad accesso aperto dei Prodotti della Ricerca IRIS-UNIFE (www.iris.unife.it) saranno comunque accessibili i metadati relativi alla tesi (titolo, autore, abstract, ecc.)

Firma del dottorando

Ferrara, li 25-05-2022 Firma del Dottorando: Edoardo Marchini 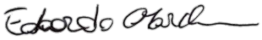

Firma del Tutore

Visto: Il Tutore Prof. Stefano Caramori - Prof. Alessandro Massi Si approva Firma del Tutore: Stefano Caramori - Alessandro Massi